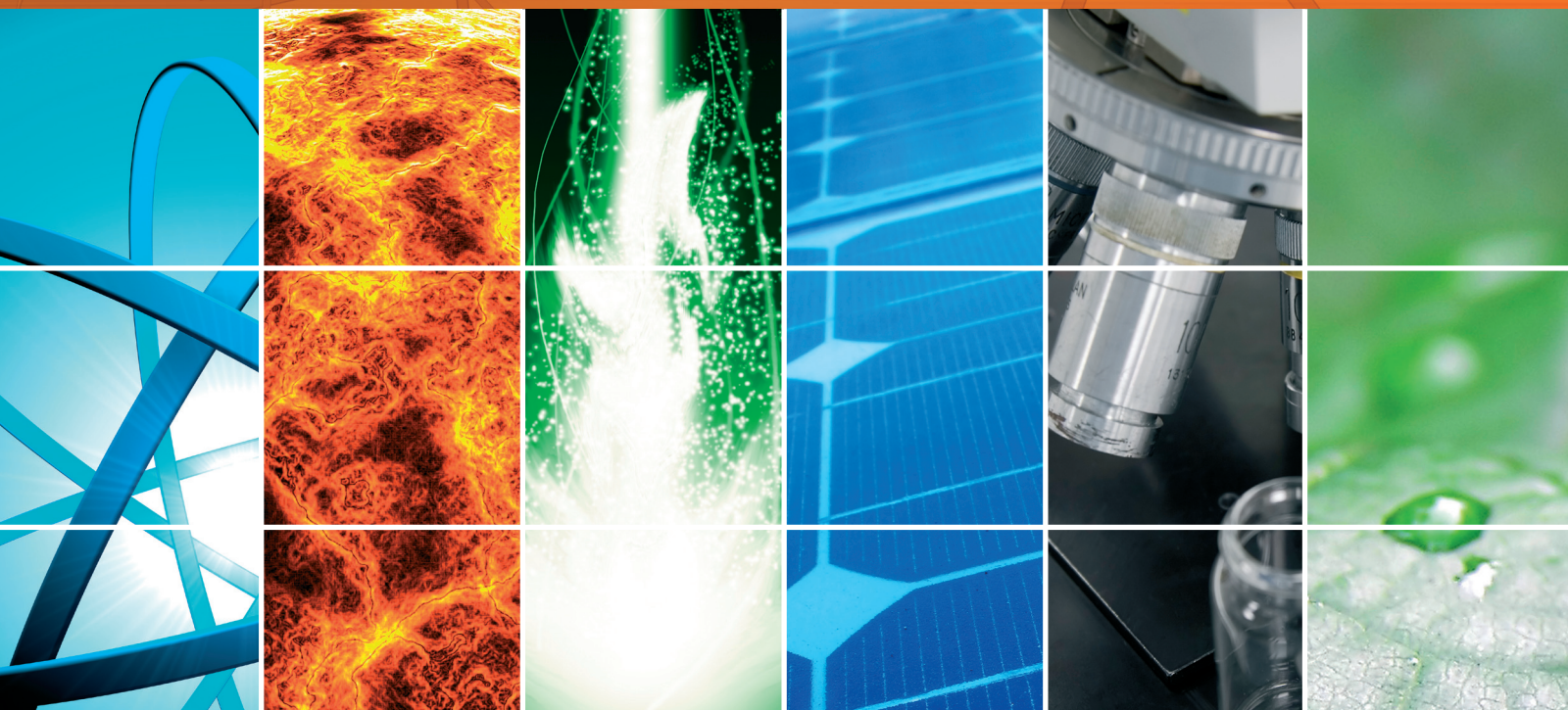# Structurally and Elementally Promoted Nanomaterials for Photocatalysis

Guest Editors: Tian-Yi Ma, Zhan-Ying Zhang, Jian-Liang Cao, Luminita Andronic, Yong Ma, and Lei Liu

Structurally and Elementally Promoted Nanomaterials for Photocatalysis

Structurally and Elementally Promoted Nanomaterials for Photocatalysis

Guest Editors: Tian-Yi Ma, Zhan-Ying Zhang, Jian-Liang Cao, Luminita Andronic, Yong Ma, and Lei Liu

Editorial Board

Contents

Editorial

Structurally and Elementally Promoted Nanomaterials for Photocatalysis

Tian-Yi Ma,[1] Zhan-Ying Zhang,[2] Jian-Liang Cao,[2] Luminita Andronic,[3] Yong Ma,[4] and Lei Liu[5]

[1] School of Chemical Engineering, The University of Adelaide, Adelaide, SA 5005, Australia

[2] School of Materials Science and Engineering, Henan Polytechnic University, Jiaozuo, Henan 454000, China

[3] Centre of Renewable Energy Systems and Recycling, Transilvania University of Brasov, Eroilor 29, 500036 Brasov, Romania

[4] College of Chemistry, Chemical Engineering and Food Safety, Bohai University, Jinzhou, Liaoning 121013, China

[5] School of Materials Science and Engineering, Shandong University of Science and Technology, Qingdao, Shandong 266590, China

Correspondence should be addressed to Tian-Yi Ma; matianyichem@gmail.com, Jian-Liang Cao; caojianliang@gmail.com and Yong Ma; mayong0416@163.com

Due to the increasingly polluted environment and the gradual depletion of fossil fuel reserves, the development of renewable technologies for environmental remediation and energy production is highly desirable. The photoenergy, specifically the solar energy, represents the ultimate energy source to sustain all lives on our planet and is also the energy source of the fossil fuels that are driving our technology. Thus, the direct harvest and conversion of solar energy into usable energy format are urgently required and considerably meet the requirements for the current issues on environment and energy, in which photocatalysis process initiated on nanomaterials is a crucial element, due to its inexpensive and clean nature by using abundant, cheap, and environmental friendly chemical reagents, energy source, and catalysts without secondary pollution [1]. Generally, nanomaterials for photocatalysis focus mainly on four aspects, namely, photocatalytic degradation of organic pollutants, photocatalytic water splitting to produce H_2 and O_2, photocatalytic reduction of CO_2, and photocatalytic synthesis for organic substances [2].

Nanostructured materials have attracted considerable attention for photocatalysis due to their unique physical and chemical properties in comparison to their bulk counterparts. These diverse nanostructures such as nanocrystals, nanopores, nanotubes, nanorods, nanowires, and other more complex hierarchical architectures with large surface areas, high surface to volume ratios, and numerous accessible catalytic active sites as well as efficient mass transport have been demonstrated to show extraordinary photocatalytic activity [3]. On the other hand, the manipulation of chemical compositions of nanomaterials is also effective in improving their photocatalysis performance, aiming at altering the electronic structures of catalysts and their surface properties. One of the well-known examples is the chemically doping of foreign elements which can greatly regulate the optical property of the resultant nanostructured TiO_2, leading to extended photoabsorption range and reducing the recombination of photoinduced electrons and holes [4].

Therefore, engineering of both the chemical composition and the morphology is of significant importance in promoting the specific photocatalytic activity of nanomaterials, which are extensively utilized by the novel works involved in this special issue, including 1 review article and 12 research papers. The review article summarized the hierarchical architectures from inorganic nanocrystal self-assembly, which show collective properties that differ from individual nanocrystals and bulk samples and exhibit many superiority in mass transfer and light harvesting, thus finding great application potential in photoenergy storage and conversion including photodegradation, photocatalytic H_2 production, photocatalytic CO_2 conversion, and sensitized solar cells.

In the research articles, different synthetic strategies were employed to construct delicate semiconductor nanostructures for photocatalysis, that is, synthesis of hierarchically porous α-FeOOH, macroporous TiO_2, and mesoporous TiO_2-SnO_2 nanocomposites via a polystyrene microsphere-templating route for high-performance photodegradation of organic dyes, sonochemical preparation of mesoporous N-doped TiO_2 nanoparticles for Rhodamine B photodegradation, solvothermal synthesis of Zn_2SnO_4 nanocrystals with high methyl orange depredating property, and fabrication of flower-like Cu_2ZnSnS_4 nanoflakes through a microwave-assisted solvothermal pathway with a direct band gap of 1.52 eV for efficient photoresponse.

Moreover, a comprehensive study was established for the synthesis of Cu-TiO_2 nanotubes by electrochemical anodization and wet impregnation for UV photocatalysis removal of low-concentration Pb (II) ions. Mesoporous nanocrystalline titania photocatalysts were prepared in both acidic and basic media with the assistance of micellar surfactants, showing high photocatalytic activity in naphthalene degradation. The visible-light driven photocatalytic and photoelectrocatalytic degradation of humic acid was achieved by Cu/N codoped TiO_2 films grown on Ti substrates.

We do believe that these review and research articles will not only enrich our knowledge on promoting the nanophotocatalysis in structural and elemental aspects but also indicate the existence of a lot more technological issues which make this field more attractive and challenging.

Acknowledgments

Tian-Yi Ma
Zhan-Ying Zhang
Jian-Liang Cao
Luminita Andronic
Yong Ma
Lei Liu

References

[1] A. L. Linsebigler, G. Lu, and J. T. Yates Jr., "Photocatalysis on TiO_2 surfaces: principles, mechanisms, and selected results," *Chemical Reviews*, vol. 95, no. 3, pp. 735–758, 1995.

[2] M. R. Hoffmann, S. T. Martin, W. Choi, and D. W. Bahnemann, "Environmental applications of semiconductor photocatalysis," *Chemical Reviews*, vol. 95, no. 1, pp. 69–96, 1995.

[3] Y. Qu and X. Duan, "Progress, challenge and perspective of heterogeneous photocatalysts," *Chemical Society Reviews*, vol. 42, pp. 2568–2580, 2013.

[4] L. Jing, W. Zhou, G. Tian, and H. Fu, "Surface tuning for oxide-based nanomaterials as efficient photocatalysts," *Chemical Society Reviews*, vol. 42, pp. 9509–9549, 2013.

Research Article

Fabrication of a Porous TiO$_2$-Coated Silica Glass Tube and Its Application for a Handy Water Purification Unit

Tsuyoshi Ochiai,[1,2] Shoko Tago,[1] Hiromasa Tawarayama,[3] Toshifumi Hosoya,[4] Hitoshi Ishiguro,[5,6] and Akira Fujishima[1,2]

[1] *Kanagawa Academy of Science and Technology, KSP building East 407, 3-2-1 Sakado, Takatsu-ku, Kawasaki, Kanagawa 213-0012, Japan*

[2] *Photocatalysis International Research Center, Tokyo University of Science, 2641 Yamazaki, Noda, Chiba 278-8510, Japan*

[3] *Optical Communications R&D Laboratories, Sumitomo Electric Industries, Ltd., 1 Taya-cho, Sakae-ku, Yokohama 244-8588, Japan*

[4] *R&D General Planning Division, Sumitomo Electric Industries, Ltd., 1-1-3 Shimaya, Konohana-ku, Osaka 554-0024, Japan*

[5] *Kanagawa Academy of Science and Technology, LiSE Lab., 3-25-13 Tonomachi, Kawasaki-ku, Kawasaki, Kanagawa 210-0821, Japan*

[6] *Department of Urology, Yokohama City University Graduate School of Medicine, 3-9 Fukuura, Kanazawa-ku, Yokohama 236-0004, Japan*

Correspondence should be addressed to Tsuyoshi Ochiai; pg-ochiai@newkast.or.jp

A simple, handy, reusable, and inexpensive water purification unit including a one-end sealed porous amorphous-silica (a-silica) tube coated with 2 μm of porous TiO$_2$ photocatalyst layers has been developed. Both TiO$_2$ and a-silica layers were formed through outside vapor deposition (OVD). Raman spectrum of the porous TiO$_2$-coated a-silica glass tube indicated that the anatase content of the TiO$_2$ layers of the tube was estimated to be approximately 60 wt%. Developed porous TiO$_2$-coated a-silica glass tube has been assayed for the tube filtering feature against *Escherichia coli* (*E. coli*) solution used as one of the typical bacteria size species or Qβ phage also used as typical virus size species and compared with the feature of porous a-silica tubes alone. The tubes removed *E. coli* completely from the aqueous suspension which contained 10^6 CFU/mL of *E. coli* without UV irradiation. The porous TiO$_2$-coated a-silica glass tube with UV-C lamps successfully reduced the Qβ phage amount in the suspension from 10^9 to 10^3 PFU/mL.

1. Introduction

In recent decades, the global human population growth has needed more water. However, there are plenty areas which still need more water purification technologies (especially a water disinfection unit) to use for area residents or industries [1]. Various water treatment systems such as solar disinfection, chlorination, and filtration to reduce illness have been studied and realized [2–7]. Among these technologies, TiO$_2$ photocatalysis has received growing attention [8, 9]. However, there is no report about a simple, handy, reusable, and inexpensive photocatalytic water purification unit yet. At the same time, there is also no report about handy photocatalytic unit for the removal of not only bacteria (several micrometers) but also viruses (several ten nanometers) because of

the viruses' extremely small size. We have reported that TiO$_2$ photocatalysts can decompose refractory chemicals [10], gaseous contaminants [11], and waterborne pathogens [12] with their strong oxidation ability [13]. Moreover, we also have reported various methods for the design and applications of TiO$_2$ photocatalyst to maximize its photocatalytic abilities [14–17]. On the other hand, we have succeeded the simple fabrication of novel one-end sealed porous amorphous-silica (a-silica) tubes with large porosity by the outside vapor deposition (OVD) method [18, 19]. The porous tube is believed to be a good supporting material for gas and/or liquid separation. Based on these backgrounds, now we report a porous TiO$_2$-coated a-silica glass tube and its application for a handy water purification unit. The units consist of the porous TiO$_2$-coated a-silica glass tubes and small
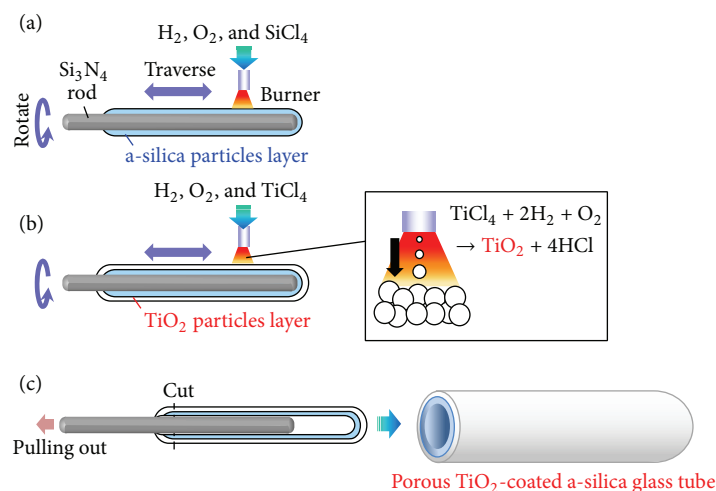
FIGURE 1: Schematic diagram of the fabrication method for porous TiO$_2$-coated a-silica glass tube by the OVD method.

UV lamps were fabricated and evaluated for their biological purification activity by using both *E. coli* (typical bacteria size species) and Qβ phage (typical virus size species).

2. Materials and Methods

2.1. Fabrication of the Porous TiO$_2$-Coated a-Silica Glass Tube. Figure 1 shows the fabrication method of the porous TiO$_2$-coated a-silica glass tube by the OVD method. Fine a-silica particles synthesized by hydrolysis of SiCl$_4$ in an oxygen-hydrogen flame burner were deposited on a rotating Si$_3$N$_4$ rod target with a diameter of 6 mm (Figure 1(a)). After the deposition of a-silica, TiO$_2$ particles synthesized by hydrolysis of TiCl$_4$ in the flame burner were deposited onto the porous a-silica glass layer (Figure 1(b)). After the deposition, a one-end sealed porous tube was obtained by pulling out the rod target from the soot body (Figure 1(c)). The external diameter and the length of the obtained porous tube were 8.5 mm and 300 mm, respectively. The morphology of the porous structure was observed with an FE-SEM (S-4800, Hitachi, Tokyo). Samples for cross-section observation were prepared by embedding in resin and then polishing with a cross-section polisher (SM-09010, JEOL, Tokyo). Pore size distribution was measured using a mercury porosimeter (AutoPore III 9420, Micromeritics Instrument, CA). For the structural characterization of the films, Raman spectroscopy excited by 532 nm Nd:YAG laser (LabRAM HR-800, HORIBA JOVIN YVON, Longjumeau, France) was used. For comparison, the porous a-silica glass tube without TiO$_2$ layer was also fabricated.

2.2. Waterborne Pathogens Removal Test. Escherichia coli NBRC3972 (*E. coli*) and Qβ phage NBRC20012 (Qβ) were used as the main test waterborne pathogens to assess the biological purification efficiency of the tubes. *E. coli* and Qβ were obtained from the Biological Resource Center of the National Institute of Technology and Evaluation (Chiba,
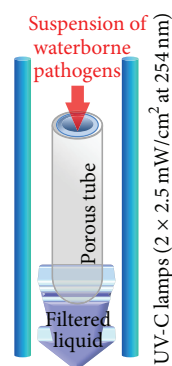
FIGURE 2: Schematic illustration of a handy water purification unit consisted of the porous tube and a pair of UV-C lamps.

Japan). *E. coli* and Qβ were propagated and assayed by previously described methods [12, 20]. The aqueous suspensions of *E. coli* or Qβ were used as the biologically contaminated water models. In this study, the numbers of *E. coli* and Qβ in the suspension were approximately 10^6 colony-forming units per mL (CFU/mL) and 10^9 plaque-forming units per mL (PFU/mL), respectively. Figure 2 shows a handy water purification unit consisting of the porous tube and a pair of super-small-sized cold cathode UV-C lamps (2.5 mW/cm^2 @ 254 nm, ϕ 6 mm × 30 mm, Sankyo Denki Co., Ltd., Kanagawa, Japan). The UV intensity at 254 nm at the surface of the porous tube was measured by a UV-radiometer UVR-300 with a sensor head UD-250 (Topcon Corporation, Japan). In a typical run (TiO$_2$(+), UV(+)), 4 mL of the Qβ suspension was poured into the porous TiO$_2$-coated a-silica glass tube and was filtered by applying pressure at the filtration rate of 0.4 mL/min for 1 min under UV-C irradiation. Filtered suspension was collected to test tube and assayed by previously described methods [12, 20] to analyze the viability of Qβ. The effective filtration area of the porous tube was approximately 27 cm^2 (the effective filtration length of the porous tube

(a)

(b)

(c)
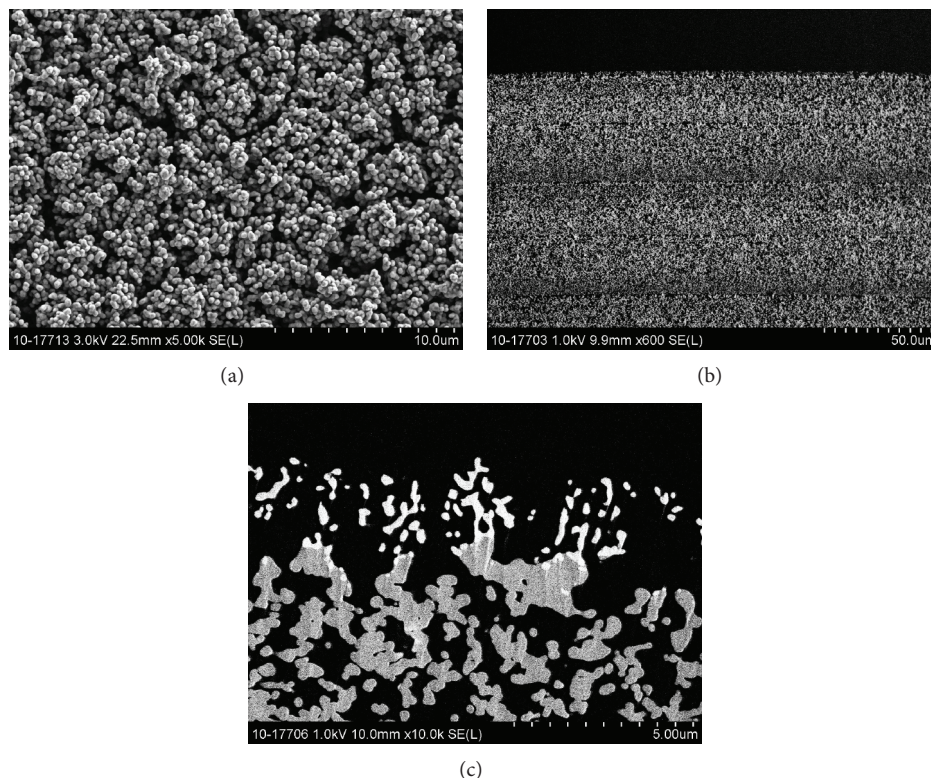
FIGURE 3: SEM images of the surface (a) and the cross-section (b) of the porous TiO_2-coated a-silica glass tube and a high-magnification SEI of cross-section of stacked TiO_2 layers over a-silica layers (c).

was 10 cm). For comparison, the porous TiO_2-coated a-silica glass tube under no UV-C irradiation ($TiO_2(+)$, UV($-$)), the porous a-silica glass tube without TiO_2 layer under UV-C irradiation ($TiO_2(-)$, UV($+$)), and the porous a-silica glass tube without TiO_2 layer under no UV-C irradiation ($TiO_2(-)$, UV($-$)) were also evaluated by the same method.

3. Results and Discussion

3.1. Characterization. SEM images of the surface and the cross-section of the porous TiO_2-coated a-silica glass tube are shown in Figures 3(a) and 3(b). The open pore structure was found to be constructed by the sintering process. Figure 3(c) shows a high-magnification secondary electron image (SEI) of cross-section of stacked TiO_2 layers over a-silica layers. White, gray, and black areas in Figure 3(c) represent TiO_2 particles, a-silica particles, and the resin intruded into the pore, respectively. Both TiO_2 and a-silica layers were porous and fit each other on the border. TiO_2 layers' average of the grains cross section area seemed to be smaller than that of a-silica. Stacked TiO_2 layers thickness on a-silica layers was approximately $2\,\mu m$. This thickness is enough to impart photocatalytic property onto the surface. An average porosity and an average bulk density of the porous tubes were 0.62 and $0.84\,g/cm^3$, respectively. We have found that porous tubes with different apparent porosities can be prepared by changing deposition temperature and the average pore diameter slightly and gradually decreased from 0.40 to $0.35\,\mu m$ with

decreasing the porosity from 0.64 to 0.39 [19]. Based on this insight, the pore diameter of the porous tubes in this research can be estimated to be $0.40\,\mu m$.

The Raman spectrum of the porous TiO_2-coated a-silica glass tube is shown in Figure 4. The Raman bands at 138, 235, 446, and $607\,cm^{-1}$ almost agree with the spectrum of the rutile phase [21]. By contrast, anatase phase shows 147, 198, 398, 515, and $640\,cm^{-1}$ [21]. Oh and Ishigaki synthesized TiO_2 nanopowders with various anatase/rutile ratio using in-flight oxidation of TiN powder in a radio frequency thermal plasma reactor and characterized its microstructure by X-ray diffraction and Raman spectroscopy [22]. They concluded that O_2 rapidly diffused from the oxidized shell into the TiN core; simultaneously, the evaporation of the particles was accelerated. The vaporized species rapidly solidified into anatase or rutile nanopowders, depending on the ambient O_2 concentration. In this research, Raman spectrum of the porous TiO_2-coated a-silica glass tube is similar to the spectrum of the TiO_2 nanopowders with 60 wt% of anatase content prepared by in-flight oxidation of TiN powder under relatively low O_2 concentration (3-4 vol%). Therefore, the Raman spectroscopy indicates that TiO_2 layers in the porous TiO_2-coated a-silica glass tube are consisted of both rutile and anatase crystals. Repeating heat process with a burner in OVD method seemed to lead some amount of rutile crystals.

3.2. Result of Waterborne Pathogens Removal Test. The *E. coli* concentration in the prepared *E. coli* solution was determined
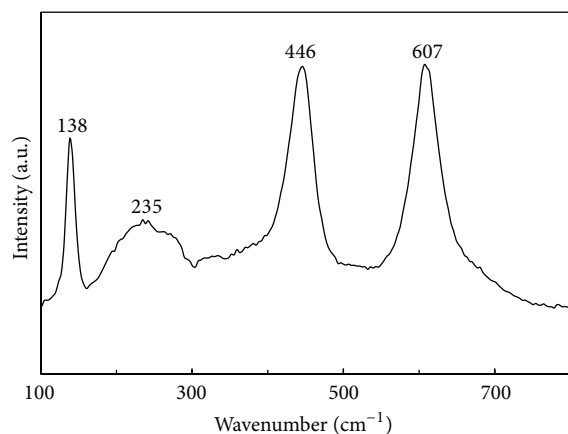
FIGURE 4: Raman spectrum of the surface of the porous TiO_2-coated a-silica glass tube.

FIGURE 5: The $Q\beta$ reduction test result with the porous a-silica glass tube without TiO_2 layer under no UV-C irradiation ($TiO_2(-)$, UV($-$)), the porous TiO_2-coated a-silica glass tube under no UV-C irradiation ($TiO_2(+)$, UV($-$)), the porous a-silica glass tube without TiO_2 layer under UV-C irradiation ($TiO_2(-)$, UV($+$)), and the porous TiO_2-coated a-silica glass tube under UV-C irradiation ($TiO_2(+)$, UV($+$)).

as 6.6×10^6 CFU/mL. There was no *E. coli* colony on agar plate which incubated filtered *E. coli* solution drops with a porous a-silica tube or a porous TiO_2 covered a-silica tube without UV-C lamps. Controlling the pressure with a pump makes filtering rate faster without *E. coli* leakage from the porous tubes. Then, it can be said that the range of pore size 0.40 μm of the porous tubes in this research is big enough to let water pass through it and small enough to remove bacteria. However, this pore size of the porous tubes is larger than the viruses' size (viruses are 100 times smaller than bacteria). Thus, in contrast to the physical method of using the porous tubes to retain bacteria, removal of viruses would require a more chemical approach such as electrostatic charge [23]. In order to satisfy this requirement, photocatalytic $Q\beta$ removal test was carried out.

Figure 5 shows the result of $Q\beta$ removal test. The $Q\beta$ concentration in the prepared $Q\beta$ solution was determined as 1.6×10^9 PFU/mL. Filtering $Q\beta$ solutions by the porous a-silica tube (Ti($-$), UV($-$)) and TiO_2 covered a-silica tube (Ti($+$), UV($-$)) reduced $Q\beta$ by 97.9% and 97.3%, respectively. The result indicates that filtering $Q\beta$ solutions reduces $Q\beta$ concentration; however, there are still plenty amounts of $Q\beta$ (3.3×10^7 and 4.4×10^7 PFU/mL, resp.). Nevertheless, there was no much difference between the two filtering features against the $Q\beta$ solution without UV-C lamps. On the other hand, with UV-C lamps turned on, filtering $Q\beta$ solution by the porous a-silica tube (Ti($-$), UV($+$)) and TiO_2 covered a-silica tube (Ti($+$), UV($+$)) significantly reduced $Q\beta$ by 99.99973 (5.6-log reduction) and 99.99994% (6.2-log reduction). The result showed that UV-C lamps removed $Q\beta$ effectively while filtering and dropping the $Q\beta$ solution between the lamps. The U.S. Environmental Protection Agency's microbiological reduction requirements for bacteria and viruses are 6-log and 4-log reduction, respectively. Therefore, it is found that UV-C lamps greatly improve the device ability to remove/inactivate $Q\beta$ by inducing of the photocatalysis.

It is well known that anatase TiO_2 exerts higher photocatalytic activity than the rutile one in many reactions [24–26]. However, there have been a few reports which deal with biocidal activities of TiO_2 with different crystalline structures. Sato
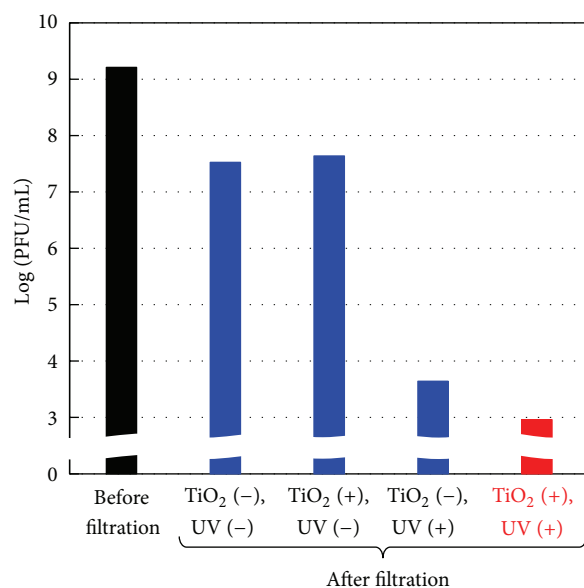
and Taya reported that the biocidal activity of TiO_2 particles against bacteriophage MS2 phage was maximized at 70 wt% of anatase ratio in mixture of TiO_2 particles as compared with the activity at 0 and 100 wt% [27]. They suggested that the contact between both types of TiO_2 in aggregations caused the enhancement of the quantum yield of TiO_2 suspension and thereby the reactive oxygen species generation, which leads to the encouragement of biocidal activity of the TiO_2 particles. Therefore, optimization of anatase ratio from 60 to 70 wt% in the TiO_2 layer of the tube by controlling the OVD condition is effective for the increased photocatalytic biocidal activity.

4. Conclusions

A handy water purification unit including a porous TiO_2-coated a-silica glass tube prepared by the OVD method was investigated. The porous TiO_2 layers were successfully deposited onto porous a-silica glass tube surface with 2 μm of thickness. An average porosity and an average bulk density of the porous tubes were 0.62 and 0.84 g/cm^3, respectively. The pore diameter of the porous tubes was estimated to be 0.40 μm. This size was big enough to let water pass through the tubes and small enough to retain *E. coli*. Raman spectrum of the porous TiO_2-coated a-silica glass tube indicated that the anatase content of the TiO_2 layers of the tube was estimated to be approximately 60 wt%. The photocatalytic activity of the porous TiO_2-coated a-silica glass tube with UV-C lamps showed the highest $Q\beta$ reduction efficiency (6.2-log reduction) compared with the filtration by using the porous

a-silica glass tube alone (1.7-log reduction), the porous TiO_2-coated a-silica glass tube alone (1.7-log reduction), and the porous a-silica glass tube without TiO_2 layer with UV-C lamps (5.6-log reduction). Therefore, a porous TiO_2-coated a-silica glass tube has great potential as a handy water purification unit.

Conflict of Interests

The authors declare that there is no conflict of interests regarding the publication of this paper.

Acknowledgments

References

[1] G. Howard, M. E. Ince, O. Schmoll, and M. D. Smith, *Rapid Asssessment of Drinking-Water Quality: A Handbook for Implementation*, World Health Organization, 2012.

[2] H. van der Laan, D. van Halem, P. W. M. H. Smeets et al., "Bacteria and virus removal effectiveness of ceramic pot filters with different silver applications in a long term experiment," *Water Research*, vol. 51, pp. 47–54, 2014.

[3] P. R. Hunter, "Household water treatment in developing countries: comparing different intervention types using meta-regression," *Environmental Science and Technology*, vol. 43, no. 23, pp. 8991–8997, 2009.

[4] C. Young-Rojanschi and C. Madramootoo, "Intermittent versus continuous operation of biosand filters," *Water Research*, vol. 49, pp. 1–10, 2014.

[5] S. Kroll, L. Treccani, K. Rezwan, and G. Grathwohl, "Development and characterisation of functionalised ceramic microtubes for bacteria filtration," *Journal of Membrane Science*, vol. 365, no. 1-2, pp. 447–455, 2010.

[6] S. Malato, P. Fernández-Ibáñez, M. I. Maldonado, J. Blanco, and W. Gernjak, "Decontamination and disinfection of water by solar photocatalysis: recent overview and trends," *Catalysis Today*, vol. 147, no. 1, pp. 1–59, 2009.

[7] V. R. Hill, A. M. Kahler, N. Jothikumar, T. B. Johnson, D. Hahn, and T. L. Cromeans, "Multistate evaluation of an ultrafiltration-based procedure for simultaneous recovery of enteric microbes in 100-liter tap water samples," *Applied and Environmental Microbiology*, vol. 73, no. 13, pp. 4218–4225, 2007.

[8] M. N. Chong, B. Jin, C. W. K. Chow, and C. Saint, "Recent developments in photocatalytic water treatment technology: a review," *Water Research*, vol. 44, no. 10, pp. 2997–3027, 2010.

[9] T. Ochiai and A. Fujishima, "Photoelectrochemical properties of TiO_2 photocatalyst and its applications for environmental purification," *Journal of Photochemistry and Photobiology C: Photochemistry Reviews*, vol. 13, no. 4, pp. 247–262, 2012.

[10] T. Ochiai, Y. Iizuka, K. Nakata et al., "Efficient decomposition of perfluorocarboxylic acids in aqueous suspensions of a TiO_2 photocatalyst with medium-pressure ultraviolet lamp irradiation under atmospheric pressure," *Industrial and Engineering Chemistry Research*, vol. 50, no. 19, pp. 10943–10947, 2011.

[11] T. Ochiai, K. Nakata, T. Murakami, Y. Morito, S. Hosokawa, and A. Fujishima, "Development of an air-purification unit using a photocatalysis-plasma hybrid reactor," *Electrochemistry*, vol. 79, no. 10, pp. 838–841, 2011.

[12] T. Ochiai, H. Nanba, T. Nakagawa et al., "Development of an O_3-assisted photocatalytic water-purification unit by using a TiO_2 modified titanium mesh filter," *Catalysis Science and Technology*, vol. 2, no. 1, pp. 76–78, 2012.

[13] A. Fujishima and K. Honda, "Electrochemical photolysis of water at a semiconductor electrode," *Nature*, vol. 238, no. 5358, pp. 37–38, 1972.

[14] K. Nakata, T. Kagawa, M. Sakai et al., "Preparation and photocatalytic activity of robust titania monoliths for water remediation," *ACS Applied Materials & Interfaces*, vol. 5, no. 3, pp. 500–504, 2013.

[15] T. Ochiai, T. Hoshi, H. Slimen et al., "Fabrication of a TiO_2 nanoparticles impregnated titanium mesh filter and its application for environmental purification," *Catalysis Science and Technology*, vol. 1, no. 8, pp. 1324–1327, 2011.

[16] B. Liu, K. Nakata, M. Sakai et al., "Hierarchical TiO_2 spherical nanostructures with tunable pore size, pore volume, and specific surface area: facile preparation and high-photocatalytic performance," *Catalysis Science & Technology*, vol. 2, no. 9, pp. 1933–1939, 2012.

[17] K. R. Reddy, K. Nakata, T. Ochiai, T. Murakami, D. A. Tryk, and A. Fujishima, "Facile fabrication and photocatalytic application of Ag nanoparticles-TiO_2 nanofiber composites," *Journal of nanoscience and nanotechnology*, vol. 11, no. 4, pp. 3692–3695, 2011.

[18] V. Petit, A. Le Rouge, F. Béclin, H. El Hamzaoui, and L. Bigot, "Experimental study of SiO2 soot deposition using the outside vapor deposition method," *Aerosol Science and Technology*, vol. 44, no. 5, pp. 388–394, 2010.

[19] H. Tawarayama, R. Yamaguchi, M. Kanezashi et al., "Fabrication and characterization of porous amorphous silica tubes via the outsidevapor deposition method," Manuscript to be submitted.

[20] Y. Yao, T. Ochiai, H. Ishiguro, R. Nakano, and Y. Kubota, "Antibacterial performance of a novel photocatalytic-coated cordierite foam for use in air cleaners," *Applied Catalysis B: Environmental*, vol. 106, no. 3-4, pp. 592–599, 2011.

[21] U. Balachandran and N. G. Eror, "Raman spectra of titanium dioxide," *Journal of Solid State Chemistry*, vol. 42, no. 3, pp. 276–282, 1982.

[22] S.-M. Oh and T. Ishigaki, "Preparation of pure rutile and anatase TiO_2 nanopowders using RF thermal plasma," *Thin Solid Films*, vol. 457, no. 1, pp. 186–191, 2004.

[23] A. Sato, R. Wang, H. Ma, B. S. Hsiao, and B. Chu, "Novel nanofibrous scaffolds for water filtration with bacteria and virus removal capability," *Journal of Electron Microscopy*, vol. 60, no. 3, pp. 201–209, 2011.

[24] A. Mills and P. Sawunyama, "Photocatalytic degration of 4-chlorophenol mediated by TiO_2: a comparative study of the activity of laboratory made and commercial TiO_2 samples," *Journal of Photochemistry and Photobiology, A: Chemistry*, vol. 84, no. 3, pp. 305–309, 1994.

[25] A. Sclafani and J. M. Herrmann, "Comparison of the photoelectronic and photocatalytic activities of various anatase and rutile forms of titania in pure liquid organic phases and in aqueous solutions," *The Journal of Physical Chemistry*, vol. 100, no. 32, pp. 13655–13661, 1996.

[26] U. Sirimahachai, S. Phongpaichit, and S. Wongnawa, "Evaluation of bactericidal activity of TiO$_2$ photocatalysts: a comparative study of laboratory-made and commercial TiO$_2$ samples," *Songklanakarin Journal of Science and Technology*, vol. 31, no. 5, pp. 517–525, 2009.

[27] T. Sato and M. Taya, "Enhancement of phage inactivation using photocatalytic titanium dioxide particles with different crystalline structures," *Biochemical Engineering Journal*, vol. 28, no. 3, pp. 303–308, 2006.

Research Article

Synergy of the Combination of Titanate Nanotubes with Titania Nanoparticles for the Photocatalytic Hydrogen Generation from Water-Methanol Mixture Using Simulated Sunlight

Marco Serra and Hermenegildo Garcia

Instituto Universitario de Tecnología Química CSIC-UPV, Universitat Politècnica de València, Avenida de los Naranjos s/n, 46022 Valencia, Spain

Correspondence should be addressed to Hermenegildo Garcia; hgarcia@qim.upv.es

Alkali digestion of titanium nanoparticles leads, after neutralization, to the formation of titanate nanotubes with long aspect ratio. One salient change in the formation of titanate nanotubes is the observation of an extended visible absorption band up to 550 nm, responsible for their brown colour. Combination of titanate nanotubes with commercial titanium dioxide nanoparticles, either Evonik P25 or Millennium PC500, results in an enhanced photocatalytic activity for hydrogen generation from water-methanol mixtures. This synergy between the two titanium semiconductors has an optimum for a certain proportion of the two components and is observed in both the absence and the presence of platinum or gold nanoparticles. The best efficiency under simulated sunlight irradiation was for a combination of 12 wt.% titanate nanotubes containing 0.32 wt.% platinum in 88 wt.% Millennium PC500, where a two-time increase in the hydrogen generation is observed versus the activity of Millennium PC500 containing platinum. This synergy is proposed to derive from the interfacial electron transfer from titanate nanotubes undergoing photoexcitation at wavelengths in which Millennium PC500 does not absorb this form of titania nanoparticles. Our results illustrate how the combination of several titanium semiconductors can result in an enhancement efficiency with respect to their individual components.

1. Introduction

Photocatalysis applied to solar fuel production is a topic of much current interest and a long-term alternative to fossil fuels [1–5]. Considering the current low efficiency of the photocatalytic activity in solar fuel production enhancement of the efficiency is a continuous task. A strategy to improve the efficiency of a photocatalytic system is to combine two semiconductors in intimate contact in such a way that photoexcitation of one of the components can lead to heterojunction electron transfer between the two components [6–9]. The case that has been more extensively studied corresponds to the use of two different semiconductors such as quantum dots supported on titanium dioxide or transition metal oxide, including RuO_2 and WO_3, on titania [10]. While the titanium dioxide in the anatase phase or the commercial Evonik P25 having a proportion of about 20%/80% rutile/anatase

is the most widely used photocatalyst, the possibility of enhancing the photocatalytic activity of this material by adding a second different form of titanium dioxide remains to be explored. In the present paper, we will show the synergy in the photocatalytic activity derived from combining TiO_2 nanoparticles with titanate nanotubes. The present case is also another example of optimization of the photocatalytic activity of TiO_2, in this case, by adding a different form of titanium oxide.

This synergy between titanate nanotubes and titania nanoparticles has been observed for two different types of commercial titanium dioxide nanoparticles, both in the absence and in the presence of platinum or gold as cocatalyst. The interest of this research is to show the possibility that the combination of various forms of titanium-containing materials offers to optimize the photocatalytic efficiency. This synergy seems to arise from the interfacial charge transfer

between the two titanium semiconductors. We have demonstrated the applicability of this strategy based on exclusive use of titanium-containing materials for the hydrogen generation from water-methanol mixtures using simulated solar light, that is, a process of large interest in the context of conversion of sunlight into chemical energy [11–17].

2. Materials and Methods

2.1. Sample Preparation. The TiO_2 precursor used for nanotube production was a commercial TiO_2 powder (Millennium PC500, anatase) consisting of pure anatase phase. TiO_2 powder (3.6 g) was treated with 90 mL of aqueous 10 M NaOH solution in a Teflon-lined autoclave (total volume 200 mL) at 125°C for 4 days. After the hydrothermal treatment, the solid was collected by filtration and washed by suspending the solid with 2 L HCl solution (pH = 1.3) and finally was washed with water until neutral pH. The material was dried at 110°C for 1 day. The deposition of gold or platinum nanoparticles was carried out by deposition-precipitation method. 0.5 g of titanate nanotubes was added to an aqueous solution containing the amount of chloroplatinic or chloroauric acid corresponding to 0.5 wt.% of metal loading. The pH was equilibrated to pH 10 by adding an aqueous solution of sodium hydroxide 0.2 M. The solid was washed with MilliQ water and dried in vacuum at ambient temperature. The metal was reduced using a H_2 flow (100 mL/min) at 300°C for 5 h.

The preparation of mixed materials was carried out by mixing an amount of nanotubes (50 mg) with the amount of titania needed to reach a composition of 6%, 12%, 25%, and 50% in weight of nanotubes. The powders were suspended in water and the suspensions were sonicated (150 W) for 30 min to improve the homogeneity of the suspension and then were maintained under magnetic stirring overnight. The suspension was finally filtered and dried at 110°C.

2.2. Photocatalytic Tests for Hydrogen Production. A suspension of the catalyst (25 mL, $1 g \times L^{-1}$) was sonicated for 10 min and placed in a gas-tight reactor with an irradiation window of $12.56 cm^2$ provided with temperature and pressure controllers. The reactor was placed in a thermostatic bath with a set point temperature of 25°C. The suspension was purged with an argon flow of 2 psi for 15 minutes prior to irradiation. The photoreaction was performed from the top of the photoreactor by using a solar simulator (Thermo Oriel 1000 W) with an irradiation spot of $100 cm^2$ placed at distance of 10 cm. The light of the solar simulator was filtered through an Air Mass 1.5 filter and contained approximately 5% of UV irradiation. The amount of hydrogen collected in the headspace of the reactor was analysed by injecting 100 μL in a gas chromatograph using a MOLSieve column, argon as carrier gas, and a TC detector.

3. Result and Discussion

It had been reported that digestion of TiO_2 nanoparticles in strong alkali condition leads to the formation of titanates appearing with morphology of nanotubes with long aspect
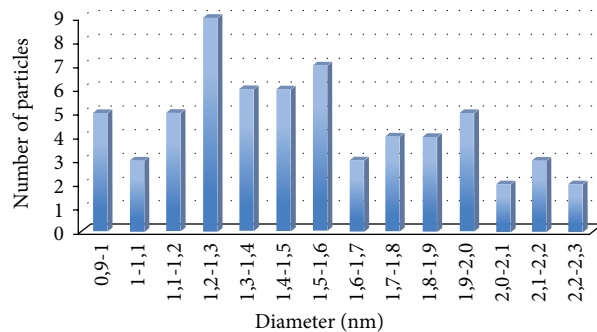
(a)
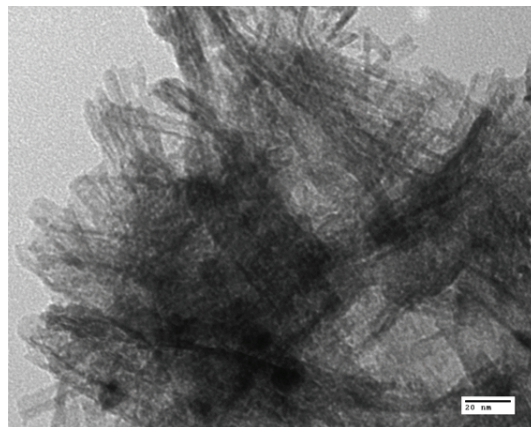
(b)

Figure 1: Diameter distribution and TEM image of the titanate nanotubes obtained in the present work.

ratio [18]. The average length dimension is several hundred nanometers, with diameters lower than 10 nm. We have been able to reproduce this remarkable morphological change from nanoparticles to nanotubes. Figure 1 shows representative TEM images of the resulting titanate nanotubes.

This change in morphology is accompanied by a change in the X-ray diffraction pattern, indicating that NaOH digestion has produced a phase transition from anatase to structure as presented in Figure 2.

As shown in Figure 3, a remarkable feature of these titanate nanotubes, besides the long aspect ratio, is the appearance of a residual optical absorption spanning into the visible region with a decreasing absorptivity towards long wavelengths.

This optical absorption had not been mentioned in the original report of the preparation of these materials [18]. By analogy with the reported black color for some titanium dioxide [19], we propose similarly that the brown colour of titanate nanotubes is due to the formation of a thin amorphous layer on the titanate nanotubes on top of the crystalline layers. This proposal is parallel to that recently suggested to rationalize the black colour in crystalline titanium dioxide samples obtained by submitting small titanium dioxide nanoparticles to thermal treatment at 500°C under hydrogen atomsphere [19]. In the present study, we have shown that these titanate nanotubes with optical absorption in the visible region
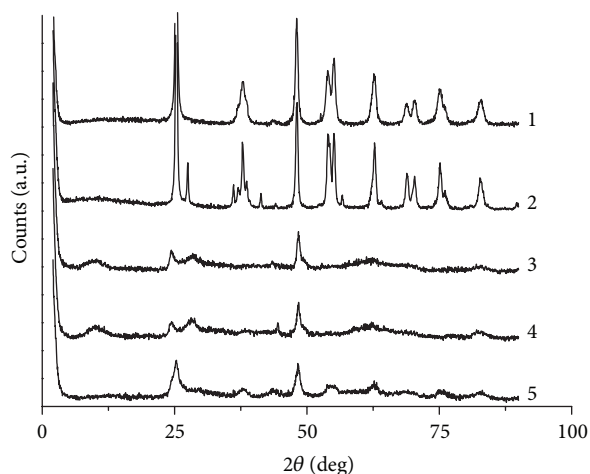
FIGURE 2: XRD of the titanium-containing samples. See Table 1 for the sample code.
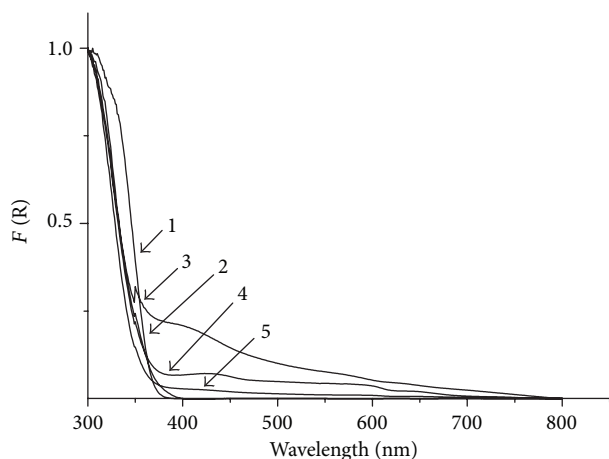
FIGURE 3: Diffuse reflectance UV-Vis absorption spectra (plotted as the Kubelka-Munk function of the remittance (R)) of the set of titanium samples under study. Refer to Table 1 for the sample code.

can exhibit activity for hydrogen generation from water-methanol mixtures with visible light. In the present case, we reasoned that the combination of these titanate nanotubes in a certain percentage with titanium dioxide nanoparticles could lead to an improved photocatalytic system due to the formation of bulk heterojunction, even for different titanium-containing particles.

To test this hypothesis we selected two different commercial titanium dioxide nanoparticles that had been widely used as photocatalysts, for both dye degradation and hydrogen generation, namely, Evonik P25 and Millennium PC500 TiO_2. To each of these two nanoparticulate titania dioxide samples, increasing proportions of titanate nanotubes from 0 to 100% were added, and the resulting mixtures were evaluated for hydrogen production under ambient conditions using simulated solar light. Figure 4 shows the temporal profiles of hydrogen evolution for some selected mixtures, while Table 1 compiles all the data of hydrogen productivity as a function of the composition of the photocatalyst.
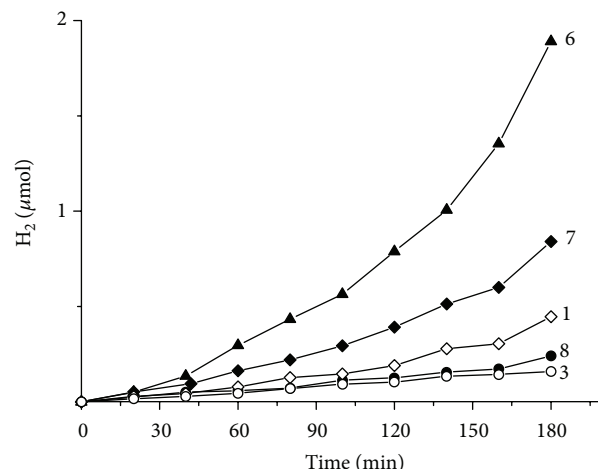
(a)
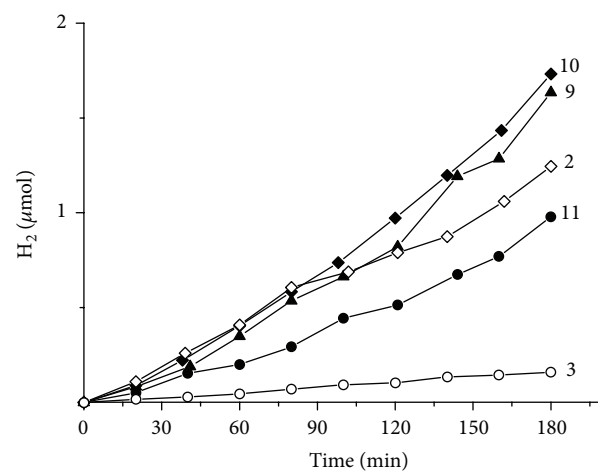
(b)

FIGURE 4: Photocatalytic hydrogen production from water-methanol (3 : 1) mixtures of selected samples as photocatalysts under simulated sunlight irradiation. Reaction conditions are water-methanol (3 : 1) mixtures 25 mL and catalyst concentration 1.0 g $\times$ L^{-1}. Refer to Table 1 for sample codes and a complete set of hydrogen production values. (a) Samples containing titanate nanotubes and Millennium PC500 TiO_2 particles. (b) Samples containing titanate nanotubes and Evonik P25 TiO_2 particles.

The results indicate that pure Evonik P25 or Millennium PC500 TiO_2 exhibits lower productivity for hydrogen generation than mixtures in which titanate nanotubes are present. The optimal efficiency corresponds to 12% or 6% titanate for Evonik P25 or Millennium TiO_2, respectively. Interestingly, larger proportion of titanate nanotubes is detrimental for the photocatalytic efficiency.

It should be noted that the results provided in Figure 4 and Table 1 (entries 1–11) correspond to photocatalytic mixture in which platinum or another noble metal was not present. It is well known in the state of the art that the presence of platinum or gold enhances considerably the photocatalytic efficiency of titania by acting as cocatalyst for the evolution of hydrogen gas and by providing the Schottky barrier reducing electron-hole recombination [20, 21]. In

Table 1: Code, sample composition, and photocatalytic data of the samples under study.

Sample	Mix composition (wt.%)	H$_2$ production (μmol) measured at 3 h of solar simulator irradiation
1	100% Millennium PC500 TiO$_2$	0.44
2	100% Evonik P25 TiO$_2$	1.2
3	100% titanate nanotubes	0.15
4	100% Au NP/titanate nanotubes (0.5 wt.%)	5.10
5	100% Pt NP/titanate nanotubes (0.3 wt.%)	28.8
6	6% of 3 + 94% of 1	1.89
7	12% of 3 + 88% of 1	0.84
8	25% of 3 + 75% of 1	0.24
9	6% of 3 + 94% of 2	1.55
10	12% of 3 + 88% of 2	1.73
11	25% of 3 + 75% of 2	0.97
12	6% of 4 + 94% of 1	6.25
13	12% of 4 + 88% of 1	13.57
14	25% of 4 + 75% of 1	27.92
15	50% of 4 + 50% of 1	29.77
16	6% of 5 + 94% of 1	34.19
17	12% of 5 + 88% of 1	71.87
18	25% of 5 +75% of 1	137.18
19	50% of 5 + 50% of 1	153.71
20	6% of 5 + 94% of 2	35.46
21	12% of 5 − 88% of 2	74.41
22	25% of 5 − 75% of 2	81.99

view of this, it is also of interest to check whether the synergy that has been observed between titanate nanotubes and titanium dioxide also takes place for samples containing some noble metals as cocatalysts or not. Furthermore, since the amount of noble metals present in the semiconductor should be minimized as much as possible, it is of interest to determine the relative efficiency in terms of the amount of noble metals present in the system.

In order to determine the influence of noble metals on the photocatalytic activity, we prepared titanate nanotubes containing platinum or gold nanoparticles that have been supported by deposition-precipitation method [22, 23] starting from aqueous solution of chloroplatinic or chloroauric acid at pH 10. The platinum or gold content of titanate nanotubes determined by chemical analysis is about 0.3 wt.% and 0.5 wt.%, respectively. These samples containing platinum or gold nanoparticles supported on modified nanotubes were used to prepare mixtures with Evonik P25 and Millennium PC500 titania in proportions ranging from 6 to 100 wt.%. The results of photocatalytic hydrogen generation of these mixtures containing some platinum or gold are also compiled

in Table 1, while Figure 5 shows the temporal evolution of hydrogen under simulated solar light irradiation.

These photocatalytic data of noble metal-containing samples indicate again a synergy due to the combination of the two titanium semiconducting solids. The maximum efficiency with noble metals seems to occur at the highest percentage of platinum containing titanate nanotubes that is observed at 25%, for both Evonik P25 and Millennium PC500 TiO$_2$. This optimized efficiency probably reflects that, in addition to the synergy between the two titanium solids, the platinum content is playing an important role as cocatalyst increasing the photocatalytic efficiency. We notice, however, that, even in the case of Millennium PC500 TiO$_2$, the platinum content of the optimal photocatalytic mixtures that is present only in the titanate nanotubes is 0.03 wt.% which is significantly low compared to the typical amounts reported for titanium dioxide. For instance, when the photocatalytic efficiency of the titanate nanotubes-titanium dioxide mixtures containing platinum is compared with the best turnover numbers for platinum either deposited on titanate nanotubes or deposited on titanium dioxide, the benefits of the combination of the two different titanium forms can be demonstrated. Thus, the turnover numbers for platinum-Millennium PC500 TiO$_2$ and platinum-Evonik P25 TiO$_2$ are 961 and 1892 which are lower than the values of 1831 and 1993 corresponding to platinum for the titanate nanotube-Millennium PC500 nanotubes and platinum for titanate nanotubes-Evonik P25 TiO$_2$, respectively.

The synergy between titanate nanotubes and titania nanoparticles can be explained based on related precedents reporting enhanced photocatalytic efficiency of heterojunction of different semiconductors. In agreement with this hypothesis, we propose that light should be preferentially absorbed by titanate nanotubes, since, as shown in Figure 3, this component has absorption beyond 380 nm where anatase does not absorb light. After light absorption in titanate nanotubes, charge separation with the generation of electron and holes would take place. Since the mobility of electron in titania semiconductors is larger than holes, it can be said that conduction band electrons migrate from the site in which they have been generated to the surface of the titanate nanotubes and, then, to the anatase nanoparticle. Interfacial electron migration from the nanotubes to anatase nanoparticles would be the key process enhancing charge separation, minimizing recombination, and extending the lifetime of the charge separated state, as it had been reported for other combinations of semiconductors [24]. This mechanism does not exclude other possibilities taking place independently in each titanium phase but would be unique for the combination of titanate nanotubes with titania nanoparticles, thus resulting in a synergy due to the junction of both phases. Scheme 1 illustrates the mechanistic proposal to rationalize the higher efficiency of the combination of titanate nanotubes with anatase nanoparticles.

4. Conclusions

In the present paper, we provide data showing that the combination of titanate nanotubes, exhibiting an absorption

(a)

(b)

(c)
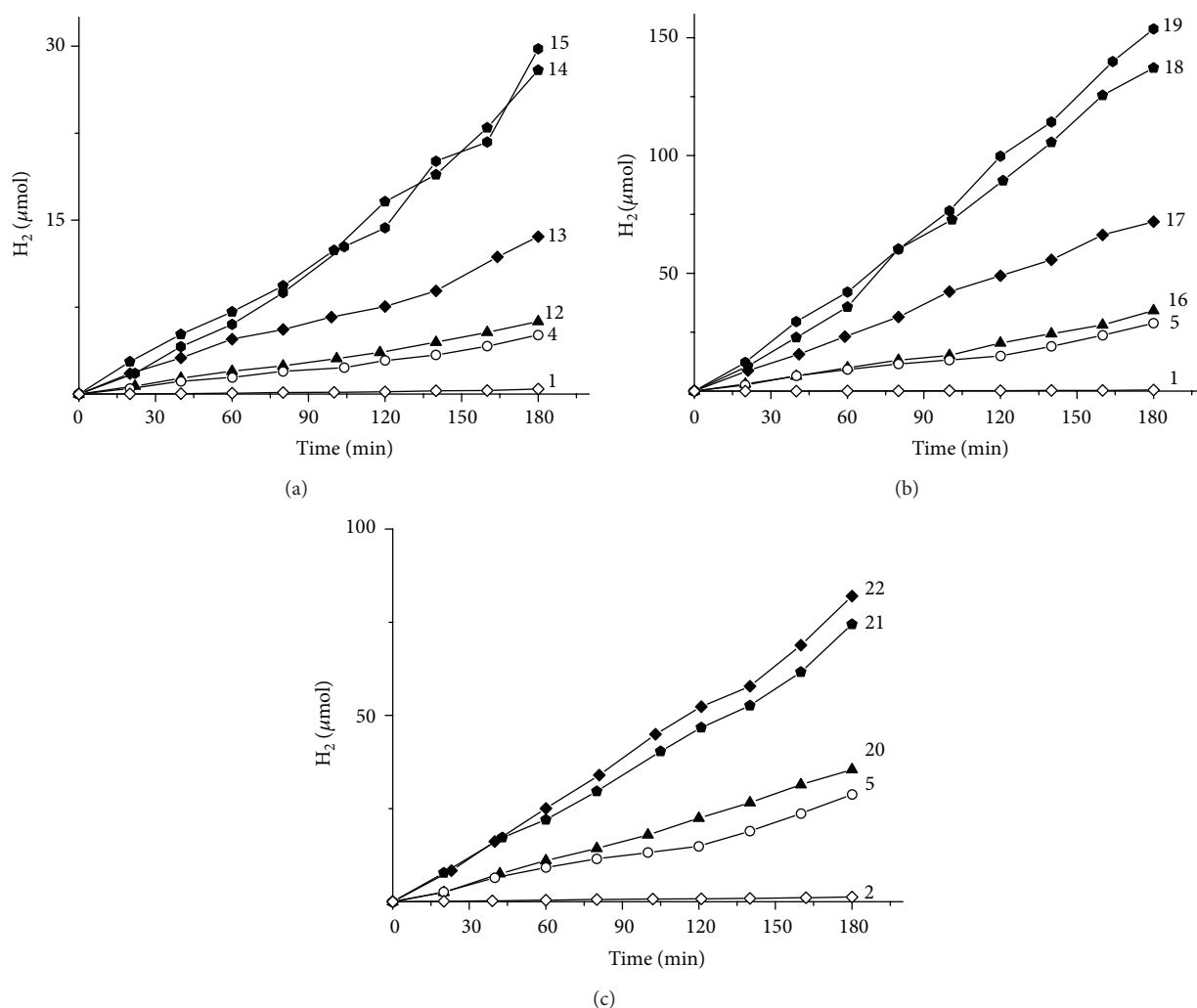
FIGURE 5: Photocatalytic hydrogen production from water-methanol (3 : 1) mixtures of selected samples as photocatalysts under simulated sunlight irradiation. Reaction conditions are water-methanol (3 : 1) mixtures 25 mL and catalyst concentration $1.0 \, g \times L^{-1}$. Refer to Table 1 for the sample codes and a complete set of hydrogen production values. (a) Samples containing gold nanoparticles supported on titanate nanotubes and Millennium PC500 TiO_2 particles. (b) Samples containing platinum nanoparticles supported on titanate nanotubes and Millennium PC500 TiO_2 particles. (c) Samples containing platinum nanoparticles supported on titanate nanotubes and Evonik P25 TiO_2 particles.
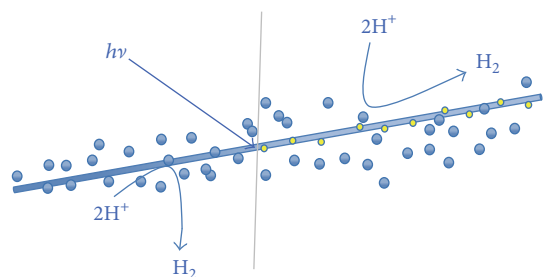
SCHEME 1: Proposal for the synergy found for the heterojunction of titanate nanotubes (long line) and titania nanoparticles (spheres).

in the visible region, and anatase nanoparticles in the appropriate proportion increases the photocatalytic activity with respect to the activity of the individual components. This synergetic effect is observed both in the absence and in the presence of noble metals platinum and gold nanoparticles acting as cocatalysts for the hydrogen generation and is proposed to derive from the interfacial electron transfer between the titanate nanotubes and titania nanoparticles; our report complements those that have shown that the morphology of titanium base semiconductors plays a role in the photocatalytic efficiency [25], since, in the present case, we have observed that the combination of two different titanium-based semiconductors with different morphology benefits the photocatalytic activity of the system.

Conflict of Interests

The authors declare that there is no conflict of interests regarding the publication of this paper.

Acknowledgments

References

[1] G. Centi and S. Perathoner, "Towards solar fuels from water and CO_2," *ChemSusChem*, vol. 3, no. 2, pp. 195–208, 2010.

[2] D. Gust, T. A. Moore, and A. L. Moore, "Solar fuels via artificial photosynthesis," *Accounts of Chemical Research*, vol. 42, no. 12, pp. 1890–1898, 2009.

[3] L. Hammarström and S. Hammes-Schiffer, "Guest editorial: artificial photosynthesis and solar fuels," *Accounts of Chemical Research*, vol. 42, no. 12, pp. 1859–1860, 2009.

[4] S. C. Roy, O. K. Varghese, M. Paulose, and C. A. Grimes, "Toward solar fuels: photocatalytic conversion of carbon dioxide to hydrocarbons," *ACS Nano*, vol. 4, no. 3, pp. 1259–1278, 2010.

[5] A. Corma and H. Garcia, "Photocatalytic reduction of CO_2 for fuel production: possibilities and challenges," *Journal of Catalysis*, vol. 308, pp. 168–175, 2014.

[6] G. Khan, S. K. Choi, S. Kim, S. K. Lim, J. S. Jang, and H. Park, "Carbon nanotubes as an auxiliary catalyst in heterojunction photocatalysis for solar hydrogen," *Applied Catalysis B: Environmental*, vol. 142-143, pp. 647–653, 2013.

[7] R. Marschall, "Semiconductor composites: strategies for enhancing charge carrier separation to improve photocatalytic activity," *Advanced Functional Materials*, 2013.

[8] S. B. Rawal, S. Bera, D. Lee, D.-J. Jang, and W. I. Lee, "Design of visible-light photocatalysts by coupling of narrow bandgap semiconductors and TiO_2: effect of their relative energy band positions on the photocatalytic efficiency," *Catalysis Science & Technology*, vol. 3, no. 7, pp. 1822–1830, 2013.

[9] L. Wu, J. Xing, Y. Hou, F. Y. Xiao, Z. Li, and H. G. Yang, "Fabrication of regular ZnO/TiO_2 heterojunctions with enhanced photocatalytic properties," *Chemistry—A European Journal*, vol. 19, no. 26, pp. 8393–8396, 2013.

[10] K. Sayama, R. Yoshida, H. Kusama, K. Okabe, Y. Abe, and H. Arakawa, "Photocatalytic decomposition of water into H_2 and O_2 by a two-step photoexcitation reaction using a WO_3 suspension catalyst and an Fe^{3+}/Fe^{2+} redox system," *Chemical Physics Letters*, vol. 277, no. 4, pp. 387–391, 1997.

[11] G. W. Crabtree, M. S. Dresselhaus, and M. V. Buchanan, "The hydrogen economy," *Physics Today*, vol. 57, no. 12, pp. 39–44, 2004.

[12] S. Dunn, "Hydrogen futures: toward a sustainable energy system," *International Journal of Hydrogen Energy*, vol. 27, no. 3, pp. 235–264, 2002.

[13] A. J. Esswein and D. G. Nocera, "Hydrogen production by molecular photocatalysis," *Chemical Reviews*, vol. 107, no. 10, pp. 4022–4047, 2007.

[14] S. H. Jensen, P. H. Larsen, and M. Mogensen, "Hydrogen and synthetic fuel production from renewable energy sources," *International Journal of Hydrogen Energy*, vol. 32, no. 15, pp. 3253–3257, 2007.

[15] R. M. Navarro, M. C. Sánchez-Sánchez, M. C. Alvarez-Galvan, F. D. Valle, and J. L. G. Fierro, "Hydrogen production from renewable sources: biomass and photocatalytic opportunities," *Energy and Environmental Science*, vol. 2, no. 1, pp. 35–54, 2009.

[16] M. Ni, M. K. H. Leung, D. Y. C. Leung, and K. Sumathy, "A review and recent developments in photocatalytic water-splitting using TiO_2 for hydrogen production," *Renewable and Sustainable Energy Reviews*, vol. 11, no. 3, pp. 401–425, 2007.

[17] J. Nowotny, C. C. Sorrell, L. R. Sheppard, and T. Bak, "Solar-hydrogen: environmentally safe fuel for the future," *International Journal of Hydrogen Energy*, vol. 30, no. 5, pp. 521–544, 2005.

[18] C.-C. Tsai and H. Teng, "Structural features of nanotubes synthesized from NaOH treatment on TiO_2 with different post-treatments," *Chemistry of Materials*, vol. 18, no. 2, pp. 367–373, 2006.

[19] X. Chen, L. Liu, P. Y. Yu, and S. S. Mao, "Increasing solar absorption for photocatalysis with black hydrogenated titanium dioxide nanocrystals," *Science*, vol. 331, no. 6018, pp. 746–750, 2011.

[20] A. Primo, T. Marino, A. Corma, R. Molinari, and H. García, "Efficient visible-light photocatalytic water splitting by minute amounts of gold supported on nanoparticulate CeO_2 obtained by a biopolymer templating method," *Journal of the American Chemical Society*, vol. 133, no. 18, pp. 6930–6933, 2011.

[21] C. G. Silva, R. Juá rez, T. Marino, R. Molinari, and H. García, "Influence of excitation wavelength (UV or visible light) on the photocatalytic activity of titania containing gold nanoparticles for the generation of hydrogen or oxygen from water," *Journal of the American Chemical Society*, vol. 133, no. 3, pp. 595–602, 2011.

[22] G. R. Bamwenda, S. Tsubota, T. Kobayashi, and M. Haruta, "Photoinduced hydrogen production from an aqueous solution of ethylene glycol over ultrafine gold supported on TiO_2," *Journal of Photochemistry and Photobiology A: Chemistry*, vol. 77, no. 1, pp. 59–67, 1994.

[23] M. Haruta, "Size- and support-dependency in the catalysis of gold," *Catalysis Today*, vol. 36, no. 1, pp. 153–166, 1997.

[24] N. Serpone, A. V. Emeline, S. Horikoshi, V. N. Kuznetsov, and V. K. Ryabchuk, "On the genesis of heterogeneous photocatalysis: a brief historical perspective in the period 1910 to the mid-1980s," *Photochemical & Photobiological Sciences*, vol. 11, no. 7, pp. 1121–1150, 2012.

[25] C. Aprile, A. Corma, and H. Garcia, "Enhancement of the photocatalytic activity of TiO_2 through spatial structuring and particle size control: from subnanometric to submillimetric length scale," *Physical Chemistry Chemical Physics*, vol. 10, no. 6, pp. 769–783, 2008.

Research Article

Synthesis of Flower-Like Cu$_2$ZnSnS$_4$ Nanoflakes via a Microwave-Assisted Solvothermal Route

Fei Long,[1,2] Shuyi Mo,[1] Yan Zeng,[1] Shangsen Chi,[1] and Zhengguang Zou[1,2]

[1] *School of Materials Science and Engineering, Guilin University of Technology, Guilin 541004, China*
[2] *Key Laboratory of Nonferrous Materials and New Processing Technology of Ministry of Education, Guilin University of Technology, Guilin 541004, China*

Correspondence should be addressed to Fei Long; long.drf@gmail.com

Flower-like Cu$_2$ZnSnS$_4$ (CZTS) nanoflakes were synthesized by a facile and fast one-pot solution reaction using copper(II) acetate monohydrate, zinc acetate dihydrate, tin(IV) chloride pentahydrate, and thiourea as starting materials. The as-synthesized samples were characterized by X-ray diffraction (XRD), Raman scattering analysis, field emission scanning electron microscopy (FESEM) equipped with an energy dispersion X-ray spectrometer (EDS), transmission electron microscopy (TEM), and UV-Vis absorption spectra. The XRD patterns shown that the as-synthesized particles were kesterite CZTS and Raman scattering analysis and EDS confirmed that kesterite CZTS was the only phase of product. The results of FESEM and TEM show that the as-synthesized particles were flower-like morphology with the average size of 1~2 μm which are composed of 50 nm thick nanoflakes. UV-Vis absorption spectrum revealed CZTS nanoflakes with a direct band gap of 1.52 eV.

1. Introduction

I$_2$–II–IV–VI$_4$ quaternary compounds, such as Cu$_2$ZnSnS$_4$ (CZTS) and Cu$_2$ZnSnSe$_4$ (CZTSe) based solar cells, exhibit optical and electronic properties comparable to Cu(In, Ga)(S, Se)$_2$(CIGS) and CdTe materials while consisting entirely of nontoxic constituents and avoid the scarcity issues associated with indium, gallium, cadmium, and tellurium. CZTS has a direct band gap of 1.4~1.5 eV and large absorption coefficient in the order of 10^4 cm^{-1} [1–3]. Previous reports show that many methods have been utilized for fabricating CZTS thin films, included sputtering [4], electrodeposition [5], coevaporation [6], and coating [7, 8]. The photoelectric conversion efficiency of CZTS-based thin film solar cells has been improved from 0.66% in 1997 [9] to 12.6% in 2013 [10]. Because the narrow thermodynamic window demonstrates that chemical-potential control was important for the growth of high-quality crystals CZTS [11], methods including coevaporation and sputter which obtained high efficiency in CIGS solar cells were not achieved good performance in CZTS thin film solar cells. However, the wet chemical processes based on printing technology have achieved the record

efficiency of CZTS solar cell [10]. Therefore, synthesis of CZTS nanoparticles by hot injection [12], solvothermal [13], hydrothermal [14], and other wet chemical [15] has attracted more attention, and the as-synthesized nanostructures including plate-like [12], sphere-like [13], and spindle-like [16] have been also researched. Although various methods have been utilized to prepare CZTS particles, searching for a simple and rapid synthetic route was still worthy of further exploration. Herein, we report a microwave-assisted solvothermal method to prepare homogeneous and dispersible CZTS flower-like particles from the direct reaction between metal salts and thiourea in ethylene glycol.

2. Experimental

Preparation of the CZTS Particles. Typically, Cu(CH$_3$COO)$_2$·H$_2$O (0.050 M), Zn(CH$_3$COO)$_2$·2H$_2$O (0.025 M), SnCl$_4$·5H$_2$O (0.025 M), and NH$_2$CSNH$_2$ (0.200 M) were added in sequence to 30 mL of ethylene glycol at room temperature under magnetic stirring until the chemistries were completely dissolved. Then the mixture was loaded into a Teflon autoclave of 90 mL capacity and putted
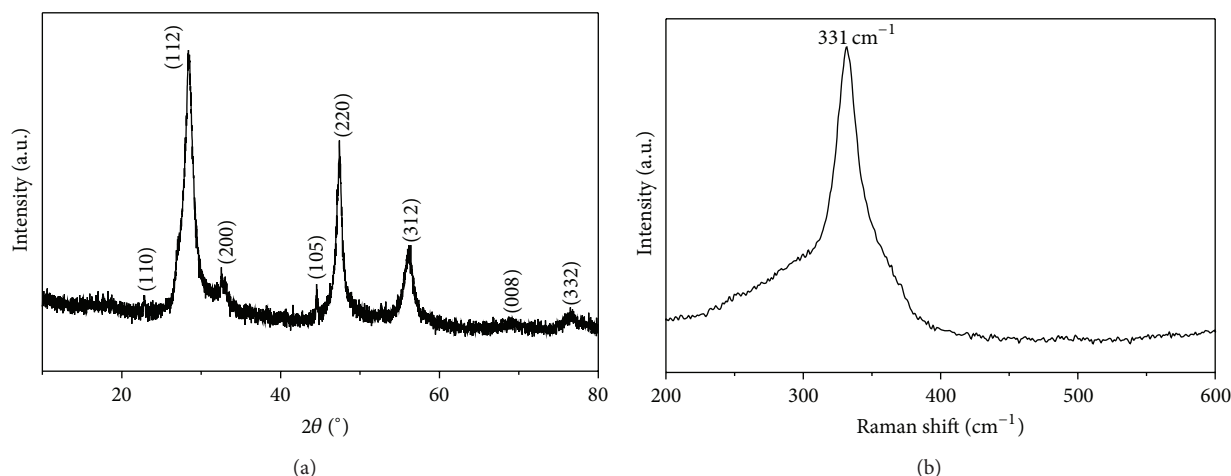
FIGURE 1: (a) XRD pattern of CZTS particles; (b) Raman scattering spectra of CZTS particles; the excitation laser wavelength is 532 nm.

into a microwave oven (2450 MHz, maximum power of 1200 W) heat to 230°C in 10 min and maintained for 1.5 h. The precipitates were centrifuged, washed by deionized water and ethanol for several times to remove by-products, followed by drying in a vacuum chamber at 80°C for 6 h.

Characterization of the CZTS Particles. The XRD patterns of as-synthesized particles were obtained on Panalytical X'Pert Pro with Cu Kα radiation ($\lambda = 1.5406$ Å) at 35 kV in a scanning range of 10°~80°. Raman spectra were recorded by using Thermo DXR Raman spectrometer at the room temperature, and the 532 nm line of an Ar$^+$ laser was used as the excitation source. FESEM images were observed by a Hitachi S-4800 field emission scanning electron microscope equipped with an energy dispersion X-ray spectrometer (EDS) and TEM images were recorded on JEOL JSF-2100 at 200 KV. Optical measurements were carried out with Shimadzu UV3600 UV-Vis spectroscopy.

3. Results and Discussion

The XRD pattern (Figure 1(a)) of the as-synthesized CZTS particles exhibits that the major XRD diffraction peaks appeared at $2\theta = 28.44$, 47.44 and 56.20 can be attributed to (112), (220), and (312) planes of the CZTS crystals (JCPDS card number 26-0575), respectively. However, the peaks of CZTS XRD patterns were similar to the ZnS (JCPDS card number 65-1691) and Cu_2SnS_3(JCPDS card number 27-0198), making it difficult to distinguish between them. So, Raman spectra have been carried out to confirm the products (Figure 1(b)), it exhibits a single intense peak at 331 cm^{-1}, which was consistence with previous study [17], and most importantly there was no peak at 275 cm^{-1}, 352 cm^{-1}, 267 cm^{-1}, 303 cm^{-1}, and 365 cm^{-1} suggest that the products absence of cubic ZnS and Cu_2SnS_3 [18].

The images of FESEM (Figures 2(a) and 2(b)) indicate that the as-synthesized CZTS particles were monodisperse superstructures with a uniform 3-dimensional flower-like morphology with the average size of 1~2 μm. Furthermore, these superstructures were built from intersectional nanoflakes with thickness about 50 nm (Figure 2(c)). The average composition of the products was $Cu : Zn : Sn : S = 2 : 0.97 : 1.02 : 3.73$ base on the result of EDS (Figure 2(d)), the slightly Sn rich and Zn poor composition deviated from stoichiometric may be due to different reactivity of starting materials.

The images of TEM, selected area electron diffraction (SAED), and high resolution transmission electron microscopy (HRTEM) of as-synthesized CZTS particles were shown in Figure 3. The average size of CZTS particles corresponds well with the FESEM images (Figure 2), and the flower-like particles were built from cross-nanoflakes (Figure 3(a)). SAED image reveals the polycrystalline nature of CZTS nanoflakes which was indicated by the presence of diffraction spots of (112), (220), and (312) planes. The HRTEM image of one nanoflake shows the interplanar spacing of 1.9 Å corresponding to the (220) planes.

The UV-Vis absorption spectrum of CZTS particles was shown in Figure 4. We determined the absorbance onset by plotting $(Ah\nu)^2$ versus $h\nu$ (A: absorbance, h: Planck's constant, and ν: frequency). From the long wavelength extrapolation of the band edge, the band gap was determined to be 1.52 eV which was in good agreement with the corresponding bulk materials [1]. This observation also eliminates existence of secondary phase of ZnS and Cu_2SnS_3. The good absorption in the visible light region may find its potential application in thin films solar cells.

4. Conclusions

Single phase kesterite CZTS has been prepared at 230°C for only 1.5 h via a microwave-assisted solvothermal without any surfactant; the CZTS particles with flower structure built from intersectional nanoflakes have been obtained, $Cu : Zn : Sn : S = 2 : 0.97 : 1.02 : 3.73$. Its founded microwave has strongly activated the process of solvothermal synthesis which significantly speeds up the reaction compared with
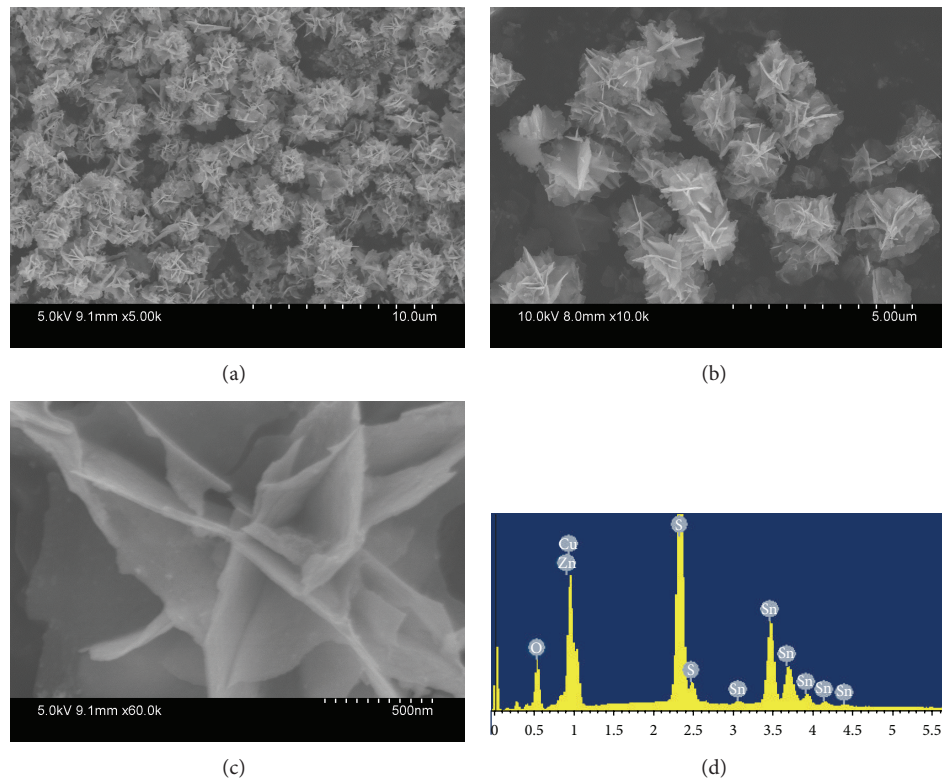
FIGURE 2: (a)–(c) FESEM images of CZTS particles; (d) EDS of CZTS particles.
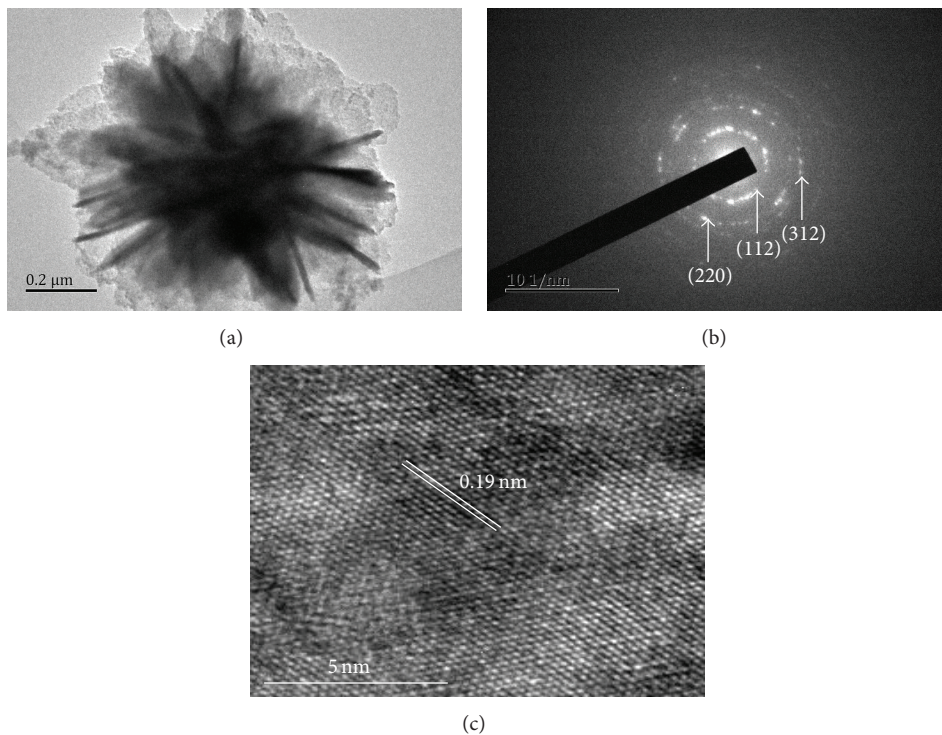
FIGURE 3: (a) TEM images of CZTS particles dispersed in ethanol; (b) SAED pattern; (c) HRTEM image.
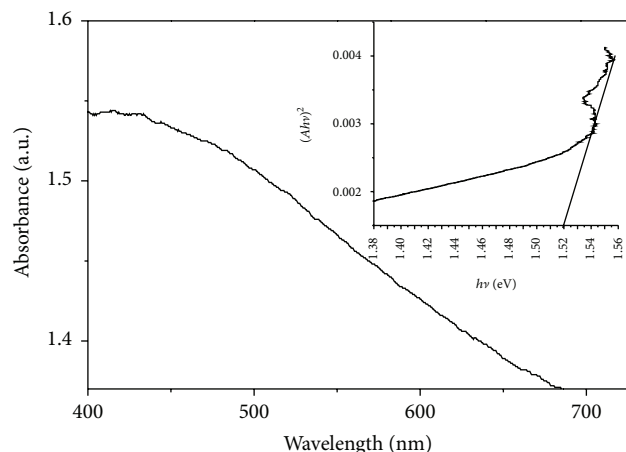
FIGURE 4: UV-Vis absorption spectrum of CZTS particles. The inset image shows a band gap of 1.52 eV.

traditional solvothermal synthetic methods. The UV-Vis absorption spectra of the products revealed that the band gap was 1.52 eV, which is optimal for photovoltaic applications.

Conflict of Interests

The authors declared that they do not have a direct financial relation with the commercial identities mentioned in this paper that might lead to any conflict of interest for any of the authors.

Acknowledgments

References

[1] K. Ito and T. Nakazawa, "Electrical and optical properties of stannite-type quaternary semiconductor thin films," *Japanese Journal of Applied Physics*, vol. 27, no. 11, pp. 2094–2097, 1988.

[2] H. Katagiri, K. Saitoh, T. Washio, H. Shinohara, T. Kurumadani, and S. Miyajima, "Development of thin film solar cell based on Cu$_2$ZnSnS$_4$ thin films," *Solar Energy Materials and Solar Cells*, vol. 65, no. 1–4, pp. 141–148, 2001.

[3] H. Matsushita, T. Maeda, A. Katsui, and T. Takizawa, "Thermal analysis and synthesis from the melts of Cu-based quaternary compounds Cu–III–IV–VI$_4$ and Cu$_2$–II–IV–VI$_4$ (II = Zn, Cd; III = Ga, In; IV = Ge, Sn; VI = Se)," *Journal of Crystal Growth*, vol. 208, no. 1–4, pp. 416–422, 2000.

[4] H. Katagiri, K. Jimbo, S. Yamada et al., "Enhanced conversion efficiencies of Cu$_2$ZnSnS$_4$-based thin film solar cells by using preferential etching technique," *Applied Physics Express*, vol. 1, no. 4, Article ID 041201, 2008.

[5] A. Shafaat, K. B. Reuter, O. Gunawan, L. Guo, L. T. Romankiw, and H. Deligianni, "A high efficiency electrodeposited

[6] B. Shin, O. Gunawan, Y. Zhu, N. A. Bojarczuk, S. J. Chey, and S. Guha, "Thin film solar cell with 8.4% power conversion efficiency using an earth-abundant Cu$_2$ZnSnS$_4$ absorber," *Progress in Photovoltaics: Research and Applications*, vol. 21, no. 1, pp. 72–76, 2013.

[7] D. A. R. Barkhouse, O. Gunawan, T. Gokmen, T. K. Todorov, and D. B. Mitzi, "Device characteristics of a 10.1% hydrazine-processed Cu$_2$ZnSn(Se,S)$_4$ solar cell," *Progress in Photovoltaics: Research and Applications*, vol. 20, no. 1, pp. 6–11, 2012.

[8] Q. Guo, G. M. Ford, W.-C. Yang et al., "Fabrication of 7.2% efficient CZTSSe solar cells using CZTS nanocrystals," *Journal of the American Chemical Society*, vol. 132, no. 49, pp. 17384–17386, 2010.

[9] H. Katagiri, N. Sasaguchi, S. Hando, S. Hoshino, J. Ohashi, and T. Yokota, "Preparation and evaluation of Cu$_2$ZnSnS$_4$ thin films by sulfurization of E-B evaporated precursors," *Solar Energy Materials and Solar Cells*, vol. 49, no. 1–4, pp. 407–414, 1997.

[10] W. Wang, M. T. Winkler, O. Gunaman et al., "Device characteristics of CZTSSe thin-film solar cells with 12.6% efficiency," *Advanced Energy Materials*, 2013.

[11] A. Walsh, S. Chen, S. H. Wei, and X. G. Gong, "Kesterite thin-film solar cells: advances in materials modelling of Cu$_2$ZnSnS$_4$," *Advanced Energy Materials*, vol. 2, no. 4, pp. 400–409, 2012.

[12] H. Wei, W. Guo, Y. Sun, Z. Yang, and Y. Zhang, "Hot-injection synthesis and characterization of quaternary Cu$_2$ZnSnSe$_4$ nanocrystals," *Materials Letters*, vol. 64, no. 13, pp. 1424–1426, 2010.

[13] Y.-L. Zhou, W.-H. Zhou, Y.-F. Du, M. Li, and S.-X. Wu, "Sphere-like kesterite Cu$_2$ZnSnS$_4$ nanoparticles synthesized by a facile solvothermal method," *Materials Letters*, vol. 65, no. 11, pp. 1535–1537, 2011.

[14] C. C. Kang, H. F. Chen, T. C. Yu, and T. C. Lin, "Aqueous synthesis of wurtzite Cu$_2$ZnSnS$_4$ nanocrystals," *Materials Letters*, vol. 96, pp. 24–26, 2013.

[15] J. J. Li, J. Shen, Z. Q. Li et al., "Wet chemical route to the synthesis of kesterite Cu$_2$ZnSnS$_4$ nanocrystals and their applications in lithium ion batteries," *Materials Letters*, vol. 92, pp. 330–333, 2013.

[16] W. Ming, Q. Y. Du, D. C. Wang, W. F. Liu, G. S. Jiang, and C. F. Zhu, "Synthesis of spindle-like kesterite Cu$_2$ZnSnS$_4$ nanoparticles using thiorea as sulfur source," *Materials Letters*, vol. 79, pp. 177–179, 2012.

[17] S. R. Kumar, B. D. Ryu, S. Chandramohan, J. K. Seol, S. K. Lee, and C. H. Hong, "Rapid synthesis of sphere-like Cu$_2$ZnSnS$_4$ microparticles by microwave irradiation," *Materials Letters*, vol. 86, pp. 174–177, 2012.

[18] P. A. Fernandes, P. M. P. Salomé, and A. F. da Cunha, "Study of polycrystalline Cu$_2$ZnSnS$_4$ films by Raman scattering," *Journal of Alloys and Compounds*, vol. 509, no. 28, pp. 7600–7606, 2011.

Review Article

Hierarchical Structures from Inorganic Nanocrystal Self-Assembly for Photoenergy Utilization

Yun-Pei Zhu,[1] Tie-Zhen Ren,[2] Tian-Yi Ma,[1,3] and Zhong-Yong Yuan[1]

[1] *Key Laboratory of Advanced Energy Materials Chemistry (Ministry of Education),*
   Collaborative Innovation Center of Chemical Science and Engineering (Tianjin), College of Chemistry,
   Nankai University, Tianjin 300071, China
[2] *School of Chemical Engineering and Technology, Hebei University of Technology, Tianjin 300130, China*
[3] *School of Chemical Engineering, University of Adelaide, Adelaide, SA 5005, Australia*

Correspondence should be addressed to Zhong-Yong Yuan; zyyuan@nankai.edu.cn

Self-assembly has emerged as a powerful strategy for controlling the structure and physicochemical properties of ensembles of inorganic nanocrystals. Hierarchical structures from nanocrystal assembly show collective properties that differ from individual nanocrystals and bulk samples. Incorporation of structural hierarchy into nanostructures is of great importance as a result of enhancing mass transportation, reducing resistance to diffusion, and high surface areas for adsorption and reaction, and thus much effort has been devoted to the exploration of various novel organizing schemes through which inorganic porous structure with architectural design can be created. In this paper, the recent research progress in this field is reviewed. The general strategies for the synthesis of hierarchical structures assembled from nanobuilding blocks are elaborated. The well-defined hierarchical structures provide new opportunities for optimizing, tuning, and/or enhancing the properties and performance of these materials and have found applications in photoenergy utilization including photodegradation, photocatalytic H_2 production, photocatalytic CO_2 conversion, and sensitized solar cells, and these are discussed illustratively.

1. Introduction

With the rapid development of modern society, energy and environmental issues have received tremendous attention. Traditional fossil fuels, such as coal, petroleum, and natural gas, are exceedingly depleted, which is usually accompanied by the emission of harmful chemicals. In response to the energy crisis and environmental contaminations, clean energy and sustainable development are the basic principles. Photoenergy, especially solar energy, is regarded as unlimited and environmental-friendly resource. Notably, where the core ideology lies is the invention and development of advanced functional materials, which is essential for alternative and renewable sources, and reducing the harmful substances [1–3].

Nanomaterials are a kind of advanced materials that exhibit remarkable physicochemical properties. They are promising in various areas, ranging from adsorption, separation, catalysis, sensing, to the burgeoning biotechnology [4–6]. Just as nanocrystalline particles display properties that are distinct from the bulk samples, the ensembles of nanocrystals should possess collective properties that are different from the individual nanocrystals and bulk materials [7]. Thus recent interest has turned to the ensembles of inorganic nanocrystals and the resultant potential in functional devices [8, 9]. It is noteworthy that many of these peculiarities and possible applications are mainly dependent on our ability to adjust the self-assembly process and interactions among the electronic, magnetic, and optical properties of the single nanocrystalline building unit. Self-assembly, as a fascinating method for promoting the disordered morphologies of materials into ordered ones, has attracted much interest [10]. Plentiful types of porous materials have been fabricated by self-assembly strategy, such as nanoporous Mn_3O_4 [11],

butterfly-like $CaTiO_3$ dendrite [12], and porous microcapsule [13], which usually involve noncovalent or weak covalent interactions and thus simplify the synthesis technology. Self-assembly has emerged as a powerful, efficient, and facile technique for controlling the porosity and morphologies of the nanocrystalline ensembles [14, 15], resulting in extended performances from adsorption/separation to shape-selective catalysis and biology.

Natural materials demonstrate admirable and intriguing hierarchical structures on the basis of comparatively simple components such as brittle minerals with large variety of functions. Nanomaterials with hierarchical architectures at different length scale have been heavily involved in the newly developed photoenergy conversion and storage systems. This is due to that hierarchical porosity and structures present obvious superiorities over other conventional materials in terms of increased mass transport through the pore channels of the materials and maintenance of a specific surface area on the level of fine pore systems, leading to the enhancement of diffusion efficiency and accessibility to the interior interfaces by guest species [16–18]. By incorporation of macroporosity in materials, the improved efficiency of light harvesting can be realized via multiple scattering [19], showing the significance of macrochannels in light relevant systems such as photocatalysis and photovoltaics.

Motivated by the controllable synthesis of nanomaterials, recent efforts have tended to the assembly of nanocrystals into hierarchical architectures. Plentiful 1D, 2D, and 3D secondary assemblies (even super crystals of binary nanocrystal superlattice) have been reported to date [20–24]. Well-ordered assembly composed of tailored nanoscaled building blocks provides new opportunities to enhance the resulting performance. In this review article, we highlight recent advances in self-assembly strategies for constructing hierarchically structured materials. Their involvement in photoenergy utilization including photodegradation, photocatalytic H_2 production, photocatalytic CO_2 conversion, and sensitized solar cells are elaborated. The intimate linkage between the hierarchically structured materials and the resultant performances in photoenergy storage and conversion can promote the rational design of novel structures with advanced properties.

2. Strategies for Self-Assembly of Nanocrystals

2.1. Self-Assembly in the Absence of Templates or External Fields. Self-assembly of nanocrystals without the assistance of templates or external fields is schematically illustrated in Figure 1. Typically, the assembly is governed by the balance of attractive forces (e.g., covalent or hydrogen bonding, electrostatic attraction among the oppositely charged units, depletion forces, or dipole-dipole interactions) and repulsive forces (e.g., steric forces and electrostatic repulsion between ligands of same charge) [25]. Self-organization of nanocrystals generates a variety of structures, including chains [26, 27], sheets [28, 29], vesicles [30], three-dimensional (3D) crystals [31, 32], and even complicated 3D architectures [33]. The template-free route usually initiates assembly from the weak interaction between the precursor molecules or particles.
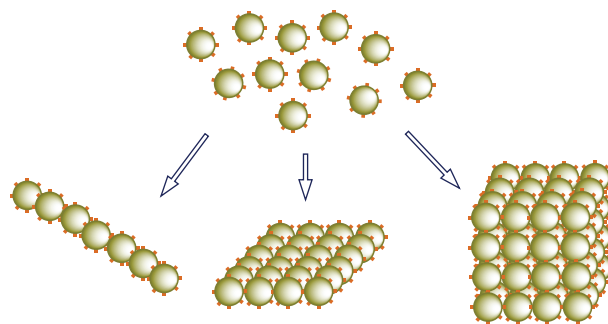
Figure 1: Schematic illustration of the organization of nanocrystals into chains, 2D sheets and 3D structures.

Their loosely packing or oriented attachment allows porous morphologies rather than dense materials to be obtained. Various conditions such as precursors, temperature, and solvents can be judiciously adjusted to conduct the self-assembly process. Based on the synthesis systems, different mechanisms and routes have been successfully employed to obtain hierarchical structures.

Oriented aggregation (OA) is a special case of self-organization that provides an important route to produce hierarchical nanostructured materials. This growth mechanism involves the irreversible and crystallographically specific self-assembly of primary nanocrystals [34, 35]. This process is usually driven by the reduction of the surface energy of the whole system [36]. Direct attachment is the most common way. Recent examples include the formation of 1D nanorods from their respective 0D nanocrystallites such as ZnO [37] and Cu_2O [38]. Site-specific interactions of chemically heterogeneous Au nanorods would result in end-by-end or side-by-side ensembles, which were driven by triggering attraction between the distinct ligands attached to the long and short facets of the nanorods [39]. Furthermore, two- and three-dimensional OA could be extended to some new architecture. Mesoporous hexagonal nanoplates of manganese oxides were prepared hydrothermally from metal Mn foils/powders and manganese acetate precursors under basic conditions [40]. The oriented aggregation-based assembly of the nanoparticles of mixed $MnOOH/Mn_3O_4$ phases gave rise to hexagonal nanoplates with irregular mesopores, which transformed into mesoporous single-crystalline Mn_5O_8 and α-Mn_2O_3 plates after calcination at 400 and 700°C, respectively. With the increase of calcination temperature, the interior mesopores in each plate were enlarged by the growth and rearrangement of nanocrystals, and the dynamic adjustment of mesopores occurred during the phase transformation and the fusion of nanocrystals, resulting in mesopores regular-shaped (polyhedral or even well-defined rectangular). Thus, porous structures could be generated from the noncompact aggregation of these building blocks. That is to say, some surfaces of these building units are not in close contact with others. If the solvent system is properly selected with suitable viscosity and potential barrier, the control of the dynamic process of nanocrystal building blocks in assembly process is feasible. Interestingly, the moving speed, frequency, and

direction of ligand-free ZnO nanocrystal building blocks were controllable by designing a methanol/diethyl carbonate/chloroform (MDC) system with suitable viscosity and potential barrier [41]. The synthesized ZnO nanocrystals could dissolve in methanol and chloroform but not in diethyl carbonate. Thus, the synthesized ZnO nanocrystals could move freely in methanol/chloroform if diethyl carbonate was not added. However, a potential barrier arised in the solvent system after the addition of diethyl carbonate, which affected evidently the collision process of ZnO nanocrystals, wherein the coalescence between nanocrystals might take place [42]. Therefore, with aging time extended, the nuclei grew gradually by the OA of ZnO nanocrystals both along and perpendicular to the c axis due to the impact of the viscosity and potential barrier [41], leading to the final mesoporous ellipsoids formed with almost perfect crystallographic orientations and high specific surface area of $136 \, m^2/g$.

Nanomaterials with the similar composition but distinct morphologies present substantially different physical, chemical, and mechanical properties. Some typical examples are nanoparticles, nanowires, nanorods, hollow materials, nanotubes, and many other unique structures. Among the various unique structures, hollow nanomaterials have received much research interest due to their special properties including large fractional void space, large specific surface area, low density, and tunable refractive index. SnO_2 polyhedra with 3D hollow structures were synthesized through the OA mechanism [43], while the as-synthesized SnO_2 nanocrystallites in a narrow size range of 3–5 nm could assemble into triangular sheets. With additional two-dimensional crystallite aggregation on the edges, these triangular aggregates could self-turn into three-dimensional hollow octahedra sequentially. The presence of ethylenediamine, in combination with water-alcohol cosolvent, was crucial to the stabilization of SnO_2 sheets while maintaining their small crystallite size in this template-free approach.

Besides OA mechanism, the well-known physical phenomenon Ostwald ripening and Kirkendall effect have been widely employed in template-free fabrication of porous nanostructures [44–47]. Based on the combination of Kirkendall effect and Ostwald ripening, mesoporous $SrTiO_3$ nanowires could be synthesized by a template-free hydrothermal process [48]. The Kirkendall effect was the first experimental proof that atomic diffusion occurs through vacancy exchange and not by the direct interchange of atoms. The net directional flow of matter was balanced by an opposite flow of vacancies, which could commonly lead to the formation of porosity [45]. In the hydrothermal system for the synthesis of mesoporous $SrTiO_3$ nanowires, H_2O and highly concentrated OH^- would access the inner fibrous titanate to generate titanium hydroxyl species, which could subsequently react with Sr^{2+} ions in the outside layer of irregular particles to form $SrTiO_3$. Thus an outward flow of $HTiO_3^-$ was formed in order to supply enough reagents for the interaction between $HTiO_3^-$ in the Ti domain and Sr^{2+} ions in the Sr domain at the interface of these two moieties; according to the Kirkendall effect, this outward flow of ions should be balanced by the inward flow of vacancies into the fibrous structure.

As the reaction continued, the outside layer of irregular Sr species was continuously consumed in the reaction and incorporated into the fibrous structure, and the surface became smooth and clean, while the mesopores were formed inside the fibers from the condensation of supersaturated vacancies. The 1D structure grew at the cost of the small particles into longer NWs, with reduction in surface energy as the primary driving force for the morphology evolution. Finally, mesoporous NWs could be obtained (Figure 2), which led to higher photocatalytic activity for the degradation of organic dyes than commercial P25 under UV light excitation. This provides a facile template-free method to prepare cubic perovskite structures of $BaTiO_3$ or even other ternary oxides like $MgTa_2O_6$ and $Co_xTi_{1-x}O_{2-x}$ and some quaternary oxides like $PbZrTiO_3$ and $Ba_xSr_{1-x}TiO_3$.

Marvellous interfacial chemistry among various moieties presents a promising platform to synthesize various hierarchical structured materials. Recently, Wang and coworkers have developed a general emulsion-based bottom-up self-assembly (EBS) approach for assembling various kinds of ligand-stabilized nanocrystal building blocks into 3D colloidal spheres with mesoporous characteristics in which an organic ligand played a key role for the successful assembly of 3D microstructures [49–51]. On the other hand, a variety of hierarchical porous nanoarchitectures of different compositions could be prepared through microemulsion methodology. Hierarchical meso-/macroporous hydrangea-like ZnO-CeO_2 clusters with an average diameter of 4-5 μm were fabricated by the polymerization of mesostructured ZnO-CeO_2 sols surrounding the emulsion drops [52]. Squamalike Ce-doped TiO_2 (Ce/TiO_2) with hierarchical porous structure were also fabricated [14]. The obtained Ce/TiO_2 squamae were hundreds of nanometers in size with an average thickness of 30–50 nm, which aggregated loosely, leaving a disordered arrangement with plenty of interspaces between them and in the inner blocks. Each Ce/TiO_2 sheet was composed of accessible mesopores with a wormhole-like array that were formed by the assembly of the nanoparticles with the regular size of tens of nanometers. A further step could be realized to prepare hierarchical meso-/macroporous phosphonate-based inorganic-organic hybrids [3, 53].

It is very attractive and desirable to design a novel approach so that the inorganic nanocrystal units can be used to directly assemble the hierarchical structures under relatively mild conditions. Nevertheless, the control over the dynamic behaviours of inorganic nanocrystals is still difficult due to their tendency to agglomerate. Therefore, a key challenge is how to control the assembling dynamics of nanocrystal building blocks so as to obtain the expected structures instead of a fast and irregular agglomeration.

2.2. Template-Mediated Self-Assembly.

A broad range of matrixes can be employed as templates for nanocrystal organization. Strong interactions between nanocrystalline units and templates would favour the arrangement of nanocrystals in structures that are generally predefined by the shapes of the templates. The templates involved in self-assembly can be classified into two categories: hard and soft templates. Hard
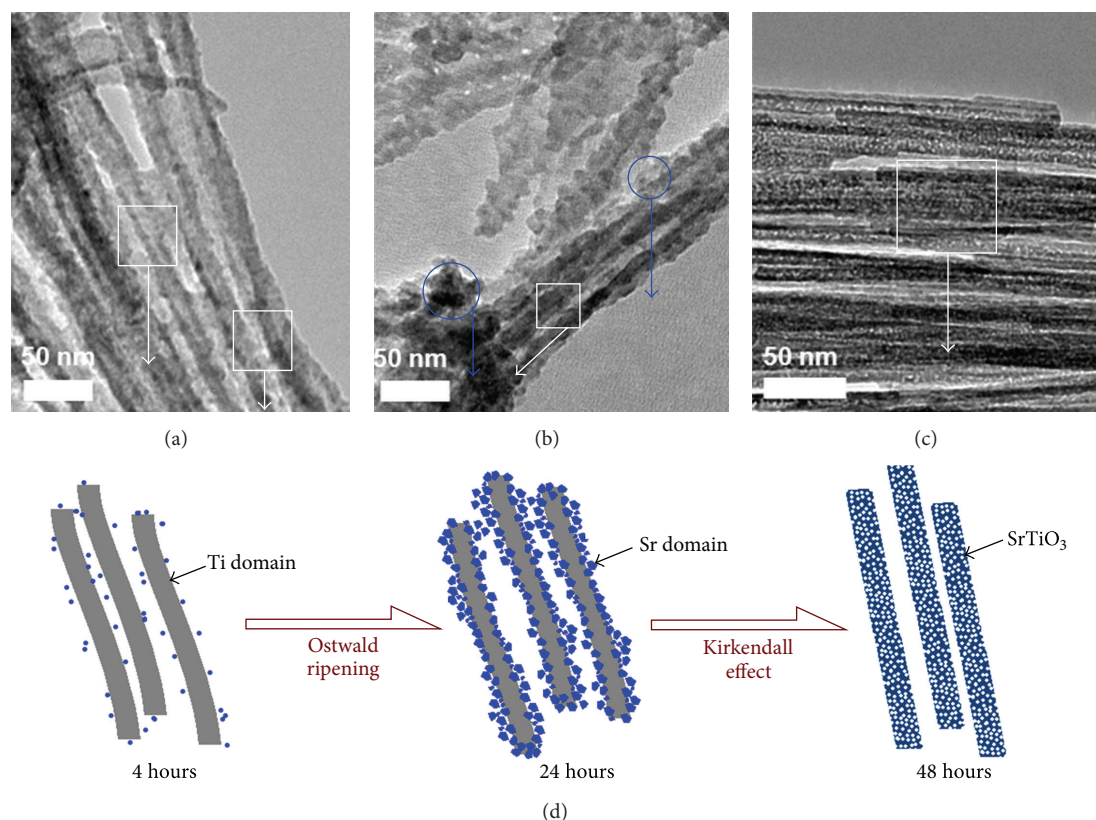
FIGURE 2: TEM ((a), (b), (c)) images for aliquots of the mixture after autoclaving for different time. A proposed mechanism for the mesoporous NWs (d) [48].

templating method generally involves the accomplishment of preorganized templates, the casting of the precursors, and subsequent removal of templates. With respect to soft templating strategy, the formation of hierarchical structures, based on the specific interaction between supramolecules and nanocrystals, can be realized.

Hard templates such as carbon nanotubes, carbon spheres, silica, and zeolite offer well-defined shapes for nanoparticle assembly [54]. Although the corresponding high efficiency and field, in general, they lack control of the spacing between the deposited nanocrystals. The hierarchical structures in natural materials play a vital role in creating different functionalities and in energy related processes in nature. Biomimic hierarchical porous materials have received great attention [55, 56]. For example, natural leaves constitute a hierarchical structure that strongly favors efficient light harvesting because of a series of evolutionarily optimized processes including light focusing, multiple scattering and adsorption, propagation, and harvesting. To better understand and use all these efficient natural processes to develop man-made materials "artificial leaves" that may replicate similar processes, natural leaves have been used as biotemplates to replicate all the fine hierarchical structures of leaves using a pure inorganic structure of TiO_2 with same hierarchy (**Figure 3**) [57]. The typical synthesis included the infiltration of inorganic precursors and then the calcination of the biotemplates. All the photosynthetic pigments were

replaced by man-made catalysts such as Pt nanoparticles. The obtained leaf replica with catalyst components was used for efficient light-harvesting and photochemical hydrogen production. Compared with TiO_2 nanoparticles prepared without biotemplates, the average absorbance intensities within visible range increased 200–234% for artificial leaves. This should certainly contribute to hierarchical architectures with all the fine structures of leaves imprinted in artificial leaves.

Soft templates possess distinct chemical structures, providing multiple well-defined binding sites for the attachment of nanocrystals. Supramolecular self-assembly provides routes to a range of materials with diverse multicomponent structures of atoms, ions, and/or molecules. The weak noncovalent between supramolecules and nanocrystals can drive inorganic-organic assembly to form inorganic frameworks [58]. Chane-Ching et al. fabricated a series of ordered crystalline nanostructured CeO_2, ZrO_2, and CeO_2-$Al (OH)_3$ based upon the cooperative self-assembly of colloidal nanoparticles and a copolymer surfactant [59]. The assembly process was driven by weakly attractive interactions between the surfaces of the nanoparticles and the templates. Also, Yuan et al. reported the spontaneous generation of mesostructured TiO_2 having an unusual interior macroporous structure, synthesized in an ethanol solution of surfactant $C_{16}(EO)_{10}$ containing small quantity of preformed water (**Figure 4**) [60]. The resulting particles had quite a thick
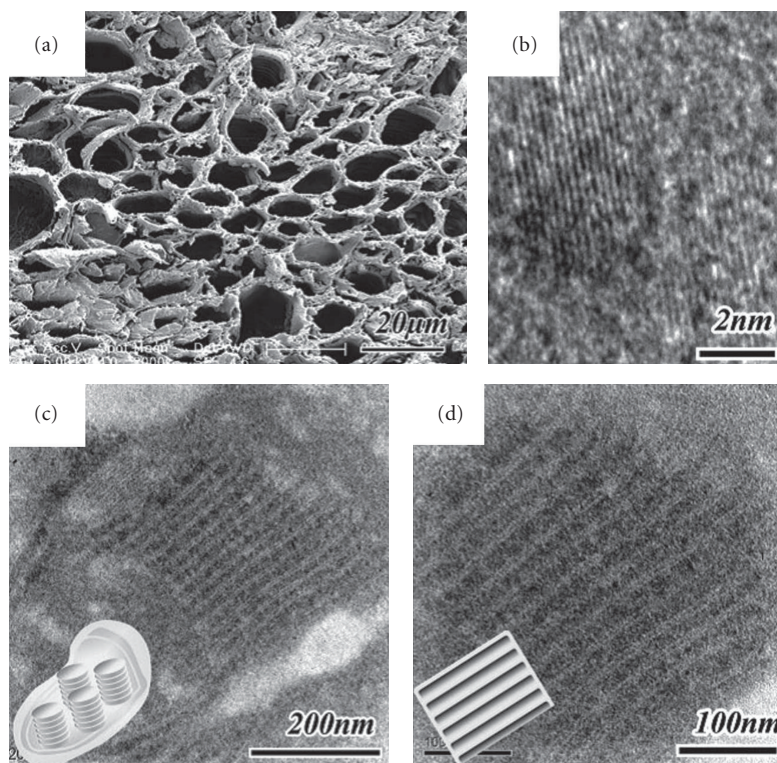
FIGURE 3: (a) SEM image of a cross-section of AIL-TiO$_2$ derived from *A. vitifolia Buch. leaf.* ((b), (c)) TEM images of a layered nanostructure in AIL1-TiO$_2$, with a corresponding illustration of the 3D structures. (d) TEM image of Pt nanoparticles deposited on TiO$_2$ [57].
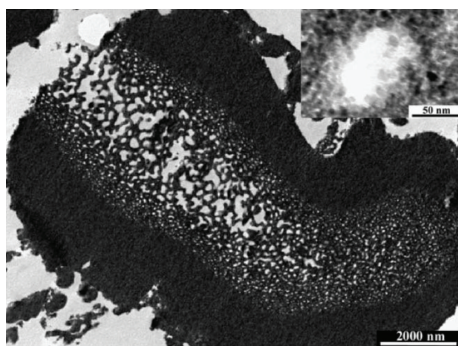
FIGURE 4: Cross-section TEM images of hierarchically mesostructured titania with an interior macroporous structure [60].

shell and a core having a spongelike macroporous structure with a uniform pore size gradient, such that the macropore sizes increased progressively from the shell layer to the core. Both the shell layers and the macroporous framework of the core had a disordered wormhole-like mesoporous structure of TiO$_2$ nanoparticle assembly. It is proposed that this hierarchical structure might be formed by combining a reverse micelle ("quasi-reverse-emulsion") templating pathway with a conventional surfactant templating technique of a hybrid composite mesostructured phase.

Alkoxide hydrolysis has been used extensively to prepare spontaneously the porous metal oxide [61]. A porous network maybe generate by cross-linking of the sol particles thorough an innovative self-formation procedure. Hierarchical meso-/macroporous metal oxides, such as zirconia [62], alumina [63], and binary mixed oxides [64] have been reported through the surfactant-assisted technique in combination with the hydrolysis from the corresponding single/mixed metal alkoxide precursors. The synthesized materials generally exhibited a parallel-arrayed channel-like macroporous structure, having a dense layer on the face of the monolithic particles under the end of macrochannels. The macroporous framework was composed of accessible mesopores with a wormhole-like array. In fact, various surfactants have been used in the construction of hierarchical porosity, but the surfactants played no role in the formation of micro- and macropores other than to influence the hydrodynamic conditions during synthesis, which could influence the textural properties of the final materials.

Templating methods have proven their generality and high-efficiency in obtaining hierarchically structured materials. Nonetheless, the further removal of the templates may not only perplex the fabrication procedures but also result in the collapse of the frameworks, and even detrimentally introduce some impurities. Thus one should choose a suitable pathway depending on the practical situation.

2.3. Self-Assembly in the Presence of External Fields. Self-assembly of nanocrystals under the action of external fields such as electric or magnetic fields, light, or sonochemistry offers a combination of speed and precision, as well as

the capability to manipulate nanocrystal assemblies. Magnetic fields have been used for the assembly of metals, metal oxides, and the corresponding nanocomposites. Ferromagnetic nanocrystals with sufficiently pinned magnetic moments undergo spontaneous assembly due to the dipole-dipole association, while the application of the magnetic field enhances the organization [65]. Distinctively, superparamagnetic nanocrystals with a randomly changing magnetic moment exerted assembly when torque exerted by a magnetic field exceeds their thermal excitation energy [66]. Electric fields induce polarization of nanoparticles, causing dipole-dipole interactions between adjacent nanoparticles. The strength of interactions increases with increasing polarizability of nanocrystals. It is worthy of noting that ensembles of inorganic nanocrystals usually show up in the form of chains due to the characteristics of the magnetic or electronic field. Moreover, the length of chains changes with the strength of electric field, the concentration of nanoparticles, and the dielectric permittivity of the media [67, 68].

Light-assisted self-assembly of nanocrystals depends on optical confinement techniques or irradiation-induced alteration of photoactive ligands [69, 70]. Especially, azobenzene functional groups undergo *trans-cis* isomerization under ultraviolet light radiation, and molecules with spirobenzopyran functional groups undergo ring-opening isomerization. When gold nanoparticles stabilized with *trans*-azobenzene dithiol ligands [70], ultraviolet radiation caused *trans-cis* isomerization of the ligands and induced molecular dipoles on the azobenzene units, triggering nanoparticle self-assembly into ordered 3D arrays. At high ligand-density, the resultant assemblies were stable without UV irradiation and withstood heating and sonication as well.

The sonochemical method has been extensively employed to generate novel materials with unusual properties and has proven to be efficient for preparing nanomaterials in a short period of time. Physical and chemical effects during the period of ultrasonic irradiation for fragmentation to small particles, acceleration of the reaction, and production of new materials with novel properties are desirable [71]. Hierarchically structured zinc oxides were synthesized at room temperature using ultrarapid sonochemistry and used as photoanodes in dye-sensitized solar cells, showing high photoelectric conversion efficiency of up to 6.42% under simulated sunlight irradiation [72]. The sonochemical synthesis of nanocrystals embedded in $CdS/ZnS/In_2S_3$ complex microspheres has been reported [73]. Mesoporous sphalerite ZnS nanomaterials with high surface area and well-structured mesoporosity were prepared through a sonochemistry-assisted method in an ethanol system, while the synchronously-formed $NaNO_3$ could inhibit the growth of the ZnS nanoparticles and further preserve the surface defects (Figure 5) [74]. Ultrasonic waves were essential to obtain a high specific surface area and uniform pore size distribution due to the significant chemical and physical roles of sonochemistry. The synthesized ZnS with valuable optical properties showed outstanding photocatalytic activity for the photodegradation of organic Rhodamine B dye.

A great diversity of external fields, such as magnetic or electronic field, light, and sonochemistry, have been used to obtain sophisticated hierarchical nanostructured materials. The synthesized materials show various architectures and valuable properties. The general syntheses involve special preparation techniques and the physicochemical characteristics of the nanocrystals. Furthermore, the resultant hierarchical structures are adjustable at the microscale, exhibiting great operability and precision.

Template-free routes in the absence of external field to obtain hierarchical nanostructures have initially gained tremendous research interest due to the synthesis simplicity and the resulting wonderful architectures. But the uncontrollability during the synthesis process makes it difficult in preparing the desired structures with high yield and repeatability. Diverse factors have great influence on the structural and porous hierarchy, including the types of precursors, temperature, reaction time, and solvent. By contrast, the templating method has been testified to be an effective way, which is on the basis of replica of the hard templates and the intimate interacting between soft templates and nanocrystals, leading to superior hierarchical structures. Further removal of the templates may perplex the fabrication procedures and result in the collapse of the frameworks and even detrimentally introduce some impurities. This makes it suitable to synthesize materials with solid frameworks such carbons, metal oxides and carbides, and silicas. Much recently, self-organization of nanoparticles assisted by external fields is emerging as a strategy for the preparation of hierarchical, multifunctional structures with programmable properties, which is mainly resulted from the accuracy and homogeneity of external fields over the whole synthesis systems. The direction interaction and even reactions can lead to well-structured hierarchy. Thus, one should choose the right synthetic strategies to prepare hierarchically structured materials according to the nature of the materials and the ultimate applications.

3. Applications of Self-Assembled Hierarchical Architectures

The organization of inorganic nanocrystalline building blocks into hierarchical porous architectures has presented an alternative for preparing interesting architectures of discrete but complex nanocomposites. The rapid growth of emerging applications of these hierarchical architectures in the area of photoenergy utilization including photodegradation, photocatalytic H_2 production, photocatalytic CO_2 conversion, and sensitized solar cells was also observed. They have displayed much superiority in physicochemical properties and application potential.

3.1. Photodegradation of Contaminants. Construction of ensembles of nanocrystals is desired to combine the initial properties of the nanocrystals with the collective properties. Semiconductor photocatalysts offer huge potential for elimination of toxic chemicals. To improve the photoactivity of the photocatalysts, three key factors should be noted: (1) extension of excitation wavelength; (2) prohibition of charge carrier recombination; and (3) promotion of active
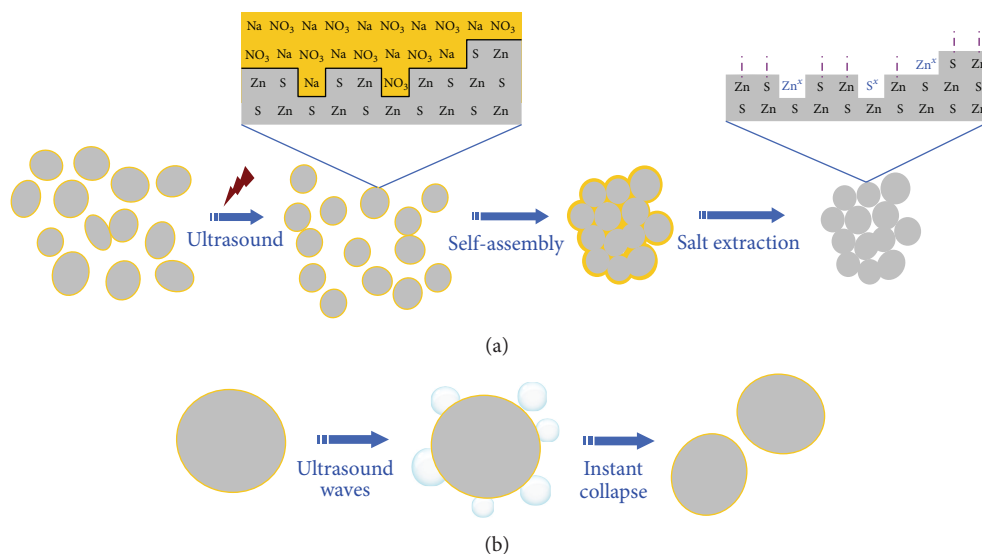
FIGURE 5: Formation mechanism of mesoporous ZnS nanomaterials (a) and simulated variation to a single nanoparticle during the period of ultrasound irradiation (b) [74].

sites. Attempts have been made and several strategies have been developed as follows [75–79]: (1) doping with foreign elements; (2) surface coupling with other materials so as to build heterostructures; (3) improving the structure of photocatalysts in order to enhance their surface area and porosity. The structural features of these hierarchical structured materials assembled from nanocrystal building blocks promise their uses as potential catalysts in heterogeneous catalysis for bulkier molecules where diffusion of reactant molecules could be facilitated. Hierarchically nanostructured hematite hollow spheres assembled by nanosheets through a microwave-assisted solvothermal route exhibited superior photocatalytic activities in the degradation of salicylic acid [80]. The hollow structure is favorable for the enhancement of the photocatalytic performance. The red-shift of the absorption edge of photocatalysts could even lead to some impressive photocatalytic behaviors under simulated solar light irradiation. Porous ZnO nanomaterials prepared through assembly of ZnO nanoclusters in aqueous solution demonstrate good photoactivity in the decomposition of phenol in wastewater [81]. The resulted superior activity than commercial ZnO powder and ZnO nanopowder may be attributed to the unique surface features and higher surface area.

Hierarchical structured meso-/macroporous Ce-doped TiO_2 [14] and $ZnO-CeO_2$ binary oxides [52] were found to be effective photocatalysts for photodecomposition of Rhodamine B. The catalysts showed higher photocatalytic reactivity than that of commercial Degussa P25. The hierarchical three-dimensional structure made up of a large number of loosely aggregated porous sheets or clusters could act as a light-transfer path for the distribution of photon energy onto the inner surface of the catalysts, benefiting the photocatalytic ability by increasing the efficiency of photoabsorption and improving mass transfer. Nonmetallic doping such as F^- was also testified to be an efficient way to improve the photocatalytic activity of TiO_2 microstructures for acetone oxidation [82]. This was due to that fluoride ions not only suppressed the formation of brookite phase but also prevented phase transition of anatase to rutile. Porous titania-phosphonate materials, synthesized through sol-gel method with the use of organically bridged tetra- or penta-phosphonates [83], possess irregular mesoporosity formed by the assembly of nanoparticles in a crystalline anatase phase, while claw molecules of ethylene diamine tetra(methylene phosphonic acid) and diethylene triamine penta(methylene phosphonic acid) were anchored to the titania network homogeneously. These porous titania-phosphonate materials exhibited higher photocatalytic activity in photodecomposition of Rhodamine B dye molecules than that of mesoporous pure TiO_2 whether under UV or visible-light irradiation. This indicated that the homogeneous incorporation of phosphonate groups into the titania framework contributed to the efficient improvement in the photocatalytic ability.

Incorporation of Ag to the porous "brick-like" $NiFe_2O_4$ superstructure would lead to attractive photovoltage response and remarkable photocatalytic activity in degradation of toluene [84]. The degradation ratio reached to 79.7% after 6 h of light irradiation. Alternatively, introduction of carbonaceous nanomaterials with unique structures and properties can add attractive features to photocatalysts. Generally, the photocatalytic enhancement can be assigned to the suppressed recombination of photogenerated charges, extended excitation wavelength, and increased surface-adsorbed reactant, although the underlying mechanisms are still unclear. Graphene has attracted immense attention recently due to the tremendous in-plane conductivity and extraordinary mechanical properties. Du et al. reported the coupling of hierarchically ordered macro-/mesoporous titania films with grapheme by a confined self-assembly method [85]. It was

found that the existence of interconnected macropores in mesoporous films considerably enhanced the mass transport through the film and increased the accessible surface area within the thin film. The apparent rate constants for macromesoporous films without and with graphene were about 11 and 17 times higher than that of pure mesoporous titania films.

3.2. Photocatalytic H_2 Production.

Hydrogen has been considered as an alternative energy source and the most potential in the future energy source economy. Dissociation of water to produce hydrogen thus has gathered more attention. However, the unfavorably large energy barrier of this simple progress makes it considerably difficult in the viewpoint of scientific research [86]:

$$2H_2O\,(l) \longrightarrow 2H_2\,(g) + O_2\,(g), \qquad \Delta G = +474\,kJ/mol \tag{1}$$
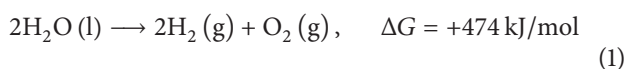
The judicious design of a photocatalyst to reduce this activation energy and make the process feasible with photons within the solar spectrum is the core ideology. Since 1972, Fujishima and Honda carried out a pioneering work on photoelectrochemical decomposition of water on electrodes modified by titanium dioxide materials under UV-irradiation [87], a mass of research articles about photocatalysis on water splitting by various pholocatalysts have been largely covered. On the other hand, just a small percentage of the sunlight that reaches the earth's surface is capable of fulfilling the current energy needs of human beings. One of the important tasks is to find advanced materials with suitable structures to use sunlight for photoelectrochemical decomposition of water for H_2 production. Accordingly, hierarchal structures from the assembly of nanocrystals endow them with the capability of harvesting light and improving mass transfer owing to the special structural properties.

Leaf skeleton could perform dual roles as a template and a carbon source for the formation of the iron or iron carbide materials through one-step carbothermal reduction of iron (II) precursors [88]. The obtained magnetic iron carbide materials were perfect replicas of a hierarchical leaf skeleton, which could be further used as electrodes for water splitting. This method has great promise for the synthesis of a variety of hierarchically microstructured objects for catalytic and electrochemical purposes due to the biomimic feature. Hierarchical porous structures with enhanced photocatalytic activity for H_2 production through facile template-free routes have also been reported recently. Peng and coworkers prepared hierarchical porous $ZnIn_2S_4$ microspheres using a facile template-free hydrothermal method [89]. The prepared $ZnIn_2S_4$ demonstrated high photocatalytic H_2 production efficiency. The photocatalytic activity could be further enhanced with the assistance of a Pt cocatalyst under visible light irradiation. Moreover, Hartmann et al. compared the photoelectrochemical properties of two kinds of hierarchically porous TiO_2 films prepared by the prevalent methods [90]. It was found that sol-gel derived hierarchically porous TiO_2 films demonstrated about 10 times higher efficiency for the water splitting reaction than the counterparts prepared

from crystalline TiO_2 nanoparticles. Indeed, the photocatalytic performance of nanoparticle-based TiO_2 films might suffer from insufficient electronic connectivity, while the hierarchical porous TiO_2 films through the sol-gel method could provide not only sufficient electronic connectivity but also hierarchically meso-/macroporosity for efficient mass transport and high surface area during the photocatalytic process.

Metal chalcogenide aerogels composed of physically interconnected nanobuilding blocks without organic spacers represent one class of semiconducting inorganic porous nanostructure [91]. Highly porous networks of self-assembled metal chalcogenide gels including aerogels, xerogels, and chalcogels are able to store vast amounts of electric charge, which could be tuned to absorb throughout the solar spectrum for photocatalysis and photovoltaic applications [92]. For example, CuS/ZnS nanoporous nanosheets assembled from nanocrystals exhibited high visible light photocatalytic H_2 production activity due to the heterojunctions built between ZnS and CuS, which could facilitate the interfacial charge transfer [93].

Significant advances have been achieved in the exploring and designing of novel structures for photocatalytic water splitting in the past years. Nevertheless, the efficient and facile synthesis of desired porous materials with well-defined hierarchical structures is still insufficient. Thus further investigation endeavours should be of significance and invested subsequently.

3.3. Hierarchical Structures for CO_2 Conversion.

The CO_2 amount in the earth's atmosphere levels is increasing rapidly with the fast development of industrialization, which has caused the alteration of the temperature of the atmosphere and the acidity of the ocean. Reversely, CO_2 can serve as C1 building block for various organic chemicals. Photocatalytic conversion of thermodynamically stable CO_2 into valuable hydrocarbon products has been one feasible option to curtail the rise of the threat [94]. Many kinds of products including formic acid, formaldehyde, methanol, and methane could be obtained during the photocatalytic process, and a multiple reduction process is usually involved:

$$H_2O + 2h^+ \longrightarrow \frac{1}{2}O_2 + 2H^+ \tag{2}$$

$$CO_2\,(aq.) + 2H^+ + 2e^- \longrightarrow HCOOH \tag{3}$$

$$HCOOH + 2H^+ + 2e^- \longrightarrow HCHO + H_2O \tag{4}$$

$$HCHO + 2H^+ + 2e^- \longrightarrow CH_3OH \tag{5}$$

$$CH_3OH + 2H^+ + 2e^- \longrightarrow CH_4 + H_2O \tag{6}$$
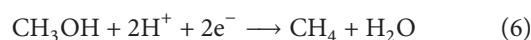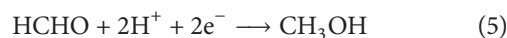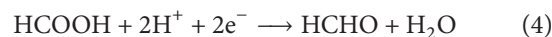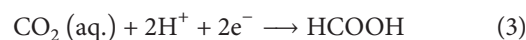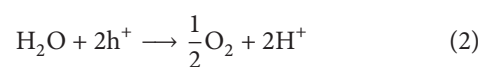
where h^+ and e^- represent the photogenerated holes and electrons, respectively. Since hierarchical porous materials possess accessible surface and considerable porosity, the use of porous nanomaterials for photocatalytic CO_2 conversion has received much attention recently. For example, it was found that titanium species incorporated mesoporous silicas

exhibit a much higher activity than bulk TiO_2 in the photoreduction of CO_2 with water to generate methanol and methane under UV irradiation [95]. After incorporation of Cu/TiO_2 nanocomposites into mesoporous silica through one-pot sol-gel method, the CO_2 photoreduction rates were significantly enhanced due to the synergistic combination of Cu deposition and high surface area silica support [96]. CO was found to be the primary product of CO_2 reduction for TiO_2-SiO_2 catalysts without Cu. CH_4 was selectively produced when Cu species was deposited on TiO_2. The rate limiting step for this reaction may be the desorption of the reaction intermediates from the active sites.

It is well known that zeolites can offer unique nanoscaled pore reaction fields and an unusual internal surface topology. TiO_2 catalysts based on zeolites have been widely studied for photocatalytic reduction of CO_2. High efficiency and high selectivity for methanol could be achieved, which might be due to that the charge-transfer excited state of the highly dispersed TiO_2 species was thought to play a key role in the high selectivity for CH_3OH, in contrast to the selectivity to CH_4 obtained on bulk TiO_2 [97]. Ti silicalite molecular sieve (TS-1) as photocatalyst under UV light illumination and using methanol as an electron donor could synthesize the main product of formic acid [98]. Up to now, many studies have demonstrated that molecular sieves and porous silica films that coupled with highly dispersed TiO_2 active species are promising photocatalysts for photocatalytic CO_2 conversion in comparison with bulk TiO_2. In addition, a large amount of other semiconductors such as ZnO, WO_3, CdS, and ZnS has testified to be effective for photoreduction of CO_2 [99, 100]. Notably, the suitable band-gap positions of semiconductors are indispensable for efficient CO_2 photocatalysis conversion.

Considering the hierarchical architectures own special optical properties and porous advantages, the use of hierarchical porous structures for CO_2 photoreduction should enhance the efficiency and the selectivity of the products. Disappointedly, there are still rare reports about the practical application of hierarchical structured materials for CO_2 photoreduction. Recycling of CO_2 via photocatalysis provides a promising approach for CO_2 conversion to hydrocarbons which mimics photosynthesis in green plants, showing greater superiorities than the conventional CO_2 capture strategy. Correspondingly, the hierarchical architectures replicated from the biotemplates should fit the qualification to be a guide for the rational design of advanced materials for photocatalytic CO_2 conversion.

On the other hand, a wide variety of natural plants and some microorganisms can perform CO_2 and H_2O conversion to chemicals by photosynthesis with great efficiency. In order to achieve the benefits of photosynthesis process of CO_2 and H_2O conversion in useful chemical compounds under sunlight irradiation, one can imagine an artificial system performing photosynthesis as leaves and other microorganisms do by encapsulating or immobilizing the biological photosynthetic matter, organelles, and whole cells within an inert support [101]. For instance, the encapsulation of unicellular cyanobacteria and a series of algae have been introduced into 3D hierarchically porous silica matrix for the conversion of water and CO_2 under light excitation [102, 103].

The immobilized species have shown survival times of up to 5 months with the photosynthetic production of oxygen recorded as much as 17 weeks after immobilization. As a result, the immobilization of cells could allow the continuous exploitation of cells in a nondestructive way to produce metabolites as biofuels. In comparison with well-known photocatalysts (e.g., TiO_2), which generally reduce CO_2 into hydrocarbons under UV irradiation, high temperature, and high pressure [104], these photochemical materials operate under ambient conditions. The environmental impact and energy required are lower. These photochemical materials could thus contribute towards future initiatives in helping to mitigate the energy crisis and reduce CO_2 emission.

3.4. Sensitized Solar Cells.

As the direct conversion of sunlight to electricity, photovoltaic technology has received much attention. In order to increase solar/electricity efficiency, sensitized solar cells (SSCs) have been intensively investigated since 1991 [105, 106]. Dye-sensitized solar cells (DSSCs) and quantum-dot-sensitized solar cells (QDSSCs) have been widely investigated as next generation solar cells because of their advantages of excellent performance and low production cost [107]. Typical SSCs consisted of three parts: work electrodes (WE), counter electrodes (CE), and liquid or polymeric electrolytes. The WE are crucial in light harvesting, which determines the overall conversion efficiency. The ideal WE should have a well-defined nanostructures to support photoactive dyes and QDs. The presence of hierarchical structures can thus optimize the optical path length and enhance the light absorbance efficiency.

Self-assembly of TiO_2 nanoparticles to generate hierarchical pores for DSSCs application has been reported [108, 109]. The resultant high surface area of nanoparticles and hierarchical pores can offer channels for mass transfer and light harvesting. TiO_2 spheres with hierarchical pores via grafting polymerization and sol-gel process could be used as photoanodes for DSSCs, showing improved photovoltaic efficiency as compared to the counterpart of smoother TiO_2 nanoparticles [108]. This might be due to the increased surface areas and light scattering. SnO_2 hollow nanospheres enclosed by single crystalline nanoparticles were prepared by a one-step surfactant-free hydrothermal reaction (Figure 6) [110]. The SnO_2 hollow nanospheres could adsorb a large amount of dye molecules due to their large specific surface area and have a high light harvesting efficiency resulting from the light scattering and reflection abilities of their hollow morphology, as well as the efficient charge separation and transport properties of their single crystalline structure, and thus they are a favourable structure for dye-sensitized solar cells. The dye-sensitized solar cells showed a high short-circuit current intensity of 14.59 mA/cm^2 and superior light/electricity conversion efficiency of 6.02%. Particularly, the template-free strategy offers an opportunity to assemble the nanostructures with exposed high surface energy to demonstrate high performance on DSSCs.

ZnO is a promising candidate for the photoanode of DSSCs. In comparison with TiO_2, ZnO exhibits similar band gap and the electron-injection process but higher electronic
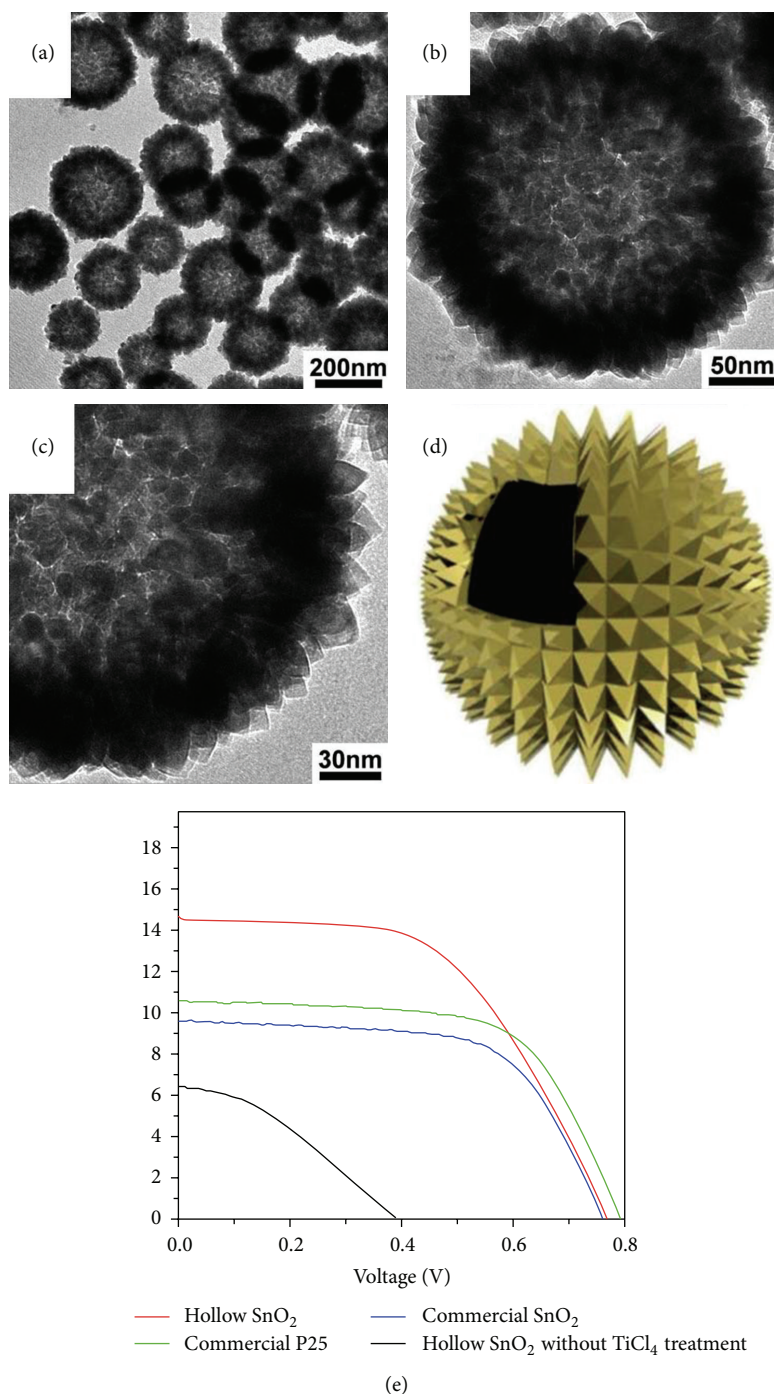
FIGURE 6: ((a), (b), (c)) TEM images of SnO_2 hollow nanospheres; (d) a schematic image of the hollow sphere; (e) photocurrent-photovoltage characteristics of DSSCs assembled from as-prepared SnO_2 hollow nanospheres, commercial P25, and commercial SnO_2 with $TiCl_4$ treatment, as well as SnO_2 hollow nanospheres without $TiCl_4$ treatment [110].

mobility that would favour photoinduced electron transport. The reduced recombination of photoexcited electrons and holes can improve the solar conversion efficiency when used in DSSCs [111]. Chou and coworkers synthesized hierarchically porous ZnO structures generated through aggregation of ZnO nanocrystals. A significantly enhanced power conversion efficiency (PCEs) of 5.4% could be achieved [112–114].

The PCE could further be increased to 6.9% after modifying the surface of ZnO with lithium [115]. Cheng and Hsieh fabricated hierarchically structured ZnO by self-assembly of secondary nanoparticles, which could be used as an effective photoelectrode for DSSCs [116]. The hierarchical architecture could provide more photon harvesting owing to significant light scattering without sacrificing the specific surface area.

The improvement of the open-circuit photovoltage and the short-circuit photocurrent density of ZnO based DSSCs was ascribed to the effective suppression of electron recombination.

The amount of dye adsorption is one of the key factors to improve solar/electricity conversion efficiency of DSSCs. Besides the conventional DSSCs, an alternative strategy for the construction of new DSSCs was proposed by using hybrid metal sulfonate or phosphonate mesoporous materials with large conjugated hybrid framework [117]. The one-pot condensation between metal precursors and dyes allows the molecular-level penetration of large π-aromatic groups into the semiconductor network homogenously, resulting in an unprecedented large loading amount of organic dyes, but without the disadvantages of dye aggregation and poor electron transmission due to the isolation of single dye centers by surrounding semiconductor oligomers.

In the context of solar energy conversion, QDSSCs are a promising alternative to existing photovoltaic technologies due to the tunable band gap and promise of stable, low-cost performance. Moreover, QDs open up a way to utilize hot electrons and to generate multiple electron-hole pairs with a single photon through impact ionization. Incorporation of QDs into hierarchical porous structures that are assembled from nanocrystal building blocks is provided with the combined photoelectric and structural qualities [118]. CdS quantum dots with surface modified by mercaptosuccinic acid were assembled onto bare TiO_2 porous films and presented a better-covered quantum dot monolayer on the TiO_2 surface and lower charge transport resistance of the surface linker, both of which were responsible for the conversion efficiencies of QDSSCs [119]. Furthermore, the electron injection yield depends on the distance between QDs and TiO_2 and it decreases with the increase of linkage chain length. This is a nonignorable item in understanding functionality of phosphonic linkers and rational design of better photoelectrochemical materials.

4. Summary and Perspective

The self-assembly of inorganic nanocrystals into sophisticated hierarchical structures has much promise for advanced materials and devices that may challenge the current lithography techniques and natural architectural designs. A number of assembly processes from nanocrystal building blocks can be harnessed in the creation of hierarchical nanostructured materials. The different interactions between nanocrystallites can force to generate temporary or permanent engagement or interconnection among the nanobuilding blocks. The assembled hierarchical nanostructured materials with improved and tailorable properties have found application potential in the field of photoenergy utilization including photodegradation of contaminants, photocatalytic H_2 production, photocatalytic CO_2 conversion, and sensitized solar cells. The enhanced performances can be attributed to the high surface area for active sites dispersion and porosity to optimize mass transfer and light harvesting.

However, research in nanomaterials still faces many challenges in synthesis, property characterization, and device fabrication. Synthetic architecture of complex inorganic nanostructures is just in its infancy compared with other well-established chemical syntheses. Design rules are urgently needed for the synthesis of hierarchical nanostructured systems by exploiting the analogy of nanoparticles. Robust and highly reproducible synthesis is vital for such studies. Alternatively, rational preparation of inorganic nanocrystals is emerging as a means to enhance their size- and shape-dependent properties and thus the self-assembly process. Furthermore, it is of great significance to characterize the process of self-assembly in a much more rigorous manner than is done at present. Simulations of self-assembly with particular thermodynamic parameters and architectural features are emerging as a powerful tool in obtaining novel structures and guiding the formation of existing architectures. To realize the potential of nanocrystalline ensembles, the models and experiments should mutually inform each other. Along the way, principles and methods should be learned that allow us not only to assemble functional nanostructures but also to judiciously design them so that future advances are not exclusively on the basis of experimental trial. And a combination of bottom-up and top-down methods in nanoparticle assembly would lead to large area high-quality hierarchical architectures. The self-organization of nanocrystals with the assistance of surfactant, biotemplates and external fields is emerging as a strategy for the preparation of multifunctional structures with well-structured hierarchy.

Conflict of Interests

The authors declare that there is no conflict of interests regarding the publication of this paper.

Acknowledgments

References

[1] Y. P. Zhu, T. Z. Ren, and Z. Y. Yuan, "Mesoporous non-siliceous inorganic-organic hybrids: a promising platform for designing multifunctional materials," *New Journal of Chemistry*, 2014.

[2] T. Y. Ma, L. Liu, and Z. Y. Yuan, "Direct synthesis of ordered mesoporous carbons," *Chemical Society Reviews*, vol. 42, pp. 3977–4003, 2013.

[3] T.-Y. Ma and Z.-Y. Yuan, "Metal phosphonate hybrid mesostructures: environmentally friendly multifunctional materials for clean energy and other applications," *ChemSusChem*, vol. 4, no. 10, pp. 1407–1419, 2011.

[4] Y. Sun, B. Mayers, and Y. Xia, "Metal nanostructures with hollow interiors," *Advanced Materials*, vol. 15, no. 7-8, pp. 641–646, 2003.

[5] T. Nakashima and N. Kimizuka, "Interfacial synthesis of hollow TiO$_2$ microspheres in ionic liquids," *Journal of the American Chemical Society*, vol. 125, no. 21, pp. 6386–6387, 2003.

[6] Y. L. Hou, H. Kondoh, and T. Ohta, "Self-assembly of Co nanoplatelets into spheres: synthesis and characterization," *Chemistry of Materials*, vol. 17, no. 15, pp. 3994–3996, 2005.

[7] Z. H. Nie, A. Petukhova, and E. Kumacheva, "Properties and emerging applications of self-assembled structures made from inorganic nanoparticles," *Nature Nanotechnology*, vol. 5, no. 1, pp. 15–25, 2010.

[8] M. R. Buck and R. E. Schaak, "Emerging strategies for the total synthesis of inorganic nanostructures," *Angewandte Chemie*, vol. 52, pp. 2–27, 2013.

[9] C. M. Doherty, D. Buso, A. J. Hill, S. Furukawa, S. Kitagawa, and P. Falcaro, "Using functional nano- and microparticles for the preparation of metal-organic framework composites with novel properties," *Accounts of Chemical Research*, vol. 47, pp. 396–405, 2014.

[10] G. M. Whitesides and B. Grzybowski, "Self-assembly at all scales," *Science*, vol. 295, no. 5564, pp. 2418–2421, 2002.

[11] I. E. Rauda, R. Buonsanti, L. C. Saldarriaga-Lopez et al., "General method for the synthesis of hierarchical nanocrystal-based mesoporous materials," *ACS Nano*, vol. 6, pp. 6386–6399, 2012.

[12] W. X. Dong, G. L. Zhao, B. Song, G. Xu, J. Zhou, and G. R. Han, "Surfactant-free fabrication of CaTiO$_3$ butterfly-like dendrite via a simple one-step hydrothermal route," *CrystEngComm*, vol. 14, pp. 6990–6997, 2012.

[13] B. Xie, H. Shi, G. Liu et al., "Preparation of surface porous microcapsules templated by self-assembly of nonionic surfactant micelles," *Chemistry of Materials*, vol. 20, no. 9, pp. 3099–3104, 2008.

[14] T.-Y. Ma, J.-L. Cao, G.-S. Shao, X.-J. Zhang, and Z.-Y. Yuan, "Hierarchically structured squama-like cerium-doped titania: synthesis, photoactivity, and catalytic CO oxidation," *Journal of Physical Chemistry C*, vol. 113, no. 38, pp. 16658–16667, 2009.

[15] Z.-Y. Yuan and B.-L. Su, "Insights into hierarchically meso-macroporous structured materials," *Journal of Materials Chemistry*, vol. 16, no. 7, pp. 663–677, 2006.

[16] A. Stein, S. G. Rudisill, and N. D. Petkovich, "Perspective on the influence of interactions between hard and soft templates and precursors on morphology of hierarchically structured porous materials," *Chemistry of Materials*, vol. 26, pp. 259–276, 2014.

[17] T.-Y. Ma, X.-J. Zhang, G.-S. Shao, J.-L. Cao, and Z.-Y. Yuan, "Ordered macroporous titanium phosphonate materials: synthesis, photocatalytic activity, and heavy metal ion adsorption," *Journal of Physical Chemistry C*, vol. 112, no. 8, pp. 3090–3096, 2008.

[18] T.-Y. Ma, X.-Z. Lin, X.-J. Zhang, and Z.-Y. Yuan, "Hierarchical mesostructured titanium phosphonates with unusual uniform lines of macropores," *Nanoscale*, vol. 3, no. 4, pp. 1690–1696, 2011.

[19] Y. Li, Z. Y. Fu, and B. L. Su, "Hierarchically structured porous materials for energy conversion and storage," *Advanced Functional Materials*, vol. 22, pp. 3634–4667, 2012.

[20] T. Q. Wang, X. L. Wang, Y. Lu et al., "Self-assembly of hierarchical Fe$_3$O$_4$ microsphere/graphene nanosheet composite: towards a promising high-performance anode for Li-ion batteries," *RSC Advances*, vol. 4, pp. 322–330, 2014.

[21] Y. Zhong, Z. X. Wang, R. F. Zhang et al., "Interfacial self-assembly driven formation of hierarchically structured nanocrystals with photocatalytic activity," *ACS Nano*, vol. 8, pp. 827–833, 2014.

[22] L.-H. Chen, X.-Y. Li, G. Tian et al., "Highly stable and reusable multimodal zeolite TS-1 based catalysts with hierarchically interconnected three-level micro-meso-macroporous structure," *Angewandte Chemie*, vol. 50, no. 47, pp. 11156–11161, 2011.

[23] X.-Y. Yang, G. Tian, L.-H. Chen et al., "Well-organized zeolite nanocrystal aggregates with interconnected hierarchically micro-meso-macropore systems showing enhanced catalytic performance," *Chemistry*, vol. 17, no. 52, pp. 14987–14995, 2011.

[24] R. Dang, L. L. Song, W. J. Dong et al., "Synthesis and self-assembly of large-area Cu nanosheets and their application as an aqueous conductive ink on flexible electronics," *ACS Applied Materials Interfaces*, vol. 6, pp. 622–629, 2014.

[25] K. J. M. Bishop, C. E. Wilmer, S. Soh, and B. A. Grzybowski, "Nanoscale forces and their uses in self-assembly," *Small*, vol. 5, no. 14, pp. 1600–1630, 2009.

[26] Y. J. Kang, K. J. Erickson, and T. A. Taton, "Plasmonic nanoparticle chains via a morphological, sphere-to-string transition," *Journal of the American Chemical Society*, vol. 127, no. 40, pp. 13800–13801, 2005.

[27] K. K. Caswell, J. N. Wilson, U. H. F. Bunz, and C. J. Murphy, "Preferential end-to-end assembly of gold nanorods by biotin-streptavidin connectors," *Journal of the American Chemical Society*, vol. 125, no. 46, pp. 13914–13915, 2003.

[28] Z. Y. Tang, Z. L. Zhang, Y. Wang, S. C. Glotzer, and N. A. Kotov, "Self-assembly of CdTe nanocrystals into free-floating sheets," *Science*, vol. 314, no. 5797, pp. 274–278, 2006.

[29] N. N. Zhao, K. Liu, J. Greener, Z. H. Nie, and E. Kumacheva, "Close-packed superlattices of side-by-side assembled au-cdse nanorods," *Nano Letters*, vol. 9, no. 8, pp. 3077–3081, 2009.

[30] S. Park, J.-H. Lim, S.-W. Chung, and C. A. Mirkin, "Self-assembly of mesoscopic metal-polymer amphiphiles," *Science*, vol. 303, no. 5656, pp. 348–351, 2004.

[31] D. Nykypanchuk, M. M. Maye, D. van der Lelie, and O. Gang, "DNA-guided crystallization of colloidal nanoparticles," *Nature*, vol. 451, no. 7178, pp. 549–552, 2008.

[32] C. R. Iacovella and S. C. Glotzer, "Complex crystal structures formed by the self-assembly of ditethered nanospheres," *Nano Letters*, vol. 9, no. 3, pp. 1206–1211, 2009.

[33] J. Sharma, R. Chhabra, A. Cheng, J. Brownell, Y. Liu, and H. Yan, "Control of self-assembly of DNA tubules through integration of gold nanoparticles," *Science*, vol. 323, no. 5910, pp. 112–116, 2009.

[34] J. F. Banfield, S. A. Welch, H. Z. Zhang, T. T. Ebert, and R. L. Penn, "Aggregation-based crystal growth and microstructure development in natural iron oxyhydroxide biomineralization products," *Science*, vol. 289, no. 5480, pp. 751–754, 2000.

[35] R. L. Penn and J. F. Banfield, "Imperfect oriented attachment: dislocation generation in defect-free nanocrystals," *Science*, vol. 281, no. 5379, pp. 969–971, 1998.

[36] D. Zitoun, N. Pinna, N. Frolet, and C. Belin, "Single crystal manganese oxide multipods by oriented attachment," *Journal of the American Chemical Society*, vol. 127, no. 43, pp. 15034–15035, 2005.

[37] J. J. Teo, Y. Chang, and H. C. Zeng, "Fabrications of hollow nanocubes of Cu$_2$O and Cu via reductive self-assembly of CuO nanocrystals," *Langmuir*, vol. 22, no. 17, pp. 7369–7377, 2006.

[38] C. Pacholski, A. Kornowski, and H. Weller, "Self-assembly of ZnO: from nanodots to nanorods," *Angewandte Chemie Intenational Edition*, vol. 41, no. 7, pp. 1188–1191, 2002.

[39] Z. H. Nie, D. Fava, E. Kumacheva, S. Zou, G. C. Walker, and M. Rubinstein, "Self-assembly of metal-polymer analogues of amphiphilic triblock copolymers," *Nature Materials*, vol. 6, no. 8, pp. 609–614, 2007.

[40] T.-Z. Ren, Z.-Y. Yuan, W. Hu, and X. Zou, "Single crystal manganese oxide hexagonal plates with regulated mesoporous structures," *Microporous and Mesoporous Materials*, vol. 112, no. 1–3, pp. 467–473, 2008.

[41] Y. X. Liu, D. S. Wang, Q. Peng, D. R. Chu, X. W. Liu, and Y. D. Li, "Directly assembling ligand-free ZnO nanocrystals into three-dimensional mesoporous structures by oriented attachment," *Inorganic Chemistry*, vol. 50, no. 12, pp. 5841–5847, 2011.

[42] X. Xu, F. Liu, K. Yu, W. Huang, B. Peng, and W. Wei, "A kinetic model for nanocrystal morphology evolution," *ChemPhysChem*, vol. 8, no. 5, pp. 703–711, 2007.

[43] H. G. Yang and H. C. Zeng, "Self-construction of hollow SnO_2 octahedra based on two-dimensional aggregation of nanocrystallites," *Angewandte Chemie*, vol. 43, no. 44, pp. 5930–5933, 2004.

[44] J. Li and H. C. Zeng, "Hollowing Sn-doped TiO_2 nanospheres via Ostwald ripening," *Journal of the American Chemical Society*, vol. 129, no. 51, pp. 15839–15847, 2007.

[45] A. Cabot, M. Ibáñez, P. Guardia, and A. P. Alivisatos, "Reaction regimes on the synthesis of hollow particles by the Kirkendall effect," *Journal of the American Chemical Society*, vol. 131, no. 32, pp. 11326–11328, 2009.

[46] H. J. Fan, M. Knez, R. Scholz et al., "Monocrystalline spinel nanotube fabrication based on the Kirkendall effect," *Nature Materials*, vol. 5, no. 8, pp. 627–631, 2006.

[47] Y. D. Yin, R. M. Rioux, C. K. Erdonmez, S. Hughes, G. A. Somorjal, and A. P. Alivisatos, "Formation of hollow nanocrystals through the nanoscale Kirkendall effect," *Science*, vol. 304, no. 5671, pp. 711–714, 2004.

[48] T.-Y. Ma, H. Li, T.-Z. Ren, and Z.-Y. Yuan, "Mesoporous $SrTiO_3$ nanowires from a template-free hydrothermal process," *RSC Advances*, vol. 2, no. 7, pp. 2790–2796, 2012.

[49] F. Bai, D. S. Wang, Z. Y. Huo et al., "A versatile bottom-up assembly approach to colloidal spheres from nanocrystals," *Angewandte Chemie*, vol. 46, no. 35, pp. 6650–6653, 2007.

[50] L. Y. Wang, P. Li, J. Zhuang et al., "Carboxylic acid enriched nanospheres of semiconductor nanorods for cell imaging," *Angewandte Chemie*, vol. 47, no. 6, pp. 1054–1057, 2008.

[51] C. Chen, C. Y. Nan, D. S. Wang et al., "Mesoporous multicomponent nanocomposite colloidal spheres: ideal high-temperature stable model catalysts," *Angewandte Chemie*, vol. 50, no. 16, pp. 3725–3729, 2011.

[52] T.-Y. Ma, Z.-Y. Yuan, and Q. J.-L. Cao, "Hydrangea-like meso-macroporous $ZnO-CeO_2$ binary oxide materials: synthesis, photocatalysis and CO oxidation," *European Journal of Inorganic Chemistry*, no. 5, pp. 716–724, 2010.

[53] T.-Y. Ma, X.-Z. Lin, X.-J. Zhang, and Z.-Y. Yuan, "High surface area titanium phosphonate materials with hierarchical porosity for multi-phase adsorption," *New Journal of Chemistry*, vol. 34, no. 6, pp. 1209–1216, 2010.

[54] M. A. Correa-Duarte, J. Pérez-Juste, A. Sánchez-Iglesias, M. Giersig, and L. M. Liz-Marzán, "Aligning Au nanorods by using carbon nanotubes as templates," *Angewandte Chemie*, vol. 44, no. 28, pp. 4375–4378, 2005.

[55] S. R. Hall, H. Bolger, and S. Mann, "Morphosynthesis of complex inorganic forms using pollen grain templates," *Chemical Communications*, vol. 9, no. 22, pp. 2784–2785, 2003.

[56] Y. S. Shin, J. Liu, J. H. Chang, Z. M. Nie, and G. Exarhos, "Hierarchically ordered ceramics through surfactant-templated sol-gel mineralization of biological cellular structures," *Advanced Materials*, vol. 13, pp. 728–732, 2001.

[57] H. Zhou, X. Li, T. Fan et al., "Artificial inorganic leafs for efficient photochemical hydrogen production inspired by natural photosynthesis," *Advanced Materials*, vol. 22, no. 9, pp. 951–956, 2010.

[58] H. E. Bakkali, A. Castiñeiras, I. García-Santos, J. M. González-Pérez, and J. Niclós-Gutiérrez, "Metallo-supramolecular structures by self-assembly through weak interactions in mixed ligand metal complexes of adenine and malonate," *Crystal Growth & Design*, vol. 14, no. 1, pp. 249–260, 2014.

[59] J.-Y. Chane-Ching, F. Cobo, D. Aubert, H. G. Harvey, M. Airiau, and A. Corma, "A general method for the synthesis of nanostructured large-surface-area materials through the self-assembly of functionalized nanoparticles," *Chemistry*, vol. 11, no. 3, pp. 979–987, 2005.

[60] Z.-Y. Yuan, T.-Z. Ren, and B.-L. Su, "Hierarchically mesostructured titania materials with an unusual interior macroporous structure," *Advanced Materials*, vol. 15, no. 17, pp. 1462–1465, 2003.

[61] X.-Y. Yang, A. Léonard, A. Lemaire, G. Tian, and B.-L. Su, "Self-formation phenomenon to hierarchically structured porous materials: design, synthesis, formation mechanism and applications," *Chemical Communications*, vol. 47, no. 10, pp. 2763–2786, 2011.

[62] Z.-Y. Yuan, A. Vantomme, A. Léonard, and B.-L. Su, "Surfactant-assisted synthesis of unprecedented hierarchical meso-macrostructured zirconia," *Chemical Communications*, vol. 9, no. 13, pp. 1558–1559, 2003.

[63] T.-Z. Ren, Z.-Y. Yuan, and B.-L. Su, "Microwave-assisted preparation of hierarchical mesoporous-macroporous boehmite AlOOH and gamma-Al_2O_3," *Langmuir*, vol. 20, no. 4, pp. 1531–1534, 2004.

[64] Z.-Y. Yuan, T.-Z. Ren, A. Vantomme, and B.-L. Su, "Facile and generalized preparation of hierarchically mesoporous-macroporous binary metal oxide materials," *Chemistry of Materials*, vol. 16, no. 24, pp. 5096–5106, 2004.

[65] S. L. Tripp, R. E. Dunin-Borkowski, and A. Wei, "Flux closure in self-assembled cobalt nanoparticle rings," *Angewandte Chemie*, vol. 42, no. 45, pp. 5591–5593, 2003.

[66] G. A. Held, G. Grinstein, H. Doyle, S. H. Sun, and C. B. Murray, "Competing interactions in dispersions of superparamagnetic nanoparticles," *Physical Review B*, vol. 64, Article ID 012408, 124084 pages, 2001.

[67] K. D. Hermanson, S. O. Lumsdon, J. P. Williams, E. W. Kaler, and O. D. Velev, "Dielectrophoretic assembly of electrically functional microwires from nanoparticle suspensions," *Science*, vol. 294, no. 5544, pp. 1082–1086, 2001.

[68] S. Acharya, I. Patla, J. Kost, S. Efrima, and Y. Golan, "Switchable assembly of ultra narrow CdS nanowires and nanorods," *Journal of the American Chemical Society*, vol. 128, no. 29, pp. 9294–9295, 2006.

[69] C. Bechinger, M. Brunner, and P. Leiderer, "Phase behavior of two-dimensional colloidal systems in the presence of periodic light fields," *Physical Review Letters*, vol. 86, no. 5, pp. 930–933, 2001.

[70] R. Klajn, K. J. M. Bishop, and B. A. Grzybowski, "Light-controlled self-assembly of reversible and irreversible nanoparticle suprastructures," *Proceedings of the National Academy of*

Sciences of the United States of America, vol. 104, no. 25, pp. 10305–10309, 2007.

[71] G. Cravotto and P. Cintas, "Power ultrasound in organic synthesis: moving cavitational chemistry from academia to innovative and large-scale applications," *Chemical Society Reviews*, vol. 35, no. 2, pp. 180–196, 2006.

[72] Y. T. Shi, C. Zhu, L. Wang et al., "Ultrarapid sonochemical synthesis of ZnO hierarchical structures: from fundamental research to high efficiencies up to 6.42% for quasi-solid dye-sensitized solar cells," *Chemistry of Materials*, vol. 25, pp. 1000–1012, 2013.

[73] Z. Y. Shen, G. Chen, Q. Wang, Y. G. Yu, C. Zhou, and Y. Wang, "Sonochemistry synthesis and enhanced photocatalytic H_2 production activity of nanocrystals embedded in $CdS/ZnS/In_2S_3$ microspheres," *Nanoscale*, vol. 4, no. 6, pp. 2010–2017, 2012.

[74] Y. P. Zhu, J. Li, T. Y. Ma, Y. P. Liu, G. H. Du, and Z. Y. Yuan, "Sonochemistry-assisted synthesis and optical properties of mesoporous ZnS nanomaterials," *Journal of Materials Chemistry A*, vol. 2, pp. 1093–1101, 2014.

[75] X. F. Yang, J. Chen, L. Gong, M. M. Wu, and J. C. Yu, "Cross-medal arrays of Ta-doped rutile titania," *Journal of the American Chemical Society*, vol. 131, no. 34, pp. 12048–12049, 2009.

[76] S. Shanmugam, A. Gabashvili, D. S. Jacob, J. C. Yu, and A. Gedanken, "Synthesis and characterization of $TiO_2@C$ core-shell composite nanoparticles and evaluation of their photocatalytic activities," *Chemistry of Materials*, vol. 18, no. 9, pp. 2275–2282, 2006.

[77] H. J. Wang, F. Q. Sun, Y. Zhang et al., "Photochemical growth of nanoporous SnO_2 at the air-water interface and its high photocatalytic activity," *Journal of Materials Chemistry*, vol. 20, no. 27, pp. 5641–5645, 2010.

[78] G.-S. Shao, F.-Y. Wang, T.-Z. Ren, Y. Liu, and Z.-Y. Yuan, "Hierarchical mesoporous phosphorus and nitrogen doped titania materials: synthesis, characterization and visible-light photocatalytic activity," *Applied Catalysis B: Environmental*, vol. 92, no. 1-2, pp. 61–67, 2009.

[79] G.-S. Shao, X.-J. Zhang, and Z.-Y. Yuan, "Preparation and photocatalytic activity of hierarchically mesoporous-macroporous $TiO_{2-x}N_x$," *Applied Catalysis B: Environmental*, vol. 82, no. 3-4, pp. 208–218, 2008.

[80] S.-W. Cao and Y.-J. Zhu, "Hierarchically nanostructured α-Fe_2O_3 hollow spheres: preparation, growth mechanism, photocatalytic property, and application in water treatment," *Journal of Physical Chemistry C*, vol. 112, no. 16, pp. 6253–6257, 2008.

[81] F. Xu, P. Zhang, A. Navrotsky et al., "Hierarchically assembled porous ZnO nanoparticles: synthesis, surface energy, and photocatalytic activity," *Chemistry of Materials*, vol. 19, no. 23, pp. 5680–5686, 2007.

[82] J. C. Yu, J. G. Yu, W. K. Ho, Z. T. Jiang, and L. Z. Zhang, "Effects of F^- doping on the photocatalytic activity and microstructures of nanocrystalline TiO_2 powders," *Chemistry of Materials*, vol. 14, no. 9, pp. 3808–3816, 2002.

[83] X.-J. Zhang, T.-Y. Ma, and Z.-Y. Yuan, "Titania-phosphonate hybrid porous materials: preparation, photocatalytic activity and heavy metal ion adsorption," *Journal of Materials Chemistry*, vol. 18, no. 17, pp. 2003–2010, 2008.

[84] Z. R. Zhu, X. Y. Li, Q. D. Zhao, H. Li, Y. Shen, and G. H. Chen, "Porous "brick-like" $NiFe_2O_4$ nanocrystals loaded with Ag species towards effective degradation of toluene," *Chemical Engineering Journal*, vol. 165, no. 1, pp. 64–70, 2010.

[85] J. Du, X. Lai, N. Yang et al., "Hierarchically ordered macro-mesoporous TiO_2-graphene composite films: improved mass

transfer, reduced charge recombination, and their enhanced photocatalytic activities," *ACS Nano*, vol. 5, no. 1, pp. 590–596, 2011.

[86] M. D. Hernández-Alonso, F. Fresno, S. Suárez, and J. M. Coronado, "Development of alternative photocatalysts to TiO_2: challenges and opportunities," *Energy and Environmental Science*, vol. 2, no. 12, pp. 1231–1257, 2009.

[87] A. Fujishima and K. Honda, "Electrochemical photolysis of water at a semiconductor electrode," *Nature*, vol. 238, no. 5358, pp. 37–38, 1972.

[88] Z. Schnepp, W. Yang, M. Antonietti, and C. Giordano, "Biotemplating of metal carbide microstructures: the magnetic leaf," *Angewandte Chemie*, vol. 49, no. 37, pp. 6564–6566, 2010.

[89] B. Chai, T. Peng, P. Zeng, X. Zhang, and X. Liu, "Template-free hydrothermal synthesis of $ZnIn_2S_4$ floriated microsphere as an efficient photocatalyst for H_2 production under visible-light irradiation," *Journal of Physical Chemistry C*, vol. 115, no. 13, pp. 6149–6155, 2011.

[90] P. Hartmann, D.-K. Lee, B. M. Smarsly, and J. Janek, "Mesoporous TiO_2: comparison of classical sol-gel and nanoparticle based photoelectrodes for the water splitting reaction," *ACS Nano*, vol. 4, no. 6, pp. 3147–3154, 2010.

[91] S. Bag, I. U. Arachchige, and M. G. Kanatzidis, "Aerogels from metal chalcogenides and their emerging unique properties," *Journal of Materials Chemistry*, vol. 18, no. 31, pp. 3628–3632, 2008.

[92] I. U. Arachchige and S. L. Brock, "Sol-gel assembly of CdSe nanoparticles to form porous aerogel networks," *Journal of the American Chemical Society*, vol. 128, no. 24, pp. 7964–7971, 2006.

[93] J. Zhang, J. G. Yu, Y. M. Zhang, Q. Li, and J. R. Gong, "Visible light photocatalytic H_2-production activity of CuS/ZnS porous nanosheets based on photoinduced interfacial charge transfer," *Nano Letters*, vol. 11, no. 11, pp. 4774–4779, 2011.

[94] H.-C. Yang, H.-Y. Lin, Y.-S. Chien, J. C.-S. Wu, and H.-H. Wu, "Mesoporous TiO_2/SBA-15, and Cu/TiO_2/SBA-15 composite photocatalysts for photoreduction of CO_2 to methanol," *Catalysis Letters*, vol. 131, no. 3-4, pp. 381–387, 2009.

[95] J.-S. Hwang, J.-S. Chang, S.-E. Park, K. Ikeue, and M. Anpo, "Photoreduction of carbondioxide on surface functionalized nanoporous catalysts," *Topics in Catalysis*, vol. 35, no. 3-4, pp. 311–319, 2005.

[96] Y. Li, W.-N. Wang, Z. Zhan, M.-H. Woo, C.-Y. Wu, and P. Biswas, "Photocatalytic reduction of CO_2 with H_2O on mesoporous silica supported Cu/TiO_2 catalysts," *Applied Catalysis B: Environmental*, vol. 100, no. 1-2, pp. 386–392, 2010.

[97] G. N. Nomikos, P. Panagiotopoulou, D. I. Kondarides, and X. E. Verykios, "Kinetic and mechanistic study of the photocatalytic reforming of methanol over Pt/TiO_2 catalyst," *Applied Catalysis B: Environmental*, vol. 146, pp. 249–257, 2014.

[98] N. Ulagappan and H. Frei, "Mechanistic study of CO_2 photoreduction in Ti silicalite molecular sieve by FT-IR spectroscopy," *Journal of Physical Chemistry A*, vol. 104, no. 33, pp. 7834–7839, 2000.

[99] S. C. Roy, O. K. Varghese, M. Paulose, and C. A. Grimes, "Toward solar fuels: photocatalytic conversion of carbon dioxide to hydrocarbons," *ACS Nano*, vol. 4, no. 3, pp. 1259–1278, 2010.

[100] H. Takeda and O. Ishitani, "Development of efficient photocatalytic systems for CO_2 reduction using mononuclear and multinuclear metal complexes based on mechanistic studies,"

Coordination Chemistry Reviews, vol. 254, no. 3-4, pp. 346–354, 2010.

[101] C. F. Meunier, J. C. Rooke, A. Léonard, H. Xie, and B.-L. Su, "Living hybrid materials capable of energy conversion and CO_2 assimilation," *Chemical Communications*, vol. 46, no. 22, pp. 3843–3859, 2010.

[102] A. Léonard, J. C. Rooke, C. F. Meunier, H. Sarmento, J.-P. Descy, and B.-L. Su, "Cyanobacteria immobilised in porous silica gels: exploring biocompatible synthesis routes for the development of photobioreactors," *Energy and Environmental Science*, vol. 3, no. 3, pp. 370–377, 2010.

[103] A. Léonard, P. Dandoy, E. Danloy et al., "Whole-cell based hybrid materials for green energy production, environmental remediation and smart cell-therapy," *Chemical Society Reviews*, vol. 40, no. 2, pp. 860–885, 2011.

[104] S. S. Tan, L. Zou, and E. Hu, "Photocatalytic reduction of carbon dioxide into gaseous hydrocarbon using TiO_2 pellets," *Catalysis Today*, vol. 115, no. 1–4, pp. 269–273, 2006.

[105] B. O'Regan and M. Grätzel, "A low-cost, high-efficiency solar cell based on dye-sensitized colloidal TiO_2 film," *Nature*, vol. 353, pp. 737–739, 1991.

[106] J. Burschka, N. Pellet, S. J. Moon et al., "Sequential deposition as a route to high-performance perovskite-sensitized solar cells," *Nature*, vol. 499, pp. 316–320, 2013.

[107] S. Rühle, M. Shalom, and A. Zaban, "Quantum-dot-sensitized solar cells," *ChemPhysChem*, vol. 11, no. 11, pp. 2290–2304, 2010.

[108] J. T. Park, D. Y. Roh, R. Patel, E. Kim, D. Y. Ryu, and J. H. Kim, "Preparation of TiO_2 spheres with hierarchical pores via grafting polymerization and sol-gel process for dye-sensitized solar cells," *Journal of Materials Chemistry*, vol. 20, no. 39, pp. 8521–8530, 2010.

[109] D. Hwang, H. Lee, S.-Y. Jang et al., "Electrospray preparation of hierarchically-structured mesoporous TiO_2 spheres for use in highly efficient dye-sensitized solar cells," *ACS Applied Materials and Interfaces*, vol. 3, no. 7, pp. 2719–2725, 2011.

[110] H. Wang, B. Li, J. Gao et al., "SnO_2 hollow nanospheres enclosed by single crystalline nanoparticles for highly efficient dye-sensitized solar cells," *CrystEngComm*, vol. 14, pp. 5177–5181, 2012.

[111] Q. Zhang, C. S. Dandeneau, X. Zhou, and C. Cao, "ZnO nanostructures for dye-sensitized solar cells," *Advanced Materials*, vol. 21, no. 41, pp. 4087–4108, 2009.

[112] T. P. Chou, Q. F. Zhang, G. E. Fryxell, and G. Z. Cao, "Hierarchically structured ZnO film for dye-sensitized solar cells with enhanced energy conversion efficiency," *Advanced Materials*, vol. 19, no. 18, pp. 2588–2592, 2007.

[113] Q. F. Zhang, T. P. Chou, B. Russo, S. A. Jenekhe, and G. Cao, "Aggregation of ZnO nanocrystallites for high conversion efficiency in dye-sensitized solar cells," *Angewandte Chemie*, vol. 47, no. 13, pp. 2402–2406, 2008.

[114] Q. F. Zhang, T. P. Chou, B. Russo, S. A. Jenekhe, and G. Z. Cao, "Polydisperse aggregates of ZnO nanocrystallites: a method for energy-conversion-efficiency enhancement in dye-sensitized solar cells," *Advanced Functional Materials*, vol. 18, no. 11, pp. 1654–1660, 2008.

[115] Q. F. Zhang, C. S. Dandeneau, S. Candelaria et al., "Effects of lithium ions on dye-sensitized ZnO aggregate solar cells," *Chemistry of Materials*, vol. 22, no. 8, pp. 2427–2433, 2010.

[116] H.-M. Cheng and W.-F. Hsieh, "High-efficiency metal-free organic-dye-sensitized solar cells with hierarchical ZnO photoelectrode," *Energy and Environmental Science*, vol. 3, no. 4, pp. 442–447, 2010.

[117] T.-Y. Ma, Y.-S. Wei, T.-Z. Ren, L. Liu, Q. Guo, and Z.-Y. Yuan, "Hexagonal mesoporous titanium tetrasulfonates with large conjugated hybrid framework for photoelectric conversion," *ACS Applied Materials and Interfaces*, vol. 2, no. 12, pp. 3563–3571, 2010.

[118] H. N. Kim, T. W. Kim, I. Y. Kim, and S.-J. Hwang, "Cocatalyst-free photocatalysts for efficient visible-light-induced H2 production: porous assemblies of CdS quantum dots and layered titanate nanosheets," *Advanced Functional Materials*, vol. 21, no. 16, pp. 3111–3118, 2011.

[119] Y.-J. Shen and Y.-L. Lee, "Assembly of CdS quantum dots onto mesoscopic TiO_2 films for quantum dot-sensitized solar cell applications," *Nanotechnology*, vol. 19, no. 4, Article ID 045602, 2008.

Research Article

Modification of One-Dimensional TiO$_2$ Nanotubes with CaO Dopants for High CO$_2$ Adsorption

Chin Wei Lai

Nanotechnology & Catalysis Research Centre (NANOCAT), Institute of Postgraduate Studies (IPS), Universiti Malaya, 3rd Floor, Block A, 50603 Kuala Lumpur, Malaysia

Correspondence should be addressed to Chin Wei Lai; cwlai@um.edu.my

One-dimensional calcium oxide (CaO-) based titanium dioxide (TiO$_2$) nanotubes were successfully synthesized through a rapid electrochemical anodization and chemical wet impregnation techniques. In this study, calcium nitrate solution was used as a calcium source precursor. The reaction time and concentration of calcium source on the formation of CaO-TiO$_2$ nanotubes were investigated using field emission microscopy, energy dispersion X-ray spectroscopy, and X-ray diffraction. The adsorption capacity of CO$_2$ was determined by thermal gravimetric analyzer. A maximum of 4.45 mmol/g was achieved from the CaO-TiO$_2$ nanotubes (6.64 at% of Ca). The finding was attributed to the higher active surface area for CaO to adsorb more CO$_2$ gas and then formed CaCO$_3$ compound during cyclic carbonation-calcination reaction.

1. Introduction

Recently, solid CO$_2$ adsorbents are used as an alternative and potentially less-energy-intensive separation technology. These CO$_2$ adsorbents can be utilized from ambient temperature up to 973 K by yielding less waste during cycle. In addition, their waste can be disposed of without undue environmental precautions as compared to liquid adsorbent [1]. A variety of solid physical adsorbents have been considered for CO$_2$ capture including microporous and mesoporous materials (carbon-based sorbents, such as activated carbon and carbon molecular sieves, zeolites, and chemically modified mesoporous materials), metal oxides, and hydrotalcite-like compounds [2, 3]. These listed adsorbents usually can be classified into three types based on their sorption/desorption temperatures: (1) low temperature adsorbent: <473 K (carbon, zeolites, MOFs/ZIFs, alkali metal carbonates, and amine-based materials), (2) intermediate temperature adsorbent: 473–673 K (hydrotalcite-like compounds, HTLcs/layered double hydroxides, LDHs), and (3) high-temperature adsorbents: >673 K (calcium based and alkali ceramic). The summary of those adsorbents with their efficiency and operating parameters are shown in Table 1.

According to Table 1, CaO and alkali ceramics are promising candidates for CO$_2$ adsorption. Therefore, CaO-based adsorbent has gained great attention due to its great capability (11.6 mmol/g) as compared to other adsorbents in capturing CO$_2$ gases through cyclic carbonation-calcination reaction. In addition, CaO-based adsorbent has high reactivity with CO$_2$ gases, high capacity, and low material cost [4]. The carbonation temperature for CaO-based adsorbents is between 873 and 973 K and their regeneration temperature is normally above 1223 K. The reversible reaction between CaO and CO$_2$ is

$$CaO\,(s) + CO_2\,(g) \rightleftharpoons CaCO_3\,(s)$$
$$\Delta H^{\circ}_{873.15\,K} = -171.2\ \text{kJ mol}^{-1}\ \ \text{(for carbonation)} \tag{1}$$
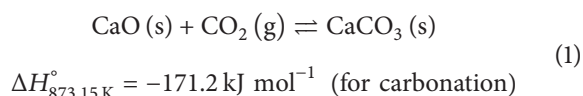
In this manner, nanocrystalline of CaO has been proven to be useful in the noncatalytic removal of CO$_2$ in H$_2$ production [5]. The nanocrystalline of CaO with vacancies/defects, which often related to the presence of basic and acidic sites within their lattice. The structural defects normally are involved in the basic-acidic catalytic reactions. It is a well-known fact that CaO has highly reactive and strong basic sites because of the isolated O^{2-} centers as well as weak

TABLE 1: The different types of solid CO_2 adsorbents based on their sorption/desorption temperatures.

Adsorbent	Total capacity (mmol/g)	Temperature (K)	Pressure (atm)	Reference
Low temperature adsorbents				
Amine based				
Amine-modified mesoporous silica	4.5	348	1	(Liu et al., 2010) [12]
Amine-modified ordered mesoporous silica (OMS)	1.5	—	—	(Zeleňák et al., 2008) [13]
Amine-modified OMSs	0.2–1.4	348	1	(Liu et al., 2010) [12]
Amine tetraethylenepentamine (TEPA)/OMSs	4.6	348	1	(Liu et al., 2010) [12]
MOFs/ZIFs				
MOF-2	3.2	—	41	(Millward and Yaghi, 2005) [14]
Carbon/activated carbon based				
Coal-based activated carbon	0.3	323	0.001	(Deng et al., 2011) [15]
Porous carbon nitride (CN)	2.90	298	—	(Li et al., 2010) [16]
N-doped carbons template from zeolite	6.9	273	1	(Xia et al., 2011) [17]
Activated carbon/N_2	3.75			
Activated carbon/H_2	3.49	293	1	(Zhang et al., 2010) [18]
Activated carbon/NH_3	3.22			
Activated carbon	1.5	303	40	(Drage et al., 2009) [19]
Activated carbon	3.5	275	1	(Wang et al., 2008) [20]
Carbon nanotubes (CNTs)/3-aminopropyltriethoxysilane (APTS)	2.45	323	—	(Su et al., 2011) [21]
Alumina based				
γ-Al_2O_3	0.31	295	—	(Rege and Yang, 2001) [22]
Zeolite based				
Y-type zeolite/tetraethyl-enepentamine (TEPA)	4.27	303–333		(Su et al., 2010) [23]
Natural zeolite	2.05			
Treated zeolite/H_3PO_4	1.95	298	0.1	(Ertan and Çakicioğlu-Özkan, 2005) [24]
Synthetic zeolite-5X	5.49			
Synthetic zeolite-13A	6.82			
LilSX	0.17			
NaLX	0.23	—	1	(Brandani and Ruthven, 2004) [25]
CaX	0.24			
13X (NaX)	2.94	295	—	(Rege and Yang, 2001) [22]
Magnesium based				
MgO/Al_2O_3	1.36	333	1	(Li et al., 2010) [26]
Intermediate temperature adsorbents				
LDH				
Mg-Al-CO_3 LDHs	0.49	473	0.05	(Ram Reddy et al., 2006), [27]
High temperature adsorbents				
Lithium orthosilicates				
Li_4SiO_4	6.14	773	1	(Kato et al., 2002), [28]
Lithium zirconates				
Li_2ZrO_3	4.55	773	1	(Ida and Lin, 2003), [29]
Li_2ZrO_3	4.50	823	1	(Ochoa-Fernández et al., 2005), [30]
Li_2ZrO_3 (nanocrystalline)	6.14	848	1	(Ochoa-Fernández et al., 2006), [31]

TABLE 1: Continued.

Adsorbent	Total capacity (mmol/g)	Temperature (K)	Pressure (atm)	Reference
Calcium oxide based				
CaO	2.3	923	—	(Satrio et al., 2005), [32]
CaO/Al_2O_3	11.6	923	—	(Li et al., 2006), [33]
Cs/CaO	4.9			
Rb/CaO	4.5	723	0.4	(Reddy and Smirniotis, 2004), [34]
K/CaO	3.8			
Na/CaO	3.1			
$CaCO_3$	1.5	573	1	(Kuramoto et al., 2003), [35]
CaO/Al_2O_3	6.02	923	1	(Wu et al., 2007), [36]
Nano CaO/Al_2O_3	6.02	650	—	(Wu et al., 2008), [37]

(a)

(b)

(c)

FIGURE 1: FESEM top view image of nanotubes subjected to wet impregnation of 0.6 M calcium nitrate solution for (a) 24 hours, (b) 48 hours, and (c) 72 hours and subsequent annealing at 673 K in Ar gas for 4 hours.

residual OH groups which appear when mixed with the rare earths [6]. However, these CO_2 adsorbents suffer severely from textural degradation during the sorption/desorption operations. These CO_2 adsorbents can only run several tens of cycles before any obvious degradation and are still far from practical applications [3]. Instantly, the conversion of CaO decreased sharply from 70% in the first cycle to 20%

in the eleventh cycle when tested in fluidized bed [7]. The deactivation primarily results from the formation of thick layer structured from $CaCO_3$ surrounding the CaO, which severely hinders the diffusion of CO_2 gas to react with the inner core. Besides, it has also been reported that the adsorption capacity for CaO-based sorbents decays as a function of the sintering of CaO grain at high temperature

Figure 2: EDX spectra of nanotubes subjected to wet impregnation of 0.6 M calcium nitrate solution for (a) 24 hours, (b) 48 hours, and (c) 72 hours (all EDX spectrums are noneditable format based on our FESEM-EDX system).

and a certain loss in the porosity. When pores smaller than a critical value (e.g., 200 nm) are filled, the reaction gets much slower [8]. Therefore, great efforts have to be made in order to further improve the cyclic stability of CaO-based sorbents.

One of the most promising solutions to improve the cyclic stability of CaO is controlling their architecture into one-dimensional nanomaterials. The main reason might be attributed to the fast reaction (chemical reaction) and the slow reaction (diffusion controlled) could be achieved during CO_2 adsorption. In this case, the diffusion of CO_2 into the particle interior to react with Ca dopants could be prevented and the whole CO_2 adsorption process could then be diffusion-controlled [2, 3]. Theoretically, the small particles size of sorbent (e.g., 30–50 nm) would perform better carbonation-calcination reaction, which allowed carbonation to take place at the rapid reaction-controlled regime. Another promising solution to improve cyclic stability is to incorporate high stability metal oxide (titanium dioxide) into CaO particles. The prevention of CaO oxidation during calcination stage could be expected. Therefore, detail investigation on one-dimensional CaO-TiO$_2$ nanotubes for effective CO_2 adsorption will be discussed.

2. Experimental Procedure

One-dimensional TiO$_2$ nanotube arrays were synthesized using a rapid-anodic oxidation electrochemical anodization technique. A high purity of Ti foil (99.6%, Strem Chemical,

USA) with a thickness of 127 μm was selected as substrate to grow TiO$_2$ nanotubes. This process was conducted in a bath with electrolytes composed of ethylene glycol ($C_2H_6O_2$, >99.5%, Merck, USA), 5 wt% ammonium fluoride (NH$_4$F, 98%, Merck, USA), and 5 wt% hydrogen peroxide (H$_2$O$_2$, 30% H_2O_2 and 70% H_2O, J. T. Baker, USA) for 60 minutes at 60 V. This experimental condition was selected because it favors the formation of well-aligned TiO$_2$ nanotube arrays [9, 10]. After the anodization process, as-anodized samples were cleaned using distilled water and dried under a nitrogen stream. CaO-TiO$_2$ nanotubes were then prepared through wet impregnation technique using calcium nitrate tetrahydrate (Ca(NO$_3$)$_2$·4H$_2$O, Merck, USA) as the precursor. This was an ex situ approach that was used to incorporate Ca^{2+} ions into TiO$_2$ nanotubes. Two different concentrations of calcium nitrate tetrahydrate solution (0.6, 1.2 M) were prepared at different reaction times (24, 48, 72 hours) in a water bath of 80°C. Subsequently, the samples were thermal-annealed at 673 K in an argon atmosphere for 4 h in order to produce crystalline TiO$_2$ nanotubes.

The surface morphologies of the synthesized samples were observed through field emission scanning electron microscopy (FESEM) using a Zeiss SUPRA 35 VP, which is operated at a working distance of 1 mm and 5 kV. The energy dispersive X-ray spectroscopy (EDX) was applied to elemental analysis of the CaO-TiO$_2$ nanotubes sorbents, which is equipped in the FESEM. The structural variations and phase determination for CaO-TiO$_2$ nanotubes sorbents
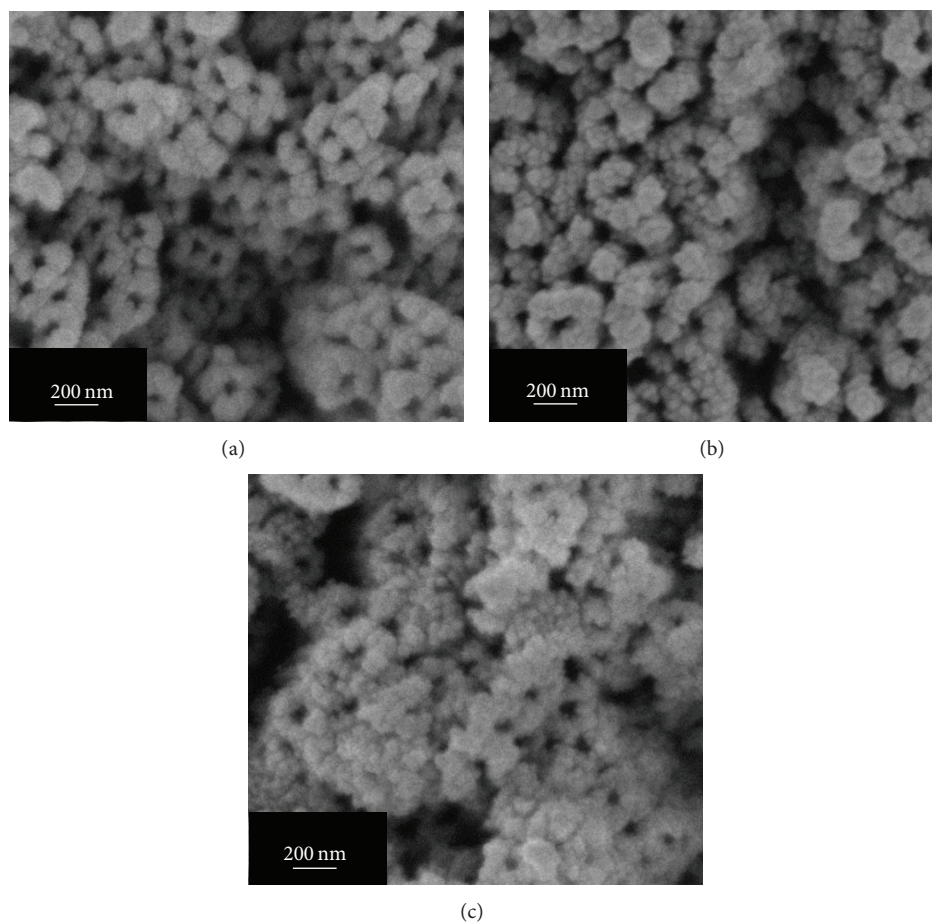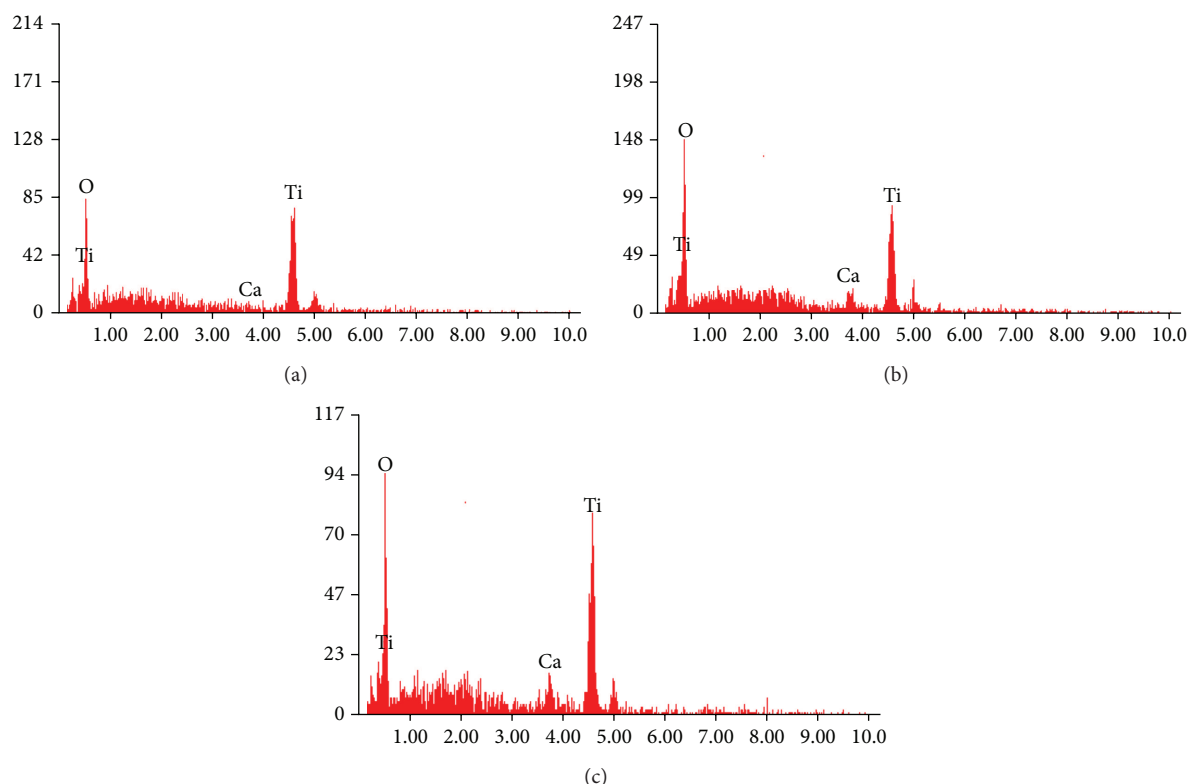
(a)

(b)

(c)

FIGURE 3: FESEM top view image of nanotubes subjected to wet impregnation of 1.2 M calcium nitrate solution for (a) 24 hours, (b) 48 hours, and (c) 72 hours and subsequent annealing at 673 K in Ar gas for 4 hours.

were determined using a Philips PW 1729 X-ray diffraction (XRD), which operated at 45 kV and 40 mV patterns. The thermogravimetric analysis (TGA) was used to investigate the CO_2 adsorption for CaO-TiO$_2$ nanotubes sorbents (STA 6000, Perkin Elmer, USA). The steps included are N_2 gas flow at a rate of 10°C/min from room temperature to 673 K and then holding for 30 min in CO_2 and finally cooling down to 573 K by N_2 gas. In the present study, carbonation-calcination reaction is set to be 673 K because nanotubular structure can be collapsed at high temperature (above 773 K) [11].

3. Results and Discussion

The surface morphologies of CaO-TiO$_2$ nanotubes synthesized in 0.6 M calcium nitrate solution for 24, 48, and 72 hours were subsequently observed via FESEM as presented in Figures 1(a) to 1(c), respectively. As shown in the FESEM images, the opening of the nanotubular structure showed aggregation of CaO species on wall surface of TiO$_2$ nanotubes. The wall thickness of the nanotubes dramatically increased to

75 nm, which resulted in a narrow pore entrance for 24 hours reaction time (Figure 1(a)). Meanwhile, as the reaction time increased to 48 hours, the wall thickness of the nanotubes increased from about 75 nm to 100 nm (Figure 1(b)). With further increase of the reaction time to 72 hours, it was found that the nanotubes were covered with excess CaO species and clogged the pore entrance (Figure 1(c)). A rough, irregular, and corrugated surface was formed. Based on the FESEM images, it could be concluded that the appearance of TiO$_2$ nanotubes was dependent on the reaction time in calcium nitrate solution. A narrow or blocked pore entrance of nanotubes was formed as increasing soaking period in the solution. Next, the average atomic percentage (at%) of the elements within CaO-TiO$_2$ nanotubes was determined using EDX analysis. The numerical EDX analyses of the samples are listed in Table 2. As determined through EDX analysis, the average Ca contents of the nanotubes for 24, 48, and 72 hours were 1.01 at%, 3.67 at%, and 4.59 at%, respectively. The intensity of the Ca peak (3.69 keV) increased with increasing reaction time in calcium nitrate solution as presented in

(a)

(b)

(c)
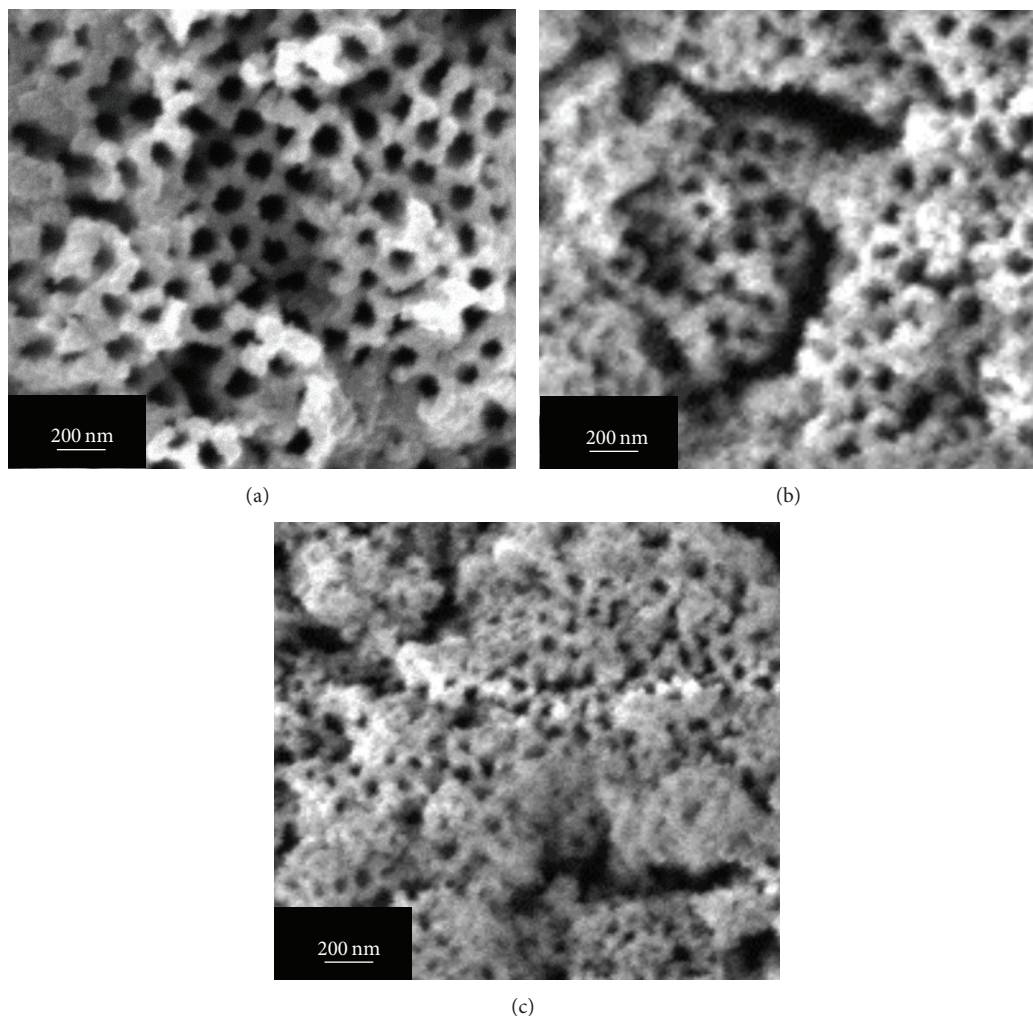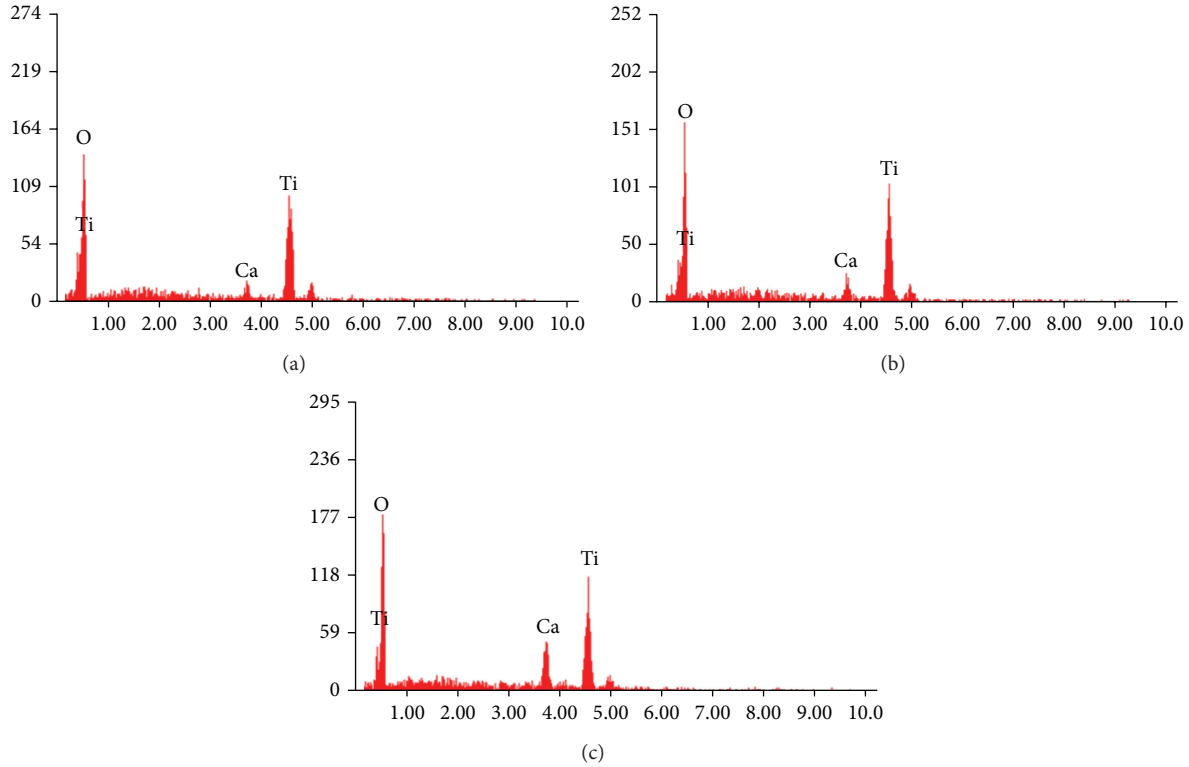
FIGURE 4: EDX spectra of nanotubes subjected to wet impregnation of 1.2 M calcium nitrate solution for (a) 24 hours, (b) 48 hours, and (c) 72 hours (all EDX spectrums are noneditable format based on our FESEM-EDX system).

Figures 2(a) to 2(c). Another set of experiments was conducted to form $CaO\text{-}TiO_2$ nanotubes in 1.2 M calcium nitrate solution for 24, 48, and 72 hours. All morphologies of the samples showed similar appearance of $CaO\text{-}TiO_2$ nanotubes synthesized in 0.6 M calcium nitrate solution. The irregular CaO layer covered all of the TiO_2 nanotubular structure and nanoporous structure arranged in a nonordered manner which could be observed in Figures 3(a) to 3(c). The chemical stoichiometry of the resultant samples was determined via EDX analysis as shown in Figures 4(a) to 4(c). A high Ca content of 9.78 at% was determined from those synthesized in 1.2 M calcium nitrate solution for 72 hours, indicating that the incorporation of the CaO became prominent with increasing the concentration of calcium nitrate solution. Based on the FESEM images and EDX analysis, the small Ca^{2+} ions could be diffused into TiO_2 nanotubes in the presence of lattice defects, especially nearby to the wall of nanotubes. In this case, the diffusion rate of Ca^{2+} ions increased significantly when increasing the reaction time and concentration of precursor. However, the content of small Ca^{2+} ions that diffused into the TiO_2 lattice could reach a saturation condition and start to accumulate on the surface of nanotubes. The number of nucleation sites for Ca^{2+} ions loaded on the wall surface of the nanotubes increased with longer reaction time and higher concentration of precursor, which produced nanotubes with thicker walls. The diffusion of the Ca^{2+} ions formed Ca–O bonding with O–Ti–O bonding; thus, charge neutrality could be achieved.

TABLE 2: EDX result of $CaO\text{-}TiO_2$ with different soaking time in 0.6 M and 1.2 M calcium nitrate solution.

Concentration of calcium nitrate solution (M)	Element (at%)/reaction time (h)	Ti	O	Ca
0.6	24	46.07	52.92	01.01
	48	38.88	57.45	03.67
	72	42.30	53.11	04.59
1.2	24	36.44	60.66	02.90
	48	32.64	60.64	06.64
	72	28.83	61.10	09.78

In the present study, XRD analysis was used to determine the crystallographic structure and the changes in the phase structure of the $CaO\text{-}TiO_2$ nanotubes synthesized in different reaction times and concentrations of precursor are presented in Figures 5 and 6. Numerous studies reported that heat treatment at about 400°C could transform the amorphous structure of TiO_2 into the crystalline anatase phase. The obvious diffraction peaks from the XRD pattern attributed to the anatase phase (JCPDS no. 21-1272) were detected from the XRD patterns (Figure 5(a)). The diffraction peaks are allocated at 25.32°, 37.84°, 38.42°, 48.02°, 53.87°, 55.09°, 62.93°, 70.65°, and 76.23°, which correspond to 101, 004, 112, 200, 105, 211, 204, 220, and 301 crystal planes for the anatase
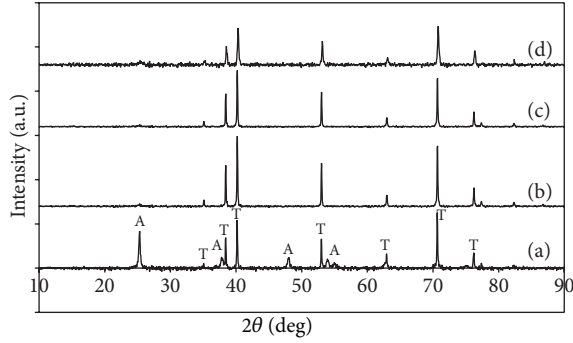
FIGURE 5: XRD pattern of TiO$_2$ nanotubes incorporated with Ca in 0.6 M Ca(NO$_3$)$_2$ solution at different soaking period: (a) pure TiO$_2$, (b) 24 hours, (c) 48 hours, and (d) 72 hours (A = anatase phase; T = titanium phase).
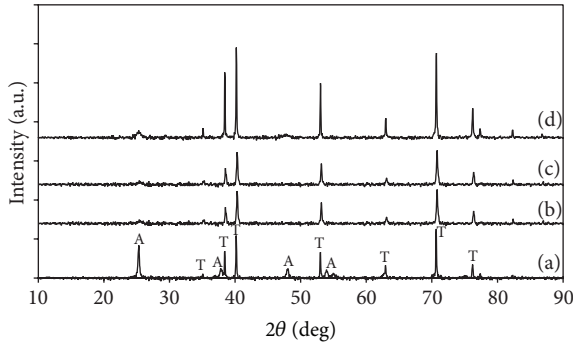
FIGURE 6: XRD pattern of TiO$_2$ nanotubes incorporated with Ca in 1.2 M Ca(NO$_3$)$_2$ solution at different soaking period: (a) pure TiO$_2$, (b) 24 hours, (c) 48 hours, and (d) 72 hours (A = anatase phase; T = titanium phase).

FIGURE 7: TGA curve of soaking in 0.6 M of Ca for different periods of time.
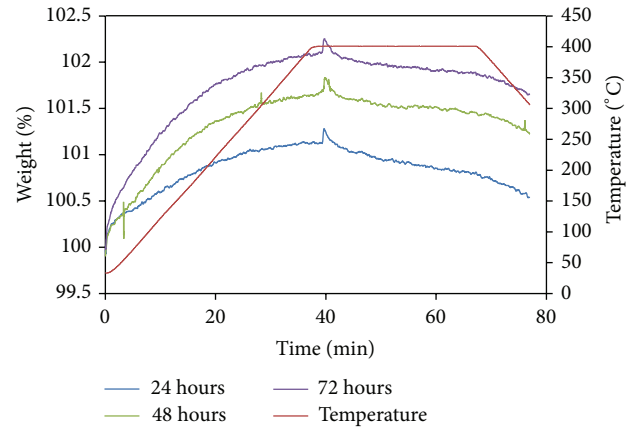
FIGURE 8: TGA curve of soaking in 1.2 M of Ca for different periods of time.

TABLE 3: CO$_2$ adsorption capacity of the CaO-TiO$_2$ samples.

Concentration of calcium nitrate solution (M)	Soaking period (hours)	CO$_2$ adsorption capacity (mmol/g)
	24	3.89
0.6	48	3.32
	72	4.00
	24	3.59
1.2	48	4.45
	72	3.80

phase, respectively. Apparently, the incorporation of Ca^{2+} ions into the lattice of TiO$_2$ hindered the crystallization of TiO$_2$, resulting in the peak intensity of the 101 peak at 25.32° decrease. The decrease in anatase phase is maybe due to the interruption of Ca atom, which diffused into TiO$_2$ nanotubes and inhibited the formation of the anatase. The XRD pattern of the sample soaked in 1.2 M for 72 hours exhibits additional peaks 220 and 400 crystal planes at 54° and 80°, corresponding to CaO phase. This indicates that crystalline CaO are formed once the concentration of Ca in TiO$_2$ reaches a higher level. Next, the resultant anodized CaO-TiO$_2$ nanotubes were used in the characterization of CO$_2$ adsorption using TGA analysis. The processing steps involved in TGA analysis are N$_2$ gas flow at a rate of 10°C/min from room temperature to 673 K and then holding for 30 min in CO$_2$ and finally cooling down to 573 K by N$_2$ gas. The TGA curves for 0.6 M of Ca and 1.2 M of Ca are shown in Figures 7 and 8, respectively, while the CO$_2$ adsorption capacity is summarized in Table 3. Based on the TGA analysis, it could be observed that all CaO-TiO$_2$ samples showed their CO$_2$ adsorption capacity in the range of 3.3 mmol/g to 4.5 mmol/g. A maximum CO$_2$ adsorption capacity of up to 4.45 mmol/g was observed from the CaO-TiO$_2$ nanotubes synthesized in

1.2 M of calcium nitrate solution for 48 hours. Basically, the CO$_2$ adsorption capacity based CaO-TiO$_2$ sorbents used the following reaction: CaO + CO$_2$ $\rightarrow$ CaCO$_3$. In this case, the sorbent weight is increased significantly when CO$_2$ gas is applied to the TGA system, where all the weight added is CO$_2$ adsorbed. This reason clearly explains that CO$_2$ adsorption capacity is increased after carbonation process.

4. Conclusion

The present study demonstrated that one-dimensional CaO-TiO$_2$ nanotubes sorbent was successfully formed using oxidation electrochemical anodization and wet impregnation techniques. All of the resultant CaO-TiO$_2$ nanotubes sorbent exhibited promising CO$_2$ adsorption capacity in the range of 3.3 mmol/g to 4.5 mmol/g. It is shown that high active surface area of CaO-TiO$_2$ nanotubes sorbent showed good stability during extended cyclic carbonation-calcination reaction.

Conflict of Interests

The author declares that there is no conflict of interests regarding the publication of this paper.

Acknowledgments

References

[1] Q. Wang, J. Luo, Z. Zhong, and A. Borgna, "CO$_2$ capture by solid adsorbents and their applications: current status and new trends," *Energy & Environmental Science*, vol. 4, no. 1, pp. 42–55, 2011.

[2] D. M. D'Alessandro, B. Smit, and J. R. Long, "Carbon dioxide capture: prospects for new materials," *Angewandte Chemie International Edition*, vol. 49, no. 35, pp. 6058–6082, 2010.

[3] S. Wang, S. Yan, X. Ma, and J. Gong, "Recent advances in capture of carbon dioxide using alkali-metal-based oxides," *Energy & Environmental Science*, vol. 4, no. 10, pp. 3805–3819, 2011.

[4] N. H. Florin and A. T. Harris, "Reactivity of CaO derived from nano-sized CaCO$_3$ particles through multiple CO$_2$ capture-and-release cycles," *Chemical Engineering Science*, vol. 64, no. 2, pp. 187–191, 2009.

[5] J. García, T. López, M. Álvarez, D. H. Aguilar, and P. Quintana, "Spectroscopic, structural and textural properties of CaO and CaO-SiO$_2$ materials synthesized by sol-gel with different acid catalysts," *Journal of Non-Crystalline Solids*, vol. 354, no. 2-9, pp. 729–732, 2008.

[6] V. R. Choudhary, S. A. R. Mulla, and B. S. Uphade, "Oxidative coupling of methane over alkaline earth oxides deposited on commercial support precoated with rare earth oxides," *Fuel*, vol. 78, no. 4, pp. 427–437, 1999.

[7] D. Alvarez and J. C. Abanades, "Pore-size and shape effects on the recarbonation performance of calcium oxide submitted to repeated calcination/recarbonation cycles," *Energy and Fuels*, vol. 19, no. 1, pp. 270–278, 2005.

[8] J.-R. Li, Y. Ma, M. C. McCarthy et al., "Carbon dioxide capture-related gas adsorption and separation in metal-organic frameworks," *Coordination Chemistry Reviews*, vol. 255, no. 15-16, pp. 1791–1823, 2011.

[9] S. Sreekantan, L. C. Wei, and Z. Lockman, "Extremely fast growth rate of TiO$_2$ nanotube arrays in electrochemical bath containing H$_2$O$_2$," *Journal of the Electrochemical Society*, vol. 158, no. 12, pp. C397–C402, 2011.

[10] C. W. Lai and S. Sreekantan, "Dimensional control of TiO$_2$ nanotube arrays with H$_2$O$_2$ content for high photoelectrochemical water splitting performance," *Micro & Nano Letters*, vol. 7, no. 5, pp. 443–447, 2012.

[11] Y. K. Lai, J. Y. Huang, H. F. Zhang et al., "Nitrogen-doped TiO$_2$ nanotube array films with enhanced photocatalytic activity under various light sources," *Journal of Hazardous Materials*, vol. 184, no. 1–3, pp. 855–863, 2010.

[12] S.-H. Liu, C.-H. Wu, H.-K. Lee, and S.-B. Liu, "Highly stable amine-modified mesoporous silica materials for efficient CO$_2$ capture," *Topics in Catalysis*, vol. 53, no. 3-4, pp. 210–217, 2010.

[13] V. Zeleňák, M. Badaničová, D. Halamová et al., "Amine-modified ordered mesoporous silica: effect of pore size on carbon dioxide capture," *Chemical Engineering Journal*, vol. 144, no. 2, pp. 336–342, 2008.

[14] A. R. Millward and O. M. Yaghi, "Metal-organic frameworks with exceptionally high capacity for storage of carbon dioxide at room temperature," *Journal of the American Chemical Society*, vol. 127, no. 51, pp. 17998–17999, 2005.

[15] H. Deng, H. Yi, X. Tang, P. Ning, and Q. Yu, "Adsorption of CO$_2$ and N$_2$ on coal-based activated carbon," *Advanced Materials Research*, vol. 204-210, pp. 1250–1253, 2011.

[16] Q. Li, J. Yang, D. Feng et al., "Facile synthesis of porous carbon nitride spheres with hierarchical three-dimensional mesostructures for CO$_2$ capture," *Nano Research*, vol. 3, no. 9, pp. 632–642, 2010.

[17] Y. Xia, R. Mokaya, G. S. Walker, and Y. Zhu, "Superior CO$_2$ adsorption capacity on N-doped, high-surface-area, microporous carbons templated from zeolite," *Advanced Energy Materials*, vol. 1, pp. 678–683, 2011.

[18] Z. Zhang, M. Xu, H. Wang, and Z. Li, "Enhancement of CO$_2$ adsorption on high surface area activated carbon modified by N$_2$, H$_2$ and ammonia," *Chemical Engineering Journal*, vol. 160, no. 2, pp. 571–577, 2010.

[19] T. C. Drage, J. M. Blackman, C. Pevida, and C. E. Snape, "Evaluation of activated carbon adsorbents for CO$_2$ capture in gasification," *Energy and Fuels*, vol. 23, no. 5, pp. 2790–2796, 2009.

[20] Y. Wang, Y. Zhou, C. Liu, and L. Zhou, "Comparative studies of CO$_2$ and CH$_2$ sorption on activated carbon in presence of water," *Colloids and Surfaces A: Physicochemical and Engineering Aspects*, vol. 322, no. 1–3, pp. 14–18, 2008.

[21] F. Su, C. Lu, and H.-S. Chen, "Adsorption, desorption, and thermodynamic studies of CO$_2$ with high-amine-loaded multiwalled carbon nanotubes," *Langmuir*, vol. 27, no. 13, pp. 8090–8098, 2011.

[22] S. U. Rege and R. T. Yang, "A novel FTIR method for studying mixed gas adsorption at low concentrations: H$_2$O and CO$_2$ on NaX zeolite and γ-alumina," *Chemical Engineering Science*, vol. 56, no. 12, pp. 3781–3796, 2001.

[23] F. Su, C. Lu, S.-C. Kuo, and W. Zeng, "Adsorption of CO$_2$ on amine-functionalized y-type zeolites," *Energy and Fuels*, vol. 24, no. 2, pp. 1441–1448, 2010.

[24] A. Ertan and F. Çakicioğlu-Özkan, "CO$_2$ and N$_2$ adsorption on the acid (HCl, HNO$_3$, H$_2$SO$_4$ and H$_3$PO$_4$) treated zeolites," *Adsorption*, vol. 11, no. 1, pp. 151–156, 2005.

[25] F. Brandani and D. M. Ruthven, "The effect of water on the adsorption of CO$_2$ and C$_3$H$_8$ on type X zeolites," *Industrial & Engineering Chemistry Research*, vol. 43, no. 26, pp. 8339–8344, 2004.

[26] L. Li, X. Wen, X. Fu et al., "MgO/Al$_2$O$_3$ sorbent for CO$_2$ capture," *Energy and Fuels*, vol. 24, no. 10, pp. 5773–5780, 2010.

[27] M. K. Ram Reddy, Z. P. Xu, G. Q. Lu, and J. C. D. Da Costa, "Layered double hydroxides for CO$_2$ capture: structure evolution and regeneration," *Industrial & Engineering Chemistry Research*, vol. 45, no. 22, pp. 7504–7509, 2006.

[28] M. Kato, S. Yoshikawa, and K. Nakagawa, "Carbon dioxide absorption by lithium orthosilicate in a wide range of temperature and carbon dioxide concentrations," *Journal of Materials Science Letters*, vol. 21, no. 6, pp. 485–487, 2002.

[29] J.-I. Ida and Y. S. Lin, "Mechanism of high-temperature CO$_2$ sorption on lithium zirconate," *Environmental Science and Technology*, vol. 37, no. 9, pp. 1999–2004, 2003.

[30] E. Ochoa-Fernández, H. K. Rusten, H. A. Jakobsen, M. Rønning, A. Holmen, and D. Chen, "Sorption enhanced hydrogen production by steam methane reforming using Li$_2$ZrO$_3$ as sorbent: sorption kinetics and reactor simulation," *Catalysis Today*, vol. 106, no. 1-4, pp. 41–46, 2005.

[31] E. Ochoa-Fernández, M. Rønning, T. Grande, and D. Chen, "Synthesis and CO$_2$ capture properties of nanocrystalline lithium zirconate," *Chemistry of Materials*, vol. 18, no. 25, pp. 6037–6046, 2006.

[32] J. A. Satrio, B. H. Shanks, and T. D. Wheelock, "Development of a novel combined catalyst and sorbent for hydrocarbon reforming," *Industrial & Engineering Chemistry Research*, vol. 44, no. 11, pp. 3901–3911, 2005.

[33] Z.-S. Li, N.-S. Cai, and Y.-Y. Huang, "Effect of preparation temperature on cyclic CO$_2$ capture and multiple carbonation-calcination cycles for a new Ca-based CO$_2$ sorbent," *Industrial & Engineering Chemistry Research*, vol. 45, no. 6, pp. 1911–1917, 2006.

[34] E. P. Reddy and P. G. Smirniotis, "High-temperature sorbents for CO$_2$ made of alkali metals doped on CaO supports," *The Journal of Physical Chemistry B*, vol. 108, no. 23, pp. 7794–7800, 2004.

[35] K. Kuramoto, S. Fujimoto, A. Morita et al., "Repetitive carbonation-calcination reactions of Ca-based sorbents for efficient CO$_2$ sorption at elevated temperatures and pressures," *Industrial & Engineering Chemistry Research*, vol. 42, no. 5, pp. 975–981, 2003.

[36] S. F. Wu, T. H. Beum, J. I. Yang, and J. N. Kim, "Properties of Ca-base CO$_2$ sorbent using Ca(OH)$_2$ as precursor," *Industrial & Engineering Chemistry Research*, vol. 46, no. 24, pp. 7896–7899, 2007.

[37] S. F. Wu, Q. H. Li, J. N. Kim, and K. B. Yi, "Properties of a nano CaO/Al$_2$O$_3$ CO$_2$ sorbent," *Industrial & Engineering Chemistry Research*, vol. 47, no. 1, pp. 180–184, 2008.

Research Article

Solvothermal Synthesis of Zn_2SnO_4 Nanocrystals and Their Photocatalytic Properties

Guang Sun, Saisai Zhang, and Yanwei Li

Cultivating Base for Key Laboratory of Environment-Friendly Inorganic Materials in University of Henan Province,
School of Materials Science and Engineering, Henan Polytechnic University, Jiaozuo, Henan 454000, China

Correspondence should be addressed to Guang Sun; mcsunguang@163.com

Crystalline Zn_2SnO_4 nanoparticles were successfully synthesized via a simple solvothermal route by using $Zn(CH_3COO)_2 \cdot 2H_2O$ and $SnCl_4 \cdot 5H_2O$ as source materials, NaOH as mineralizing agent, and water and ethanol as mixed solvents. The used amount of NaOH was found to have an important influence on the formation of Zn_2SnO_4. When the molar ratio of $OH^- : Zn^{2+} : Sn^{4+}$ was set in the range from $4 : 2 : 1$ to $8 : 2 : 1$, Zn_2SnO_4 nanoparticles with different shape and size were obtained. However, when the molar ratio of $OH^- : Zn^{2+} : Sn^{4+}$ was set as $10 : 2 : 1$, a mixture phase of ZnO and $ZnSn(OH)_6$ instead of Zn_2SnO_4 was obtained. Photodegradation measurements indicated that the Zn_2SnO_4 nanoparticles own better photocatalytic property to depredate methyl orange than the Zn_2SnO_4 nanopolyhedrons. The superior photocatalytic properties of Zn_2SnO_4 nanoparticles may be contributed to their small crystal size and high surface area.

1. Introduction

In recent years, metal oxide semiconductors (MOSs) have been paid more and more attentions due to their diverse function and promising application in various fields. Among these MOSs, besides the widely studied binary oxides such as ZnO [1], SnO_2 [2], TiO_2 [3], and Fe_2O_3 [4], the ternary MOSs, including Zn_2SnO_4 and $ZnSnO_3$, have also been investigated [5, 6]. Stimulated by the prominent morphology (shape and size) dependent physical and chemical properties of nanostructured MOS, many researchers have devoted their efforts to the design and synthesis of MOS nanostructures. Up to now, a variety of nanostructures, such as zero-dimensional nanoparticles, one-dimensional nanowires, nanorods and nanotubes, two-dimensional nanosheets, and three-dimensional hierarchical micro/nanostructures that assembled with low dimensional nanobuilding blocks, have been synthesized and investigated. However, it is still a meaningful and important work to develop facile and feasible techniques for the synthesis of MOS nanomaterials with controlled shape and size in the field of nanoscience and nanotechnology.

Zn_2SnO_4, as an important ternary MOS, is a typical n-type semiconductor with the band-gap of 3.6 eV. Because of its high chemical sensitivity, low visible absorption, and excellent optical electronic properties, Zn_2SnO_4 has many promising applications in gas sensors [5, 7, 8], solar cells [9, 10], photocatalysts [11–15], and negative materials for rechargeable lithium ion batteries [16, 17]. Driven by these potential applications, an increasing research interest has focused on the synthesis of Zn_2SnO_4. In order to achieve Zn_2SnO_4, some traditional high-temperature techniques are usually employed, including high-temperature solid-reaction between solid ZnO and SnO_2 [18, 19], thermal evaporation method by heating metal or metal oxides at high temperature [20–23], and the chemical vapor deposition methods [24]. However, these reported methods are usually of high energy consumption, and thus not suitable for practical production in industry from the view point of environment protection. Recently, hydrothermal synthesis methods have been successfully developed to prepare Zn_2SnO_4 [5, 11, 25–29]. Compared with the high-temperature synthesis methods mentioned above, the hydrothermal synthesis method has the merits of low cost and being friendly to environment and is thus considered as one of the most promising methods that can be applied in practical production. Up to now, various micro/nanostructures of Zn_2SnO_4 have been synthesized

by hydrothermal methods, such as nanowires [23, 24, 29], nanorods [28], irregular particles [17], well-defined polyhedra [22, 30], and hierarchical cube-like microstructures assembled with nanoplates [8]. As an evolution method of hydrothermal synthesis, the solvothermal synthesis is also an important wet chemical synthesis method that can be used to fabricate MOS nanostructures. However, compared with the widely reported hydrothermal synthesis methods for Zn_2SnO_4, few reports are about the synthesis of Zn_2SnO_4 nanostructure via solvothermal method.

In this paper, a simple and efficient solvothermal route was developed to synthesize crystalline Zn_2SnO_4 nanoparticles by using water and ethanol as mixed solvents. The prepared samples were characterized by X-ray diffraction (XRD), transmission electron microscopy (TEM), Fourier infrared spectroscopy (FTIR), and nitrogen-sorption techniques. It was found that the crystallinity, particle size, and shape of Zn_2SnO_4 are strongly dependent on the amount of alkali. The photocatalytic properties of the prepared Zn_2SnO_4 were investigated by photodegradation of methyl orange dye. Results indicated that the irregular Zn_2SnO_4 nanoparticles own better photodegradation capacity than Zn_2SnO_4 nanopolyhedrons perhaps due to their smaller crystal size and higher surface area.

2. Experimental Section

2.1. Synthesis of the Zn_2SnO_4.
All of the chemical reagents were analytical grade and used as received without further purification. In this paper, Zn_2SnO_4 was prepared via a simple solvothermal method by using $Zn(CH_3COO)_2 \cdot 2H_2O$ and $SnCl_4 \cdot 5H_2O$ as starting materials, NaOH as mineralizing agent, and distilled water and absolute ethanol as mixed solvents. In a typical experiment for synthesizing Zn_2SnO_4, the molar ratio of $OH^- : Zn^{2+} : Sn^{4+}$ was set as 6 : 2 : 1. In detail, 0.525 g $SnCl_4 \cdot 5H_2O$ and 0.659 g $Zn(CH_3COO)_2 \cdot 2H_2O$ were dissolved in 20 mL ethanol under magnetic stirring, followed by dropping 20 mL aqueous solution of NaOH (0.45 M). After stirring for 30 min, the obtained white slurry was transferred to a 50 mL Teflon-lined autoclave and then maintained at 160°C for 24 h. When the autoclave was cooled down to room temperature naturally, the white precipitates were collected by centrifugation, washed several times with absolute ethanol and distilled water, and finally dried at 80°C in air for 5 h to get the final products. For comparison, parallel experiments were also carried out by varying the molar ratio of $OH^- : Zn^{2+} : Sn^{4+}$. The samples prepared at the molar ratio of $OH^- : Zn^{2+} : Sn^{4+}$ of 4 : 2 : 1, 6 : 2 : 1, 8 : 2 : 1 and 10 : 2 : 1 were denoted as 4S, 6S, 8S, and 10S, respectively.

2.2. Characterization.
The phase structure and purity of the as-prepared products were characterized by powder X-ray diffraction (XRD) on Bruker D8 diffractometer with Cu Kα radiation (λ = 1.54056 nm). The transmission electron microscopy (TEM) images, selected area electron diffraction (SAED) patterns, and high resolution TEM (HRTEM) images were collected on a JEM-2100 TEM. N_2 adsorption-desorption isotherms were collected at liquid nitrogen temperature using Quantachrome AsiQM0000-3 sorption

analyzer. The specific surface area was calculated using multipoint Brunauer-Emmett-Teller (BET) method. The pore size distribution was determined from the adsorption branch of the isotherms using the DFT method. Before carrying out the measurement, each sample was degassed at 180°C for more than 6 h.

2.3. Measurement of Photocatalytic Activities.
The photocatalytic activities of the as-prepared Zn_2SnO_4 were measured by photodegradation of methyl orange (MO) at room temperature. In a typical experiment, 50 mg as-prepared catalyst was suspended in 100 mL MO aqueous solutions (20 mg/L) in a water-jacketed reactor with the capacity of 200 mL. The UV lamp (TUV 4W/G4 T5, Philips, wavelength 254 nm) was placed above the reactor, and the distance between the lamp and liquid level was 10 cm. Before UV-light irradiation, the suspensions were stirred in dark for 30 min to ensure the establishment of absorption-desorption equilibrium. During the experiment, 3 mL reaction solution was taken out from the reaction system at a certain time interval and then centrifuged to remove the solid catalyst. After that, the obtained MO solution was analyzed on a UV-Vis spectrophotometer (TU-1810) in the wavelength range of 200–700 nm.

3. Results and Discussion

3.1. Characterization of the Prepared Samples

3.1.1. XRD Analysis.
The phase structure and purity of the prepared samples was analyzed by XRD. Figure 1 shows the typical XRD patterns of the samples prepared at different conditions. It can be seen that when the molar ratio of $OH^- : Zn^{2+} : Sn^{4+}$ was in the range of 4 : 2 : 1–8 : 2 : 1, cubic inverse spinal Zn_2SnO_4 phases can be successfully obtained. For example, as shown in Figure 1 (c), all the appeared reflection peaks from low angle area to high angle area can be indexed as perfect cubic inverse spinal Zn_2SnO_4 (JCPDS no. 24-1470). In the XRD patterns of 4S, 6S, and 8S (Figure 1 (a) to (c), resp.), no peaks from other crystal phases are detected, such as ZnO and SnO_2. This result indicates that the samples prepared at present condition are of pure Zn_2SnO_4 phase. Compared with 8S, the refection peaks of 4S and 6S are seriously broaden, which suggested that the used amount of alkali has important influences on the crystallinity of Zn_2SnO_4. In contrast, when the molar ratio of $OH^- : Zn^{2+} : Sn^{4+}$ was increased to 10 : 2 : 1, as shown, the XRD pattern of 10S in Figure 1 (d), two crystalline phases of cubic $ZnSn(OH)_6$ (JCPDS file no. 20-1455), and hexagonal ZnO (JCPDS file no. 36-1451) are observed, which indicates that a mixture of $ZnSn(OH)_6$ and ZnO is obtained instead of the single Zn_2SnO_4 phase. Such result may be attributed to using excessive amount of alkali.

3.1.2. FT-IR Analysis.
The chemical-bond types of the prepared Zn_2SnO_4 were investigated by FT-IR. Figure 2 shows the typical FT-IR spectra of the prepared 4S, 6S, and 8S. From the FT-IR spectra, we can see that the three samples exhibit similar characteristics of infrared adsorption bands, which are quite similar to the spinal Zn_2SnO_4 reported in previous
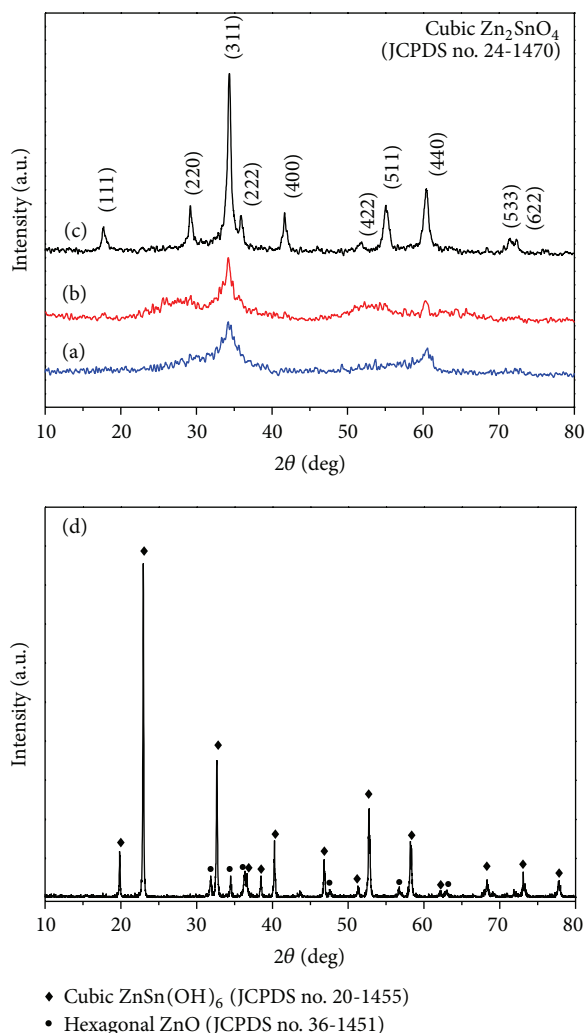
Figure 1: XRD patterns of the prepared samples (a) 4S, (b) 6S, (c) 8S, and (d) 10S.

Figure 2: FT-IR spectra of (a) 4S, (b) 6S, and (c) 8S.

literatures [11, 31]. Therein, the broad absorption peaks at 3426 and 1602 cm^{-1} can be ascribed to the vibration of absorptive water, and the absorption peaks at 546, 1038, and 1410 cm^{-1} are due to the vibration of M–O or M–O–M groups in Zn_2SnO_4. The results given by FT-IR analysis further confirm the formation of Zn_2SnO_4 and thus corroborate the results obtained in XRD analysis.

3.1.3. TEM Analysis. In order to obtain the detailed structural information of the as-prepared Zn_2SnO_4, further measurements by TEM and HR-TEM were performed. Figures 3(a)–3(c) show the typical TEM images of the prepared Zn_2SnO_4 samples. From Figures 3(a) and 3(b), it can be seen that a large scale of nanosized particles with irregular shapes are obtained in 4S and 6S, respectively. The size of these nanoparticles is measured to be about 5–8 nm for 4s and 12–15 nm for 6S. In order to minimize their surface energy, most of these formed nanoparticles aggregated together loosely. As for 8S, besides the irregular nanoparticles, many polyhedron-like particles with the size about 30 nm are also

formed (Figure 3(c)), being obviously different from that observed in 6S and 8S. The different crystallite size and shape in the obtained Zn_2SnO_4 samples indicated that the used amount of alkali may have important influence on the formation of Zn_2SnO_4. Relatively high concentration of NaOH is favorable for achieving Zn_2SnO_4 with larger size. Moreover, it is worthy to be mentioned that in the three samples numerous nanopores with different size were formed in the interspaces among the nanoparticles due to their loosely aggregated characteristics, as shown in Figures 1 (a), (b), and (c). The existence of porous structure in the prepared Zn_2SnO_4 samples can be further convinced by following N_2-sorption analysis. The insets in Figures 3(a)–3(c) show the corresponding selected area electron diffraction (SAED) images of 4S, 6S, and 8S, respectively. The appeared diffraction rings in the SAED patterns demonstrate the polycrystalline nature of the prepared Zn_2SnO_4 samples. Figure 3(d) displays a representative HR-TEM image taken from one of the observed Zn_2SnO_4 nanoparticles in Figure 3(b). The distance between the adjacent lattice fringes is measured to be 0.263 nm, which can be attributed to the (311) crystal plane of cubic inverse spinal Zn_2SnO_4 (JCPDS no. 24-1470). This result is consistent with the XRD analysis, which further proved the preparation of crystalline Zn_2SnO_4 by the present solvothermal method.

3.1.4. N_2-Sorption Analysis. N_2-sorption measurements were further performed on the prepared Zn_2SnO_4 samples to obtain the information of specific surface area and pore structure. Figure 4 depicts the nitrogen adsorption-desorption isotherms and the corresponding pore size distributions of 4S, 6S, and 8S. From Figure 4(a) it can be seen that the adsorption-desorption isotherms of all three samples exhibit a type of IV-like behavior including a type H3 hysteresis loop according to the IUPAC classification. Such result demonstrated the existence of mesoporous structure in the prepared samples, which is in agreement with the TEM

(a)

(b)

(c)

(d)
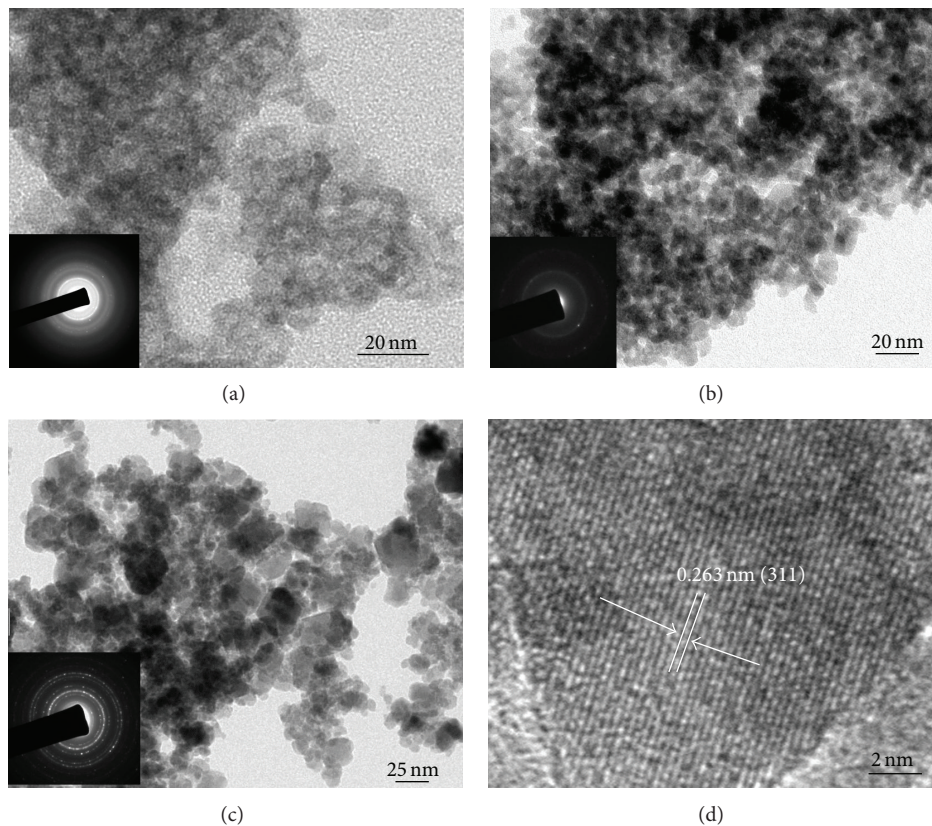
FIGURE 3: TEM images of (a) 4S, (b) 6S, and (c) 8S and (d) the HR-TEM image corresponding to (c). The SAED patterns are shown as an inset in corresponding TEM images.
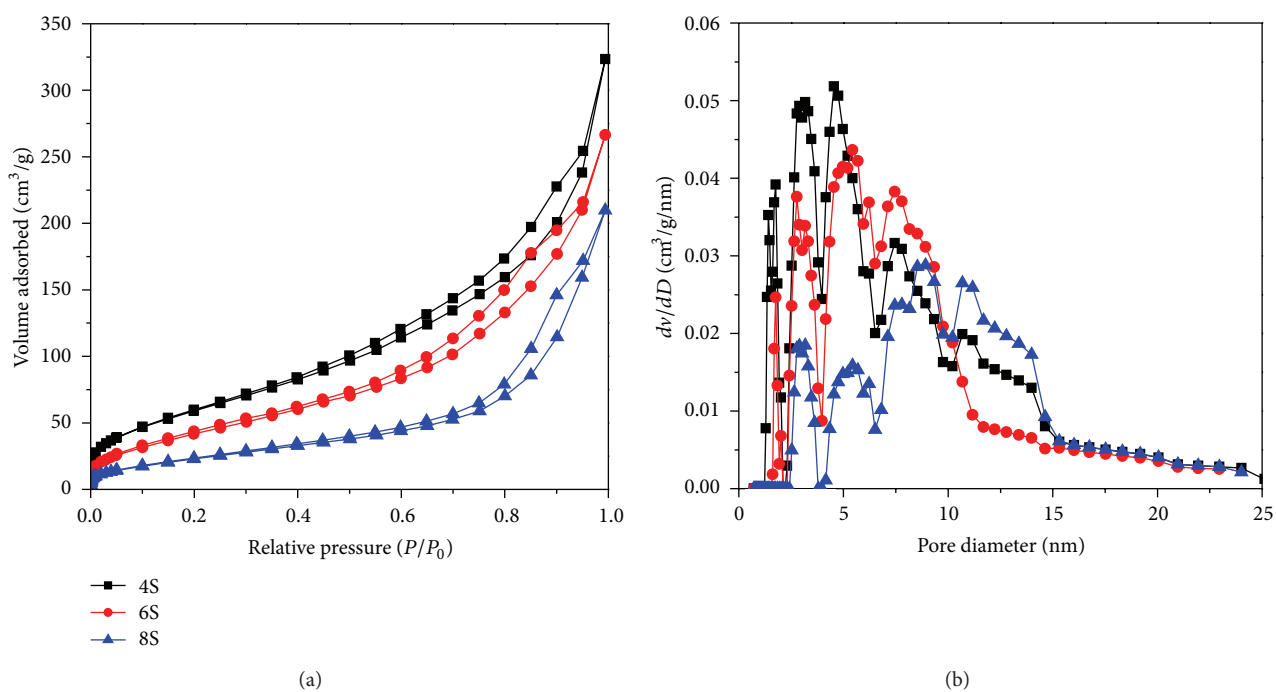
(a)

(b)

FIGURE 4: (a) N_2 adsorption-desorption isotherms and (b) the corresponding pore size distribution curves of 4S, 6S, and 8S.

(a)

(b)

(c)

(d)
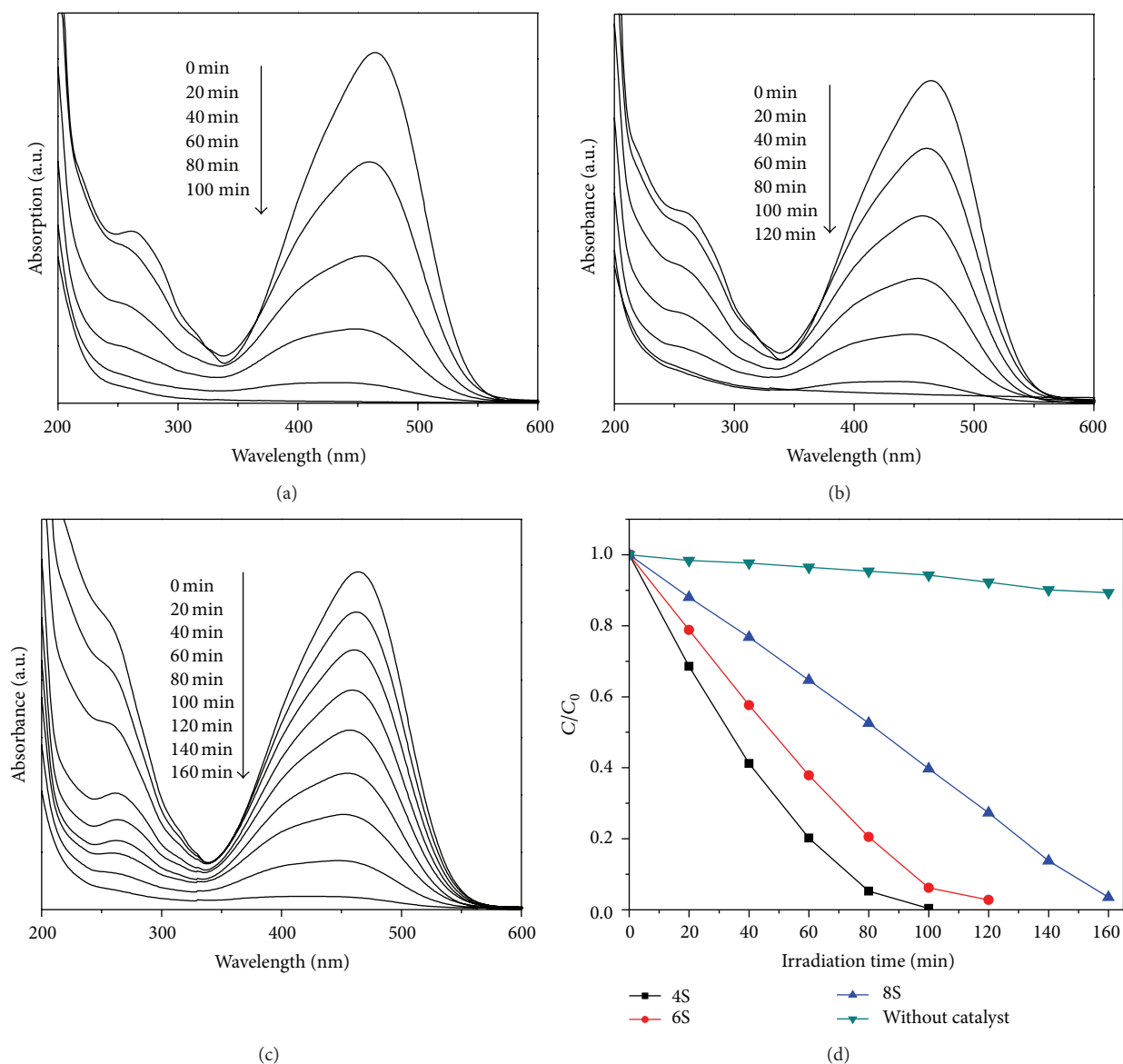
FIGURE 5: Temporal evolution of MO absorption spectra under irradiation of UV-light by using as-prepared Zn_2SnO_4 as photocatalyst: (a) 4S, (b) 6S, and (c) 8S; (d) photodegradation of MO as a function of irradiation time, in which C is the concentration of MO and C_0 is the initial concentration.

observation. The pore size distribution curves (Figure 4(b)) of the prepared Zn_2SnO_4 samples, being estimated based on the DFT method from the adsorption branch of the isotherm, indicated that the pore size distribution range for 4S and 6S was mainly centered at 1.7–10 nm, which was smaller than that of 8S (3–14.5 nm). As for the three Zn_2SnO_4 samples, the relative wide pore-size distribution may be mainly contributed to the random and disordered aggregation characteristics of Zn_2SnO_4 nanocrystals in the products. The calculated BET surface areas for 4S, 6S, and 8S were found to be 226, 166, and $91\,m^2{\cdot}g^{-1}$, respectively. Obviously, the surface area of 4S and 6S was higher than that of 8S. Combined with the TEM analysis, it can be concluded that the surface area of the prepared samples seriously decreased with the increasing of crystal size of Zn_2SnO_4.

3.2. Photocatalytic Properties Studies.

In general, the photocatalytic properties of MOS can be influenced by many factors, such as the crystal size, exposed crystal plane, morphology, and band structure. In terms of our experiment, the crystal size and the surface area of Zn_2SnO_4 can be controlled by adjusting the used amount of alkali in the reaction system. Therefore, it was expected that the Zn_2SnO_4 samples prepared under different conditions can bring different photocatalytic activities. So, in order to evaluate the photocatalytic activity of the prepared Zn_2SnO_4, the experiments of photodegradation of methyl orange (MO) were performed under UV-light irradiation. Figures 5(a)–5(c) show the time-dependent absorption spectra of MO solution containing different Zn_2SnO_4 catalysts during the UV-light irradiation. It can be seen that the characteristic absorption

peak of MO centered around 465 nm decreased rapidly in intensity with the irradiation time and almost disappeared after undergoing a certain time of irradiation. The decreased speed of MO concentration in Figures 5(a) and 5(b) was found to be faster than that in Figure 5(c), indicating that the photodegradation capacity of 4S and 6S is stronger than that of 8S. The photodegradation plots of MO under UV-light by using different Zn_2SnO_4 samples as catalysts are shown in Figure 5(d), in which A_0/A was substituted by C_0/C, where C_0 and C are the initial and actual concentration of MO, respectively, because the normalized concentration of the solution equals the normalized maximum absorbance. For comparison, the degradation plot of MO without any catalyst is also displayed in Figure 5(d). It can be seen that when there was no catalyst in the reaction system, the decrease of C_0/C is very slow and almost negligible. After irradiating for 100 min, only about 0.5% of total MO molecules were depredated. However, once the catalyst of Zn_2SnO_4 was added, a rapid decrease of C/C_0 was observed, indicating that the prepared Zn_2SnO_4 samples are effective to depredate MO molecules. Under the same irradiation period, the values of C_0/C for 4S and 6S were larger than thos for 8S, indicating their better photocatalytic activity than 8S. After 100 min irradiation, the C_0/C values for 4S, 6S, and 8S are about 0, 0.06, and 0.6, corresponding to the degradation about 100%, 96%, and 40% of total MO molecules, respectively. The superior photocatalytic activity of 4S and 6S can be explained by their smaller crystal size and larger surface area. It is generally accepted that the catalytic process is mainly related to the adsorption and desorption of organic dye molecules on the surface of the catalyst. The higher specific surface area of 4S ($226 \, m^2 \cdot g^{-1}$) and 6S ($166 \, m^2 \cdot g^{-1}$) can provide more unsaturated surface coordination sites exposed to the solution and more opportunities for dye molecules to absorb on the surface of catalysts, resulting in the production of more active reaction sites. Moreover, the mesoporous structures in the catalysts enable storage of more dye molecules, which can also promote the photocatalytic properties. Furthermore, the bandgap of the catalyst material may be another important factor that can influence the photocatalytic properties. In our experiment, the crystallite size of Zn_2SnO_4 in 4S and 6S was observed to be less than 20 nm. Therefore, the bandgap of Zn_2SnO_4 catalyst may be broadened by the quantum size effect. The broadened bandgap can not only bring higher redox potentials but also promote electrons transferring form the conductive band of Zn_2SnO_4 with high electric potential to those with low electric potential. Thus, the recombination of the photogenerated electron-hole pair can be hampered, which in turn results in the enhancement of the charge-transfer rates in the catalyst.

4. Conclusions

In summary, a simple solvothermal route was successfully developed for controlled synthesis of Zn_2SnO_4 nanocrystals with different shape and size. Irregular Zn_2SnO_4 nanoparticles about 5–8 nm (4S) and 12–15 nm in size (6S) and polyhedron-like Zn_2SnO_4 nanoparticles about 30 nm in size (8S) can be easily obtained by adjusting the used amount of alkali. The BET surface areas of the prepared samples of 4S, 6S, and 8S were measured to be 226, 166, and $91 \, m^2 \cdot g^{-1}$, respectively. Due to the higher specific surface area and quantum size effects, the 4S and 6S exhibited higher photocatalytic activity to degrade MO than 8S.

Conflict of Interests

The authors have no conflict of interests in relation to the instrumental companies directly or indirectly.

Acknowledgments

References

[1] D.-F. Zhang, L.-D. Sun, J.-L. Yin, C.-H. Yan, and R.-M. Wang, "Attachment-driven morphology evolvement of rectangular ZnO nanowires," *Journal of Physical Chemistry B*, vol. 109, no. 18, pp. 8786–8790, 2005.

[2] C. Wang, G. H. Du, K. Ståhl, H. X. Huang, Y. J. Zhong, and J. Z. Jiang, "Ultrathin SnO_2 nanosheets: oriented attachment mechanism, nonstoichiometric defects, and enhanced lithium-ion battery performances," *Journal of Physical Chemistry C*, vol. 116, no. 6, pp. 4000–4011, 2012.

[3] X. C. Ma, Y. Dai, M. Guo, and B. B. Huang, "Relative photooxidation and photoreduction activities of the 100, 101, and 001 surfaces of Anatase TiO_2," *Langmuir*, vol. 29, no. 44, pp. 13647–13654, 2013.

[4] X. D. Xu, R. G. Cao, S. Y. Jeong, and J. Cho, "Spindle-like mesoporous α-Fe_2O_3 anode material prepared from MOF template for high-rate Lithium batteries," *Nano Letters*, vol. 12, no. 9, pp. 4988–4991, 2012.

[5] Y.-Q. Jiang, X.-X. Chen, R. Sun, Z. Xiong, and L.-S. Zheng, "Hydrothermal syntheses and gas sensing properties of cubic and quasi-cubic Zn_2SnO_4," *Materials Chemistry and Physics*, vol. 129, no. 1-2, pp. 53–61, 2011.

[6] J. R. Huang, X. J. Xu, C. P. Gu et al., "Size-controlled synthesis of porous $ZnSnO_3$ cubes and their gas-sensing and photocatalysis properties," *Sensors and Actuators B*, vol. 171-172, pp. 572–579, 2012.

[7] Z. Chen, M. H. Cao, and C. W. Hu, "Novel Zn_2SnO_4 hierarchical nanostructures and their gas sensing properties toward ethanol," *Journal of Physical Chemistry C*, vol. 115, no. 13, pp. 5522–5529, 2011.

[8] Y. Q. Jiang, C. X. He, R. Sun, Z. X. Xie, and L. S. Zheng, "Synthesis of Zn_2SnO_4 nanoplate-built hierarchical cube-like structures with enhanced gas-sensing properties," *Materials Chemistry and Physics*, vol. 136, pp. 689–704, 2012.

[9] B. Tan, E. Toman, Y. G. Li, and Y. Y. Wu, "Zinc stannate (Zn_2SnO_4) dye-sensitized solar cells," *Journal of the American Chemical Society*, vol. 129, no. 14, pp. 4162–4163, 2007.

[10] J. J. Chen, L. Y. Lu, and W. Y. Wang, "Zn_2SnO_4 nanowires as photoanode dye-sensitized solar cells and improvement on open-circuit voltage," *The Journal of Physical Chemistry C*, vol. 116, no. 20, pp. 10841–10847, 2012.

[11] J. Zeng, M. D. Xin, K. W. Li, H. Wang, H. Yan, and W. J. Zhang, "Transformation process and photocatalytic activities of hydrothermally synthesized Zn_2SnO_4 nanocrystals," *Journal of Physical Chemistry C*, vol. 112, no. 11, pp. 4159–4167, 2008.

[12] M. A. Alpuche-Aviles and Y. Wu, "Photoelectrochemical study of the band structure of Zn_2SnO_4 prepared by the hydrothermal method," *Journal of the American Chemical Society*, vol. 131, no. 9, pp. 3216–3224, 2009.

[13] Z. Ai, S. Lee, Y. Huang, W. Ho, and L. Zhang, "Photocatalytic removal of NO and HCHO over nanocrystalline Zn_2SnO_4 microcubes for indoor air purification," *Journal of Hazardous Materials*, vol. 179, no. 1–3, pp. 141–150, 2010.

[14] Z. Tian, C. Liang, J. Liu, H. Zhang, and L. Zhang, "Zinc stannate nanocubes and nanourchins with high photocatalytic activity formethyl orange and 2, 5-DCP degradation," *Journal of Materials Chemistry*, vol. 22, no. 33, pp. 17210–17214, 2012.

[15] T. K. Jia, J. W. Zhao, F. Fu et al., "Synthesis, characterization, and photocatalytic activity of Zn-Doped SnO_2/Zn_2SnO_4 coupled nanocomposites," *International Journal of Photoenergy*, vol. 2012, Article ID 198497, 6 pages, 2012.

[16] N. Feng, S. L. Peng, X. L. Sun et al., "Synthesis of monodisperse single crystal Zn_2SnO_4 cubes with high lithium storage capacity," *Materials Letters*, vol. 76, pp. 66–68, 2012.

[17] A. Rong, X. P. Gao, G. R. Li et al., "Hydrothermal synthesis of Zn_2SnO_4 as anode materials for Li-ion battery," *Journal of Physical Chemistry B*, vol. 110, no. 30, pp. 14754–14760, 2006.

[18] T. Hashemi, H. M. Al-Allak, J. Illingsworth, A. W. Brinkman, and J. Woods, "Sintering behaviour of zinc stannate," *Journal of Materials Science Letters*, vol. 9, no. 7, pp. 776–778, 1990.

[19] G. B. Palmer, K. R. Poeppelmeier, and T. O. Mason, "$Zn_{2-x}Sn_{1-x}In_{2x}O_{4-\delta}$: an indium-substituted spinel with transparent conducting properties," *Journal of Solid State Chemistry*, vol. 134, no. 1, pp. 192–197, 1997.

[20] J. S. Jie, G. Z. Wang, X. H. Han et al., "Growth of ternary oxide nanowires by gold-catalyzed vapor-phase evaporation," *Journal of Physical Chemistry B*, vol. 108, no. 24, pp. 8249–8253, 2004.

[21] H. Y. Chen, J. X. Wang, H. C. Yu, H. X. Yang, S. S. Xie, and J. Q. Li, "Transmission electron microscopy study of pseudoperiodically twinned Zn_2SnO_4 nanowires," *Journal of Physical Chemistry B*, vol. 109, no. 7, pp. 2573–2577, 2005.

[22] J.-W. Zhao, L.-R. Qin, and L.-D. Zhang, "Single-crystalline Zn_2SnO_4 hexangular microprisms: fabrication, characterization and optical properties," *Solid State Communications*, vol. 141, no. 12, pp. 663–666, 2007.

[23] Y. X. Du and P. Ding, "Thermal evaporation route to zinc stannate nanowires and the cathodoluminescence of the individual nanowires," *Journal of Alloys and Compounds*, vol. 502, no. 1, pp. L14–L16, 2010.

[24] Q. R. Hu, P. Jiang, H. Xu et al., "Synthesis and photoluminescence of Zn_2SnO_4 nanowires," *Journal of Alloys and Compounds*, vol. 484, no. 1-2, pp. 25–27, 2009.

[25] X. Lou, X. Jia, J. Xu, S. Liu, and Q. Gao, "Hydrothermal synthesis, characterization and photocatalytic properties of Zn_2SnO_4 nanocrystal," *Materials Science and Engineering A*, vol. 432, no. 1-2, pp. 221–225, 2006.

[26] S. Baruah and J. Dutta, "Zinc stannate nanostructures: hydrothermal synthesis," *Science and Technology of Advanced Materials*, vol. 12, no. 1, Article ID 013004, 2011.

[27] J. Fang, A. H. Huang, P. X. Zhu et al., "Hydrothermal preparation and characterization of Zn_2SnO_4 particles," *Materials Research Bulletin*, vol. 36, no. 7-8, pp. 1391–1397, 2001.

[28] H. L. Zhu, D. R. Yang, G. X. Yu, H. Zhang, D. L. Jin, and K. H. Yao, "Hydrothermal synthesis of Zn_2SnO_4 nanorods in the diameter regime of sub-5 nm and their properties," *Journal of Physical Chemistry B*, vol. 110, no. 15, pp. 7631–7634, 2006.

[29] L. S. Wang, X. Z. Zhang, X. Liao, and W. G. Yang, "A simple method to synthesize single-crystalline Zn_2SnO_4 (ZTO) nanowires and their photoluminescence properties," *Nanotechnology*, vol. 16, no. 12, pp. 2928–2931, 2005.

[30] M. Miyauchi, Z. Liu, Z.-G. Zhao, S. Anandan, and K. Hara, "Single crystalline zinc stannate nanoparticles for efficient photoelectrochemical devices," *Chemical Communications*, vol. 46, no. 9, pp. 1529–1531, 2010.

[31] C. G. Anchieta, D. Sallet, E. L. Foletto, S. S. Da Silva, O. Chiavone-Filho, and C. A. O. do Nascimento, "Synthesis of ternary zinc spinel oxides and their application in the photoderadation of organic pollutant," *Ceramicas International*, vol. 40, no. 3, pp. 4173–4178, 2014.

Research Article

Fabrication and Characteristics of Macroporous TiO$_2$ Photocatalyst

Guiyun Yi,[1] Baolin Xing,[1] Jianbo Jia,[1] Liwei Zhao,[2] Yuanfeng Wu,[1] Huihui Zeng,[1] and Lunjian Chen[1]

[1] *School of Materials Science and Engineering, Henan Polytechnic University, Jiaozuo, Henan 454000, China*
[2] *Petroleum Engineering Research Institute of Dagang Oilfield, Tianjin 300270, China*

Correspondence should be addressed to Guiyun Yi; ygyun@hpu.edu.cn and Lunjian Chen; lunjianc@hpu.edu.cn

Macroporous TiO$_2$ photocatalyst was synthesized by a facile nanocasting method using polystyrene (PS) spherical particles as the hard template. The synthesized photocatalyst was characterized by transmission electron microscope (TEM), scanning electron microscopy (SEM), thermogravimetry-differential thermogravimetry (TG-DTG), X-ray diffraction (XRD), and N$_2$-sorption. TEM, SEM, and XRD characterizations confirmed that the macroporous TiO$_2$ photocatalyst is composed of anatase phase. The high specific surface area of 87.85 m^2/g can be achieved according to the N$_2$-sorption analysis. Rhodamine B (RhB) was chosen as probe molecule to evaluate the photocatalytic activity of the TiO$_2$ catalysts. Compared with the TiO$_2$ materials synthesized in the absence of PS spherical template, the macroporous TiO$_2$ photocatalyst sintered at 500°C exhibits much higher activity on the degradation of RhB under the UV irradiation, which can be assigned to the well-structured macroporosity. The macroporous TiO$_2$ material presents great potential in the fields of environmental remediation and energy conversion and storage.

1. Introduction

For the environment protection purpose, the disposal of various toxic dyes from the textile industry has attracted extensive attention. Rhodamine B (RhB) is widely used as a colorant in textiles and food stuffs and is also a well-known water tracer fluorescent [1]. It is harmful to human beings and animals and causes irritation of the skin, eyes, and respiratory tract.

Owing to high photocatalytic efficiency, good oxidation capability, stable chemical reaction, low cost, and nontoxicity, titanium dioxide (TiO$_2$) has been applied widely in wastewater treatment [2–4], environment purification [5, 6], solar energy transfer [7, 8], chemical sensing [9, 10]. Recently, it was found that incorporation of well-defined porosity of TiO$_2$ materials could greatly enhance the photoactivity in the area of environmental remediation and energy conversion [11–13]. For a variety of practical applications, the fabrication of desired structure with network is important as well as control in grain size, crystallinity, and composition [14–16].

At present, porous TiO$_2$, combining the outstanding properties of TiO$_2$ with their porous structure, has gained great research interests, and various synthetic techniques had been developed. For example, Liu et al. prepared anatase TiO$_2$ porous thin films by sol-gel method with CTAB surfactant as a pore-forming agent, and many factors were studied [17]. Bala et al. fabricated hollow spheres of anatase TiO$_2$ by spherical CaCO$_3$ nanoparticles as a template and investigated the photocatalytic activity [18]. Zheng et al. synthesized rutile and anatase TiO$_2$ mesoporous single crystals with diverse mophologies by silica-templated hydrothermal method [19]. Dong et al. prepared highly ordered transparent TiO$_2$ macropore arrays via a glass-clamping method and investigated the potential application in degradation of organic dyes [20]. However, the general synthesis usually involved complicated multistep to obtain porous skeleton. Firstly, it is required to assemble spheres into colloidal crystals as templates, and then the precursor is filled into interstices among the crystals for several times [21–23]. Moreover, for an efficient photodegradation catalyst, the macroporous structure is essential due

to the run-through-macropore network which maximizes the uptake and the diffusion of the organic molecules [24–26]. Additionally, the porous structures are propitious to enhance the light scattering and improve the utilization rate of irradiation light [27–29].

Herein, a simple method without assembly and filling steps was introduced in this work for the preparation of macroporous TiO_2 through a sol-gel process using polystyrene spheres as sacrificial templates. Compared with the TiO_2 materials synthesized in the absence of PS spherical template [30, 31], the macroporous TiO_2 photocatalyst sintered at 500°C exhibits much higher activity on the degradation of RhB under the UV irradiation. The macroporous TiO_2 material present great potential in the fields of environmental remediation and energy conversion and storage.

2. Experiment

2.1. Materials.
Tetrabutyl titanate $(Ti(OC_4H_9)_4)$, sodium styrene sulfonate, sodium hydrogen carbonate, potassium persulfate, ethanol, Rhodamine B (RB), acetic acid, and nitric acid were all analytical grade and used without further purification. Styrene was washed by 5% NaOH solution several times to remove polymerization inhibitor. All of the reagents were purchased from Shanghai Chemical Reagent Ltd. Co.

2.2. Preparation of PS Microspheres.
PS spheres were obtained by emulsion polymerization of styrene according to previous reports [32–34]. At first, 150 g deionized water was poured into a 300 mL jacket reactor, which was kept at 85°C until the end of the reaction. Then, 0.08 g sodium styrene sulfonate as the emulsifier and 0.0633 g sodium hydrogen carbonate as the buffer were dissolved in the deionized water. Under constant stirring, 18.30 mL styrene monomer was added to this solution, accompanied with nitrogen protection. After 1 h, 0.0833 g potassium persulfate as an initiator was introduced into the solution. After 18 h polymerization, the monodispersed PS spheres with the average diameter of 278 nm were obtained, and the standard deviation of spheres was less than 2.76%.

2.3. Preparation of TiO_2 Sol.
With the $Ti(OC_4H_9)_4$ as precursor, ethanol as solvent and glacial acetic acid as inhibitor, TiO_2 sol was synthesized by sol-gel method according to references elsewhere [35, 36]. The procedure can be divided into three steps. At first, solution A was prepared by mixing 3 mL deionized water and 16 mL absolute ethyl alcohol. And then solution B was obtained by adding 10 mL $Ti(OC_4H_9)_4$ and 2 mL glacial acetic acid into 32 mL ethanol slowly with the rapid stirring. At last, solution A was dripped slowly into solution B under rapid stirring. The homogeneous and transparent solution of TiO_2 sol was thus obtained.

2.4. Preparation of Macroporous TiO_2.
In a typical synthesis of macroporous TiO_2, 11 mL PS spheres suspension with the concentration of 5.88 wt% was added slowly into 10 mL as-prepared TiO_2 sol. The intimate mixture was obtained by

stirring and ultrasonication. Then, the mixture was placed in an oven at 70°C for 12 h and then TiO_2/PS sphere composites were obtained. To prepare macroporous TiO_2, the as-obtained composites were sintered in muffle furnace at 500°C for 2 h in air. The ultima product was denoted as m-TiO_2. For contrast, the synthesis of TiO_2 nanoparticles was the similar to the preparation of macroporous TiO_2 without adding the PS spheres, which was labeled as r-TiO_2.

2.5. Characterization.
Field emission scanning electron microscopy (FE-SEM) was carried out on FEI Sirion-200 and transmission electron microscopy TEM was taken on JEOL JEM-2100. The XRD patterns of the synthesized samples were obtained by a Bruker-AXS D8 Advance diffractometer with CuKα radiation ($\lambda = 0.15418$ nm). To determine the proper sintering temperature and analyze the weight content of PS spheres in the TiO_2/PS composites, both the as-prepared PS spheres and TiO_2/PS composites were investigated by thermogravimetry and derivative thermogravimetry (TG-DTG), which was operated at a program-controlled temperature elevation rate of 10°C/min in the air. N_2 adsorption-desorption isotherms were measured on a Quantachrome NOVA 2000e sorption analyzer at liquid nitrogen temperature (77 K). The samples were degassed at 120°C overnight prior to the measurement. The surface areas were calculated by the multipoint Brunauer-Emmett-Teller (BET) method.

2.6. Photocatalytic Experiment.
The photocatalytic activity tests of the synthesized TiO_2 were performed by the degradation of Rhodamine B (RhB) under UV light irradiation under ambient conditions. The experiment was performed in a water-jacket reactor operated at 20°C. The light source was a 450 W high-pressure mercury lamp (Foshan Electrical and Lighting Co. Ltd.) with a strong peak centered at 362 nm. The distance between the sample and the lamp was about 10 cm. In a typical process, 0.1 g of the obtained product was placed into 100 mL of RhB aqueous solution (2×10^{-5} mol/L) under magnetic stirring. 5 mL of the mixture was collected at a given time interval of 15 min and was then centrifuged to discard any sediment. Then the concentration of RhB was determined on a TU-1810 UV-vis spectrophotometer at $\lambda_{max} = 553$ nm [37, 38]. The decomposition efficiency of RhB was calculated by the following formula:

$$\text{Decomposition efficiency} = \frac{A_0 - A_t}{A_0} \times 100\%, \quad (1)$$

where A_0 and A_t represent the absorbance of the RhB solution before irradiation and the absorbance at time t, respectively.

3. Results and Discussion

3.1. Material Characterization.
TG-DTG curves of both PS spheres and the TiO_2/PS composites are shown in Figure 1. For PS spheres, three weight loss stages, below 300, 300–400, and 400–500°C, can be observed. The PS spheres undergo endothermic desorption of physically adsorbed water and
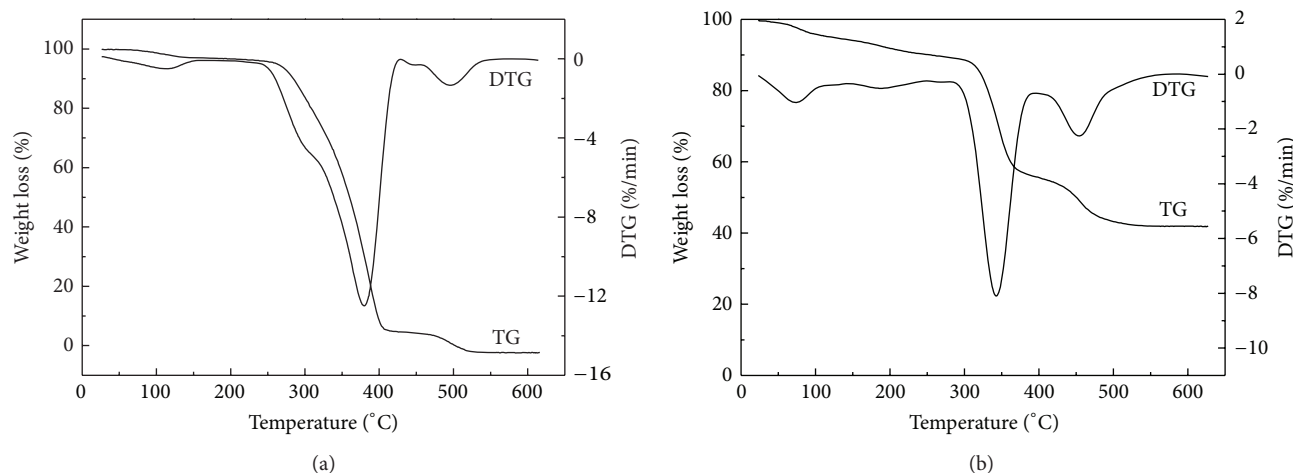
(a)

(b)

FIGURE 1: TG-DTG curves of the PS spheres (a) and the TiO$_2$/PS composite.

residual solvent at low temperature below 300°C. The major weight loss of about 90% between 300 and 400°C can be assigned to the thermal decomposition of the polystyrene, which was decomposed from long chain to shorter chain and then depolymerized into volatile monomers with low molecular weight. While, the third stage in the range of 400–500°C can be attributed to the combustion of the residual coke. With respect to the TiO$_2$/PS nanocomposite, it is found that PS spheres can be completely removed at 500°C (Figure 1(b)). Thus, 500°C was selected as the calcination temperature to prepare the macroporous TiO$_2$ photocatalyst. The weight content of TiO$_2$ in the TiO$_2$/PS nanocomposite is calculated to be 43.2%.

XRD are employed to characterize the crystallite structure of the synthesized TiO$_2$ catalysts. It can be seen from Figure 2(a) that the diffraction peaks of TiO$_2$ after being calcinated at 450°C can be indexed to anatase phase TiO$_2$ (JCPDS NO. 21-1272) and rutile phase TiO$_2$ (JCPDS NO. 21-1276), indicating that the sample calcined at 450°C is composed of bicrystalline phase. When the calcination temperature was increased to 500°C, all diffraction peaks can be indexed to pure anatase phase (JCPDS NO. 21-1272), and no characteristic peaks of other impurities can be detected. Thus, 500°C is a proper sintering temperature to prepare anatase phase macroporous TiO$_2$, which is in accordance with the TG-DTG analysis (Figure 1). The sharp diffraction peaks in Figure 2(b) illustrate the well crystallization of m-TiO$_2$ after the heat treatment. The crystallite size (D) was calculated to be about 10 nm according to the Scherrer formula $D = K\lambda/\beta\cos\theta$ [39], where K is a constant (shape factor, about 0.9), λ is the X-ray wavelength (0.15418 nm), β is the full-width at half-maximum, and θ is the diffraction angle. The values of β and θ were taken from TiO$_2$ (101) diffraction line.

TEM images of the PS spheres and m-TiO$_2$ are given in Figure 3. Figure 3(a) shows the TEM image of the PS spheres. The size of the PS spheres is about 278 nm, and the standard deviation of monodispersed spheres is less than 2.76%. This

○ Anatase
● Rutile
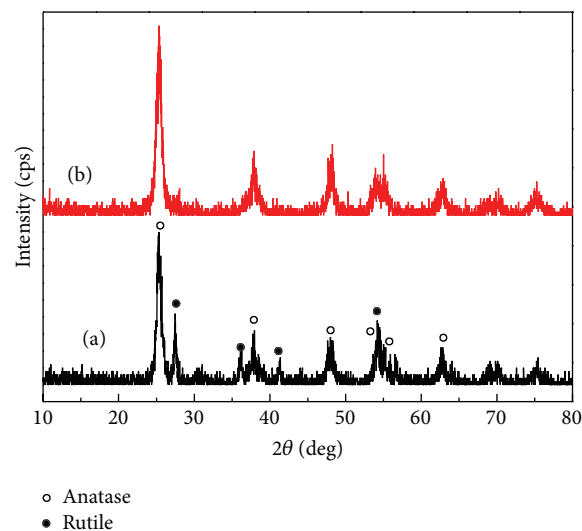
FIGURE 2: XRD patterns of TiO$_2$ prepared through calcining the TiO$_2$/PS composite at different temperatures: (a) 450°C and (b) 500°C.

indicates that the PS spheres are suitable to be employed as macroporous templates. As shown in Figure 3(b), the PS spheres are wrapped by TiO$_2$ nanoparticles before being sintered. Figure 3(c) shows the low-magnification TEM image of macroporous TiO$_2$ sintered at 500°C in air, from which macropores can be clearly seen, suggesting that PS spheres have been completely removed after calcination at 500°C in air. And the SEM image (Figure 3(e)) also demonstrates well-defined macroporous structure. The size of the hollow spheres is about 240 nm, which is smaller than the size of original PS spheres template, suggesting the significant shrinkage after the PS removal via calcination. Additionally, Figure 3(c) also illustrates that run-through-macropore network structure was formed. And the SEM images in Figure 3(e) further confirm that the macropores left by the templates are interconnective with neighboring hollow

(a)

(b)

(c)

(d)

(e)
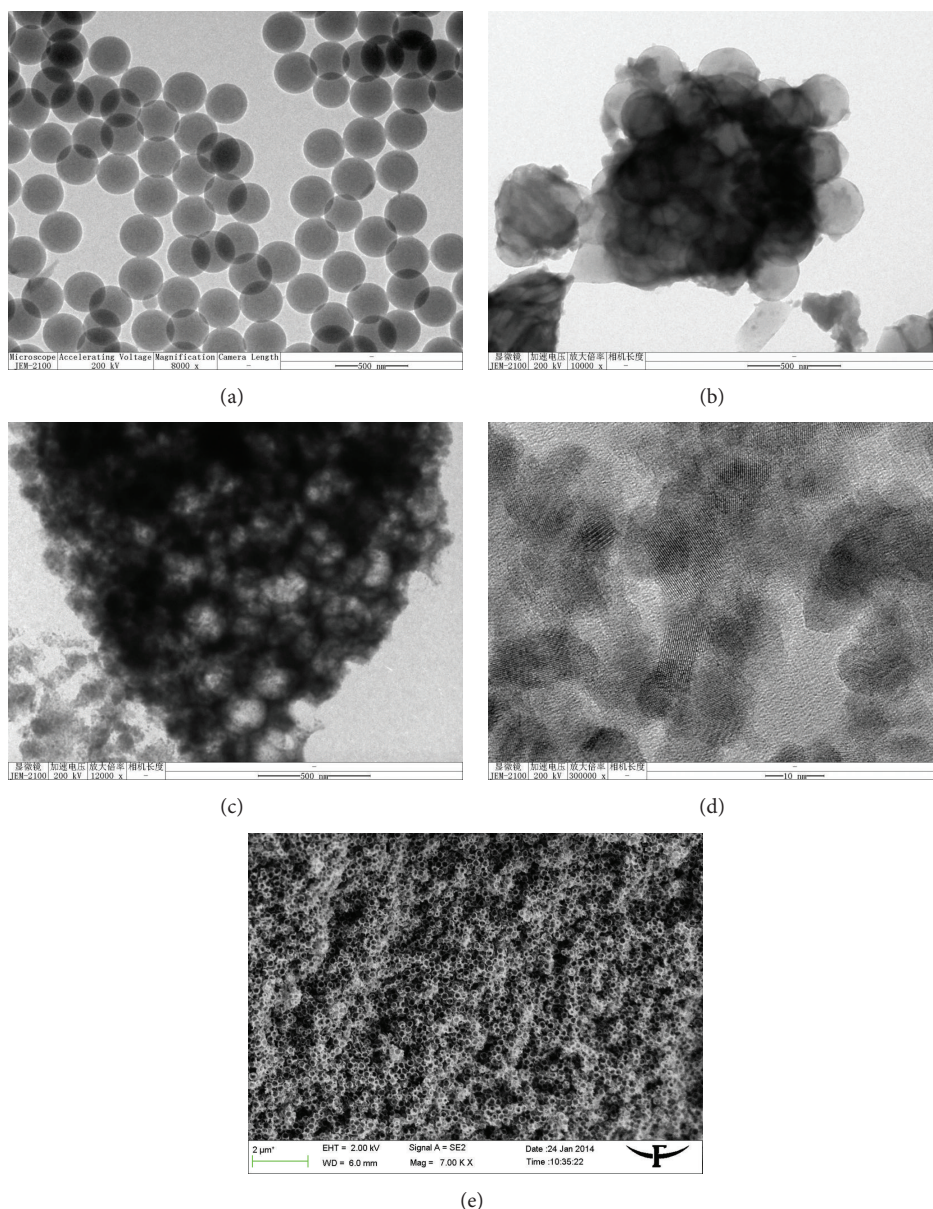
FIGURE 3: Low-magnification TEM images of (a) the PS spheres, (b) the TiO_2/PS composites, (c) the m-TiO_2 catalyst after calcination at 500°C, and the high-resolution TEM image (d) and SEM image (e) of the m-TiO_2 sample.

spheres. High-resolution TEM image (Figure 3(d)) displays that the crystalline size of TiO_2 nanoparticles is about 10 nm, which is in good agreement with the XRD analysis.

N$_2$ adsorption-desorption measurements were performed to investigate the textural properties of the macroporous TiO_2. The N$_2$ adsorption-desorption isotherms of r-TiO_2 and m-TiO_2 are shown in Figure 4. One can see that the isotherm of the r-TiO_2 is of typical type IV, characteristic of mesoporous materials, according to IUPAC classification. The adsorbed nitrogen volume for m-TiO_2 becomes steep in the P/P_0 range of 0.8–1.0, which indicates the presence of large macropores. Based on the Brunauer-Emmett-Teller (BET) equation, the specific surface areas of r-TiO_2 and

m-TiO_2 were evaluated to be about 91.2 and 87.8 m^2/g, respectively.

3.2. Photocatalytic Activity Test. The photocatalytic activities of the prepared TiO_2 samples were examined through the photodegradation of RhB under UV light irradiation. The degradation efficiency was illustrated by the change of the RhB concentration during the photodegradation process and the results were shown in Figure 5. The photocatalytic results reveal that the photocatalytic activity of the macroporous TiO_2 was significantly improved as compared to that of the traditional TiO_2 nanoparticles. For the macroporous TiO_2, 92.63% of the RhB was decomposed after 2 h irradiation.
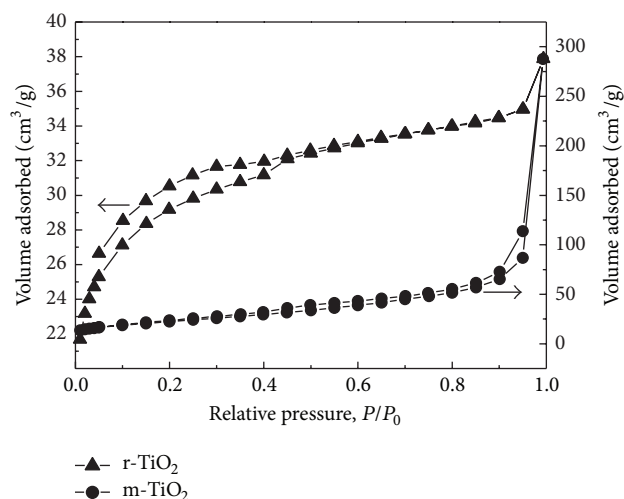
FIGURE 4: Nitrogen adsorption-desorption isotherms of the r-TiO$_2$ and m-TiO$_2$ after calcination at 500°C for 2 h.
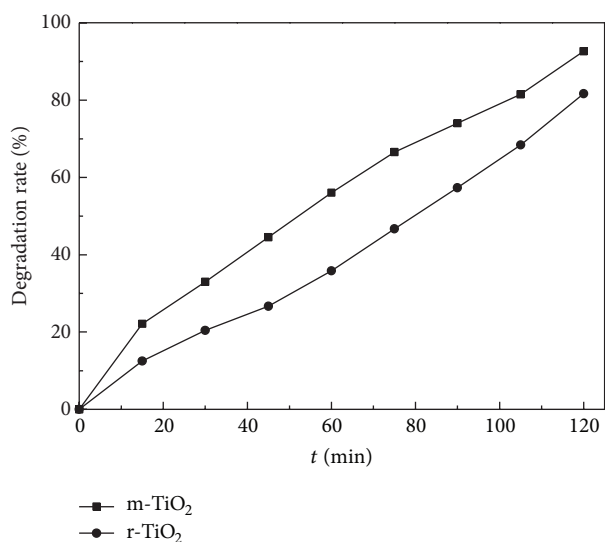
FIGURE 5: Degradation efficiency curves of RhB for the r-TiO$_2$ and m-TiO$_2$ after calcination at 500°C for 2 h.

However, as to the r-TiO$_2$ sample, the degradation percentage is only 81.66%. Here, the macroporous structure is believed to facilitate the transportation of reactant molecules and products through the interior space due to the run-through-macropore networks [40–43] and to favor the harvesting of exciting light due to enlarged surface area and multiple scattering within the porous framework [43, 44]. So the enhanced photoactivity of m-TiO$_2$ could be achieved.

4. Conclusions

In summary, macroporous TiO$_2$ photocatalyst was successfully synthesized via a simple sol-gel method using polystyrene spheres as sacrificial templates. The prepared macroporous TiO$_2$ exhibited higher photocatalytic activity than the TiO$_2$ sample through a template-free approach in catalyzing the degradation of RhB under UV light illumination. And the superior photocatalytic performance can be related to the run-through-macropore network structure. Considering the facile preparation and high photocatalytic activity, the macroporous TiO$_2$ materials display a good potential in the fields of environmental remediation and energy conversion and storage.

Conflict of Interests

The authors have no conflict of interests in relation to the instrumental companies directly or indirectly.

Acknowledgments

References

[1] S. D. Richardson, C. S. Willson, and K. A. Rusch, "Use of rhodamine water tracer in the marshland upwelling system," *Ground Water*, vol. 42, no. 5, pp. 678–688, 2004.

[2] J. Ryu and W. Choi, "Substrate-specific photocatalytic activities of TiO$_2$ and multiactivity test for water treatment application," *Environmental Science and Technology*, vol. 42, no. 1, pp. 294–300, 2008.

[3] H. Cui, H. Liu, J. Shi, and C. Wang, "Function of TiO$_2$ lattice defects towards photocatalytic process: view of electronic driven force," *International Journal of Photoenergy*, vol. 2013, Article ID 364802, 16 pages, 2013.

[4] P. Chou, S. Matsui, K. Misaki, and T. Matsuda, "OH radical formation at distinct faces of rutile TiO$_2$ crystal in the procedure of photoelectrochemical water oxidation," *The Journal of Physical Chemistry C*, vol. 117, no. 45, pp. 23832–23839, 2013.

[5] R. Daghrir, P. Drogui, and D. Robert, "Modified TiO$_2$ for environmental photocatalytic applications: a review," *Industrial & Engineering Chemistry Research*, vol. 52, no. 10, pp. 3581–3599, 2013.

[6] H. Huang, H. Huang, P. Hu, X. Ye, and D. Y. C. Leung, "Removal of formaldehyde using highly active Pt/TiO$_2$ catalysts without irradiation," *International Journal of Photoenergy*, vol. 2013, Article ID 350570, 6 pages, 2013.

[7] R. Giovannetti, M. Zannotti, L. Alibabaeu, and S. Ferraro, "Equilibrium and kinetic aspects in the sensitization of monolayer transparent TiO$_2$ thin films with porphyrin dyes for DSSC applications," *International Journal of Photoenergy*, vol. 2014, Article ID 834269, 9 pages, 2014.

[8] B. Wang and L. L. Kerr, "Stability of CdS-coated TiO$_2$ solar cells," *Journal of Solid State Electrochemistry*, vol. 16, no. 3, pp. 1091–1097, 2012.

[9] S. Phanichphant, C. Liewhiran, K. Wetchakun, A. Wisitsoraat, and A. Tuantranont, "Flame-made Nb-doped TiO$_2$ ethanol and acetone sensors," *Sensors*, vol. 11, no. 1, pp. 472–484, 2011.

[10] L.-C. Jiang and W.-D. Zhang, "Electrodeposition of TiO$_2$ nanoparticles on multiwalled carbon nanotube arrays for hydrogen peroxide sensing," *Electroanalysis*, vol. 21, no. 8, pp. 988–993, 2009.

[11] V. Tajer-Kajinebaf, H. Sarpoolaky, and T. Mohammadi, "Synthesis of nanostructured anatase mesoporous membranes with photocatalytic and separation capabilities for water ultrafiltration process," *International Journal of Photoenergy*, vol. 2013, Article ID 509023, 11 pages, 2013.

[12] C. S. Guo, M. Ge, L. Liu, G. Gao, Y. Feng, and Y. Wang, "Directed synthesis of mesoporous TiO$_2$ microspheres: catalysts and their photocatalysis for bisphenol A degradation," *Environmental Science and Technology*, vol. 44, no. 1, pp. 419–425, 2010.

[13] Y.-C. Park, Y.-J. Chang, B.-G. Kum et al., "Size-tunable mesoporous spherical TiO$_2$ as a scattering overlayer in high-performance dye-sensitized solar cells," *Journal of Materials Chemistry*, vol. 21, no. 26, pp. 9582–9586, 2011.

[14] C. J. W. Ng, H. Gao, and T. T. Yang Tan, "Atomic layer deposition of TiO$_2$ nanostructures for self-cleaning applications," *Nanotechnology*, vol. 19, no. 44, Article ID 445604, 2008.

[15] Z. Bian, J. Zhu, F. Cao, Y. Huo, Y. Lu, and H. Li, "Solvothermal synthesis of well-defined TiO$_2$ mesoporous nanotubes with enhanced photocatalytic activity," *Chemical Communications*, vol. 46, no. 44, pp. 8451–8453, 2010.

[16] H. Z. Zhang, F. Dong, S. N. Zhai, X. J. Kang, and S. M. Fang, "Preparation of ordered TiO$_2$ macroporous membrane using PBMA colloid crystal as template," *Advanced Materials Research*, vol. 399–401, pp. 677–682, 2012.

[17] G. Q. Liu, Z. G. Jin, X. X. Liu, T. Wang, and Z. F. Liu, "Anatase TiO$_2$ porous thin films prepared by sol-gel method using CTAB surfactant," *Journal of Sol-Gel Science and Technology*, vol. 41, no. 1, pp. 49–55, 2007.

[18] H. Bala, Y. Yu, and Y. Zhang, "Synthesis and photocatalytic oxidation properties of titania hollow spheres," *Materials Letters*, vol. 62, no. 14, pp. 2070–2073, 2008.

[19] X. Zheng, Q. Kuang, K. Yan, Y. Qiu, J. Qiu, and S. Yang, "Mesoporous TiO$_2$ single crystals: facile shape-, size-, and phase-controlled growth and efficient photocatalytic performance," *ACS Applied Materials & Interfaces*, vol. 5, no. 21, pp. 11249–11257, 2013.

[20] Y. Dong, J. Chao, Z. Xie, X. Xu, Z. Wang, and D. Chen, "Highly ordered TiO$_2$ macropore arrays as trandparent photocatalysts," *Journal of Nanomaterials*, vol. 2012, Article ID 762510, 6 pages, 2012.

[21] P. Jiang, J. Cizeron, J. F. Bertone, and V. L. Colvin, "Preparation of macroporous metal films from colloidal crystals," *Journal of the American Chemical Society*, vol. 121, no. 34, pp. 7957–7958, 1999.

[22] M. Sadakane, T. Horiuchi, N. Kato, C. Takahashi, and W. Ueda, "Facile preparation of three-dimensionally ordered macroporous alumina, iron oxide, chromium oxide, manganese oxide, and their mixed-metal oxides with high porosity," *Chemistry of Materials*, vol. 19, no. 23, pp. 5779–5785, 2007.

[23] M. Davis, D. A. Ramirez, and L. J. Hope-Weeks, "Formation of three-dimensional ordered hierarchically porous metal oxides via a hybridized epoxide assisted/colloidal crystal templating approach," *Applied Materials & Interfaces*, vol. 5, no. 16, pp. 7786–7792, 2013.

[24] T. Kimura, N. Miyamoto, X. Meng, T. Ohji, and K. Kato, "Rapid fabrication of mesoporous titania films with controlled macroporosity to improve photocatalytic property," *Chemistry*, vol. 4, no. 9, pp. 1486–1493, 2009.

[25] X.-Y. Li, L.-H. Chen, Y. Li et al., "Self-generated hierarchically porous titania with high surface area: photocatalytic activity enhancement by macrochannel structure," *Journal of Colloid and Interface Science*, vol. 368, no. 1, pp. 128–138, 2012.

[26] R.-F. Zhang, J. Ye, and N.-B. Long, "Large-sized TiO$_2$/SiO$_2$ macroporous materials for photodegradation of organic compounds in water and air," *Advanced Materials Research*, vol. 306-307, pp. 1157–1161, 2011.

[27] L. Szymanski, P. Surolia, O. Byrne, K. R. Thampi, and C. Stubenrauch, "Porous "sponge-like" anatase TiO$_2$ via polymer templates: synthesis, characterization, and performance as a light-scattering material," *Colloid and Polymer Science*, vol. 291, no. 4, pp. 805–815, 2013.

[28] F. Z. Huang, D. H. Chen, X. L. Zhang, R. A. Caruso, and Y.-B. Cheng, "Dual-function scattering layer of submicrometer-sized mesoporous TiO$_2$ beads for high-efficiency dyesensitized solar cells," *Advanced Functional Materials*, vol. 20, no. 8, pp. 1301–1305, 2010.

[29] T. Yan, L. Li, G. Li, Y. Wang, W. Hu, and X. Guan, "Porous SnIn$_4$S$_8$ microspheres in a new polymorph that promotes dyes degradation under visible light irradiation," *Journal of Hazardous Materials*, vol. 186, no. 1, pp. 272–279, 2011.

[30] G. Cappelletti, "TiO$_2$ nanoparticles: traditional and novel synthetic methods for photocatalytic paint formulations," in *Nanoparticles: Properties, CLassification Characterization and Fabrication, S.L*, pp. 213–254, Nova Science Publishers, 2010.

[31] S. Yurdakal, B. S. Tek, O. Alagöz et al., "Photocatalytic selective oxidation of 5-(Hydroxymethyl)-2-furaldehyde to 2,5-Furandicarbaldehyde in water by using anatase, rutile, and brookite TiO$_2$ nanoparticles," *Sustainable Chemistry & Engineering*, vol. 1, no. 5, pp. 456–461, 2013.

[32] Q. Zhou, P. Dong, G.-Y. Yi, L.-X. Liu, and B.-Y. Cheng, "Preparation of TiO$_2$ inverse opal via a modified filling process," *Chinese Physics Letters*, vol. 22, no. 5, pp. 1155–1158, 2005.

[33] X.-D. Wang, P. Dong, and G.-Y. Yi, "Evaporation self-assembly method to fabricate high-quality polystyrene microsphere colloid crystal," *Acta Physica Sinica*, vol. 55, no. 4, pp. 2092–2098, 2006.

[34] X.-D. Wang, G.-Y. Yi, and Y. Liu, "Preparation of Al$_2$O$_3$ catalytic material with run-through-macropore network structure," *Chemical Journal of Chinese Universities*, vol. 30, no. 2, pp. 349–354, 2009.

[35] C. Wang, Z.-X. Deng, G. Zhang, S. Fan, and Y. Li, "Synthesis of nanocrystalline TiO$_2$ in alcohols," *Powder Technology*, vol. 125, no. 1, pp. 39–44, 2002.

[36] Y. Li, T. J. White, and S. H. Lim, "Low-temperature synthesis and microstructural control of titania nano-particles," *Journal of Solid State Chemistry*, vol. 177, no. 4-5, pp. 1372–1381, 2004.

[37] E. T. Soares, M. A. Lansarin, and C. C. Moro, "A study of process variables for the photocatalytic degradation of rhodamine B," *Brazilian Journal of Chemical Engineering*, vol. 24, no. 1, pp. 29–36, 2007.

[38] K. Byrappa, A. K. Subramani, S. Ananda, K. M. Lokanatha Rai, R. Dinesh, and M. Yoshimura, "Photocatalytic degradation of rhodamine B dye using hydrothermally synthesized ZnO," *Bulletin of Materials Science*, vol. 29, no. 5, pp. 433–438, 2006.

[39] H. P. Klong and L. E. Alexander, *X-Ray Diffraction Procedures for Crystalline and Amorphous Solids*, Wiley, New York, NY, USA, 1954.

[40] Z.-Y. Yuan and B.-L. Su, "Insights into hierarchically mesomacroporous structured materials," *Journal of Materials Chemistry*, vol. 16, no. 7, pp. 663–677, 2006.

[41] C. M. A. Parlett, K. Wilson, and A. F. Lee, "Hierarchical porous materials: catalytic applications," *Chemical Society Reviews*, vol. 42, pp. 3876–3893, 2013.

[42] J. G. Yu, S. W. Liu, and H. G. Yu, "Microstructures and photoactivity of mesoporous anatase hollow microspheres fabricated by fluoride-mediated self-transformation," *Journal of Catalysis*, vol. 249, no. 1, pp. 59–66, 2007.

[43] G. Kaune, M. Memesa, R. Meier et al., "Hierarchically structured titania films prepared by polymer/colloidal templating," *ACS Applied Materials and Interfaces*, vol. 1, no. 12, pp. 2862–2869, 2009.

[44] X. C. Wang, J. C. Yu, C. Ho, Y. D. Hou, and X. Z. Fu, "Photocatalytic activity of a hierarchically macro/mesoporous titania," *Langmuir*, vol. 21, no. 6, pp. 2552–2559, 2005.

Research Article

Photocatalytic Degradation of Rhodamine B Dye over Novel Porous TiO$_2$-SnO$_2$ Nanocomposites Prepared by Hydrothermal Method

Yan Wang,[1] **Zhaoli Yan,**[2] **and Xiaodong Wang**[2]

[1] *School of Safety Science and Engineering, Henan Polytechnic University, Jiaozuo, Henan 454000, China*
[2] *School of Materials Science and Engineering, Henan Polytechnic University, Jiaozuo, Henan 454000, China*

Correspondence should be addressed to Xiaodong Wang; wangxd0863@aliyun.com

The photocatalytic degradation of Rhodamine B dye was successfully carried out under UV irradiation over porous TiO$_2$-SnO$_2$ nanocomposites with various molar ratios of Ti/Sn (4–12) synthesized by hydrothermal method using polystyrene microspheres as template. The combination of TiO$_2$ with SnO$_2$ can obtain high quantum yield of TiO$_2$, and then achieve the high photocatalytic activity. And its porous structure can provide large surface area, leading to more adsorption and fast transfer of dye pollutant. Structural and textural features of the samples were investigated by X-ray diffraction (XRD), transmission electron microscopy (TEM), and N$_2$ sorption techniques. Both adsorption and UV irradiation contribute to decolorization of about 100% of Rhodamine B dye over the sample TiSn10 after 30 min of the photocatalytic reaction, while the decomposition of Rhodamine B dye is only 62% over pure titania (Degussa P25).

1. Introduction

The disposal of various toxic dyes from the textile industry has attracted extensive attention in the field of water pollution prevention and cure. Rhodamine B (RB) is one of the famous dyes and is widely used as a colorant in foodstuffs and textiles due to its high stability. It is harmful to human beings and animals and causes irritation of the skin, eyes, and respiratory tract. The removal methods of toxic dyes have been considered in recent studies in the literature. These include physical adsorption [1, 2], chemical degradation [3], biological degradation [4], photodegradation, or the synergic treatments of different methods. Recently, much attention has been paid to the photocatalytic degradation of dye pollutants using nanodispersed catalysts TiO$_2$ [5], SnO$_2$ [6], and so forth. It uses light energy to initiate chemical reactions in the presence of photocatalysts which are mostly semiconductor materials. Heterogeneous photocatalysis using semiconductors is an effective and rapid technique for the removal of dye pollutants from wastewater [7].

TiO$_2$ is regarded as a promising semiconductor in degradation of various dye pollutants for its strong oxidizing power,

nontoxicity, low cost, chemical stability, and high photocatalytic activity [8]. The degradation process involves the exposure of TiO$_2$ to UV light which is associated with formation of positive hole and negative electrons in the valence and conduction bands that oxidize and reduce the dye pollutants. However, there are some issues that limit the photocatalytic activity of TiO$_2$ materials, such as the low quantum yield, the wide band gap energy (3–3.2 eV), and the low mass transport **a**rates. Therefore, the researchers conduct many works to solve these essential drawbacks. An effective strategy is to couple TiO$_2$ with other semiconductors, transition elements, and noble metals which can improve the photodegradation activity owing to the role of dopants in improving the optical features of the samples by extending the absorption activity to visible region and preventing the recombination of the charge carriers [9–12]. And another useful means is to increase its surface area via synthesis of porous TiO$_2$ monoliths, leading to more adsorption and fast transfer of dye pollutants. More attention has been paid to Sn$_x$Ti$_{1-x}$O$_2$ system in recent years by coupling TiO$_2$ with SnO$_2$ [13–17]. It is generally accepted that this new nanocomposite exhibits high photocatalytic reactivity compared with pure TiO$_2$. It is well known that the

band gaps of SnO_2 and TiO_2 are 3.6 and 3.2 eV, respectively. The combination of these two semiconductors leads to the accumulation of electron in the conduction band of SnO_2 and the photogenerated holes in the valence band of the TiO_2 particle, which improve the separation of photogenerated charges, shifting the photoexcitation of the sample toward visible light, and increase the oxidizing power of TiO_2 [14–16].

In this work, we reported a novel hierarchical macroporous-mesoporous TiO_2-SnO_2 nanocomposite prepared by hydrothermal method using polystyrene microspheres as template. The textural and structural properties of the as-prepared photocatalysts were characterized by means of XRD, TEM, and N_2 sorption. And the photocatalytic activities of the as-prepared catalysts were evaluated by the photocatalytic degradation of RB dye pollutant under UV light. The effect of the molar ratios of Ti/Sn on the crystal structure, morphology, and optical properties of the final products was investigated.

2. Experimental Section

2.1. Materials. Titanium n-butoxide (TBOT, $Ti(OC_4H_9)_4$), tin(IV) chloride, tetrahydrofuran (THF), and acetone were used without any further purification. All chemicals used in this study were of analytical grade and purchased from Sinopharm Chemical Reagent Co., Ltd. or Tianjin Dengke Chemical Reagent Co., Ltd. Polystyrene (PS) microspheres were obtained by emulsion polymerization of styrene which had been discussed in our previous reports [18, 19]. In a typical procedure, 150 g deionized water was poured into a 300 mL jacket reactor, which was kept at 85°C until the end of the reaction. Then, 0.075 g sodium styrene sulfonate and 0.0633 g sodium hydrogen carbonate were dissolved in the deionized water. Under constant stirring, 17.50 mL styrene monomer was added to this solution under the nitrogen protection. After 1 h, 0.0833 g potassium persulfate was introduced into the solution. After 18 h polymerization, the monodispersed PS spheres with the diameter of 247 nm were obtained.

2.2. Preparation of TiO_2-SnO_2 Composites. The TiO_2-SnO_2 photocatalysts were prepared by hydrothermal method using polystyrene microspheres as template. In a typical procedure, 1.052 g $SnCl_4 \cdot 5H_2O$ and the calculated volume of TBOT with various molar ratios of Ti/Sn (4–12) were dissolved in 60 mL of anhydrous ethanol under stirring; then the calculated amount of PS microspheres (100 g PS microspheres per mole of solutes) was added to the prepared solution under magnetic stirring. After ultrasonic dispersion for 20 min, the distilled water was slowly dripped into the resulting suspension under vigorous stirring until the gel occurred; then distilled water for diluting the suspension continued to be added (ensure that the total volume of distilled water is 200 mL) and stirred for 30 min. Subsequently, the pH value of the suspension was regulated by adding aqueous ammonia and simultaneous stirring until pH = 8 and kept for 30 min. The solution and the resulting precipitates were placed inside a Teflon-lined stainless autoclave, and the autoclave was

heated at 150°C for 5 h. Then the mixture was cooled down to room temperature and the precipitate was separated by filtration, washed several times with distilled water and anhydrous ethanol, and dried 10 h in air at 60°C. Finally, the obtained sample was placed in a glass soxhlet extractor and PS microspheres were extracted by the mixed solution of THF/acetone (1/1 of v/v) for four days, dried 6 h in air at 80°C, and ground to 60–80 mesh. The series of as-prepared samples were named as TiSn4, TiSn6, TiSn8, TiSn10, and TiSn12 corresponding to the samples with various molar ratios of Ti/Sn = 4, 6, 8, 10, and 12, respectively.

2.3. Characterization. X-ray diffraction (XRD) analysis was performed on a Bruker-AXS D8 Advance diffractometer, with CuK_α radiation at 40 kV and 25 mA in a scanning range of 10–80° (2θ). The diffraction peaks of the crystalline phase were compared with those of standard compounds reported in the JCPDS Data File. N_2 adsorption-desorption isotherms were collected at liquid nitrogen temperature using a Micromeritics ASAP 2020 adsorption apparatus. Before carrying out the measurement, each sample was degassed at 60°C for more than 6 h. The specific surface areas (S_{BET}) of the samples were calculated following the multipoint BET (Brunauer-Emmett-Teller) procedure. The pore size distributions were determined from the adsorption branch of the isotherms using the BJH method. Transmission electron microscopy (TEM) analysis was performed on a JEOL JEM-2100 microscope, operating at 200 kV. The samples were dispersed in ethanol and treated with ultrasound for 5 min and then deposited on a copper grid coated with preformed holey carbon film.

2.4. Photocatalytic Activity Measurements. Rhodamine B aqueous solution under UV light was used as a model reaction to evaluate the photocatalytic activity of prepared samples. The light source was a 450 W high-pressure mercury lamp (center wavelength = 365 nm, Foshan Electrical And Lighting Co., Ltd., China) and the lamp was located 15 cm higher than the solution surrounded by a circulating water tube. A general procedure was carried out as follows. First, 100 mL aqueous Rhodamine B solution (20 mg/L) was placed in a 500 mL water-jacketed reactor, which was maintained at a temperature of 20°C. Then, 0.1 g catalyst was suspended in the solution. The suspension was stirred in dark for 30 min in order to reach the adsorption-desorption equilibrium. Finally, the suspension was irradiated under UV light. To monitor the photocatalytic process, 6 mL mixture solution was aspirated from the test tube with an interval of 10 min. The determination of Rhodamine B (RB) dye was done on a TU-1810 UV-vis spectrophotometer by measuring absorbance at λ_{max} of 553 nm. A calibration curve obtained at the RB dye concentration of 1–10 mg/L was used for determination of initial and final concentrations. The photocatalytic degradation rate was calculated by the following expression:

$$\text{Degradation rate } (\%) = \frac{C_0 - C}{C_0} \times 100\%, \quad (1)$$

where C_0 (mg/L) is the initial concentration of Rhodamine B solution which reached absorbency balance and C (mg/L) is
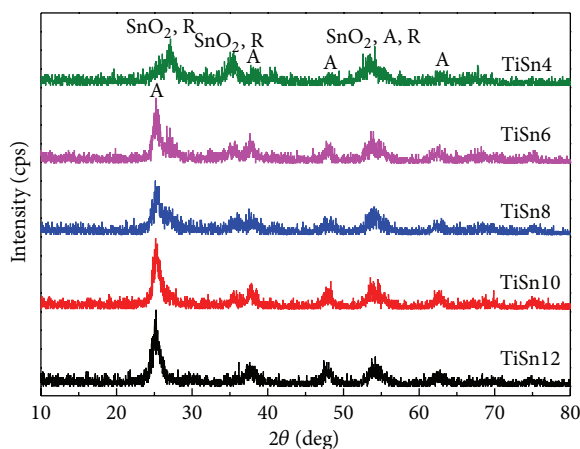
FIGURE 1: XRD patterns of the prepared samples TiSn4, TiSn6, TiSn8, TiSn10, and TiSn12.

the concentration of the dye solution at the irradiation time (t).

3. Results and Discussion

3.1. Characterization of Nanoparticles

3.1.1. X-Ray Diffraction. Figure 1 shows the typical XRD patterns of the as-prepared samples TiSn4, TiSn6, TiSn8, TiSn10, and TiSn12. When the molar ratios of Ti/Sn > 4, the diffraction peaks at 2θ = 25.2, 37.8, 48, 53.9, and 62.6° reveal the existence of predominant anatase phase (JCPDS number 21-1272). And, the relatively weak peaks detected at 2θ = 27.2, 35.5, and 53.5° are referred to as rutile phase (JCPDS number 21-1276). Simultaneously, along with the molar ratios of Ti/Sn decrease (which means the increase of SnO_2 content), the peaks intensity of anatase phase decreased and that of rutile phase was enhanced. When the molar ratios of Ti/Sn = 4, the main phase of TiO_2 converts to rutile phase. The diffraction peaks showed at 2θ = 26.6, 34.8, and 52.8° are referred to as cassiterite phase (JCPDS number 41-1445), and they are enhanced with the decrease of the molar ratios of Ti/Sn. On examining the figure, one can notice that the SnO_2 content impacts the crystalline phase of TiO_2 significantly. The excessive SnO_2 can make the main phase of TiO_2 convert from anatase to rutile phase. In addition, the sharp peaks in Figure 1 indicate the well crystallization of all the samples via the hydrothermal action.

3.1.2. TEM Analysis of TiO_2-SnO_2 Nanoparticles. Figure 2 shows the low resolution TEM (LRTEM) images of the prepared TiSn10 nanoparticles from different areas. The images clearly demonstrate that the TiSn10 sample has a disordered spherical macroporous structure, formed by the agglomeration of the uniform nanoparticles on the surface of polystyrene microspheres and the extraction of polystyrene microspheres by the mixed solution of THF/acetone. The average pore size of spherical macropores is about 580 nm, and it is obviously larger than the average particle size 247 nm of polystyrene microspheres. This may be owing to the fact

that the temperature of hydrothermal reaction (150°C) is higher than the glass transition temperature of polystyrene microspheres (120°C), which leads to the flow and fusion of liquefied polystyrene microspheres. Furthermore, it also can be seen that the spherical macroporous structure has been slightly damaged due to the hydrothermal action and grind during the preparation process.

The TEM images of the walls of spherical macropores recorded at different magnification are displayed in Figure 3. It clearly demonstrates that the walls of spherical macropore have a disordered mesoporous structure, which is formed by the agglomeration of the uniform nanoparticles. The accessible mesopores are connected randomly, lacking discernible long-range order in the pore arrangement among the small particles. And the nanoparticles in the sample are of regular morphology with the size around 10 nm (Figure 3(b)). In conclusion, the as-prepared TiSn10 sample has a hierarchical macroporous-mesoporous structure formed by nanoparticles.

3.1.3. N_2-Sorption Analysis. Figure 4 depicts N_2 adsorption-desorption isotherms and the corresponding pore size distribution curves of the prepared samples TiSn4, TiSn6, TiSn8, TiSn10, and TiSn12. The textural properties of the samples are listed in Table 1. The surface area of TiSn4 and TiSn10 is 71 m^2/g and 73 m^2/g, respectively, while the total pore volume of them is 0.28 cm^3/g and 0.23 cm^3/g, respectively. The highest surface area and pore volume (162 m^2/g and 0.51 cm^3/g) are obtained by the TiSn8 sample. From Figure 4(a), it can be seen that the isotherms of all the prepared samples are of classical type IV, characteristic of mesoporous materials according to the IUPAC, and the adsorption isotherms of the samples TiSn4, TiSn6, TiSn8, and TiSn10 exhibit a large increase at the P/P_0 above 0.8, indicating the presence of the macroporous structure (consistent with the TEM analysis results in Figures 2 and 3). In comparison to the well-known nonporous TiO_2 material (P25), the hierarchical macroporous-mesoporous structure of the prepared samples is believed to facilitate the absorption of RB dye (Table 2) and the transport of photodegradation product molecules. The pore size distribution curves of the prepared samples, which are determined by the BJH method from the adsorption branch of the isotherm, exhibit one single narrow peak centered at 7.7–13.9 nm (Figure 4(b)), indicating the good homogeneity of the pores. Besides, one can observe a progressive increase in average pore size upon decreasing the molar ratios of Ti/Sn from 12 to 4 (namely, increasing the SnO_2 content from 7.7 to 20.0%).

3.2. Photocatalytic Activity Studies.

Figure 5 displays the photocatalytic degradation rate and the pseudo-first-order kinetics of the prepared samples and pure TiO_2 (P25, the surface area of 50 m^2/g). The absorption (in dark) and photodegradation rates (under UV light) of RB dye by different photocatalysts within 30 min are presented in Table 2. From Figure 5(a), it is seen that all the prepared TiO_2-SnO_2 composites possess high degradation rate compared with pure titanium oxide P25, indicating the effectiveness of SnO_2

(a)

(b)
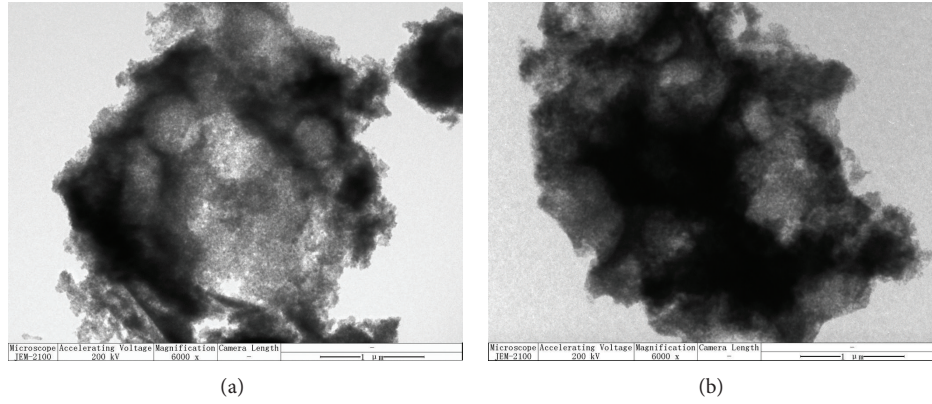
FIGURE 2: LRTEM (Low resolution TEM) images of the prepared TiSn10 nanoparticles.
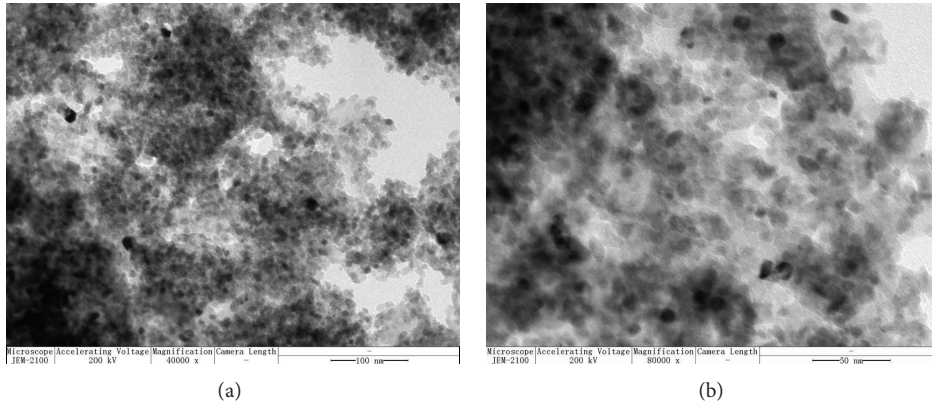

(a)

(b)

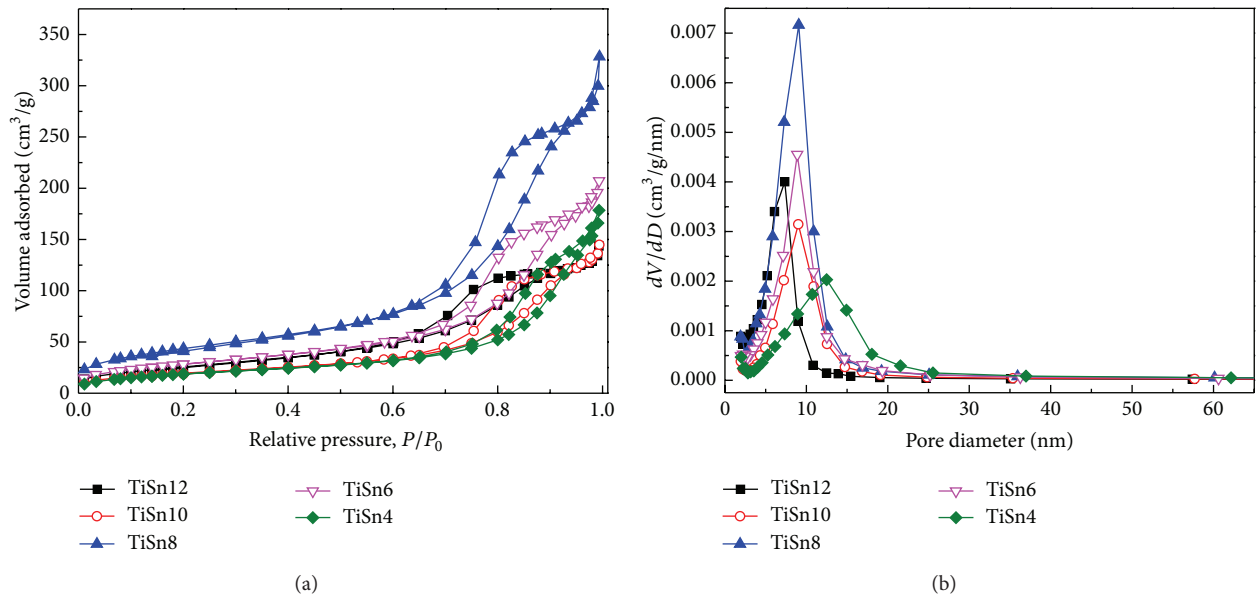FIGURE 3: TEM images of the prepared TiSn10 nanoparticles.

(a)

(b)

FIGURE 4: (a) N_2 adsorption-desorption isotherms and (b) the corresponding pore size distribution curves of the prepared samples: TiSn4, TiSn6, TiSn8, TiSn10, and TiSn12.
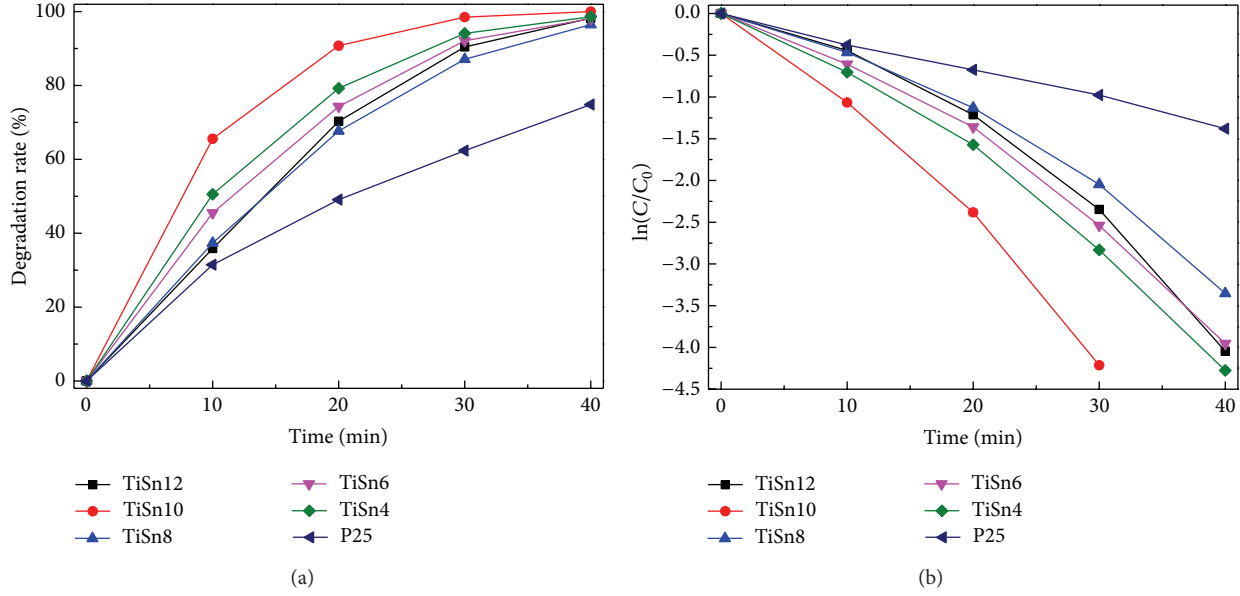
FIGURE 5: The photocatalytic degradation rate (a) and the pseudo-first-order kinetics (b) of the prepared samples and Degussa P25.

TABLE 1: The textural properties of the investigated catalysts.

Samples	Calcination temperature (°C)	Surface area[a] (m^2/g)	V_{tot} (cm^3/g)	$D_{BJH-ads}$[b] (nm)
TiSn12	80	96	0.22	7.7
TiSn10	80	73	0.23	10.9
TiSn8	80	162	0.51	10.7
TiSn6	80	106	0.32	10.3
TiSn4	80	71	0.28	13.9

[a]Multipoint BET surface area.
[b]Maximum of BJH pore diameter as determined from the adsorption branch.

TABLE 2: Absorption (in dark) and photodegradation rate (under UV light) of RB dye by different catalysts within 30 min.

Samples	TiSn12	TiSn10	TiSn8	TiSn6	TiSn4
Absorption (%)	47.0	60.4	51.4	51.9	54.5
Degradation rate (%)	90.4	98.5	87.1	92.1	94.1

doping and hierarchical macroporous-mesoporous structure. And, for these prepared samples, the relative order of photodegradation rate of RB dye solutions is TiSn10 > TiSn4 > TiSn6 ≈ TiSn12 > TiSn8. Although the samples TiSn6 and TiSn8 possess high surface area and pore volume (Table 1), they exhibit lower degradation effect. The lower activity of these two samples may be related to the smaller average pore size, which leads to the less absorption of RB dye compared with the samples TiSn10 and TiSn4 (Table 2). Furthermore, the photocatalytic activity of the sample TiSn10 is obviously higher than that of TiSn4. This may be owing to the lack of anatase phase in TiSn4, which is photocatalytic active phase that considered a predominant factor in influencing the photodegradation process. However, the sample TiSn4 with predominant rutile phase exhibits higher degradation rate than the sample TiSn6 with main anatase phase. This is possibly due to the increase of SnO_2 content in TiSn4,

which leads to more Sn doping, forming smaller energy gap among the band gap of TiO_2, producing more electron-hole pairs, and thus improving the photocatalytic activity [13]. Figure 5(b) depicts the approximate linear relationship of $\ln(C/C_0)$ versus irradiation time t for the different samples, which indicates the photodegradation process of RB dye can be considered as a pseudo-first-order kinetics reaction. And the apparent rate constants were calculated to be 0.03385, 0.10032, 0.09149, 0.0764, 0.13363, and $0.09023 \, min^{-1}$ for pure TiO_2 (P25), TiSn4, TiSn6, TiSn8, TiSn10, and TiSn12 photocatalysts, respectively.

Figure 6 shows the absorption spectra of RB dye solution over the sample TiSn10. From Figure 6, it can be seen that the RB dye solution exhibits an obvious absorption peak at 553 nm at zero time, and the absorbance of RB dye solution at 553 nm is basically reduced to zero within 30 min, indicating the effective photodegradation of RB dye under the catalysis of TiSn10. On the other hand, the absorption peak gradually shifts to left with prolonged irradiation time, then stays around at $\lambda = 496$ nm (the absorption peak of one intermediate) at 40 min, and finally disappears within 70 min. This demonstrates that the RB dye in solution is degraded completely within 30 min, and the whole RB dye along with its intermediate products is fully degraded within 70 min.
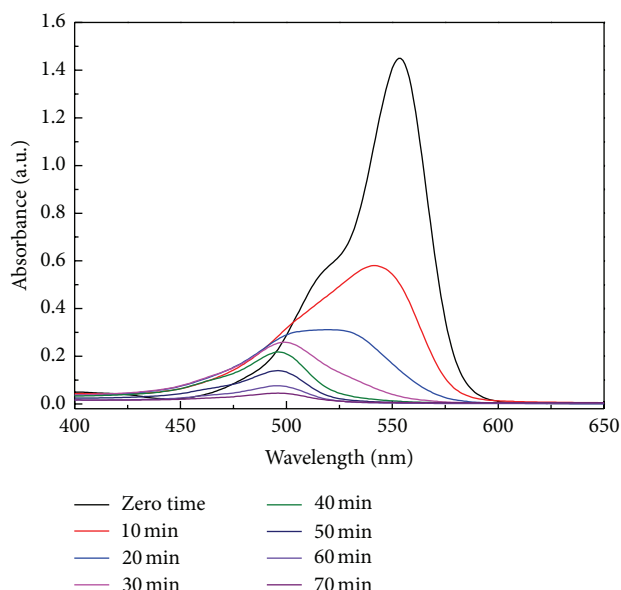
FIGURE 6: The absorption spectra of Rhodamine B solution over TiSn10.

4. Conclusions

The photocatalytic degradation of Rhodamine B dye was successfully carried out under UV irradiation over porous TiO_2-SnO_2 nanocomposites prepared by hydrothermal method by using polystyrene microspheres as template. The photocatalytic activities exhibit an order of TiSn10 > TiSn4 > TiSn6 ≈ TiSn12 > TiSn8 > pure TiO_2 (P25). The observed high photocatalytic activity is comprehensively affected by the molar ratios of Ti/Sn, hierarchical macroporous-mesoporous structure, and high surface area.

Conflict of Interests

The authors have no conflict of interests in relation to the instrumental companies mentioned in this paper directly or indirectly.

Acknowledgments

References

[1] S. Eftekhari, A. Habibi-Yangjeh, and S. H. Sohrabnezhad, "Application of AlMCM-41 for competitive adsorption of methylene blue and rhodamine B: thermodynamic and kinetic studies," *Journal of Hazardous Materials*, vol. 178, no. 1–3, pp. 349–355, 2010.

[2] X. Xue, X. He, and Y. Zhao, "Adsorptive properties of acid-heat activated rectorite for Rhodamine B removal: equilibrium, kinetic studies," *Desalination and Water Treatment*, vol. 37, no. 1–3, pp. 259–267, 2012.

[3] A. R. Tehrani-Bagha, N. M. Mahmoodi, and F. M. Menger, "Degradation of a persistent organic dye from colored textile wastewater by ozonation," *Desalination*, vol. 260, no. 1–3, pp. 34–38, 2010.

[4] R. G. Saratale, G. D. Saratale, J. S. Chang, and S. P. Govindwar, "Decolorization and biodegradation of reactive dyes and dye wastewater by a developed bacterial consortium," *Biodegradation*, vol. 21, no. 6, pp. 999–1015, 2010.

[5] M. H. Rasoulifard, S. M. M. Doust Mohammadi, A. Heidari, and G. H. Shahverdizadeh, "Photocatalytic degradation of acid red 14 from contaminated water using immobilized TiO_2 nanoparticles on glass beads activated by UV/peroxydisulfate," *Desalination and Water Treatment*.

[6] B. Esen, T. Yumak, A. Sinağ, and T. Yildiz, "Investigation of photocatalytic effect of SnO_2 nanoparticles synthesized by hydrothermal method on the decolorization of two organic dyes," *Photochemistry and Photobiology*, vol. 87, no. 2, pp. 267–274, 2011.

[7] J. C. Colmenares and R. Luque, "Heterogeneous photocatalytic nanomaterials: prospects and challenges in selective transformations of biomass-derived compounds," *Chemical Society Reviews*, vol. 43, no. 3, pp. 765–778, 2014.

[8] X. Chen and S. S. Mao, "Titanium dioxide nanomaterials: synthesis, properties, modifications and applications," *Chemical Reviews*, vol. 107, no. 7, pp. 2891–2959, 2007.

[9] Z. Liu, Y. Wang, W. Chu, Z. Li, and C. Ge, "Characteristics of doped TiO_2 photocatalysts for the degradation of methylene blue waste water under visible light," *Journal of Alloys and Compounds*, vol. 501, no. 1, pp. 54–59, 2010.

[10] F. E. Oropeza, B. Davies, R. G. Palgrave, and R. G. Egdell, "Electronic basis of visible region activity in high area Sn-doped rutile TiO_2 photocatalysts," *Physical Chemistry Chemical Physics*, vol. 13, no. 17, pp. 7882–7891, 2011.

[11] X. Zhang, G. Zhou, H. Zhang, C. Wu, and H. Song, "Characterization and activity of visible light-driven TiO_2 photocatalysts co-doped with nitrogen and lanthanum," *Transition Metal Chemistry*, vol. 36, no. 2, pp. 217–222, 2011.

[12] M. Habib, M. Shahadat, N. Bahadur, I. Ismail, and A. Mahmood, "Synthesis and characterization of ZnO-TiO_2 nanocomposites and their application as photocatalysts," *International Nano Letters*, vol. 3, no. 1, pp. 1–8, 2013.

[13] A. I. Martínez, D. R. Acosta, and G. Cedillo, "Effect of SnO_2 on the photocatalytical properties of TiO_2 films," *Thin Solid Films*, vol. 490, no. 2, pp. 118–123, 2005.

[14] J. Liqiang, F. Honggang, W. Baiqi et al., "Effects of Sn dopant on the photoinduced charge property and photocatalytic activity of TiO_2 nanoparticles," *Applied Catalysis B*, vol. 62, no. 3-4, pp. 282–291, 2006.

[15] C. Xiong and K. J. Balkus Jr., "Mesoporous molecular sieve derived TiO_2 nanofibers doped with SnO_2," *Journal of Physical Chemistry C*, vol. 111, no. 28, pp. 10359–10367, 2007.

[16] M. F. Abdel-Messih, M. A. Ahmed, and A. S. El-Sayed, "Photocatalytic decolorization of Rhodamine B dye using novel mesoporous SnO_2-TiO_2 nano mixed oxides prepared by sol-gel method," *Journal of Photochemistry and Photobiology A*, vol. 260, pp. 1–8, 2013.

[17] J. Du, G. Zhao, H. Pang, Y. Qian, H. Liu, and D. J. Kang, "A template method for synthesis of porous Sn-doped TiO_2 monolith and its enhanced photocatalytic activity," *Materials Letters*, vol. 93, pp. 419–422, 2013.

[18] X.-D. Wang, P. Dong, and G.-Y. Yi, "Evaporation self-assembly method to fabricate high-quality polystyrene microsphere colloid crystal," *Acta Physica Sinica*, vol. 55, no. 4, pp. 2092–2098, 2006.

[19] X.-D. Wang, G.-Y. Yi, and Y. Liu, "Preparation of Al_2O_3 catalytic material with run-through-macropore network structure," *Chemical Journal of Chinese Universities*, vol. 30, no. 2, pp. 349–354, 2009.

Research Article

Sonochemical Synthesis, Characterization, and Photocatalytic Activity of N-Doped TiO$_2$ Nanocrystals with Mesoporous Structure

Tiekun Jia,[1] Fang Fu,[1] Junwei Zhao,[1] Jian Chen,[1] Xiaofeng Wang,[1] Zhenghua Fan,[1] Lijun Cui,[1] and Fancheng Meng[2]

[1] *Department of Materials Science and Engineering, Luoyang Institute of Science and Technology, Luoyang 471023, China*
[2] *School of Materials Science and Engineering, Chongqing University of Technology, Chongqing 400050, China*

Correspondence should be addressed to Tiekun Jia; tiekunjia@126.com

N-Doped TiO$_2$ nanocrystals were synthesized via a simple sonochemical route, using titanium tetrachloride, aqueous ammonia, and urea as starting materials. The as-synthesized samples were characterized by X-ray diffraction (XRD), field emission scanning electron microscopy (FESEM) equipped with an energy dispersion X-ray spectrometer (EDS), transmission electron microscopy (TEM), UV-vis diffuse reflection spectroscopy, Raman spectroscopy, and nitrogen adsorption-desorption isotherms. The results of TEM and nitrogen adsorption-desorption showed that the average size and specific surface area of the as-synthesized nanocrystals are 10 nm and 107.2 m^2/g, respectively. Raman spectral characterization combined with the results of XRD and EDS revealed that N dopant ions were successfully doped into TiO$_2$. Compared with pure TiO$_2$, the adsorption band edge of N-doped TiO$_2$ samples exhibited an obvious red shift to visible region. The photocatalytic activities were evaluated by the degradation of Rhodamine B (RhB) under visible light, and the results showed that the N-doped TiO$_2$ sample synthesized by an optimal amount of urea exhibited excellent photocatalytic activity due to its special mesoporous structure and the incorporation of nitrogen dopant ions.

1. Introduction

Titanium dioxide (TiO$_2$) has attracted increasing attention for its unique physicochemical properties and wide applications in photocatalysts [1–3], lithium batteries [4], gas sensors [5], and solar cells [6, 7]. Among these applications, TiO$_2$ has been known as the most efficient photocatalysts due to its strong oxidizing power, cost effectiveness, and long-time stability against photocorrosion and chemical photocorrosion. Up to now, it has found potential application in self-cleaning coating, air purification, water purification, and water sterilization. However, pure TiO$_2$ has a wide band gap (3.2 eV) and only exhibits photocatalytic properties in the ultraviolet (UV) range (<385 nm). Furthermore, only 5% of the total irradiated natural sunlight is utilized to generate photosensitization [8]. Therefore, it is urgent to modify TiO$_2$ to gain the visible-light driven photocatalysts for utilizing solar energy efficiently.

Numerous efforts have been directed towards the modification of TiO$_2$ by the incorporation of metal and nonmetal dopant ions in order to improve the photocatalytic activity under visible illumination [9–14]. Compared with metal ions doping, nonmetal ions doping is environmentally friendly, which has less negative effect on the environment and ecosystem. Consulting the previous literatures [10–14], doping TiO$_2$ with nitrogen is one of the most effective means of narrowing the band gap and thus expands the light response range to visible light region. Surmacki et al. prepared nitrogen doped TiO$_2$ powders by an electron beam irradiation method [10]. Chen et al. synthesized nitrogen doped TiO$_2$ through a heat treatment in ammonia atmosphere route [11]. Zhou et al. proposed a hydrothermal route assisted by ultrasonic irradiation to synthesize nitrogen doped TiO$_2$ nanocrystals, using ethylenediamine, ethylene oxide/propylene oxide block copolymer (F127), and TiCl$_4$ as raw materials [12]. Qian et al.

proposed a sol-gel route for the synthesis of nitrogen doped TiO_2 nanoparticles, using tetrabutyl titanate (TBT) and urea as starting materials [13]. All the above-mentioned approaches have been proven to be impressive and effective; however, there exist some disadvantages and challenges in the synthetic process as follows. The first is that the conventional approaches need some special instruments, harsh conditions, and/or relatively toxic starting materials hazardous to environment. The second challenge is the phase purity and the yields of nitrogen-doped TiO_2 nanocrystals. The third is high specific surface area which is critical for the enhancement of photocatalytic activity of nitrogen-doped TiO_2 nanocrystals. Therefore, a simple and environment friendly approach is strongly desirable for the synthesis of nitrogen-doped TiO_2 nanocrystals with large scale.

In this paper, we reported the preparation of N-doped TiO_2 nanocrystals with mesoporous structure via a fast sonochemical route followed by calcination, using titanium tetrachloride, aqueous ammonia, and urea as starting materials. A series of measurements, including XRD, SEM, TEM, BET, and Raman spectrum, were performed to characterize the prepared N-doped TiO_2 samples. The photocatalytic activities of the as-obtained samples were evaluated by the degradation of RhB under visible-light irradiation.

2. Experimental Details

2.1. Preparation of N-Doped TiO_2.
All the reagents were used as received without purification. In a typical procedure, 7.5 mL $NH_3·H_2O$ (28 wt%) was added into 60 mL deionized water; then a certain amount of urea was added into the above solution under magnetic stirring to obtain homogeneous solution (labeled as solution A). 10 mL $TiCl_4$ was mixed with 10 mL glycol and 40 mL deionized water under magnetic stirring to obtain homogenous solution (labeled as solution B). Solution A was dropped into solution B under constant magnetic stirring. The pH value of the obtained solution was adjusted to be 4.3 by the addition of diluted H_2SO_4 (1 M). After stirring for 30 min, the above solution was irradiated by the 40 kHz ultrasonic wave at the power of 100% (240 W) for 30 min. The finial suspended solution was aged at the room temperature for 6 h. The products were centrifuged and washed with distilled water and ethanol for several times, followed by drying in a vacuum oven at 80°C for 10 h. The dried products were crushed to obtain fine powders and further calcined at 500°C for 2 h to obtain the catalysts with a heat rate of 2°C/min. For the comparison, undoped TiO_2 was prepared according to the similar procedure, using $NH_3·H_2O$ as precipitation agent in the absence of urea.

2.2. Characterization.
XRD pattern patterns were obtained on a Bruker D8 Advance X-ray diffractometer equipped with Cu Kα radiation (λ = 0.15406 nm) at 40 kV and 40 mA in a scanning range of 10°–70°. FESEM images were observed by a Hitachi S-4800 field emission scanning electron microscope equipped with an energy dispersion X-ray spectrometer (EDS). TEM images were recorded on a Philips Tecnai G20 microscope, operated at an acceleration voltage of 200 kV.
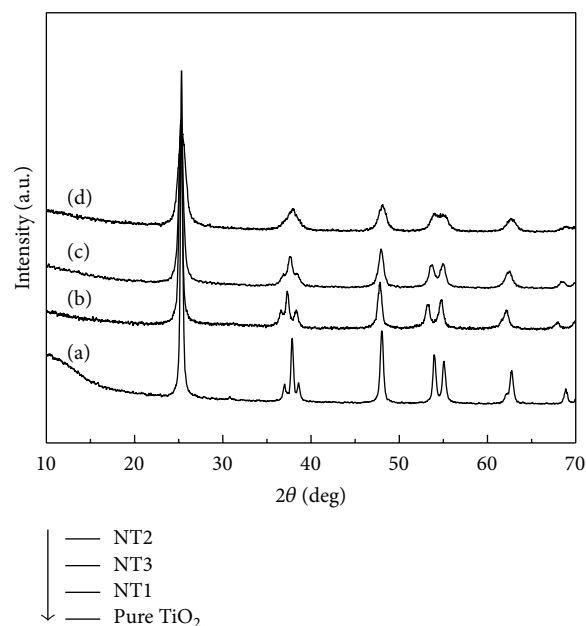
Figure 1: XRD patterns of the as-obtained samples synthesized under different conditions: (a) pure TiO_2; (b) NT1; (c) NT3; (d) NT2.

UV-vis diffuse reflectance spectra were recorded by a UV-vis spectrophotometer (TU 1901, Puxi) with $BaSO_4$ as reference. Raman spectra were recorded by using Renishaw inVia spectrometer at the room temperature, and the 514 nm line of an Ar^+ laser was used as the excitation source. The nitrogen adsorption and desorption isotherms at 77 K were measured using a Quantachrome NOVA 2000e absorption analyzer after samples were vacuum-dried at 473 K overnight.

2.3. Photocatalytic Experiments.
The photocatalytic activity was evaluated by the decolorization of RhB aqueous solution under visible light irradiation. As reported in our previous work [15, 16], 30 mL RhB aqueous solution with a concentration of $1.0 × 10^{-5}$ M was added into the dish with 0.1 g prepared catalyst. A 150 W halogen lamp was used as light source to trigger the photocatalytic reaction. A glass attenuation slice (70%) and a 420 nm cut-off quartz optical filter were placed in the front of the lamp. The distance between the lamp and the dish coated by the catalysts was 15 cm. Prior to irradiation, an adsorption-desorption equilibrium was demanded to reach among the catalyst, RhB, and water in the dark. After irradiating for a certain time, the reacted solution was filtrated to measure the concentration variation of RhB by recording the variation of the intensity of absorption peak centered at 554 nm using an UV-visible spectrophotometer (TU1901, Puxi, China). Consulting the literatures [17, 18], the photodegradation of efficiency of RhB was evaluated by C/C_0, where C is concentration of the RhB solution at reaction time t and C_0 is the adsorption/desorption equilibrium concentration of RhB solution (at reaction time 0).

3. Results and Discussion

3.1. Phase and Morphology. XRD patterns of the as-obtained samples synthesized under different conditions are shown in Figure 1. Herein, the N-doped TiO_2 samples synthesized with different molar ratios of urea to $TiCl_4$ of 1, 3, and 5 are labeled as NT1, NT2, and NT3, respectively. From Figure 1, it can be found that the XRD patterns of the pure and N-doped TiO_2 samples exhibit the same diffraction peaks at 2θ of 25.3°, 37.0°, 37.8°, 38.3°, 48.1°, 53.5°, 55.1°, 62.5°, and 68.9°. All the characteristic diffraction peaks are assigned to the anatase TiO_2 with lattice parameters comparable to the standard values (JCPDS, number 84-1285). Furthermore, it is noteworthy to be mentioned that the diffraction peaks of N-doped TiO_2 samples have no change with the increase of the dosage of urea. However, compared with those of pure TiO_2 samples, the diffraction peaks of N-doped TiO_2 samples tended to become slightly broader and the relative intensity decreased, revealing that the crystal size of N-doped TiO_2 samples decreased due to the incorporation of nitrogen ions.

Figure 2 shows the FESEM image and its EDS mapping of the NT2 sample. As seen in the typical FESEM image (Figure 2(a)), the as-prepared NT2 sample is composed of a large scale of nanoparticles. O-mapping, N-mapping, and Ti-mapping are shown in Figures 2(b), 2(c), and 2(d), respectively, revealing that as-prepared NT2 sample consists of O, N, and Ti elements. The microstructure of as-prepared NT2 sample was investigated with transmission electron microscopy (TEM) and high resolution transmission electron microscopy (HRTEM). Figure 3(a) is the TEM image with its SAED pattern inset. Figure 3(b) is the HRTEM image of the as-prepared NT2 sample. It is clearly observed from Figure 3(a) that the average size of the nanocrystal is about 10 nm. Additionally, the Deby rings shown in the inset of Figure 3(a) suggest a sequence of diffraction rings consistent with what is expected for anatase N-doped TiO_2 as the nanocrystal of the mesoporous sample. As shown in Figure 3(b), the average space between adjacent lattices is 0.35 nm, which is assigned to be the (101) planes of anatase TiO_2.

3.2. BET Surface Area and Pore Volume. Nitrogen adsorption and desorption were used to determine the specific surface area, pore volume, and pore size of the sample. Figure 4 shows the nitrogen adsorption-desorption isotherm and its pore size distribution of the obtained NT2 sample. From Figure 4, it can be concluded that the Barrett-Joyner-Halenda (BJH) pore size distribution and nitrogen adsorption-desorption isotherm correspond to type IV isotherm. As shown in Figure 4(a), the sharp decline in the desorption curve occurred, suggesting that the NT2 sample was mesoporous in nature. The specific surface area estimated by Brunauer-Emmett-Teller method is 107.2 m^2/g. Furthermore, some macropores were also observed in the BJH pore size distribution curve, which perhaps resulted from the ultrasound-induced aggregation effect [19]. Additionally, the nitrogen adsorption-desorption isotherms and pore size distribution curves of NT2 sample were similar to those of NT1 and NT3 samples and no obvious differences were observed. Therefore, the other two curves of the NT1 and NT3 samples were not presented in this paper.

3.3. Raman Spectra and UV-Vis Spectra. Raman spectra were employed to further investigate the phase structure of pure TiO_2 and N-doped TiO_2 samples. Figure 5 shows Raman spectra of pure TiO_2 and NT2 samples. It can be observed from Figure 5 that peaks centering at 145 cm^{-1} (E_g, very strong), 197 cm^{-1} (E_g, weak), 401 cm^{-1} (B_{1g}, medium), 519 cm^{-1} ($A_{1g} + B_{1g}$, medium), and 637 cm^{-1} (E_g, medium) are present, corresponding to the vibrations of the anatase lattice [20], which is consistent with the result of XRD patterns. Additionally, compared with those of the pure TiO_2 sample, the intensity of the peaks of NT2 sample was enhanced in this study, which was in agreement with the previous literature [10, 20].

Figure 6 shows the UV-vis absorbance spectra of pure TiO_2, NT1, NT2, and NT3 samples. Compared with pure TiO_2, the adsorption band edge of N-doped TiO_2 samples extends to the visible region. Additionally, it can also be seen that, with the amounts of urea increasing, the adsorption edge of the N doped TiO_2 samples shifts to high wavelength region firstly when the urea : Ti^{4+} molar ratio reaches 3 : 1 and then shifts to low wavelength region when the urea : Ti^{4+} molar ratio reaches 5 : 1 conversely, revealing that the band gap of NT2 sample is smaller than those of NT1 and NT3 samples.

3.4. Photocatalytic Activity. Figure 7 presents the variations of absorbance spectra of aqueous RhB in the presence of pure TiO_2, NT1, NT2, and NT3 samples at different periods of time under visible light irradiation. It is clearly observed from Figure 7(a) that the intensity of the characteristic adsorption peak of RhB at about 554 nm decreased with the irradiation time in the degradation process. Meanwhile, the color of the suspension faded away gradually with the irradiation time prolonging in the experiment. The percentage degradation of RhB aqueous solution induced by NT2 sample was about 94% when the irradiation time reached 60 min. The photocatalytic performance of different photocatalysts with otherwise identical conditions under visible light irradiation is shown in Figure 7(b). Blank test (RhB without any catalyst) exhibited little photolysis. Meanwhile, the variation of the concentration of RhB with the catalysts in the dark was unobvious, revealing that the adsorption of RhB on the as-prepared photocatalysts was negligible after the adsorption-desorption equilibrium was reached. Furthermore, it was also observable that pure TiO_2 and N-doped TiO_2 samples had different photocatalytic activity rates, and the order was as follows: NT2 > NT3 > NT1 > pure TiO_2. Accordingly, it comes to a conclusion that the NT2 sample had high photocatalytic efficiency. The reason could be explained as follows. It is well known that the crystallite phase, crystallite size, surface area, and porosity have a significant effect on the photocatalytic activity of TiO_2-based photocatalysts. In this paper, the most important cause for the enhancement of the photocatalytic activity is the adsorption shift to the visible light region due to the incorporation of nitrogen ions, which leads to the improvement of interfacial charge transfer and the
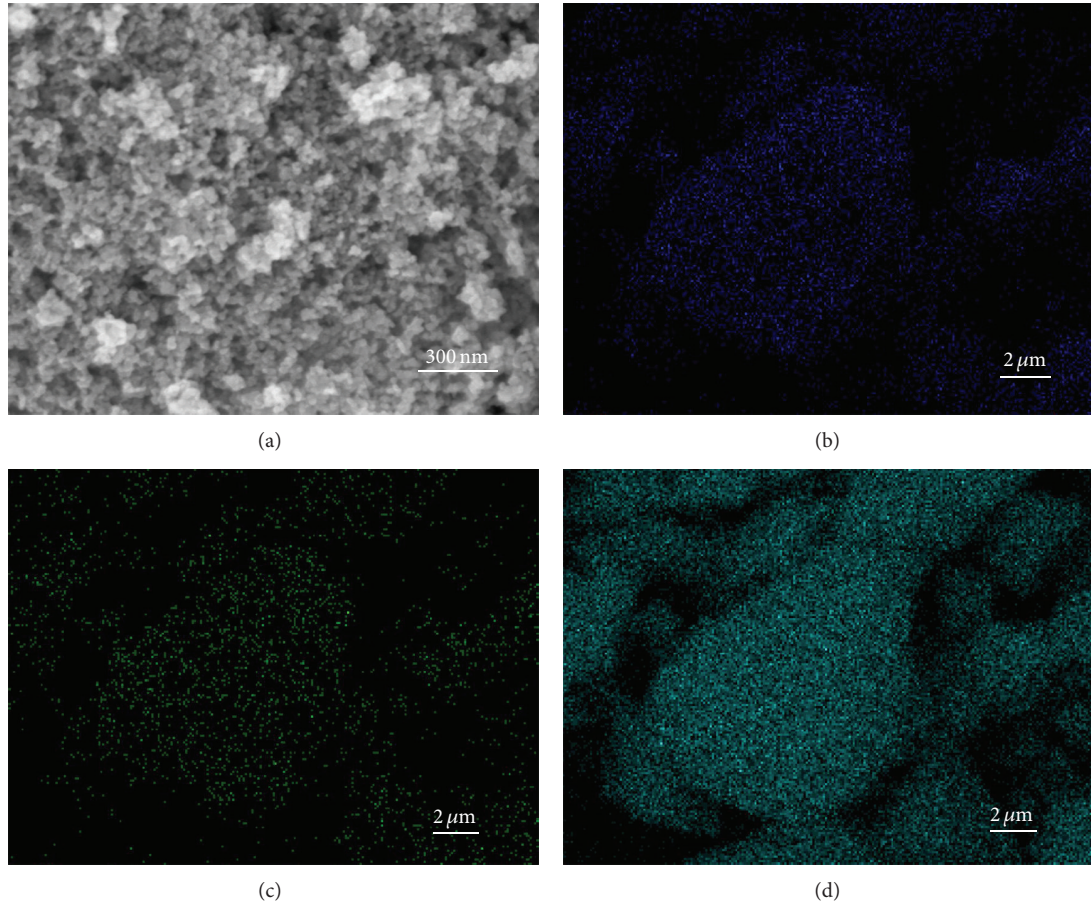
FIGURE 2: FESEM image and EDS mapping of the NT2 sample: (a) the panoramic FESEM image; (b) O-mapping; (c) N-mapping; (d) Ti-mapping.
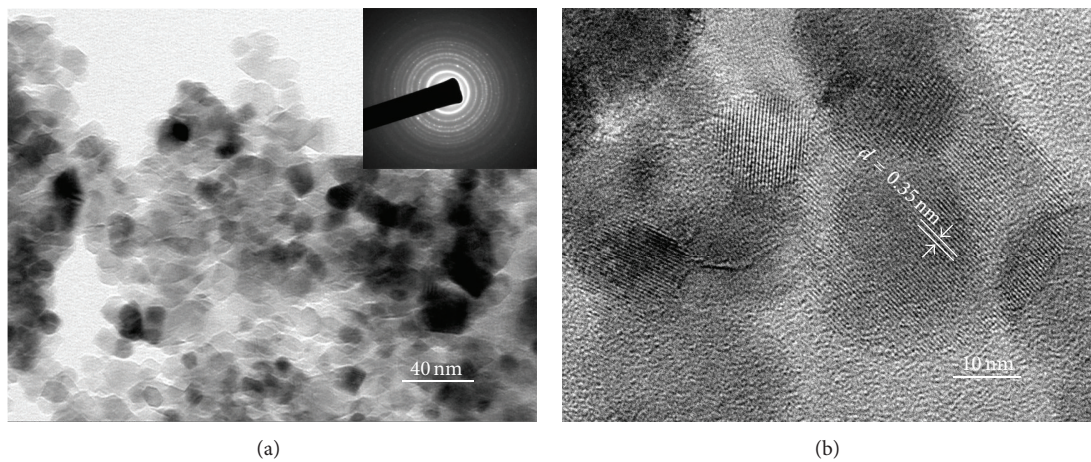
FIGURE 3: (a) TEM image with its SAED pattern inset and (b) HRTEM image of the NT2 sample.

inhibition of charge recombination when the amount of urea is relatively low. Excessive nitrogen ions in doped TiO_2 samples may act as a recombination center, leading to the deterioration of the photocatalytic activity, when the urea : Ti^{4+} molar ratio reaches 5 : 1. Based on the above

analysis, the optimal ratio of N/Ti^{4+} is crucial for the improvement of the photocatalytic activity. Additionally, the NT2 sample has high specific surface area and produces numerous surface reaction sites due to its mesoporous structure. Furthermore, the small grain size results in a shorter

(a)

(b)
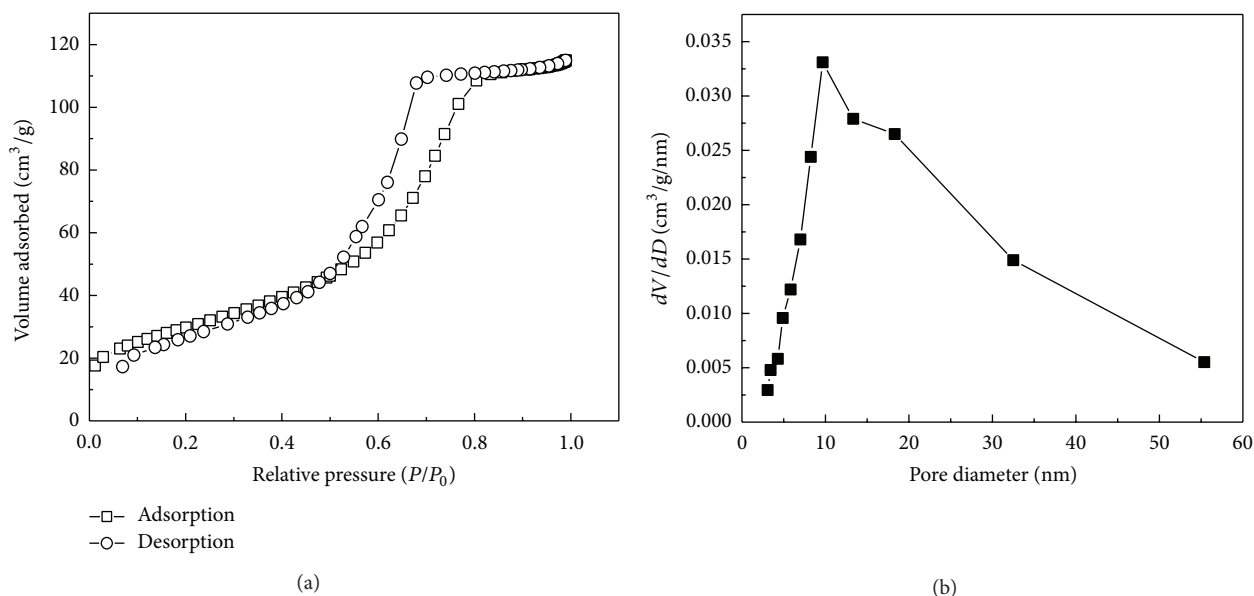
FIGURE 4: (a) The nitrogen adsorption-desorption isotherm and (b) the corresponding pore size distribution of the NT2 sample.
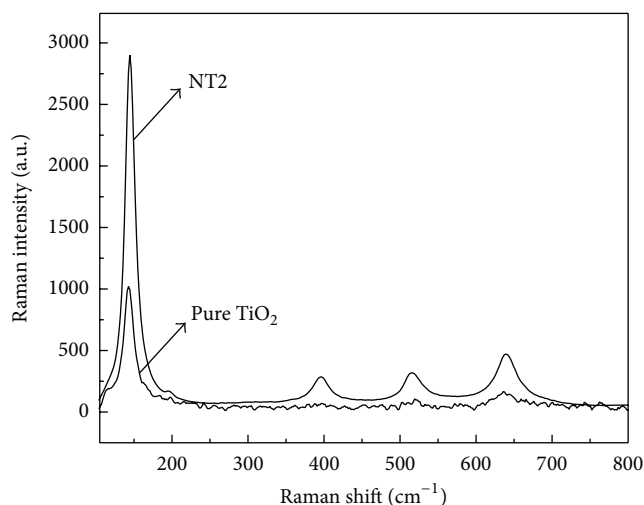
FIGURE 5: Raman spectra of the pure TiO_2 and NT2 sample.

FIGURE 6: UV-vis absorbance spectra of pure TiO_2, NT1, NT2, and NT3 samples.

distance for photoinduced electrons and holes to transfer to reaction sites, which is beneficial for the improvement for photocatalytic activity. That is why the NT2 sample excels the NT1, NT3, and pure TiO_2 samples in the degradation of RhB aqueous solution.

4. Conclusions

In summary, N-doped TiO_2 nanocrystals were successfully prepared via a simple sonochemical route. The N-doped TiO_2 sample with the size of about 10 nm has higher specific surface area with mesoporous structure. The investigation of the photocatalytic activity revealed that N-doped TiO_2 nanocrystals have excellent photocatalytic activity, which was attributed to the dopant ions induced elevated visible light

absorption and its special mesoporous structure. Moreover, our route for synthesizing N-doped TiO_2 nanocrystals is environmentally friendly with the advantages of low cost, simple processing, and easy large-scale production. This synthetic route may be scaled up for industries application.

Conflict of Interests

The authors declared that they do not have a direct financial relation with the commercial identities mentioned in this

(a)

(b)
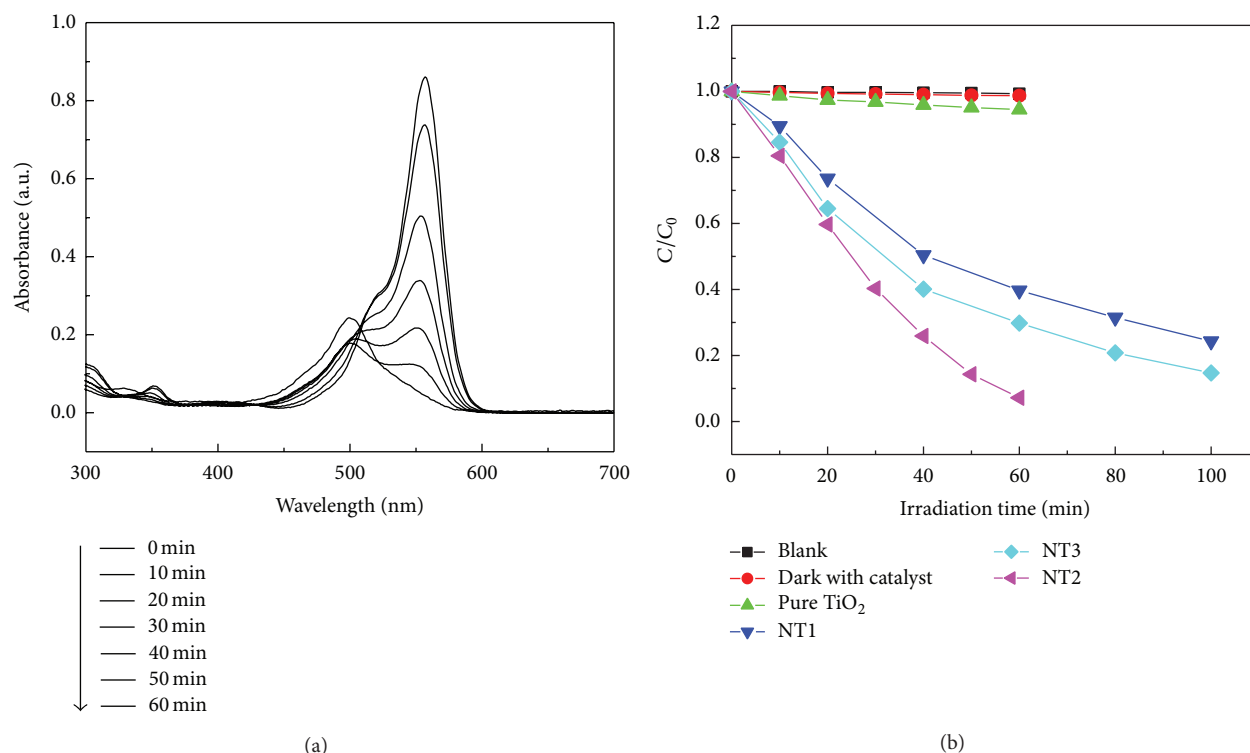
FIGURE 7: (a) The variations of absorbance spectra of aqueous RhB in the presence of the NT2 sample at different periods of time under visible light irradiation; (b) the comparisons of photocatalytic degradation activity of different photocatalysts, including pure TiO_2, NT1, NT2, and NT3 samples.

paper that might lead to any conflict of interests for any of the authors.

Acknowledgments

References

[1] M. Kitano, M. Matsuoka, M. Ueshima, and M. Anpo, "Recent developments in titanium oxide-based photocatalysts," *Applied Catalysis A*, vol. 325, no. 1, pp. 1–14, 2007.

[2] Z. Zou, J. Ye, K. Sayama, and H. Arakawa, "Direct splitting of water under visible light irradiation with an oxide semiconductor photocatalyst," *Nature*, vol. 414, no. 6864, pp. 625–627, 2001.

[3] H.-J. Oh, J.-H. Lee, Y.-J. Kim, S.-J. Suh, J.-H. Lee, and C.-S. Chi, "Synthesis of effective titania nanotubes for wastewater purification," *Applied Catalysis B*, vol. 84, no. 1-2, pp. 142–147, 2008.

[4] G. Armstrong, A. R. Armstrong, P. G. Bruce, P. Reale, and B. Scrosati, "$TiO_2(B)$ nanowires as an improved anode material for lithium-ion batteries containing $LiFePO_4$ or $LiNi_{0.5}Mn_{1.5}O_4$ cathodes and a polymer electrolyte," *Advanced Materials*, vol. 18, no. 19, pp. 2597–2600, 2006.

[5] G. Wang, Q. Wang, W. Lu, and J. Li, "Photoelectrochemical study on charge transfer properties of TiO_2-B nanowires with an application as humidity sensors," *The Journal of Physical Chemistry B*, vol. 110, no. 43, pp. 22029–22034, 2006.

[6] P. Docampo, S. Guldin, U. Steiner, and H. J. Snaith, "Charge transport limitations in self-assembled TiO_2 photoanodes for dye-sensitized solar cells," *The Journal of Physical Chemistry Letters*, vol. 4, no. 5, pp. 698–703, 2013.

[7] H. Nishikiori, Y. Uesugi, R. A. Setiawan, T. Fujii, W. Qian, and M. A. E. Sayed, "Photoelectric conversion properties of dye-sensitized solar cells using dye-dispersing titania," *The Journal of Physical Chemistry C*, vol. 116, no. 7, pp. 4848–4854, 2012.

[8] H. Tada, M. Fujishima, and H. Kobayashi, "Photodeposition of metal sulfide quantum dots on titanium(IV) dioxide and the applications to solar energy conversion," *Chemical Society Reviews*, vol. 40, no. 7, pp. 4232–4243, 2011.

[9] Y.-C. Nah, I. Paramasivam, and P. Schmuki, "Doped TiO_2 and TiO_2 nanotubes: synthesis and applications," *ChemPhysChem*, vol. 11, no. 13, pp. 2698–2713, 2010.

[10] J. Surmacki, B. Wroński, M. S. Nicze, and H. Abramczyk, "Raman spectroscopy of visible-light photocatalyst—nitrogen-doped titanium dioxide generated by irradiation with electron beam," *Chemical Physical Letters*, vol. 566, pp. 54–59, 2013.

[11] H. Chen, A. Nambu, W. Wen et al., "Reaction of NH_3 with titania: N-doping of the oxide and TiN formation," *The Journal of Physical Chemistry C*, vol. 111, no. 3, pp. 1366–1372, 2007.

[12] W. Zhou, C. Yu, Q. Fan, L. Wei, J. Chen, and J. Yu, "Ultrasonic fabrication of N-doped TiO_2 nanocrystals with mesoporous structure and enhanced visible light photocatalytic activity," *Chinese Journal of Catalysis*, vol. 34, no. 6, pp. 1250–1255, 2013.

[13] J. J. Qian, G. J. Cui, M. J. Jing, Y. Wang, M. Zhang, and J. J. Yang, "Hydrothermal synthesis of nitrogen-doped titanium dioxide and evaluation of its visible light photocatalytic activity," *International Journal of Photoenergy*, vol. 2012, Article ID 198497, 6 pages, 2012.

[14] J. Zhang, Z. H. Hang, Y. Xu, and F. Y. Kang, "Hydrothermal synthesis of iodine-doped Bi_2WO_6 nanoplates with enhanced visible and ultraviolet-induced photocatalytic activities," *International Journal of Photoenergy*, vol. 2012, Article ID 915386, 12 pages, 2012.

[15] T. K. Jia, W. M. Wang, F. Long, Z. Y. Fu, H. Wang, and Q. J. Zhang, "Synthesis, characterization, and photocatalytic activity of Zn-doped SnO_2 hierarchical architectures assembled by nanocones," *The Journal of Physical Chemistry C*, vol. 113, no. 21, pp. 9071–9077, 2009.

[16] T. K. Jia, W. M. Wang, F. Long, Z. Y. Fu, H. Wang, and Q. J. Zhang, "Fabrication, characterization and photocatalytic activity of La-doped ZnO nanowires," *Journal of Alloys and Compounds*, vol. 484, no. 1-2, pp. 410–415, 2009.

[17] H. Xu, Y. G. Xu, H. M. Li et al., "Synthesis, characterization and photocatalytic property of $AgBr/BiPO_4$ heterojunction photocatalyst," *Dalton Transactions*, vol. 41, no. 12, pp. 3387–3394, 2012.

[18] C. S. Pan and Y. F. Zhu, "Size-controlled synthesis of $BiPO_4$ nanocrystals for enhanced photocatalytic performance," *Journal of Materials Chemistry*, vol. 21, no. 12, pp. 4235–4241, 2011.

[19] C. L. Yu, Q. Shu, C. X. Zhang, Z. P. Xie, and Q. Z. Fan, "A sonochemical route to fabricate the novel porous F, Ce-codoped TiO_2 photocatalyst with efficient photocatalytic performance," *Journal of Porous Materials*, vol. 19, no. 5, pp. 903–911, 2012.

[20] C. Sun, L. Liu, L. Qi et al., "Efficient fabrication of ZrO_2-doped TiO_2 hollow nanospheres with enhanced photocatalytic activity of rhodamine B degradation," *Journal of Colloid and Interface Science*, vol. 364, no. 2, pp. 288–297, 2011.

Research Article

Synthesis and Characterization of Hierarchical Porous α-FeOOH for the Adsorption and Photodegradation of Rhodamine B

Jianliang Cao,[1] Gaojie Li,[1] Yan Wang,[2] Guang Sun,[1] Hari Bala,[1] Xiaodong Wang,[1] and Zhanying Zhang[1]

[1] *Cultivating Base for Key Laboratory of Environment-Friendly Inorganic Materials in University of Henan Province, School of Materials Science and Engineering, Henan Polytechnic University, Jiaozuo, Henan 454000, China*
[2] *School of Safety Science and Engineering, Henan Polytechnic University, Jiaozuo, Henan 454000, China*

Correspondence should be addressed to Jianliang Cao; caojianliang@gmail.com and Yan Wang; yanwang@hpu.edu.cn

Hierarchical porous α-FeOOH nanoparticles were controlled and prepared via a facile polystyrene (PS) microspheres-templated method. The α-Fe$_2$O$_3$ was obtained by the calcination of the as-prepared α-FeOOH. The resulting nanoparticles were characterized by X-ray diffraction analysis (XRD), scanning electron microscopy (SEM), transmission electron microscopy (TEM), and N$_2$-sorption techniques. The adsorption and photodegradation of Rhodamine B performance were evaluated under UV light at room temperature. The results indicated that the photocatalytic activity of the α-FeOOH nanoparticles is superior to α-Fe$_2$O$_3$-200 and α-Fe$_2$O$_3$-300 due to the hierarchically multiporous structure and high surface area. This convenient and low-cost process provides a rational synthesis alternative for the preparation of multiporous materials and the as-synthesis products have great foreground applications in many aspects.

1. Introduction

Textile dyeing is a significant consumer of water and producer of contaminated aqueous waste streams because textile dyeing processes are generally conducted in water-based dyeing baths and the dyeing processes require the addition of colorants and inorganic salts as dyeing promoter or retardant [1]. In a typical dyeing factory, about 0.2–0.5 m^3 of water is needed to produce 1 kg of finished textiles [2]. Moreover, it is well known that some dye wastewater and its products such as aromatic amines are highly carcinogenic [3, 4]. So dye wastewater has become a major problem in the environmental pollution control field [5, 6]. Rhodamine B (RB) is widely used as a colorant in textiles and food stuffs and is also a well-known water tracer fluorescent [7]. It is harmful to human beings and animals and causes irritation of the skin, eyes, and respiratory tract. The carcinogenicity, reproductive and developmental toxicity, neurotoxicity, and chronic toxicity toward humans and animals have been

experimentally proven [8]. The effluents containing dyes and pigments have been paid great attention in recent years since they can cause serious environmental problems. Water pollution containing hazardous mixtures which come from organic and inorganic pollutants had adverse effects on the environment, aquatic life, and human health. Besides this, the demand for an efficient and environmental friendly colour removal technology is also getting more attention the world over. Therefore, it is necessary to employ appropriate catalysts to degrade dyes in aqueous solution.

The removal methods of dyes have been considered in recent studies in the literature. These include physical adsorption, chemical degradation, biological degradation, photodegradation, or the synergic treatments of different methods [9–13]. Recently, much attention has been paid to photocatalytic methods for dye containing sewage decoloration using nanodispersed catalysts TiO$_2$ [14], Fe$_2$O$_3$ [15], ZnO [16, 17], SnO$_2$ [18], and so forth. These methods use light energy to initiate chemical reactions in the presence of

photocatalysts that are mostly semiconductor materials. Heterogeneous photocatalysis using a semiconductor is a new, effective, and rapid technique for the removal of pollutants from water [19]. Among those nanomaterials, metal oxides represent one of the most diverse classes of materials with both fundamental and technological importance. One of the metal oxides which occur ubiquitously in the environment is iron oxides [20, 21]. Especially, compared to other potential photocatalysts, goethite (α-FeOOH) and hematite (α-Fe$_2$O$_3$) are extremely common in soils and sediments at and near the Earth's surface [22].

So far, in order to explore its novel properties and expand its applications, many efforts have been devoted to the synthesis of α-Fe$_2$O$_3$ with different morphologies, including nanoparticles, nanowires, nanobelts, nanorods, and nanotubes [23–27]. It has been demonstrated that the semiconductor-based photocatalytic materials with hollow structures have higher photocatalytic activity due to the special hierarchical morphology and higher specific surface area [28]. Both α-FeOOH and α-Fe$_2$O$_3$ nanocrystallites exhibit unique reactivity at the nanoscale. In the catalytic oxidation of aqueous Mn^{2+}, the rate exhibited by 7 nm α-Fe$_2$O$_3$ nanocrystals is 1 to 2 orders of magnitude faster than that of 37 nm α-Fe$_2$O$_3$ nanocrystals [29]. Zeng et al. [30] studied degradation of RB solution on iron dioxided with various structures under UV light and found that the catalytic performance of the three α-Fe$_2$O$_3$ samples possesses the sequence of nanoflowers > nanorods > naoparticles, which agrees with the sequence that the surface areas of the samples decreased. To date, systematic studies of the impact of particle size and shape on photocatalytic property by iron oxides are still lacking. Over the past decade, template-based processes demonstrate high efficiency for the construction of porous structures. Organic functionalization of porous materials provides a means of tuning the surface properties to control host/guest interactions and the hydrophobicity or hydrophilicity of the surface [31] as well as the mechanical and optical properties. Therefore, hierarchical porous materials (HPM), with interconnected pores of multiple length scales as the structure character, may be more active than other materials in the process of photocatalytic. Template-based processes demonstrate high efficiency for the construction of porous structures. Mesoporous products are always achieved by using the surfactant as soft template [32–35] or the obtained mesoporous materials as hard template [36].

In the present work, we reported the preparation and characterization of hierarchical porous α-FeOOH nanoparticles via a facile polystyrene (PS) microspheres-templated method. These nanosized catalysts were characterized by the techniques such as XRD, SEM, TEM, and N$_2$-sorption. The photocatalytic activities of the as-prepared catalysts were evaluated by the photocatalytic degradation of a model pollutant, RB under UV-light. The crystal structures, morphologies, and optical properties of resulting products were studied. The effect of calcination treatment temperature on the crystal structure and morphology of the final product was also investigated.

2. Experimental Section

2.1. Materials.
Distilled water was used throughout this study. Iron nitrate nonahydrate (Fe(NO$_3$)$_3$·9H$_2$O), ethanol with absolute grade, tetrahydrofuran (THF), acetone, all chemicals used in this study were of analytical grade and were used as received without further purification. Iron nitrate nonahydrate (Fe(NO$_3$)$_3$·9H$_2$O) was purchased from Sinopharm Chemical Reagent Co., Ltd., and others were purchased from Tianjin Dengke Chemical Reagent Co., Ltd. Polystyrene (PS) microspheres were prepared by emulsion polymerization method. In a typical procedure, 150 g deionized water was poured into a 300 mL jacket reactor, which was kept at 85°C until the end of the reaction. Then, 0.075 g sodium styrene sulfonate and 0.0633 g sodium hydrogen carbonate were dissolved in the deionized water. Under constant stirring, 17.50 mL styrene monomer was added to this solution under the nitrogen protection. After 1 h, 0.0833 g potassium persulfate was introduced into the solution. After 18 h polymerization, the monodispersed PS spheres with the diameter of 247 nm were obtained.

2.2. Preparation of α-FeOOH and α-Fe$_2$O$_3$ Nanoparticles.
The α-FeOOH catalyst was prepared by a facile hydrolysis process of Fe(NO$_3$)$_3$·9H$_2$O aqueous solution using the polystyrene spheres as the template. In a typical procedure, 12.12 g Fe(NO$_3$)$_3$·9H$_2$O was dissolved in a mixed solution of 20 mL ethanol and 10 mL distalled water under ultrasound irradiation for 10 min; then 3.56 g PS microspheres was added in the prepared solution under vigorous stirring. After stirring for 30 min, the resulting suspension was transferred into a 150 mL conical flask on the constant temperature magnetic heating stirrer (85-2), heated to 60°C, and kept at the target temperature until a large tawny precipitate appeared. Then, the precipitate was dried at room temperature. The obtained sample was placed in glass soxhlet extractor and PS microspheres were extracted by the mixed solution of THF/acetone (1/1 of v/v) [31] for four days. Finally, the tawny precipitate was dried at 60°C in an oven and the tawny α-FeOOH nanoparticles were obtained. The prepared sample was calcinated by slowly increasing temperature from room temperature to 200°C (300°C) at a ramping rate of 1°C·min^{-1} and kept the target temperature for 3 h. Subsequently, the reactor was cooled to room temperature naturally. The obtained red-brown samples were nominated as α-Fe$_2$O$_3$-200 and α-Fe$_2$O$_3$-300, respectively.

2.3. Analytical Methods.
XRD analysis was performed on a Bruker-AXS D8 advance diffractometer, with CuKα radiation at 40 KV and 25 mA in a scanning range of 10–80° (2θ). The diffraction peaks of the crystalline phase were compared with those of standard compounds reported in the JCPDS Date File. The texture and morphology of the prepared samples were measured by SEM (JEOL JSM-6390LV). TEM analysis was performed on a JEOL JEM-2100 microscope, operating at 200 kV. The sample was dispersed in ethanol, treated with ultrasound for 5 min, and then deposited on a copper grid coated with preformed holey carbon film. N$_2$ adsorption-desorption isotherms were collected at liquid

nitrogen temperature using a Quantachrome NOVA 2000e sorption analyzer. The specific surface areas of the samples were calculated following the multipoint BET (Brunauer-Emmett-Teller) procedure. The pore size distributions were determined from the adsorption branch of the isotherms using the DFT method. Before carrying out the measurement, each sample was degassed at 80°C for more than 6 h.

2.4. Photocatalytic/Adsorption Activity. The photocatalytic activity experiments of the obtained catalysts were performed by the degradation of RB dye under UV light irradiation in the air at room temperature. 0.1 g of the obtained product was placed into water-jacketed reactor of 100 mL of RB aqueous solution (2×10^{-5} mol·L^{-1}). The light source was a 450 W high-pressure mercury lamp (Foshan Electrical and Lighting Co., Ltd.) and the lamp was located 10 cm higher than the solution surrounded by a circulating water tube. The reaction mixture was stirred under UV light irradiation. The mixture sampled at different times was centrifuged for 15 min to discard any sediment. The absorbance of reaction solutions was measured by a TU-1810 UV-Vis spectrophotometer at its characteristic wavelength (λ = 553 nm) [37, 38]. The decomposition rate of Rhodamine B was calculated by the following formula:

$$\text{Decomposition rate} = \frac{A_0 - A}{A_0} \times 100\%, \qquad (1)$$

where A_0 is the absorbance of the RB solution before irradiation and A is the absorbance of RB solution after irradiation.

The adsorption capacity of the catalysts was measured in the similar way to that of photocatalytic activity measurements. The only difference is that the adsorption process was carried out without UV irradiation.

3. Results and Discussion

3.1. Characterization of Nanoparticles

3.1.1. X-Ray Diffraction of α-FeOOH and α-Fe$_2$O$_3$ Samples. X-ray diffraction (XRD) was used for identification of the crystalline phases of the crystallite size. Figure 1 shows the typical XRD patterns of the as-prepared samples. It can be seen clearly from Figure 1(a) that the reflection peaks of as-prepared sample can be perfectly attributed to the standard card of α-FeOOH (JCPDS 29-713) phase. After the calcination of the α-FeOOH precursor at 200°C and 300°C for 3 h, respectively. All the diffraction peaks of the products (Figures 1(b) and 1(c)) can be well indexed to hexagonal α-Fe$_2$O$_3$ (JCPDS 33-0664). No characteristic peaks of impurities were observed, indicating the thorough phase transformation from α-FeOOH to α-Fe$_2$O$_3$. The as-prepared α-FeOOH sample (Figure 1(a)) had a weak crystallization, with the widest and weakest peaks. The enhanced peak sharpness in Figure 1(c) indicates the well crystallization of α-Fe$_2$O$_3$-300 via the heat treatment.
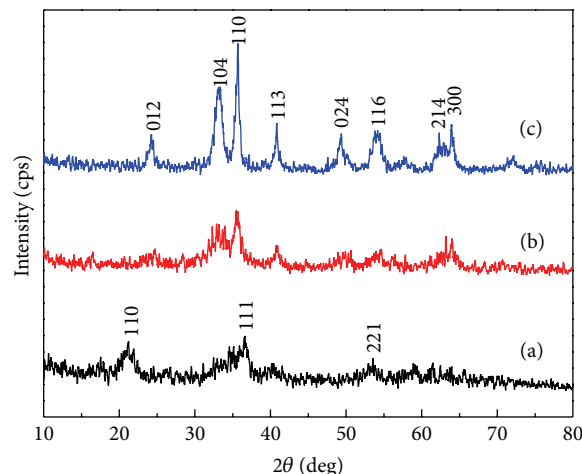

FIGURE 1: XRD patterns of (a) α-FeOOH, (b) α-Fe$_2$O$_3$-200, and (c) α-Fe$_2$O$_3$-300.

3.1.2. SEM Analysis of α-FeOOH and α-Fe$_2$O$_3$-300 Nanoparticles. Figures 2(a), 2(b), and 2(c) display the typical morphologies of the as-prepared α-FeOOH and α-Fe$_2$O$_3$-300 samples, respectively. The SEM images of Figures 2(a) and 2(b) show that the α-FeOOH sample presented a three-dimensional ordered arrangement of interconnected macropores with a mean pore diameter of about 230 nm (especially as shown in the selected area in Figure 2(a)), which was ca. 6–8% smaller than the size of the original PS microspheres template, suggesting significant shrinkage during latex sphere extraction. The pores come from the removal of PS microspheres by extraction with THF/acetone mixture. From Figure 2(c) it can be seen that the result of α-Fe$_2$O$_3$ product basically inherits the porous morphology of α-FeOOH precursor, but most pore walls of the sample were collapsed. The result suggests that the calcination temperature has a negative influence on the macroporous structure. There are a few reports that the physical properties and photochemical performance are affected by the porous structure and the particle size [22, 27, 30, 39, 40]. Since the macroporous structure and large surface area of the samples convey high adsorption abilities of the catalysts. Therefore, we hypothesize that such changes may affect their adsorption properties and catalytic performance.

3.1.3. TEM Analysis of α-FeOOH Nanoparticles. TEM analysis is expected to provide further detailed insights into the pore structure of the as-prepared sample. Figure 3 displays the TEM images of the microstructure of the as-prepared α-FeOOH nanoparticles. The results show that the walls are formed by the agglomeration of the nanoparticles, leading to significant textural mesoporosity within the walls of the structure. As seen in Figure 3(b), the sample consisted of a uniform structure with ordered macropore, which is in good agreement with the results provided by SEM (Figure 2(b)). Figure 3(c) shows that the wall thickness of α-FeOOH is evaluated 8–13 nm and the nanoparticles of the sample are of regular size around 3 nm. Hence, the electron microscopy
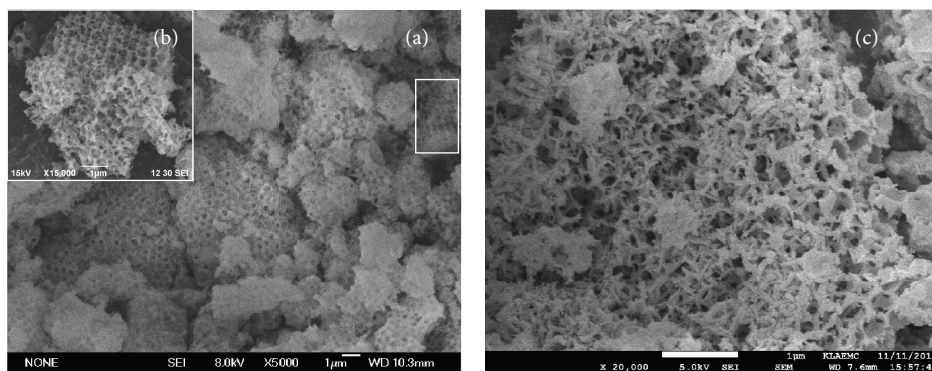
Figure 2: SEM images of α-FeOOH and α-Fe$_2$O$_3$-300 nanoparticles.
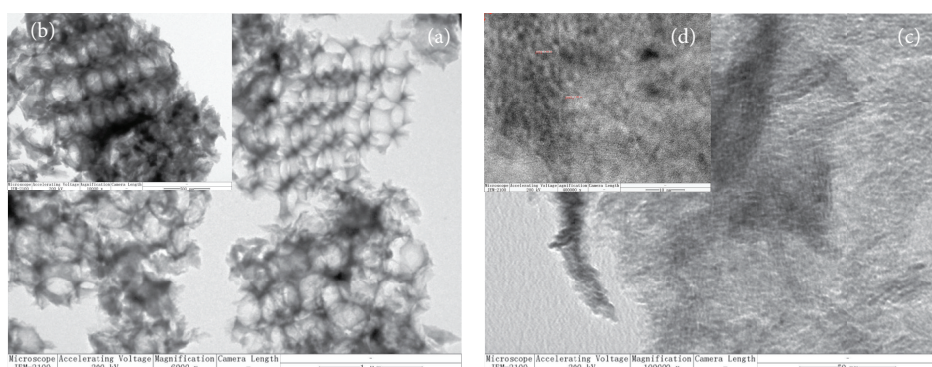

Figure 3: TEM images of α-FeOOH nanoparticles.

observation results demonstrate that the products possess hierarchical porous structure.

3.1.4. N$_2$-Sorption Analysis. Figure 4 depicts nitrogen adsorption-desorption isotherms and the corresponding pore size distributions of α-FeOOH and α-Fe$_2$O$_3$-300 samples. The textural properties of the samples are listed in Table 1. From Figure 4, we can see that the isotherms of the both of samples display type IV, characteristic of mesoporous materials according to the IUPAC. The adsorption isotherm of as-prepared samples exhibits a large increase at the P/P_0 above 0.8, indicating the presence of the hierarchical macroporous structure. The porous structure is believed to facilitate the transporting of reactant molecules and products through the interior space due to the interconnected porous networks and favor the harvesting of exciting light due to enlarged surface area and multiple scattering within the porous framework [41].

The adsorption isotherms of the prepared catalysts exhibit a large increase in the P/P_0 range of 0.2–0.4, which is characteristic of capillary condensation within mesopore. The pore size distribution curves of the α-FeOOH as estimated according to the DFT method from the adsorption branch of the isotherm exhibit one single narrow peak centered at 1.6–2.7 nm (Figure 4(b)), indicating the good homogeneity of the pores. It can be seen that the diameter range of pores located form 1.68 to 18 nm and the mean diameter of pores

is 4.7 nm. This is attributed to the mesopore-sized void space between the crystallites, which are also observed in the TEM images. After calcination at 300°C for 3 h, the surface area of the catalyst decrease from 217 to 151 m^2·g^{-1} (Table 1), accompanied with the increase of the pore volume and pore size. This may due to the collapse of the porous structure during the process of calcination. In general, the surface area varies before and after the calcination (Table 1), indicating that the characteristic structure of α-FeOOH was destroyed, which is well agreement with the SEM results. This illustrates that the calcination treatment has negative impact on the textural properties of the prepared catalysts. The high surface area of the α-FeOOH sample can be useful in the efficiency of the photocatalytic activity as it implies larger contact surfaces exposed to the reagents.

3.2. Photocatalytic/Adsorption Properties Studies. The photocatalytic activities of a series of catalysts were characterized by the degradation test of RB with UV irradiation (Figure 5 and Table 2). Figure 5(a) gives the evolution of RB absorption spectra in the presence of 0.1 g of the photocatalyst per 100 mL of RB solution after irradiated under UV light for different times. From the top plot in Figure 5(a), it can be seen that the RB solution exhibits an obvious absorption peaks at 553 nm. The absorption intensity of RB solution gradually decreases with prolonged irradiation time, indicating the effective photodegradation of RB under the catalysis of porous α-FeOOH
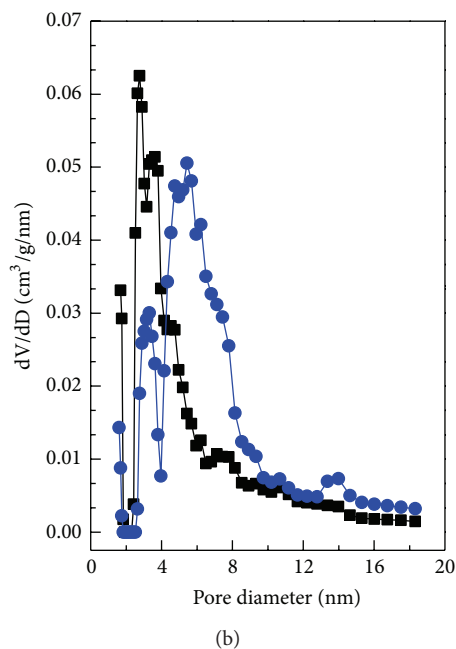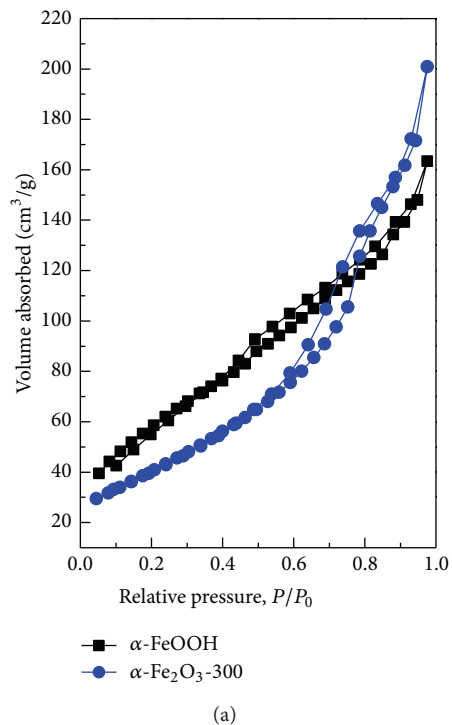
FIGURE 4: (a) N$_2$ adsorption-desorption isotherms and (b) the corresponding pore size distribution curves of α-FeOOH and α-Fe$_2$O$_3$-300.

FIGURE 5: (a) Temporal evolution of RB absorption spectra with an initial concentration C_0 of 2×10^{-5} mol·L^{-1} under UV light with porous α-FeOOH nanoparticles as photocatalyst; (b) removal efficiency of RB after photodecomposition by the different catalysts under UV light.

nanoparticles. As can be seen, with increasing irradiation time for α-FeOOH sample, the major absorbance of RB in the UV regions decreased and the positions of major absorbance were slightly shifted to low wavenumber, suggesting that both chromphore and aromatic rings of RB were destroyed, instead of being simply decolorized by adsorption process [42].

Figure 5(b) shows that the removal efficiency of RB after photodecomposition by the different catalysts under UV light. It can be clearly seen that the order of photocatalytic activity for the degradation of RB was as follows: α-FeOOH > α-Fe$_2$O$_3$-200 > α-Fe$_2$O$_3$-300. After the irradiation of 2 h, the degradation percentage of the RB reaches 92.6% with α-FeOOH as catalyst, while it is only 64.3% and 8% with α-Fe$_2$O$_3$-200 and α-Fe$_2$O$_3$-300 as catalyst, respectively. This may be caused by the higher adsorptive ability of α-FeOOH (see Table 2). It is generally accepted that the catalytic process is mainly related to the adsorption and desorption of organic molecules on the surface of photocatalyst. Since the decrease

TABLE 1: The textural properties of the as-prepared catalysts.

Sample	Surface area^a (m$^2 \cdot$g^{-1})	Pore volume^b (cm$^3 \cdot$g^{-1})	$D_{\text{DFT-ads}}$^{c} (nm)	Mean pore diameter^d (nm)
α-FeOOH	217.02	0.253	2.77	4.7
α-Fe$_2$O$_3$-300	151.63	0.311	3.32	41.0

^{a}Multipoint BET surface area.
^{b}Total pore volume at $P/P_0 = 0.97$.
^{c}Maximum of DFT pore diameter as determined from the adsorption branch.
^{d}Average pore diameter (4V/A).

TABLE 2: Absorption and photodegradation rate of RB by different catalysts within 2 h.

Sample	α-FeOOH	α-Fe$_2$O$_3$-200	α-Fe$_2$O$_3$-300
Absorption (%)	66.6	45.0	5.1
Removal rate of RB (%)	92.6	64.3	8.0

of the absorption intensity might also be caused by adsorption rather than photocatalytic degradation, we carried out the control experiments under dark in the presence of α-FeOOH for 2 h. Generally, the higher absorption capacity is, the better the photocatalytic activity of the prepared catalyst would be (see Table 2 and Figure 5(b)). The control experiments further confirm the highly adsorption performance and a certain degradation activity of the α-FeOOH nanoparticles.

The high surface area of the α-FeOOH sample can provide more unsaturated surface sites exposed to the reactants and the mesopores in the catalyst enable storage of more reactant molecules. The UV absorption measurement suggests that the high adsorption performance and a certain photocatalytic efficiency of the α-FeOOH nanoparticles are closely related to its structure. Thus, the high specific surface area, hierarchical porous structure, and finer absorptive ability are responsible for achieving better photodegradation performance.

4. Conclusions

In summary, hierarchical porous α-FeOOH network structures were successfully constructed using a facile polystyrene (PS) microspheres-templated method. The photocatalytic performances of the as-prepared samples were evaluated in the degradation of RB solution under UV light irradiation. And, the photocatalytic activities exhibit an order of α-FeOOH > α-Fe$_2$O$_3$-200 > α-Fe$_2$O$_3$-300. The observed high photocatalytic activity is related to the structural features of hierarchically multiporous structure, high surface area, and uniform distribution of α-FeOOH particles with nanoscale size. Considering the superior photocatalytic activity, good absorption property, and facile preparation method, the porous α-FeOOH nanoparticles are believed to have potential application in the field of photodegradation of dye in the waste water.

Conflict of Interests

The authors have no conflict of interests in relation with the instrumental companies directly or indirectly.

References

[1] B. Li, Y. Dong, Z. Ding, Y. Xu, and C. Zou, "Renovation and reuse of reactive dyeing effluent by a novel heterogeneous Fenton system based on metal modified PTFE fibrous catalyst/H$_2$O$_2$," *International Journal of Photoenergy*, vol. 2013, Article ID 169493, 10 pages, 2013.

[2] S. Yi, Y. Dong, B. Li, Z. Ding, X. Huang, and L. Xue, "Adsorption and fixation behaviour of CI Reactive Red 195 on cotton woven fabric in a nonionic surfactant Triton X-100 reverse micelle," *Coloration Technology*, vol. 128, no. 4, pp. 306–314, 2012.

[3] P.-H. Chou, S. Matsui, K. Misaki, and T. Matsuda, "Isolation and identification of xenobiotic aryl hydrocarbon receptor ligands in dyeing wastewater," *Environmental Science & Technology*, vol. 41, no. 2, pp. 652–657, 2007.

[4] A. Khalid, M. Arshad, and D. E. Crowley, "Biodegradation potential of pure and mixed bacterial cultures for removal of 4-nitroaniline from textile dye wastewater," *Water Research*, vol. 43, no. 4, pp. 1110–1116, 2009.

[5] W. Chen, W. Lu, Y. Yao, and M. Xu, "Highly efficient decomposition of organic dyes by aqueous-fiber phase transfer and in situ catalytic oxidation using fiber-supported cobalt phthalocyanine," *Environmental Science & Technology*, vol. 41, no. 17, pp. 6240–6245, 2007.

[6] Z. Chen, D. Li, W. Zhang et al., "Photocatalytic degradation of dyes by ZnIn$_2$S$_4$ microspheres under visible light irradiation," *The Journal of Physical Chemistry C*, vol. 113, no. 11, pp. 4433–4440, 2009.

[7] S. D. Richardson, C. S. Willson, and K. A. Rusch, "Use of rhodamine water tracer in the marshland upwelling system," *Groundwater*, vol. 42, no. 5, pp. 678–688, 2004.

[8] D. Kornbrust and T. Barfknecht, "Testing of 24 food, drug, cosmetic, and fabric dyes in the in vitro and the in vivo/in vitro rat hepatocyte primary culture/DNA repair assays," *Environmental Mutagenesis*, vol. 7, no. 1, pp. 101–120, 1985.

[9] M. Constapel, M. Schellenträger, J. M. Marzinkowski, and S. Gäb, "Degradation of reactive dyes in wastewater from the textile industry by ozone: analysis of the products by accurate masses," *Water Research*, vol. 43, no. 3, pp. 733–743, 2009.

[10] S. Eftekhari, A. Habibi-Yangjeh, and Sh. Sohrabnezhad, "Application of AlMCM-41 for competitive adsorption of methylene blue and rhodamine B: thermodynamic and kinetic studies," *Journal of Hazardous Materials*, vol. 178, no. 1–3, pp. 349–355, 2010.

[11] A. B. dos Santos, F. J. Cervantes, and J. B. van Lier, "Review paper on current technologies for decolourisation of textile wastewaters: perspectives for anaerobic biotechnology," *Bioresource Technology*, vol. 98, no. 12, pp. 2369–2385, 2007.

[12] J. M. Monteagudo, A. Durán, and C. López-Almodóvar, "Homogeneus ferrioxalate-assisted solar photo-Fenton degradation of orange II aqueous solutions," *Applied Catalysis B*, vol. 83, no. 1-2, pp. 46–55, 2008.

[13] O. Zahraa, S. Maire, F. Evenou et al., "Treatment of wastewater dyeing agent by photocatalytic process in solar reactor," *International Journal of Photoenergy*, vol. 2006, Article ID 46961, 9 pages, 2006.

[14] O. Sacco, M. Stoller, V. Vaiano, P. Ciambelli, A. Chianese, and D. Sannino, "Photocatalytic degradation of organic dyes under visible light on N-doped TiO_2 photocatalysts," *International Journal of Photoenergy*, vol. 2012, Article ID 626759, 8 pages, 2012.

[15] A. Afkhami and R. Moosavi, "Adsorptive removal of Congo red, a carcinogenic textile dye, from aqueous solutions by maghemite nanoparticles," *Journal of Hazardous Materials*, vol. 174, no. 1–3, pp. 398–403, 2010.

[16] M.-C. Chang, H.-Y. Shu, T.-H. Tseng, and H.-W. Hsu, "Supported zinc oxide photocatalysts for decolorization and mineralization of orange G dye wastewater under UV365 irradiation," *International Journal of Photoenergy*, vol. 2013, Article ID 595031, 12 pages, 2013.

[17] T.-K. Jia, W.-M. Wang, F. Long, Z.-Y. Fu, H. Wang, and Q.-J. Zhang, "Fabrication, characterization and photocatalytic activity of La-doped ZnO nanowires," *Journal of Alloys and Compounds*, vol. 484, no. 1-2, pp. 410–415, 2009.

[18] T.-K. Jia, W.-M. Wang, F. Long, Z.-Y. Fu, H. Wang, and Q.-J. Zhang, "Synthesis, characterization, and photocatalytic activity of Zn-doped SnO_2 hierarchical architectures assembled by nanocones," *The Journal of Physical Chemistry C*, vol. 113, no. 21, pp. 9071–9077, 2009.

[19] X. Chen and S. S. Mao, "Titanium dioxide nanomaterials: synthesis, properties, modifications and applications," *Chemical Reviews*, vol. 107, no. 7, pp. 2891–2959, 2007.

[20] M. F. Hochella Jr., S. K. Lower, P. A. Maurice et al., "Nanominerals, mineral nanoparticles, and earth systems," *Science*, vol. 319, no. 5870, pp. 1631–1635, 2008.

[21] A. Navrotsky, L. Mazeina, and J. Majzlan, "Size-driven structural and thermodynamic complexity in iron oxides," *Science*, vol. 319, no. 5870, pp. 1635–1638, 2008.

[22] X. Zhou, H. Yang, C. Wang et al., "Visible light induced photocatalytic degradation of rhodamine B on one-dimensional iron oxide particles," *The Journal of Physical Chemistry C*, vol. 114, no. 40, pp. 17051–17061, 2010.

[23] E. Esmaeili, M. Salavati-Niasari, F. Mohandes, F. Davar, and H. Seyghalkar, "Modified single-phase hematite nanoparticles via a facile approach for large-scale synthesis," *Chemical Engineering Journal*, vol. 170, no. 1, pp. 278–285, 2011.

[24] L.-P. Zhu, H.-M. Xiao, X.-M. Liu, and S.-Y. Fu, "Template-free synthesis and characterization of novel 3D urchin-like α-Fe_2O_3 superstructures," *Journal of Materials Chemistry*, vol. 16, no. 19, pp. 1794–1797, 2006.

[25] U. Cvelbar, Z. Chen, M. K. Sunkara, and M. Mozetič, "Spontaneous growth of superstructure α-Fe_2O_3 nanowire and nanobelt arrays in reactive oxygen plasma," *Small*, vol. 4, no. 10, pp. 1610–1614, 2008.

[26] J. Chen, L. Xu, W. Li, and X. Gou, "α-Fe_2O_3 nanotubes in gas sensor and lithium-ion battery applications," *Advanced Materials*, vol. 17, no. 5, pp. 582–586, 2005.

[27] C. Wu, P. Yin, X. Zhu, C. OuYang, and Y. Xie, "Synthesis of hematite (α-Fe_2O_3) nanorods: diameter-size and shape effects on their applications in magnetism, lithium ion battery, and gas sensors," *The Journal of Physical Chemistry B*, vol. 110, no. 36, pp. 17806–17812, 2006.

[28] F. Dong, A. Zheng, Y. Sun et al., "One-pot template-free synthesis, growth mechanism and enhanced photocatalytic activity of monodisperse $(BiO)_2CO_3$ hierarchical hollow microspheres self-assembled with single-crystalline nanosheets," *CrystEngComm*, vol. 14, no. 10, pp. 3534–3544, 2012.

[29] A. S. Madden and M. F. Hochella Jr., "A test of geochemical reactivity as a function of mineral size: manganese oxidation promoted by hematite nanoparticles," *Geochimica et Cosmochimica Acta*, vol. 69, no. 2, pp. 389–398, 2005.

[30] S. Zeng, K. Tang, T. Li et al., "Facile route for the fabrication of porous hematite nanoflowers: its synthesis, growth mechanism, application in the lithium ion battery, and magnetic and photocatalytic properties," *The Journal of Physical Chemistry C*, vol. 112, no. 13, pp. 4836–4843, 2008.

[31] R. C. Schroden, M. Al-Daous, S. Sokolov et al., "Hybrid macroporous materials for heavy metal ion adsorption," *Journal of Materials Chemistry*, vol. 12, no. 11, pp. 3261–3267, 2002.

[32] J. Lee, M. C. Orilall, S. C. Warren, M. Kamperman, F. J. Disalvo, and U. Wiesner, "Direct access to thermally stable and highly crystalline mesoporous transition-metal oxides with uniform pores," *Nature Materials*, vol. 7, no. 3, pp. 222–228, 2008.

[33] L.-L. Li, J. Xu, Q. Yuan, Z.-X. Li, W.-G. Song, and C.-H. Yan, "Facile synthesis of macrocellular mesoporous foamlike Ce–Sn mixed oxides with a nanocrystalline framework by using triblock copolymer as the single template," *Small*, vol. 5, no. 23, pp. 2730–2737, 2009.

[34] Q. Yuan, H.-H. Duan, L.-L. Li et al., "Homogeneously dispersed ceria nanocatalyst stabilized with ordered mesoporous alumina," *Advanced Materials*, vol. 22, no. 13, pp. 1475–1478, 2010.

[35] D. Niu, Z. Ma, Y. Li, and J. Shi, "Synthesis of core-shell structured dual-mesoporous silica spheres with tunable pore size and controllable shell thickness," *Journal of the American Chemical Society*, vol. 132, no. 43, pp. 15144–15147, 2010.

[36] K. Brezesinski, J. Haetge, J. Wang et al., "Ordered mesoporous α-Fe_2O_3 (hematite) thin-film electrodes for application in high rate rechargeable lithium batteries," *Small*, vol. 7, no. 3, pp. 407–414, 2011.

[37] E. T. Soares, M. A. Lansarin, and C. C. Moro, "A study of process variables for the photocatalytic degradation of rhodamine B," *Brazilian Journal of Chemical Engineering*, vol. 24, no. 1, pp. 29–36, 2007.

[38] K. Byrappa, A. K. Subramani, S. Ananda, K. M. Lokanatha Rai, R. Dinesh, and M. Yoshimura, "Photocatalytic degradation of rhodamine B dye using hydrothermally synthesized ZnO," *Bulletin of Materials Science*, vol. 29, no. 5, pp. 433–438, 2006.

[39] L. Song and S. Zhang, "Formation of α-Fe$_2$O$_3$/FeOOH nanostructures with various morphologies by a hydrothermal route and their photocatalytic properties," *Colloids and Surfaces A*, vol. 348, no. 1–3, pp. 217–220, 2009.

[40] N. Smirnova, Y. Gnatyuk, A. Eremenko et al., "Photoelectrochemical characterization and photocatalytic properties of mesoporous TiO$_2$/ZrO$_2$ films," *International Journal of Photoenergy*, vol. 2006, Article ID 85469, 6 pages, 2006.

[41] P. Madhusudan, J. Ran, J. Zhang, J. Yu, and G. Liu, "Novel urea assisted hydrothermal synthesis of hierarchical BiVO$_4$/Bi$_2$O$_2$CO$_3$ nanocomposites with enhanced visible-light photocatalytic activity," *Applied Catalysis B*, vol. 110, pp. 286–295, 2011.

[42] M. Hojamberdiev, G. Zhu, A. Eminov, and K. Okada, "Template-free hydrothermal synthesis of hollow α-FeOOH urchin-like spheres and their conversion to α-Fe$_2$O$_3$ under low-temperature thermal treatment in air," *Journal of Cluster Science*, vol. 24, no. 1, pp. 97–106, 2013.

Research Article

Photoelectrocatalytic Degradation of Humic Acids Using Codoped TiO$_2$ Film Electrodes under Visible Light

Xiao Zhou,[1] Yongxin Zheng,[1] Dan Liu,[1] and Shaoqi Zhou[1,2,3,4]

[1] *College of Environment and Energy, South China University of Technology, Guangzhou 510640, China*
[2] *State Key Laboratory of Subtropical Building Science, South China University of Technology, Guangzhou 510641, China*
[3] *Key Laboratory of Environmental Protection and Eco-Remediation of Guangdong Regular Higher Education Institutions,*
South China University of Technology, Guangzhou Higher Education Mega Center, Guangzhou 510006, China
[4] *Guizhou Academy of Sciences, Shanxi Road 1, Guiyang 550001, China*

Correspondence should be addressed to Shaoqi Zhou; fesqzhou@scut.edu.cn

Cu/N codoped TiO$_2$ films on Ti substrates were successfully prepared by electrochemical method with the goal of enhancing the photoelectrocatalytic activity under visible light. The morphology and composition of the Cu/N codoped films were characterized using field emission scanning electron microscopy (FESEM), X-ray diffraction (XRD), energy dispersive X-ray (EDX), and UV-Vis diffusion reflection spectroscopy (UV-Vis DRS). The photocatalytic activities of the Cu/N codoped TiO$_2$ films were evaluated by the degradation of humic acid. The visible light photocatalytic degradation of humic acid (HA) was tested and Cu/N codoped TiO$_2$ films showed the highest degradation efficiency up to 41.5% after 210 minutes of treatment. It showed that Cu^{2+} and NH$_4^+$ codoped TiO$_2$ film significantly improved the photocatalytic efficiency under the visible light. When +5.0 V anodic bias potential and visible light were simultaneously applied, the degradation efficiency of HA over the Cu/N codoped TiO$_2$ films significantly improved to 93.5% after 210 minutes of treatment.

1. Introduction

Humic acid (HA) is the main fraction of the humic substances existing in fresh water sources and creating problems in treatment operations. Consequently, it is the primary target of water treatment process although not considered as a pollutant. The HA is a complex mixture of organic compounds, which is derived from the decomposition of plants and animal material [1–3]. Humic acid has been reported to bring about many negative effects in drinking water, including undesirable color and taste, absorption and concentration of organic pollutants, and biochemical decomposition. Moreover, when water is treated with chlorine for sterilization, humic acid could react with chlorine by a combination of substitution and oxidation mechanisms forming potentially carcinogenic organic compounds [1, 4, 5]; this has been a problem in past drinking water treatment. Increased concern is focused on the potential toxicity of humic acid and its precursors. Hence, the degradation techniques of humic acid need to be established.

In common water treatment processes, the removal of humic acid has been accomplished by physical separation, such as adsorption of activity carbon, precipitation and flocculation, ion exchange [4], and transfer of pollutants from one phase to another or concentrating them in one phase, without actually eliminating them, which is the main disadvantage associated with these techniques. Novel methods such as the Fenton process, ozonation, and electrochemical and photochemical technologies have been developed to decompose pollutants. Titanium dioxide (TiO$_2$) electrodes have been widely utilized as a photocatalytic material technology with applications in many fields such as environmental purification and decomposition of carbonic acid gases and solar cell, especially in the decomposition of recalcitrant organic pollutants [6–10]. In the last decades, it has been demonstrated that titanium dioxide (TiO$_2$) photocatalysis is one of the suitable advanced oxidation processes' (AOPs) techniques for the decomposition of refractory HA because of its excellent photostability, relatively low cost, nontoxicity,

and its ability to photooxidatively destroy most refractory pollutants [11, 12].

However, TiO$_2$ has three major limiting factors. The first is the low separation rate of photoinduced electron-hole pairs. Second, TiO$_2$ has low utilization efficiency of visible light because of its large band gap of 3.2 eV. UV light constitutes only a small fraction (5%) of the solar spectrum [13]. The last causes difficulty in separating suspended TiO$_2$ particles from the water; simultaneously, the water will be contaminated by the TiO$_2$ particles if they are not completely separated from water. These shortcomings hold back the TiO$_2$ application in water treatment. Nevertheless, extending the absorbance of TiO$_2$ to visible light and improving the photocatalytic efficiency of TiO$_2$ have the most important prospects.

For the first and the second problems, in order to reduce the high recombination rate of photoexcited electron-holes and utilize sunlight, a variety of methods, such as metal and nonmetal doping [14, 15], composites with the other semiconductors [16], dye sensitization [17], and surface modification [18], have been extensively applied. Among such methods, metal and nonmetal doping has been demonstrated to be an effective approach, having been widely studied in literature [14]. In particular, much effort has been made to enhance the visible light photoresponse of TiO$_2$ via doping main group elements including carbon, nitrogen, and sulfur [20–22] and transition metal elements such as W^{6+}, Fe^{3+}, Zr^{4+}, V^{5+}, and Mo^{6+} [23–27]. These compounds absorb visible light. The preceding findings are supported by the results of theoretical calculations using full potential linearized augmented plane wave formalism (F-LAPW method). Metal ions doped into the TiO$_2$ crystal lattice create a narrow energy band inside the TiO$_2$ band gap; as a result, photoinduced electrons can be easily activated and the photoresponse wavelength can be expanded to visible region. This can depend on the ion location in the host lattice and characteristics of the metal ions in question [28]. Nonmetal ions doping into the TiO$_2$ lattice can replace some of the oxygen vacancies, reducing the energy band gap and extending photoactive region. It should also be noted that dopants such as N are incorporated as anions and replaced by oxygen in the TiO$_2$ lattice. The N doping not only decreases the band gap, but also hinders the growth of crystalline particles; the resulting small size can facilitate the separation of charge carrier [23].

To solve the third problem, the immobilization of TiO$_2$ on various supports such as glass, ceramics, and zeolite remains one of the prerequisites to obtain an effective catalyst because this is a technological requirement to avoid the separation/filtration step. Different supports and different immobilization techniques for TiO$_2$ photocatalysts including thermal oxidation of titanium, anodic oxidation, and sputtering have been previously investigated. Immobilization of TiO$_2$ onto conducting substrate enables the application of electrochemistry techniques.

A novel method such as anodic oxidation method has been recently developed. The anodic oxidation method is a simple, cost-effective, and straightforward method to prepare highly ordered TiO$_2$ nanofilms on Ti substrate [29, 30], a process which allows the in-situ preparation of TiO$_2$ film

electrodes. In this anodic oxidation process, using a pretreated Ti substrate as an anode and a platinum foil or other materials as the cathode, both units are placed in the electrolyte solution, and then a constant voltage is applied for a determined time. Oxidizing metallic titanium to directly create TiO$_2$ films provides a much stronger adhesion of the oxide to the substrate, a behavior which overcomes adherence problem [31, 32], therefore improving substrate stability of photocatalytic devices in flowing water and reducing resistance to electron transfer and the recombination of photogenerated electron transfer.

Vinodgopal et al. [33] published a paper in 1993 on TiO$_2$ thin film electrode degrading 4-chlorophenol efficiently under UV lamps. Subsequently, an efficient technique named photoelectrocatalysis (PEC) was proposed. In a sole photocatalysis process, the surface area of the catalyst in the film contacting pollutant molecules is reduced after TiO$_2$ powder is transformed to film; consequently, the photocatalytic degradation efficiency over TiO$_2$ film is usually lower than over TiO$_2$ powder. The difference of degradation efficiency between Degussa P25 powders and TiO$_2$ thin film could be 80% under the same degradation conditions [34]. So, to improve the degradation efficiency, photoelectrocatalytic degradation of pollutants has been developed by applying an external bias potential to various TiO$_2$ films [35–37]. The photoelectrocatalytic technique combines both electrolytic and photocatalytic processes. In the PEC process, the applied external potential is the key factor, and the separation of electron-hole pairs (e_{CB}^-/h_{VB}^+) is promoted by electron transfer via the control of an external circuit, significantly improving the performance of photocatalytic (PC) efficiency. The basic process of photocatalysis consists of ejecting an electron from the valence band (VB) to the conduction band (CB) of the TiO$_2$, thereby creating an "h$^+$" hole in the valence band. This is due to the solar irradiation of TiO$_2$ with an energy equal or superior to the band gap (3.2 eV). These charge carriers (e^-/h^+) can migrate to the surface of the catalyst, where they are then available to undergo redox reaction with substrates [38]:

$$TiO_2 + h\nu \longrightarrow e_{CB}^- + h_{VB}^+ \tag{1}$$
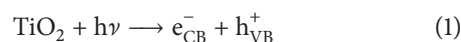
This is followed by the formation of extremely reactive radical OH$^\bullet$ at the TiO$_2$ surface and/or a direct oxidation of the polluting species (R). The redox potential of OH$^\bullet$/H$_2$O is 2.81V. Therefore, pollutants in wastewater can be degraded directly on the surface of the TiO$_2$ or indirectly by reacting with hydroxyl radicals [39]. The photogenerated hole in the valence bond can react with absorbed water molecular to form oxidative species such as OH$^\bullet$ which subsequently attack the pollutant:

$$h_{VB}^+ + H_2O \longrightarrow OH^\bullet + H^+$$
$$h_{VB}^+ + OH^- \longrightarrow OH_{ads}^\bullet \tag{2}$$
$$h_{VB}^+ + R_{ads} \longrightarrow R^+$$
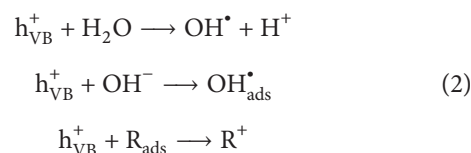
The electrons ejected to the conduction band can either react with electron acceptors such as adsorbed oxygen (O$_2$)
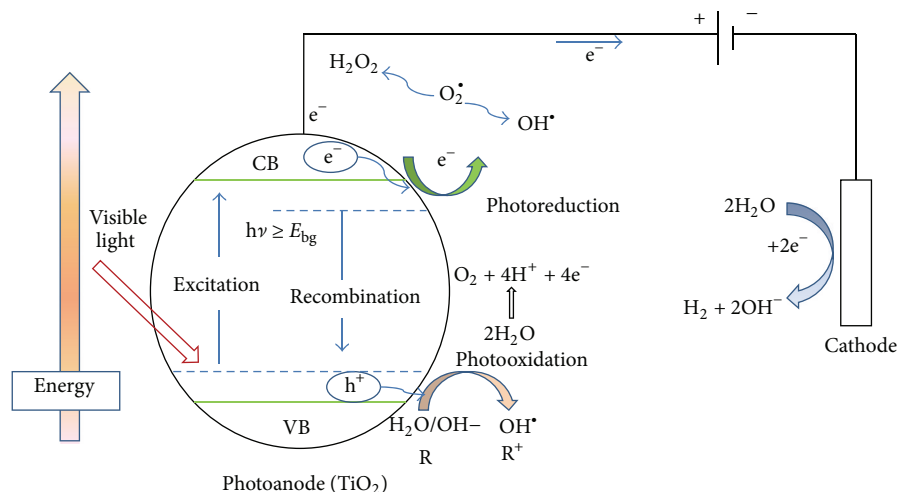
FIGURE 1: Mechanism of photoelectrocatalytic process using TiO_2 photocatalyst and the reactions that occur at the surface.

to form superoxide radicals (3) or react with adsorbed water molecule (H_2O) to form oxidative species such as hydroxyl radicals:

$$e_{CB}^- + O_2 \longrightarrow O_2^{\bullet-} \qquad (3)$$

The photogenerated electrons (e^-) reduce the recombination rate of the photogenerated electron-hole pairs and enhance the photocatalytic activity [40]. The lifetime of the pairs (e_{CB}^-/h_{VB}^+) is a few nanoseconds. Without electron donors or acceptors these electron-hole pairs can recombine to release heat or migrate to the surface of the TiO_2 and react with species that have been adsorbed there:

$$e_{CB}^- + h_{VB}^+ \longrightarrow heat \qquad (4)$$

Figure 1 shows the general mechanism of the photoelectrocatalytic process and the main reaction that occurs at the surface of TiO_2 [41]. According to the literature [41], when a positive bias is applied to the Ti/TiO_2 photoanode, the generated electrons can be transferred into the external circuit instead of the oxygen molecule. As a result, the photogenerated hole or $OH^\bullet$ will be left at the surface of the TiO_2 electrode. Therefore, the rate of photogenerated electron-hole recombination is limited while a possibility exists to improve the efficiency of oxidation at the semiconductor-electrolyte interface.

Whether in the PC or in the PEC process, the degradation rate of refractory pollutants depends on the activity of the titania film electrodes. In recent years, photoelectrocatalytic degradation of organic pollutants has attracted much interest under visible light [42–44].

Therefore, to investigate the effect of various TiO_2 films electrodes, in this work, we successfully prepared Cu/N codoped TiO_2 films by the anodic oxidation process to study the photoelectrocatalytic degradation of humic acid (HA) under visible light illumination. The surface morphology, crystallization, and photoelectrochemical characteristics of the hybrid films were investigated with various techniques, including field emission scanning electron microscopy

(FESEM), energy dispersive X-ray (EDX), X-ray diffraction (XRD), UV-Vis diffusion reflection spectroscopy (UV-Vis DRS), UV-Vis spectroscopy, and voltammetry. The photoelectrocatalytic activity of these samples was evaluated on the basis of the degradation of humic acid (HA) in aqueous solution under visible light irradiation. Using such Cu/N TiO_2 films, the visible light photoelectrocatalytic degradation of HA was also studied in detail by changing the initial concentration affecting the degradation process. The Cu-N TiO_2 samples showed better photocatalytic activity with required degradation of humic acid (HA) than the TiO_2 films in visible light regions.

2. Materials and Methods

2.1. Materials. Titanium sheets (0.2 mm × 50 mm × 50 mm, 99.6% purity) were polished by metallographic abrasive paper and then degreased by sonicating process in acetone, isopropanol, and methanol. After rinsing with water, the materials were air-dried. Graphite electrodes were procured from Guangzhou Jinlong Technology Co., Ltd. Acetone, isopropanol, methanol, HF, HNO_3, $Cu(NO_3)_2$, NH_4Cl, and the abovementioned chemicals and solvents were of analytical grade and used without further purification. Commercial humic acid (CAS no. 308067-45-0) was purchased from Shanghai, China, and was used as received. The chemical components of HA indicated that the H/C atomic ratio and the O/C atomic ratio were 0.956 and 0.412, respectively. HA was dissolved in 0.1 M sodium hydroxide solution (NaOH, CAS no. 1310-73-2) and then separated by 0.45 μm membrane. The filtrate was diluted to a desired concentration ranging from 10 to 60 mg/L. Water used in all experiments was purified using a Milli-Q Plus 185 water purification system (Millipore, Bedford, MA) with a resistivity higher than 18 MΩ cm.

2.2. Preparation of TiO_2/Ti Electrode. The anodic oxidation was accomplished with a 33 V DC-power source using titanium sheet as anode and graphite as cathode. The distance

between two electrodes was set at 5 cm in all experiments. The electrolyte contained 0.01 M HF and 0.1 M HNO_3. The anodic oxidation was carried out under 20 V for 30 min. After electrolysis, the titanium sheet was rinsed with water and then air-dried.

2.3. Preparation of Cu/N TiO_2/Ti Film Electrode.

The as-prepared TiO_2 electrode (on Ti sheet) was used as cathode and graphite as anode. The electrolyte was a mixture of different volumes of 0.2 M $Cu(NO_3)_2$ and 0.2 M NH_4Cl, and the molar ratio of Cu^{2+}/NH_4^+ was adjusted to 1:1, 1:2, 1:3; 2:1, 2:2, 2:3; and 3:1, 3:2, 3:3, respectively. The distance between two electrodes was kept at 5 cm. The entire electrochemical process was performed at 5 V for 1 h. Finally, the titanium sheet with Cu/N codoped TiO_2 surface was taken out and rinsed with water and then air-dried.

2.4. Calcination.

Cu/N codoped TiO_2 and nondoped TiO_2 electrodes were calcined under air for 2 hours at the temperature of 500°C. To indicate the ratio of Cu^{2+}/NH_4^+ in electrolyte and calcination temperature, codoped samples are expressed as the form of Cu_1N_1/TiO_2, Cu_1N_2/TiO_2, Cu_1N_3/TiO_2, and so forth, while pure TiO_2 electrodes are expressed as TiO_2.

2.5. Photoelectrocatalytic Activity Measurements.

The photoelectrocatalytic activity efficiencies for the prepared samples were tested by degradation of humic acid in aqueous suspension. The photoelectrocatalytic oxidation experiments were conducted in a glass beaker. During these experiments, different plate anode materials were tested: Cu/N TiO_2/Ti and graphite plates used as active anode surface during electrolysis. The electrodes were dipped into the beaker containing 0.6 L humic acid as working volume. A 50 W tungsten halogen lamp (EXZ MR16 SP, GE, USA) was used as visible light resource. The light intensity was 80.1 Mw cm^{-2} (380 nm~ 780 nm) measured by SpectraScan Spectroradiometers (PR-705, Photo Research, USA). The photoelectrocatalytic oxidation was carried out at a constant current using a digital DC power supply. The sample solution was agitated by a magnetic stirrer (Figure 2). Magnetic stirring at a slow speed was constantly maintained along with the reaction. The concentration of humic acid was analyzed at the maximum absorption wavelength of HA at 254 nm with a UV-Vis spectrometer (Unico UV-2800A, China).

2.6. Instruments and Analytical Methods.

UV-Vis diffuse reflectance spectra were recorded on a Shimadzu 2550 UV-Vis spectrophotometer between 200 and 800 nm with $BaSO_4$ as the background. The XRD phase detection and analysis of the crystal structure of prepared products were recorded by a Dmax-rA powder diffractometer (Bruker D8 ADVANCE, Germany), with Cu Kα as a radiation and a step width of $2\theta = 0.02°$, with 2θ ranging from 20 to 60. The morphological features of the prepared products were assessed using a LEO, 1530 Vp field-emission scanning electron microscope (FESEM) at 15 kV. SEM samples were sputter-coated with about 20 nm Au using a Polaron Sputter Coater system.
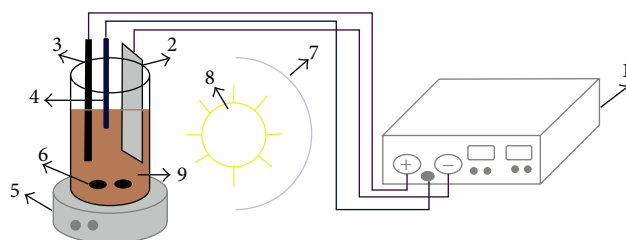

FIGURE 2: The electrochemical reactor and instrumentation. (1) DC power source, (2) Cu/N TiO_2/Ti anode, (3) graphite cathode, (4) reference electrode, (5) magnetic stirrer, (6) magnetic bar stirrer, (7) aluminum foil, (8) tungsten lamp, and (9) sample solution.

The SEM-EDX analysis was performed by a High Vacuum Tungsten Filament SEM (Hitachi S-3700N, Japan).

During the experiments, HA samples were periodically collected for analysis. No reactants or supporting electrolyte were added to the humic acid prior to the experiments. The UV-HA method was used for the measurement of HA concentration [45]. Specific UV absorbance of filtered samples was monitored at 254 nm with UV-Vis spectrophotometer (Unico UV-2800A, China), which was used to represent aromatic moieties. Additionally, UV-Vis spectrum was recorded from 200 to 600 nm. The samples were irradiated for 210 minutes. For absorbance measurement, 10 mL of sample was taken out from the reactor at given time intervals. All experiments were repeated at least two times, while reproducibility of the experiments was within 5%.

3. Results and Discussion

3.1. X-Ray Diffraction Analysis.

X-ray diffraction patterns of TiO_2 film and the Cu/N codoped TiO_2 films calcinated at 500°C for 2 h are shown in Figure 3. During the process of annealing, a crystalline phase of TiO_2 was formed. The crystalline structures of the oxide films were dependent on the type of electrolyte that was used. Mixed crystalline structure consisting of anatase and rutile TiO_2 was observed for the Cu/N codoped TiO_2 groups.

Anatase phase of the TiO_2 crystal structure could be interpreted from XRD patterns for TiO_2 and Cu/N codoped TiO_2 films, where anatase characteristic peaks are mainly crystallized to 2θ values of 25.5° (101), 37.9° (004), 48.045° (200), and 54.1° (105), respectively. Small rutile peaks were also observed at 27.4° (110) and 36.1° (101). At the temperature of 500°C, anatase phase was formed. The rutile phase began to appear when the annealing temperature was increased to 600°C. For Cu/N codoped TiO_2 films, obvious rutile peaks emerged when calcined at 500°C. It seems that Cu/N codoping is helpful for the crystalline phase transition from anatase TiO_2 to rutile TiO_2. Both anatase and rutile peak intensities increased slightly after calcination as has been reported before [46, 47]. Many studies have demonstrated that the mixture of anatase and rutile TiO_2 has greater degradation efficiency than either anatase or rutile TiO_2 alone. So the Cu/N codoped TiO_2 films in this paper can improve the PEC degradation efficiency. No peaks for CuO were observed for the low Cu doping
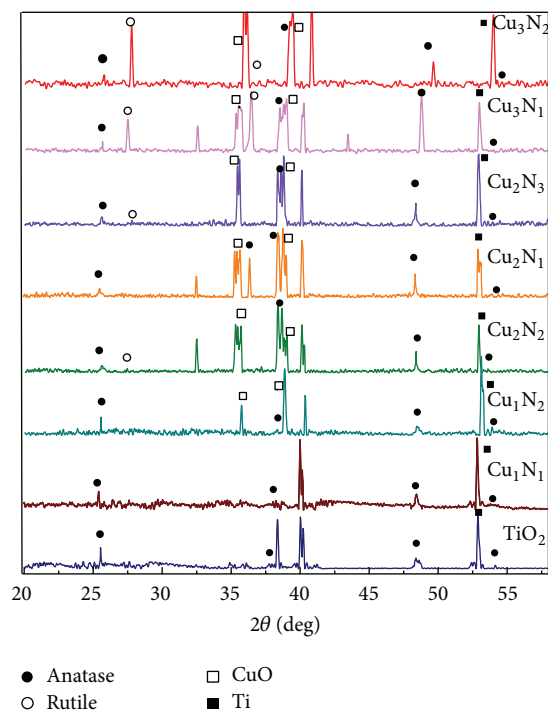
FIGURE 3: XRD patterns of TiO_2 and Cu/N codoped TiO_2 films with different Cu^{2+}/NH_4^+ molar ratios and annealed at 500°C.

samples. This was due to the low amount of Cu present. The diffraction peak intensities at $2\theta = 35.5°$ and $38.7°$, which were assigned to CuO (002 or 111) and CuO (111) [48], respectively, were observed for the samples of Cu_2N_x or Cu_3N_x, and their intensities increased with an increase in the Cu content. No nitrogen-derived peaks were detected, presumably due to the fact that content of N doping was very low.

3.2. UV-Vis Diffuse Reflection Spectroscopic Analysis.
Figure 4(a) shows UV-Vis DRS spectra for Ti, TiO_2-500, and codoped TiO_2-500 plate electrode and Figure 4(b) shows the corresponding plot of transformed Kubelka-Munk versus energy of light for TiO_2-500 and codoped TiO_2-500. It can be seen that pure TiO_2 film absorbs UV light at a wavelength less than 400 nm. While the TiO_2 film is doped with Cu^{2+} and NH_4^+, there is about 40 nm red shift of the band edge for Cu/N codoped thin film. In addition, the absorption intensity in visible light regions is increased, suggesting an improved photocatalytic activity within the visible light range (see next). On the other hand, the absorption in the UV light range decreased slightly. Cu_1N_3 and Cu_1N_2 codoped nanofilms with different Cu^{2+}/NH_4^+ molar ratios calcined at 500°C exhibited more or less similar red shift of the band edge and also reduced reflection intensity when compared with the pure TiO_2 nanofilm. The red shift can be attributed to the fact that when TiO_2 is doped with copper, Cu^{2+} species can form Cu-O-Ti bond with Ti^{4+} and then the photoinduced electrons can be effectively trapped by Cu^{2+} species. Furthermore, some Cu^{2+} species are deposited on

the surface of TiO_2 films, a condition which inhibits the absorption of visible light [48, 49].

The band gaps were estimated by application of the following equation:

$$(\alpha h\nu) = A \ (h\nu - E_g)^n, \tag{5}$$

where α, E_g, h, ν, n, and A are absorption coefficients, the band gap (eV), Planck's constant (6.6260×10^{-34}), frequency of light (s^{-1}), a number characterizing transition (for TiO_2, $n = 1/2$), and a constant, respectively. An estimation of band gap was acquired by extrapolation using tangent lines on the plot of $(\alpha h\nu)^{1/n}$ versus $h\nu$ and is shown in Figure 3(b). The results indicate that the band gap energies of Cu_1N_1, Cu_1N_2, and Cu_1N_3 codoped TiO_2 are 2.55 eV, 2.65 eV, and 2.90 eV, respectively. These band gaps are smaller than the widely accepted band gap values (3.2 eV and 3.0 eV) for pure TiO_2 and Degussa P25. The band structure of the photocatalysts played a crucial role in determining catalytic activity.

3.3. Morphology of the TiO_2 Films.
Figure 5 shows the FE-SEM images of the oxide film surfaces formed by anodic oxidation treatment. Amorphously shaped oxide films were observed on the TiO_2 (Figures 5(a) and 5(b)) and after (Figures 5(c) and 5(d)) Cu/N codoping on TiO_2 films. The films were amorphous before codoping. It is obvious that the TiO_2 particles were successfully oxidized on titanium (Figures 5(c) and 5(d)).

Based on the SEM images, it was estimated that the TiO_2 film formed on the Ti substrate had a thickness film and the TiO_2 particle size was around 50 nm (Figure 5). Most parts of the TiO_2 film displayed a less porous surface (Figure 5(a)). With respect to Cu/N codoped TiO_2 film, a number of larger Cu grains, compared with TiO_2 particulates, were obviously observed (Figure 5(d)). In addition, the size of Cu grain increased rapidly with prolonging the illumination time. The N doped in TiO_2 was small in size and mainly filled in the gaps between TiO_2 particulates.

3.4. EDX Analysis.
The EDX analysis was carried out to study the components of the deposited films (Figure 6). The result shows that these samples contain Ti substrate elements (Ti, O, and C) as well as Cu, confirming that Cu^{2+} is doped into the TiO_2 films. Further observation indicates that with increasing the concentration of Cu^{2+} in the deposition, the atom content of Cu element in the film is homologous augment (insets of Figures 6(a) and 6(b)). The actual percentage value of Cu in Cu_2N_3 codoped TiO_2 film is 3.14%. No nitrogen peaks were detected, presumably due to the fact that the content of N doping was very low and the doped N was uniformly distributed into the TiO_2 films.

3.5. Photocatalytic Activity of Cu/N Codoped TiO_2 Films.
The visible light photocatalytic (PC) degradation of humic acid over the Cu/N TiO_2/Ti films, doped with different Cu^{2+}/NH_4^+ molar ratios codoped TiO_2, was evaluated. The results indicate that all Cu/N codoped TiO_2 films have PC activity toward the degradation of HA. In contrast, unmodified TiO_2 film was not effective in degrading HA, regardless

I-1:3^{500} IV-1:1^{500}
II-1:2^{500} V-Ti
III-TiO$_2$^{500}

(a)

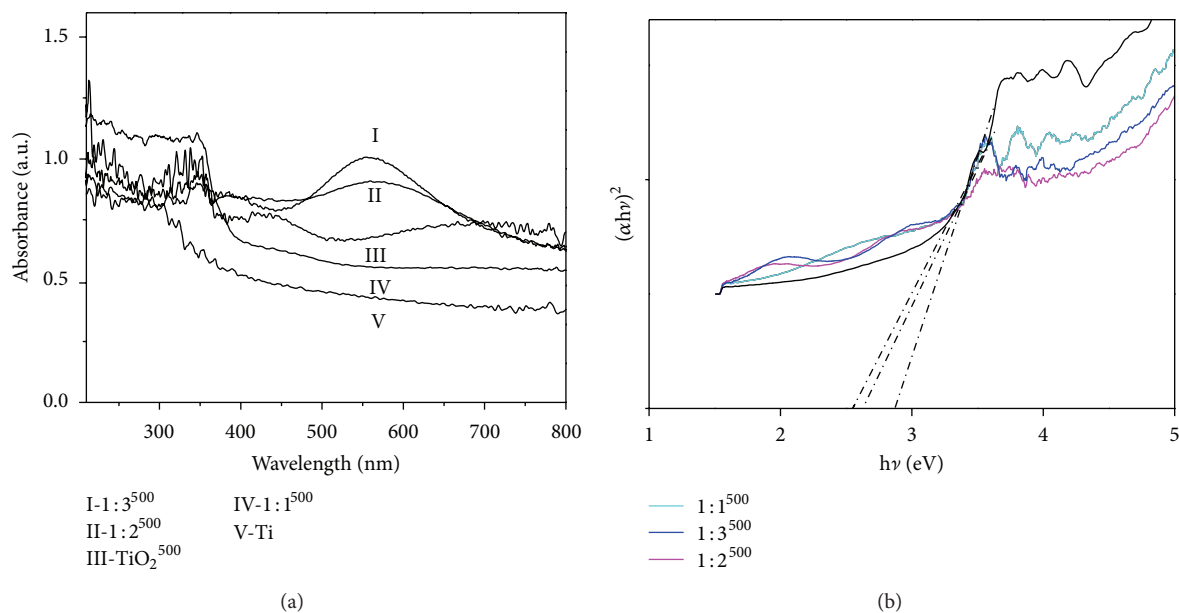1:1^{500}
1:3^{500}
1:2^{500}

(b)

Figure 4: (a) UV-Vis DRS spectra for Ti, TiO$_2$-500, and codoped TiO$_2$-500 plate electrode and the corresponding plot of transformed Kubelka-Munk versus energy of light for TiO$_2$-500 and codoped TiO$_2$-500.
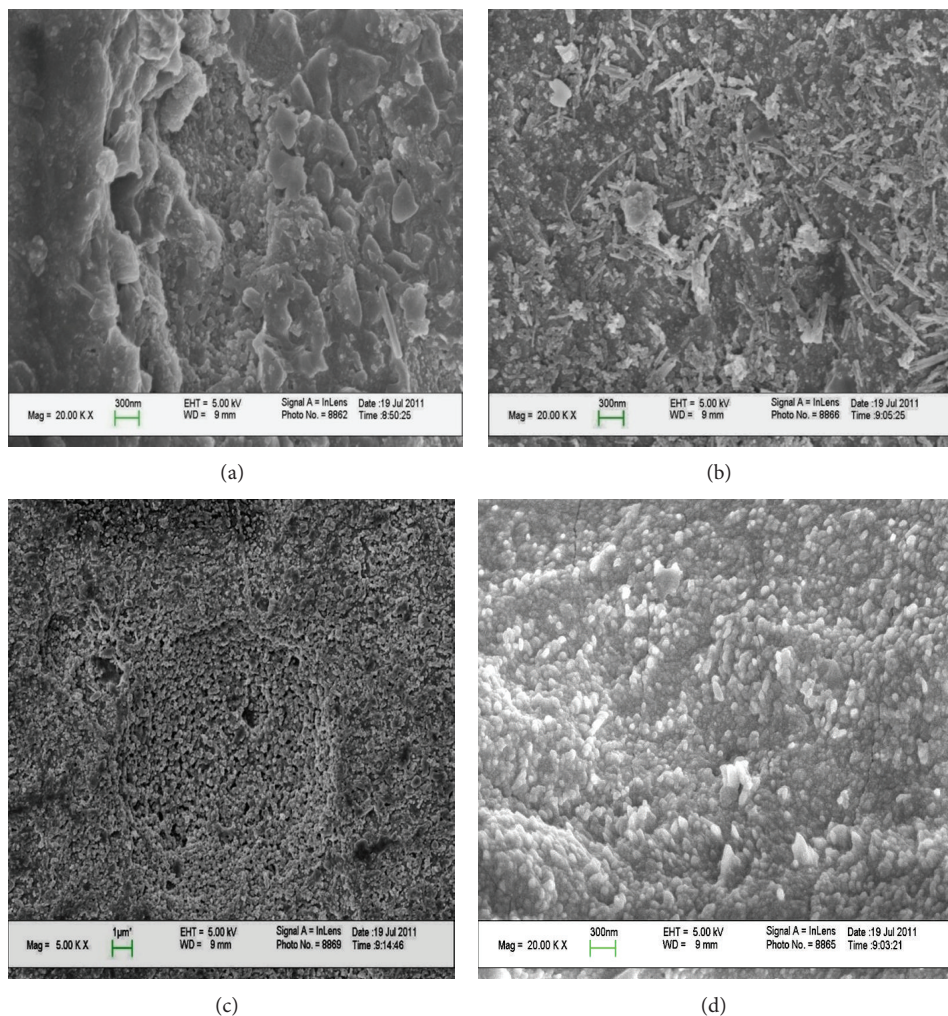

(a)

(b)

(c)

(d)

Figure 5: FESEM images of ((a) and (b)) view of pure TiO$_2$ film and ((c) and (d)) top view of Cu/N codoped TiO$_2$ film.

Element	Wt%	At%
CK	1.10	2.80
OK	26.87	51.28
TiK	72.02	45.92
Matrix	Correction	ZAF

(a)

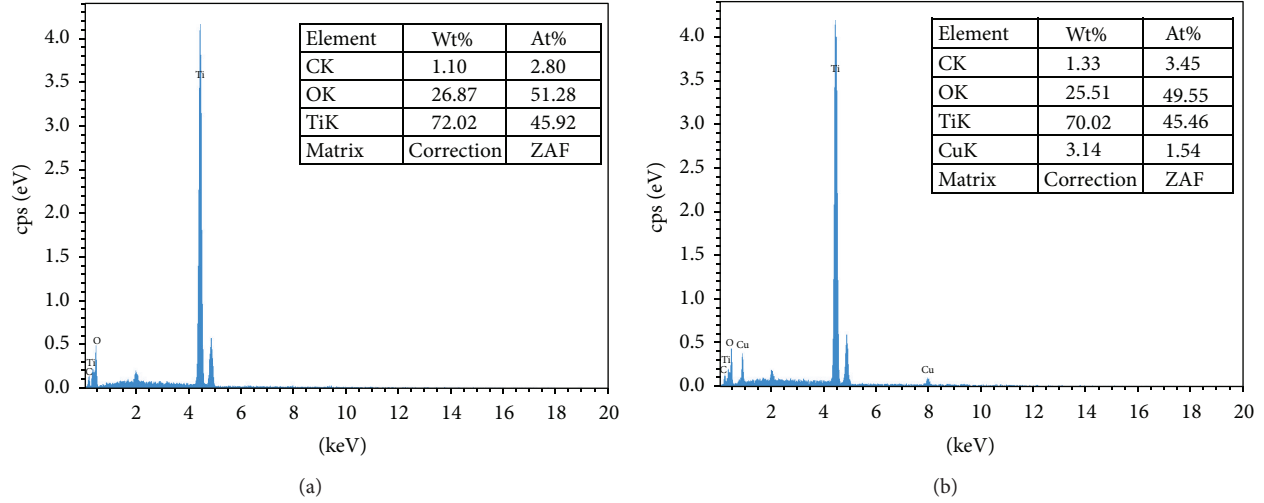| Element	Wt%	At%
CK	1.33	3.45
OK	25.51	49.55
TiK	70.02	45.46
CuK	3.14	1.54
Matrix	Correction	ZAF

(b)

FIGURE 6: EDX spectra of (a) TiO_2 and (b) Cu_2N_3-TiO_2. The insets in (a) and (b) show the element analysis of composites.
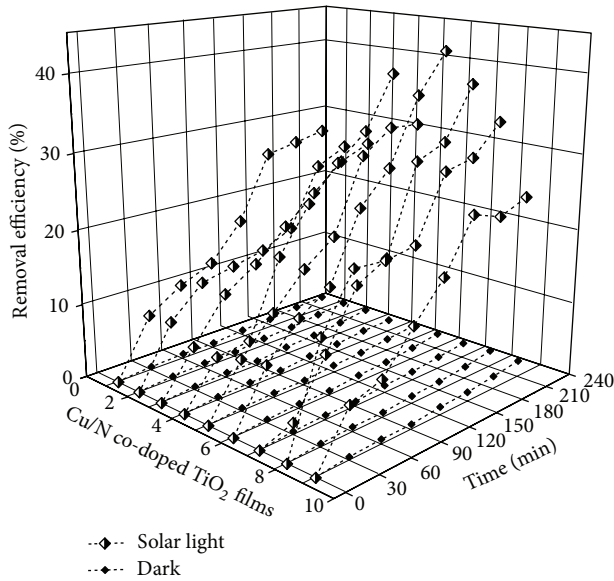

FIGURE 7: Degradation of humic acid under solar light and dark reaction over all Cu/N codoped TiO_2: (1) 1:1-500, (2) 1:2-500, (3) 1:3-500, (4) 2:1-500, (5) 2:2-500, (6) 2:3-500, (7) 3:1-500, (8) 3:2-500, and (9) 3:3-500.

FIGURE 8: Removal efficiency curves of humic acid over 2:3 Cu/N codoped TiO_2 film by photocatalysis.

of illumination with strong light intensity. The highest PC degradation efficiency was achieved on the Cu^{2+}/NH_4^+ molar ratio 2:3 TiO_2 film (Figure 7). For instance, after 210 min of treatment, the Cu^{2+}/NH_4^+ molar ratio 2:3 Cu/N codoped TiO_2 film shows about 41.5% PC degradation efficiency when there only has illumination. Upon illumination with photon energy in the excess of the band gap energy (E_g < 3.2 eV) of the Cu/N codoped TiO_2 photocatalyst, photogenerated electrons can easily be generated under the visible light due to the Cu^{2+}/NH_4^+ ions doping. These photogenerated electrons take part in photocatalytic redox reactions. Previous research has shown that the hole reacts with the electron

donors to produce free radical $OH^\bullet$ [38]. As the generation of free radical $OH^\bullet$, the humic acid decomposed into lower molecular weight compounds. When the Cu^{2+} content exceeded the optimum value (Cu_3N_x), the photocatalytic activity decreased. This result indicated that the presence of a greater amount of Cu was detrimental to the photocatalytic ability.

3.6. Effect of Initial Concentration of Humic Acid.
The influence of the initial concentration of humic acid on the photocatalytic degradation is shown in Figure 8. The result indicates that the degradation efficiency is decreased with increasing the initial concentration of humic acid. It is likely that with high initial concentration of humic acid,

FIGURE 9: Photocatalysis, electrolysis, and photoelectrolysis removal efficiency of humic acid on 2 : 3 Cu/N codoped TiO_2 film.

an increased turbidity or cloudiness reduces the incident light and therefore reduces the activity. At the same time, adsorption of pollutant on photocatalyst plays an important role in removal of pollutant [50, 51]. Although the same amount of humic acid may be removed via adsorption until all the adsorption sites are occupied, the degradation efficiency based on $(C_0 - C)/C_0$ may be reduced at high initial concentration C_0.

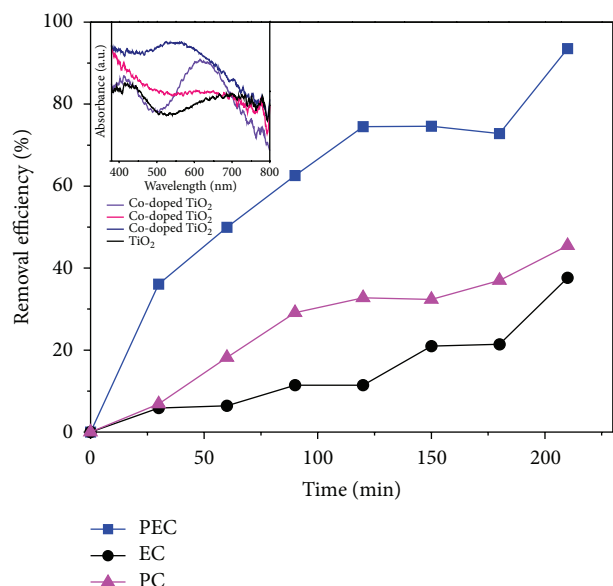*3.7. Photocatalysis, Electrolysis, and Photoelectrocatalysis of Humic Acid.* The visible light photocatalysis (PC), electrolysis (EC), and photoelectrocatalysis (PEC) activity of the Cu/N codoped TiO_2 films were evaluated for the degradation of humic acid in aqueous solution. The experimental results in Figure 9 showed that, compared with the PC oxidation, the PEC experiment was significantly higher than that of the PC process. For example, the Cu/N codoped TiO_2 film with molar ratio of 2 : 3 achieved UV254 removal efficiency of 93.5% in the PEC process, while it was only 41.5% in the PC process. The enhancement of UV-HA removal efficiency in the PEC processes can be ascribed to the following: the externally applied anodic bias drives away the photogenerated electrons accumulated on TiO_2 films via the external circuit, thus reducing the recombination of photogenerated electrons and holes and promoting the oxidation efficiency of humic acid. Figure 9 also showed that compared with the PC and PEC oxidation, EC oxidation was significantly decreased to only 37.6%.

The visible light sensitivity of the TiO_2 films caused by N doping (either substitutional or interstitial) may be related to the formation of high-energy level of steady state, which shifts the band-to-band electron transition to steady state to the conduction band transition. In the interstitial N model, the nitrogen atoms are bound to one or more oxygen atoms

and therefore are in a positive oxidation state, which could be NO^-, NO_2^-, or NO_3^-. Unpaired electrons distribute around both N and O atoms in nitrogen oxides.

The energy level formed by nitrogen oxides has a π-bond feature. The two bonding orbital energy levels lie below the top of the O 2p band, while the two antibonding orbital energy levels lie above the O 2p band. The highest steady state level for the interstitial species is 0.73 eV above the top of the valence band. Excitation from these steady state high-energy levels to the conduction band is responsible for the shift of the optical absorption of pure TiO_2 toward the lower energies (in the visible region) [34]. Furthermore, Cu doping is helpful for enhancing the separation between photoinduced electrons and holes. As a result, the Cu/N codoping not only improves photocatalytic activities of TiO_2 films, but also extends their absorbance band to visible light region.

4. Conclusion

In summary, this work improved the facile electrochemical technique for preparing a series of Cu/N codoped TiO_2 films to study the effective degradation of humic acid under visible light. The Cu/N codoped TiO_2 films were successfully fabricated. The absorption wavelength range and visible light photocatalytic activity of as-prepared Cu/N-codoped TiO_2 films were obviously affected by different molar ratios of Cu^{2+}/NH_4^+. The doping with suitable amounts of nitrogen and Cu into TiO_2 films exhibited a synergistic effect on the improvement of the photocatalytic efficiency of TiO_2 in visible light regions. Using the molar ratio 2 : 3 Cu/N TiO_2 film, the PEC degradation efficiency of humic acid under visible light illumination reached 93.5% after 210 min of treatment. Our work demonstrates that anodic oxidation technique is useful for preparing metal and nonmetal ion-doped TiO_2 films for visible light PEC degradation of organic pollutants.

Conflict of Interests

The authors declare that they have no conflict of interests regarding the publication of this paper.

Acknowledgments

References

[1] W. J. Weber Jr., Q. Huang, and R. A. Pinto, "Reduction of disinfection byproduct formation by molecular reconfiguration of the fulvic constituents of natural background organic matter,"

Environmental Science and Technology, vol. 39, no. 17, pp. 6446–6452, 2005.

[2] R. L. Wershaw, "Humus chemistry: genesis, composition, reactions: by F. J. Stevenson. Wiley-Interscience, New York, 1982, xiii + 443 pp," *Organic Geochemistry*, vol. 4, no. 3-4, 223 pages, 1983.

[3] F. J. Stevenson, *Humus Chemistry: Genesis, Composition, Reactions*, Wiley, New York, NY, USA, 1982.

[4] M. Aeschbacher, S. H. Brunner, R. P. Schwarzenbach, and M. Sander, "Assessing the effect of humic acid redox state on organic pollutant sorption by combined electrochemical reduction and sorption experiments," *Environmental Science and Technology*, vol. 46, no. 7, pp. 3882–3890, 2012.

[5] Y. Nagata, K. Hirai, H. Bandow, and Y. Kimaeda, "Decomposition of hydroxybenzoic and humic acids in water by ultrasonic irradiation," *Environmental Science and Technology*, vol. 30, no. 4, pp. 1133–1138, 1996.

[6] K. Tanaka and K. S. N. Reddy, "Photodegradation of phenoxyacetic acid and carbamate pesticides on TiO_2," *Applied Catalysis B*, vol. 39, no. 4, pp. 305–310, 2002.

[7] R. Zhang, L. Gao, and Q. Zhang, "Photodegradation of surfactants on the nanosized TiO_2 prepared by hydrolysis of the alkoxide titanium," *Chemosphere*, vol. 54, no. 3, pp. 405–411, 2004.

[8] B. Yu, J. Zeng, L. Gong, M. Zhang, L. Zhang, and X. Chen, "Investigation of the photocatalytic degradation of organochlorine pesticides on a nano-TiO_2 coated film," *Talanta*, vol. 72, no. 5, pp. 1667–1674, 2007.

[9] D. Dong, P. Li, X. Li et al., "Photocatalytic degradation of phenanthrene and pyrene on soil surfaces in the presence of nanometer rutile TiO_2 under UV-irradiation," *Chemical Engineering Journal*, vol. 158, no. 3, pp. 378–383, 2010.

[10] A. Kaur and U. Gupta, "A review on applications of nanoparticles for the preconcentration of environmental pollutants," *Journal of Materials Chemistry*, vol. 19, no. 44, pp. 8279–8289, 2009.

[11] S. Anandan, Y. Ikuma, and K. Niwa, "An overview of semiconductor photocatalysis: modification of TiO_2 nanomaterials," *Diffusion and Defect Data B*, vol. 162, pp. 239–260, 2010.

[12] J. Li, J. Wang, L. Huang, and G. Lu, "Photoelectrocatalytic degradation of methyl orange over mesoporous film electrodes," *Photochemical and Photobiological Sciences*, vol. 9, no. 1, pp. 39–46, 2010.

[13] S. Yin, Q. Zhang, F. Saito, and T. Sato, "Preparation of visible light-activated titania photocatalyst by mechanochemical method," *Chemistry Letters*, vol. 32, no. 4, pp. 358–359, 2003.

[14] A. Ghicov, B. Schmidt, J. Kunze, and P. Schmuki, "Photoresponse in the visible range from Cr doped TiO_2 nanotubes," *Chemical Physics Letters*, vol. 433, no. 4–6, pp. 323–326, 2007.

[15] D. Li, H. Huang, X. Chen et al., "New synthesis of excellent visible-light $TiO_{2-x}N_x$ photocatalyst using a very simple method," *Journal of Solid State Chemistry*, vol. 180, no. 9, pp. 2630–2634, 2007.

[16] E. D. B. Santos, J. M. De Souza E Silva, F. A. Sigoli, and I. O. Mazali, "Size-controllable synthesis of functional heterostructured TiO_2-WO_3 core-shell nanoparticles," *Journal of Nanoparticle Research*, vol. 13, no. 11, pp. 5909–5917, 2011.

[17] F. Chen, Z. Deng, X. Li, J. Zhang, and J. Zhao, "Visible light detoxification by 2,9,16,23-tetracarboxyl phthalocyanine copper modified amorphous titania," *Chemical Physics Letters*, vol. 415, no. 1–3, pp. 85–88, 2005.

[18] H.-C. Liang and X.-Z. Li, "Visible-induced photocatalytic reactivity of polymer-sensitized titania nanotube films," *Applied Catalysis B*, vol. 86, no. 1-2, pp. 8–17, 2009.

[19] A. Ghicov, B. Schmidt, J. Kunze, and P. Schmuki, "Photoresponse in thevisible range from Cr doped TiO_2 nanotubes," *Chemical Physics Letters*, vol. 433, no. 4–6, pp. 323–326, 2007.

[20] R. Asahi, T. Morikawa, T. Ohwaki, K. Aoki, and Y. Taga, "Visible-light photocatalysis in nitrogen-doped titanium oxides," *Science*, vol. 293, no. 5528, pp. 269–271, 2001.

[21] A. W. Morawski, M. Janus, B. Tryba, M. Inagaki, and K. Kałucki, "TiO_2-anatase modified by carbon as the photocatalyst under visible light," *Comptes Rendus Chimie*, vol. 9, no. 5-6, pp. 800–805, 2006.

[22] T. Ohno, N. Murakami, T. Tsubota, and H. Nishimura, "Development of metal cation compound-loaded S-doped TiO_2 photocatalysts having a rutile phase under visible light," *Applied Catalysis A*, vol. 349, no. 1-2, pp. 70–75, 2008.

[23] Y. Shen, T. Xiong, T. Li, and K. Yang, "Tungsten and nitrogen co-doped TiO_2 nano-powders with strong visible light response," *Applied Catalysis B*, vol. 83, no. 3-4, pp. 177–185, 2008.

[24] W. Y. Teoh, R. Amal, L. Mädler, and S. E. Pratsinis, "Flame sprayed visible light-active Fe-TiO_2 for photomineralisation of oxalic acid," *Catalysis Today*, vol. 120, no. 2, pp. 203–213, 2007.

[25] G. Tian, K. Pan, H. Fu, L. Jing, and W. Zhou, "Enhanced photocatalytic activity of S-doped TiO_2-ZrO_2 nanoparticles under visible-light irradiation," *Journal of Hazardous Materials*, vol. 166, no. 2-3, pp. 939–944, 2009.

[26] L. Li, C.-Y. Liu, and Y. Liu, "Study on activities of vanadium (IV/V) doped TiO_2(R) nanorods induced by UV and visible light," *Materials Chemistry and Physics*, vol. 113, no. 2-3, pp. 551–557, 2009.

[27] A. Kubacka, G. Colón, and M. Fernández-García, "Cationic (V, Mo, Nb, W) doping of TiO_2-anatase: a real alternative for visible light-driven photocatalysts," *Catalysis Today*, vol. 143, no. 3-4, pp. 286–292, 2009.

[28] E. B. Gracien, J. Shen, X. Sun et al., "Photocatalytic activity of manganese, chromium and cobalt-doped anatase titanium dioxide nanoporous electrodes produced by re-anodization method," *Thin Solid Films*, vol. 515, no. 13, pp. 5287–5297, 2007.

[29] J. Zhao, X. Wang, R. Chen, and L. Li, "Fabrication of titanium oxide nanotube arrays by anodic oxidation," *Solid State Communications*, vol. 134, no. 10, pp. 705–710, 2005.

[30] S. Kaneco, Y. Chen, P. Westerhoff, and J. C. Crittenden, "Fabrication of uniform size titanium oxide nanotubes: impact of current density and solution conditions," *Scripta Materialia*, vol. 56, no. 5, pp. 373–376, 2007.

[31] M. Anpo, S. Dohshi, M. Kitano, Y. Hu, M. Takeuchi, and M. Matsuoka, "The preparation and characterization of highly efficient titanium oxide-based photofunctional materials," *Annual Review of Materials Research*, vol. 35, pp. 1–27, 2005.

[32] C. E. Schvezov, M. A. Alterach, M. L. Vera, M. R. Rosenberger, and A. E. Ares, "Characteristics of hemocompatible TiO_2 nano-films produced by the sol-gel and anodic oxidation techniques," *JOM*, vol. 62, no. 6, pp. 84–87, 2010.

[33] K. Vinodgopal, S. Hotchandani, and P. V. Kamat, "Electrochemically assisted photocatalysis: titania particulate film electrodes for photocatalytic degradation of 4-chlorophenol," *The Journal of Physical Chemistry*, vol. 97, no. 35, pp. 9040–9044, 1993.

[34] D. Dumitriu, A. R. Bally, C. Ballif et al., "Photocatalytic degradation of phenol by TiO_2 thin films prepared by sputtering," *Applied Catalysis B*, vol. 25, no. 2-3, pp. 83–92, 2000.

[35] X. Quan, X. Ruan, H. Zhao, S. Chen, and Y. Zhao, "Photoelectrocatalytic degradation of pentachlorophenol in aqueous solution using a TiO_2 nanotube film electrode," *Environmental Pollution*, vol. 147, no. 2, pp. 409–414, 2007.

[36] Y. Xu, J. Jia, D. Zhong, and Y. Wang, "Degradation of dye wastewater in a thin-film photoelectrocatalytic (PEC) reactor with slant-placed TiO$_2$/Ti anode," *Chemical Engineering Journal*, vol. 150, no. 2-3, pp. 302–307, 2009.

[37] J. Zhang, B. Zhou, Q. Zheng et al., "Photoelectrocatalytic COD determination method using highly ordered TiO$_2$ nanotube array," *Water Research*, vol. 43, no. 7, pp. 1986–1992, 2009.

[38] J. Yang, J. Dai, C. Chen, and J. Zhao, "Effects of hydroxyl radicals and oxygen species on the 4-chlorophenol degradation by photoelectrocatalytic reactions with TiO$_2$-film electrodes," *Journal of Photochemistry and Photobiology A*, vol. 208, no. 1, pp. 66–77, 2009.

[39] K. Esquivel, L. G. Arriaga, F. J. Rodríguez, L. Martínez, and L. A. Godínez, "Development of a TiO$_2$ modified optical fiber electrode and its incorporation into a photoelectrochemical reactor for wastewater treatment," *Water Research*, vol. 43, no. 14, pp. 3593–3603, 2009.

[40] A. Fujishima, T. N. Rao, and D. A. Tryk, "Titanium dioxide photocatalysis," *Journal of Photochemistry and Photobiology C*, vol. 1, no. 1, pp. 1–21, 2000.

[41] R. Daghrir, P. Drogui, and D. Robert, "Photoelectrocatalytic technologies for environmental applications," *Journal of Photochemistry and Photobiology A*, vol. 238, pp. 41–52, 2012.

[42] Y. Su, S. Han, X. Zhang, X. Chen, and L. Lei, "Preparation and visible-light-driven photoelectrocatalytic properties of boron-doped TiO$_2$ nanotubes," *Materials Chemistry and Physics*, vol. 110, no. 2-3, pp. 239–246, 2008.

[43] X. Wang, H. Zhao, X. Quan, Y. Zhao, and S. Chen, "Visible light photoelectrocatalysis with salicylic acid-modified TiO$_2$ nanotube array electrode for p-nitrophenol degradation," *Journal of Hazardous Materials*, vol. 166, no. 1, pp. 547–552, 2009.

[44] B. S. Liu, L. P. Wen, and X. J. Zhao, "Efficient degradation of aqueous methyl orange over TiO$_2$ and CdS electrodes using photoelectrocatalysis under UV and visible light irradiation," *Progress in Organic Coatings*, vol. 64, no. 2-3, pp. 120–123, 2009.

[45] S. Park and T.-I. Yoon, "The effects of iron species and mineral particles on advanced oxidation processes for the removal of humic acids," *Desalination*, vol. 208, no. 1–3, pp. 181–191, 2007.

[46] W.-C. Hung, Y.-C. Chen, H. Chu, and T.-K. Tseng, "Synthesis and characterization of TiO$_2$ and Fe/TiO$_2$ nanoparticles and their performance for photocatalytic degradation of 1,2-dichloroethane," *Applied Surface Science*, vol. 255, no. 5, pp. 2205–2213, 2008.

[47] C. Kim, J. T. Kim, K. S. Kim, S. Jeong, H. Y. Kim, and Y. S. Han, "Immobilization of TiO$_2$ on an ITO substrate to facilitate the photoelectrochemical degradation of an organic dye pollutant," *Electrochimica Acta*, vol. 54, no. 24, pp. 5715–5720, 2009.

[48] S. Xu, J. Ng, X. Zhang, H. Bai, and D. D. Sun, "Fabrication and comparison of highly efficient Cu incorporated TiO$_2$ photocatalyst for hydrogen generation from water," *International Journal of Hydrogen Energy*, vol. 35, no. 11, pp. 5254–5261, 2010.

[49] L. Yiming, L. Wei, Z. Wanggang, Z. Jianjun, and H. Peide, "First principle study of Cu-N, Cu and N-doped anatase TiO$_2$," *Solid State Communications*, vol. 164, pp. 27–31, 2013.

[50] S. Saepurahman, M. A. Abdullah, and F. K. Chong, "Dual-effects of adsorption and photodegradation of methylene blue by tungsten-loaded titanium dioxide," *Chemical Engineering Journal*, vol. 158, no. 3, pp. 418–425, 2010.

[51] S. Bekkouche, M. Bouhelassa, N. Hadj Salah, and F. Z. Meghlaoui, "Study of adsorption of phenol on titanium oxide (TiO$_2$)," *Desalination*, vol. 166, no. 1–3, pp. 355–362, 2004.

Research Article

Preparation and Application of Mesoporous Nanotitania Photocatalysts Using Different Templates and pH Media

S. M. Abdel-Azim,[1] A. K. Aboul-Gheit,[1] S. M. Ahmed,[1] D. S. El-Desouki,[1] and M. S. A. Abdel-Mottaleb[2]

[1] *Egyptian Petroleum Research Institute, Nasr City, Cairo 11787, Egypt*
[2] *Nanophotochemistry and Solarchemistry Labs, Chemistry Department, Faculty of Science,
Ain Shams University, Abbassia, Cairo 11566, Egypt*

Correspondence should be addressed to M. S. A. Abdel-Mottaleb; phochem08@photoenergy.org

Mesoporous nanotitania photocatalysts were prepared by sol-gel method in acidic or basic media. Three types of surfactants, namely, cetyltrimethylammonium bromide, sodium dodecylbenzenesulfonate, and nonylphenol ethoxylate, were used as templating agents. The effects of surfactant type and pH on the morphology, particle size, surface area, pore-size distribution, UV-Vis absorbance, and TiO_2 phase transformation were traced by SEM, TEM, BET, and XRD. In absence of surfactants, XRD revealed 54.5% anatase at pH 3-4 and 97.0% at pH 7–9. In presence of surfactant, phase transformation of anatase has been significantly inhibited such that anatase amounts to 82–100% in acidic media. In basic media, the brookite phase appeared in low concentrations (8–15%) while rutile totally disappeared. The photocatalytic performance of the synthesized catalysts was tested via naphthalene degradation, which exhibited high activity in visible irradiation (>400 nm). The data obtained indicate that the surface area and pore volume of the current catalysts are the most effective factors for photocatalytic performance. Nevertheless, at the low pH (acidic) range, the CTAB templated catalyst gave the highest surface area (86.7 cm^3/g), which is mainly assigned to acquiring the highest photocatalytic degradation of naphthalene (97% after 4 h irradiation time).

1. Introduction

The properties of nanocrystals depend not only on their chemical compositions, but also on their structures, phases, shapes, sizes, and dimensionality [1]. Since the discovery of photocatalysis, titanium oxide (TiO_2) has attracted signification research attention due to its broad applications in the fields of water and air purification [2–4]. Also, TiO_2 has versatile potential applications besides catalysis, such as in solar-energy conversion, lithium storage, and optoelectronic devices. Many studies have described the shape and size control of inorganic nanoparticles by using conventional synthesis methods such as the sol-gel method and hydrothermal method. The sol-gel method has many advantages over other methods mainly because of the following: good homogeneity, ease of composition control, low processing temperature, large area coatings, low equipment cost, and good optical properties [5]. Mesoporous TiO_2 has better properties in many respects than ordinary TiO_2 because of its high specific surface area, uniform pore diameter, potential role in enhancing the light absorbance, and the accessibility of reactants to the active catalytic sites [6]. Mesoporous TiO_2 has been prepared as bulk powders and films [6, 7]. An interesting method to fabricate highly porous materials with desired pore structure and size for target specific applications is the use of amphiphilic organic molecules such as surfactants and block copolymers as pore directing agents in sol-gel methods [8]. Our motivation is to explore an effective technique to construct the oriented organization of nanoparticles, which is based on creating an interfacial interaction by chemical modification on the surfaces of nanoparticles (or micelle formation, that is, form colloidal-size cluster in solution called micelles which depend on surfactant concentration and salt concentration). Park et al. [9] have reported the

preparation of mesoporous titania through a modified sol-gel process in presence of CTAB surfactant. Shalan et al. [10] synthesized anatase TiO_2 nanorods with controlled size for dye-sensitized solar cells (DSSCs) via hydrothermal route at low hydrothermal temperature of $100°C$ for 24 h. A number of formation mechanism models have been proposed to explain the growth process of nanostructured materials from the inorganic precursor in the presence of surfactants self-assembles [11]. Transition metal oxides have been prepared in mesoporous forms using the amphiphilic surfactant templates such as triblock copolymers and ionic surfactants such as CTAB and neutral amines [7].

Naphthalene (NP $C_{10}H_8$) is a polycyclic aromatic hydrocarbon (PAH), which is a widespread environmental contaminant because of its generation as a combustion byproduct and use as a pesticide and pesticide synthesis intermediate and as component of fuels such as JP-8 [12]. Since it is the most water-soluble PAH (solubility 25–30 mg L^{-1} at ambient temperature), it is the dominant one in water. It has been considered as possibly carcinogenic to humans and it has both acute and chronic effects on humans and animal health. So, removing of naphthalene from water is urgently needed and possible via many techniques. Remediation and treatment of water, soil, or wastewater from PAH include conventional methods as homogeneous methods, bioremediation [13], hydrogenation [14], and ozonation, [15] and heterogeneous methods, photocatalytic degradation, fenton heterogeneous catalytic system [16], and metal oxides [17]. Advanced oxidation processes (AOPs) [18] present many advantages which are faster and can be achieved under direct sunlight making it cheaper to operate than other techniques. The total destruction of naphthalene using metal oxides with various supporting materials was carried out [19, 20]. Photocatalytic oxidation of naphthalene solution using various kinds of industrial titanium dioxide powders having anatase and rutile structure was tested as photocatalysts by Ohno et al. [21].

Other authors investigated changing the conditions they applied in preparing the nanocatalysts for use as active photocatalysts. In our work, we categorized the different types of surfactants to be used at different pH values (acidic and basic media). This scheme of work makes us able to illustrate a wide understanding of surface-active templates in nanophotocatalysts.

Therefore, in this work, we modified the sol-gel method through using three types of surfactants (cationic, anionic, or nonionic) in acidic or basic media for controlling the phase structure, size, crystallinity, mesoporosity, and hence the light absorptivity in the visible range. The photocatalytic activity of the nanostructured mesoporous TiO_2 catalyst has been tested in photodegradation of naphthalene as a water pollutant model compound.

2. Experiment

2.1. Materials.
In the current experiments, all chemicals were used as received. Titanium (IV) isopropoxide (TTIP) (97% Aldrich), isopropa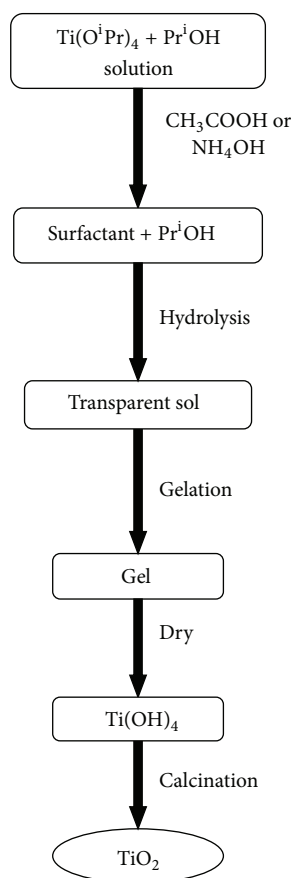nol (i-PrOH, Fisher), acetic acid (Fisher), ammonium hydroxide, cetyltrimetylammonium bromide (CTAB), sodium dodecylbenzenesulfonate (DBS), nonylphenol ethoxylate (NPE), and deionized water were used to prepare the solutions in our experiments. Naphthalene (Panreac, 98%) was used as a pollutant, acetonitrile and deionized water were used as HPLC eluent.

2.2. Synthesis of the Current Titania Catalysts.
Mesoporous nanocrystalline titania was prepared under controllable sol-gel process using titanium alkoxide in absence or presence of micellar surfactants as templating agents [22]. The molar ratio of surfactant/TTIP/i-PrOH/acetic acid or ammonium hydroxide was $R : 4 : 45 : 6$, where R is the surfactant concentration was which 0 or 1 at pH 3-4 in acetic acid or 8-9 in ammonia solution. Hydrolysis and polymerization took place in this mixture producing a transparent, homogeneous, and stable TiO_2 sol. After gelation for 24 h, the gel was dried overnight at $80°C$. The recovered powder was intermittently washed with deionized water and isopropanol five times followed by separation in a centrifuge under 10000 rpm to remove the surfactant. The resulted filtered cake was dried overnight at $100°C$ and then calcined at $550°C$ for 4 h to remove the remaining surfactant and consequently produce the desired TiO_2 nanoparticles photocatalyst (Scheme 1). The nomenclature was designed according to the pH range and the used surfactant. Preparation catalysts in acidic and basic medium were as follows: (1) without surfactant: A and B, (2) in presence of surfactants, CTAB-A, DBS-A, and NPE-A, in acidic medium, and (3) CTAB-B, DBS-B, and NPE-B in basic medium.

2.3. Photocatalytic Activity Testing.
The photocatalytic activities of the synthesized catalysts were evaluated for naphthalene degradation in an aqueous solution using a tungsten lamp (300 W) under 300–800 nm irradiation for 4 hours. In each experiment, a suspension with a volume of 200 mL containing naphthalene concentration of 80 μmol L^{-1} (10 ppm) and a TiO_2 catalyst powder of 2.5 g L^{-1} was placed in the Pyrex photoreactor under continuous stirring with a magnetic stirrer. The temperature was maintained at $20°C$ using cooling thermostat because of naphthalene volatility. Prior to illumination, the current suspension was magnetically stirred in the dark for 30 min to reach an adsorption/desorption equilibrium between the photocatalyst and naphthalene. A fixed quantity of the solution was withdrawn at regular time intervals, centrifuging the retrieved samples at 10,000 rpm.

2.4. Physical Characterization of the TiO_2 Catalysts.
Identification of the prepared TiO_2 powdered phases under the different preparation conditions at pH 3-4 or pH 8-9 with and without surfactants was examined by powder X-ray diffraction (XRD) analysis using Analytical {X$'$PERT PROMPD} X-ray diffractometer, CuKα radiation of wavelength λ = 1.5406 Å, rating of 40 KV, 40 mA, step size = 0.02, and scan step time of 0.4 sec in the 2θ range 10–80.

The morphology of the samples was checked by using transmission electron microscopy (TEM). The microstructures of the synthesized PANIs were examined by TEM

$$Ti(O^iPr)_4 + Pr^iOH \text{ solution}$$

↓ CH₃COOH or NH₄OH

$$Surfactant + Pr^iOH$$

↓ Hydrolysis

Transparent sol

↓ Gelation

Gel

↓ Dry

$$Ti(OH)_4$$

↓ Calcination

$$TiO_2$$

SCHEME 1: Preparation of TiO_2 photocatalysts.

(Tokyo, Japan) on a JEOL JEM-2000EX (Tokyo, Japan) at an accelerating voltage of 100 kV and scanning electron microscopy (SEM). The emission SEM (Tokyo, Japan) was performed with a JEOL 5400 (Tokyo, Japan).

The surface area was determined from nitrogen adsorption-desorption isotherms at liquid nitrogen temperature (77 K) using a Quantachrome AS1Win version 2.01 instrument. The TiO_2 samples were outgassed for 3 hours at 150°C. The Brunauer-Emmett-Teller (BET) method was used for surface area calculation, while pore-size distribution (pore diameter and volume) was determined by the Barrett-Joyner-Halenda (BJH) method.

Diffuse Reflectance Spectroscopy. Visible-ultraviolet spectra were obtained by diffuse reflectance spectroscopy by using a Shimadzu UV-2401 PC instrument. $BaSO_4$ was the reference sample and the spectra were recorded in the range 200–800 nm.

For photocatalytic activity measurement, high performance liquid chromatography (HPLC) using HPLC Waters 600 apparatus, equipped with an autosampler (Waters 717 plus) and a dual wavelength absorbance diode array detector (Waters 4487) set at 254 nm, was used with C18 5 μm, 4.6 mm × 250 mm column (part no. 186004117) purchased from water USA. The mobile phase was HPLC grade water/acetonitrile (30/70) operating at a flow rate of 1 cm³ min⁻¹.

3. Results and Discussion

3.1. Effect of Surfactants Type and pH on Particle Size Distribution of TiO_2. In order to prevent the growth of nano-TiO_2, the influence of the surfactant types on the particle size distribution of TiO_2, including anionic surfactant DBS, cationic surfactant CTAB, and nonionic surfactant NPE, is studied. These surfactants assist reducing the particle size of TiO_2 during their sorption on the surface of nanoparticles. The reaction depends on the interfacial energy among particles which prevents the aggregation of powders from the static repulsion and special hindrance. To study the influence of reaction conditions on the morphology and phases of TiO_2, controlled experiments have been designed with varied types of surfactants and pH. The pH of solution has a significant impact on the TiO_2 morphology. The result obtained shows that TiO_2 nanoparticles with different sizes can be formed under the conditions of hydrolysis of titanium isopropoxide at two different values, pH = 3-4 (acidic medium) and pH = 8-9 (alkaline medium). At different pH of the system, the diameter of nanoparticles becomes different, since, in acidic media, the concentration of H^+ becomes higher. The oxygen atom in Ti–O which has a lone electron pair will easily form hydrogen bond with the H^+. Thus the intensity of Ti–O bonds is weakened and the system becomes easier to hydrolyze with higher speed of TiO_2 nucleation. The products are smaller while the amount of nucleus is larger [23].

TABLE 1: Physical characterization of the current catalysts.

Catalyst	Surface area (m^2/g)	Crystal phase %	Average TEM (nm)	Absorbance (nm)	Activity %
A	16	$A = 54.63$ $R = 45.37$	14	390	37
CTAB-A	86.71	$A = 100$	8	400	97
DBS-A	57.49	$A = 82.99$ $R = 17.01$	9	395	85
NPE-A	43.01	$A = 94.73$ $R = 5.27$	9	390	24
B	12	$A = 96.45$ $R = 3.54$	11.5	380	20
CTAB-B	62.11	$A = 84.71$ $B = 15.29$	11	390	70.5
DBS-B	67.21	$A = 100$	16	410	83.5
NPE-B	70.29	$A = 91.72$ $B = 8.28$	10	430	91.6

In presence of ammonia (alkaline medium), a complex can be formed with Ti^{4+} which will facilitate the growth of nuclei and increase the peptizing speed. However, the TiO$_2$ crystal changes from anatase to brookite. So, the size of particles can be controlled by regulating the pH of solution [24].

3.2. XRD Pattern of TiO$_2$ Nanoparticles.

The XRD patterns in Figures 1 and 2 and the data listed in Table 1 show the crystalline phase content in the synthesized catalysts. The XRD patterns illustrate the effect of pH modifiers (acetic acid and ammonia) in absence or presence of surfactants. The mass fractions of anatase, rutile, and brookite are calculated from the (101) reflection of anatase at $2\theta = 25.48°$, the (110) reflection of rutile at $2\theta = 27.58°$, and (121) reflection of brookite at $2\theta = 30.8°$. The mass fraction of each phase present in the powder was calculated using the equation $x = 1 + 0.8(I_A/I_R)^{-1}$, where x is the weight fraction of rutile in the TiO$_2$ and I_A and I_R are the X-ray intensities of the anatase and rutile peaks, respectively (see Table 1). Also, the crystallite size of these phases is calculated applying Scherrer's equation $D = 0.9\lambda/\beta\cos\theta$, where D is the thickness of crystallite, λ is X-ray wavelength, β is FWHM (full width at half max), and θ is Bragg Angle. The crystallite sizes calculated are in agreement with the particle size measured by TEM.

3.2.1. Effect of pH in Absence of Surfactants.

In the XRD pattern (Figure 1) obtained for the TiO$_2$ catalyst prepared using acetic acid as a pH modifier (pH 3-4) (A) gives 54.6% anatase and 45.4% rutile forms. Parra et al. [25] have prepared pure anatase phase at pH 5-6 and reported that, in a stronger acidic medium, the rutile formation would be privileged. On the other hand, when ammonia has been used to adjust the pH at 8-9 (B), it is found to be 96.4% anatase and as low as 3.5% rutile phase. Lim et al. [26] reported that, when TiO$_2$ was prepared using NH$_4$OH at pH 7–9, the rutile phase was only observed at calcination temperatures above 500°C. Hence, it is concluded that the resistance of anatase transformation to
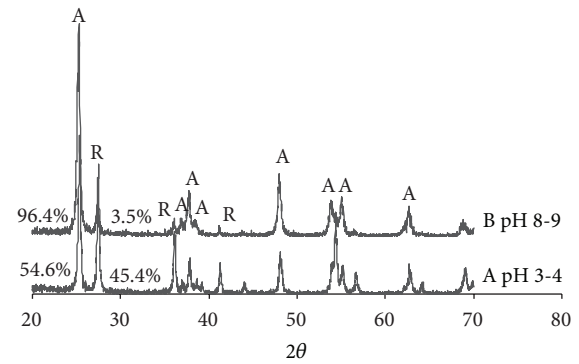
FIGURE 1: X-ray diffraction spectra for TiO$_2$ at different pH.

rutile increases more in basic medium than in acidic medium at the same calcination temperature (550°C), as with Hu et al. [27].

3.2.2. Effect of pH in Presence of Surfactants.

During the preparation of TiO$_2$ catalysts in presence of different types of surfactants, it is found that the produced TiO$_2$ is completely anatase phase using the cationic surfactant (CTAB) at pH 3-4 (CTAB-A), whereas, at pH 9, in presence of the same surfactant (CTAB-B), TiO$_2$ has been produced in two phases, anatase (84.7%) and brookite (15.3%). From XRD patterns (Figure 2 and Table 1), it is calculated from the broadening of the peaks that the crystallite size of the prepared TiO$_2$ using the CTAB surfactant in ammonia solution or acetic acid is lower than that produced in absence of surfactant (in Figure 1). Also, the presence of surfactant suppresses the anatase-rutile transformation. In sample CTAB-A, there is no rutile phase while in sample CTAB-B there is a small amount of the brookite phase. Guohui et al. [28] prepared TiO$_2$ powders using CTAB in the presence of ammonium hydroxide. The authors found that, at calcination temperatures below 600°C, TiO$_2$ samples display dominantly anatase phase together with a small amount of brookite which is in
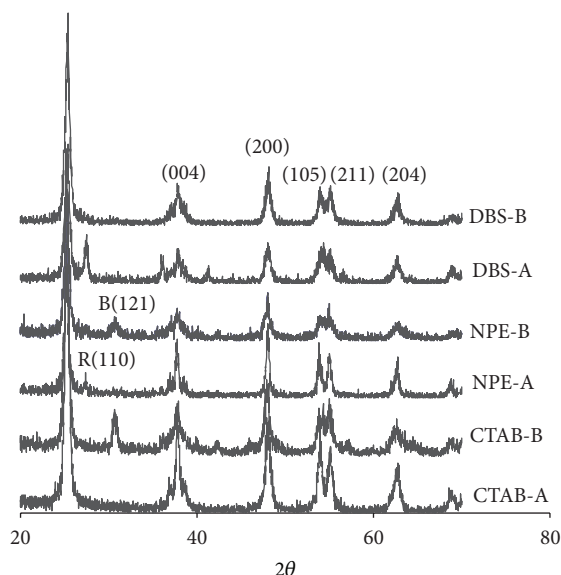
FIGURE 2: X-ray diffraction spectra for TiO$_2$ at different pH and surfactants.

agreement with our results. On using the anionic surfactant (DBS), anatase comprises 83.0% and rutile comprises 17.0% at pH 3-4 (DBS-A), whereas at pH 8-9 (DBS-B) anatase comprises 100%. Nevertheless, using the nonionic surfactant (NPE), the rutile phase comprises 5.3% in anatase/rutile mixture at pH 3-4 (NPE-A), which is less than in the absence of a surfactant. At pH 8-9, the brookite phase appears (8.28%) while the rutile phase is absent (NPE-B).

3.3. The Morphologies of TiO$_2$ Nanoparticles.

The TEM photographs obtained for the current TiO$_2$ samples prepared at different conditions using various types of surfactants are given in Figures 3 and 4. In the acidic medium (at pH 3-4) while in absence of surfactant, the sample exhibits particles mainly in the form of hexagonal prisms and rhombohedrons (Figure 3). This may be attributed to the presence of sufficient precursor for the reaction to take place. This may help also in obtaining random shapes rather than regular spherical particles. The particle size is varied from 12 to 14 nm in both acidic and basic media. It is also observed that there is an agglomeration of TiO$_2$ particles associated with low surface area and low pore volume. TEM images show many regions with shadow which have been reported to indicate the formation of curved channels between the packed particles [29]. These observations agree with our N$_2$ adsorption/desorption results (Figure 5), where H3 hysteresis loops of TiO$_2$ suggest that there are curved channels in the bulk.

From the selected area electron diffraction patterns (SAED) of TiO$_2$ with no surfactant in both basic and acidic media (inset of Figure 3), spotty sharp rings occur which are indicative of polycrystalline materials with high crystallinity. The first five SAED rings represent anatase phase indexed as (101), (004), (200), (105), and (211) (JCPDS no, 21-1272) and rutile phase indexed as (110). This result is in agreement with XRD patterns shown in Figure 1.

The TEM morphology of TiO$_2$ samples prepared using various types of surfactants in either acidic or basic medium is shown in Figure 4. It can be observed that all samples prepared with the aid of surfactant have more dispersed particles than those without surfactants, which could be attributed to the fact that surfactants prevent the aggregation of TiO$_2$ powders [30]. Chen et al. [31] have reported that (1) the surfactants could adhere on the anatase face (101) of TiO$_2$ and therefore it could modify the surface free energy of TiO$_2$ during the titania catalyst preparation and (2) during the removal of a surfactant by successive washing and calcination processes more mesopores were left in TiO$_2$. TEM images give hexagon, diamond, cohexagon, and bullet shapes.

3.4. SEM of TiO$_2$ Nanoparticles.

Figure 5 shows the SEM images obtained for current samples. The TiO$_2$ particles obtained during preparation in acidic medium in absence of a surfactant acquire heterogeneous sizes with their surface appearing rough. However, the images obtained for the samples CTAB-A, NPE-A, and DBS-A consist of large numbers of nanoparticles with relatively smooth external surfaces. The relatively smooth external surface of those nanoparticles suggests that they are composed of countless tiny primary nanoparticles. The aggregation of these tiny primary nanoparticles can produce large numbers of interaggregated pores, resulting in a highly mesoporous nanotitania as shown in Figure 5. The effect of applying surfactants on the morphology and microstructure of the mesoporous titania nanoparticles shows that there is shrinkage of the nanoparticles diameters caused by collapse of smaller pores. After washing and calcination for 5 times, the surfactants were completely removed and a porous structure was achieved in the microspheres [32, 33].

3.5. The BET Surface Characterization.

Figure 6 shows the isotherms obtained for the prepared TiO$_2$ at different pH values in absence or presence of different templating surfactants. The isotherms are of classical type IV, characteristic for mesoporous materials according to the IUPAC classification [34]. The adsorbed volume at relative pressures below 0.3 is due to monolayer coverage of the surface, while the increase of the relative pressure to 0.4–0.8 with broad hysteresis loops is due to capillary condensation within mesopores [35].

In presence of the three types of surfactants, the hysteresis loops of the photocatalysts prepared in basic medium at pH 8-9 appear at a high relative pressure P/P^0 range of 0.56–0.70 with H1 and H3 type loops, which correspond to slit shape pores [29]. However, using the same catalysts prepared in acidic medium at pH 3-4, the hysteresis loops appear at P/P^0 range of 0.4–0.6 with H2 type loops associated with ink-bottle pores [36]. The surface area, pore volume, and the average pore size of the catalysts are summarized in Table 1. In the presence of anionic and nonionic surfactants, the surface area and pore volume of the photocatalysts prepared at pH 3-4 are higher than those prepared at pH 8-9, indicating higher porosity [32]. In case of using the cationic surfactant (CTAB) at pH 3-4, higher surface area and pore volume have been obtained.
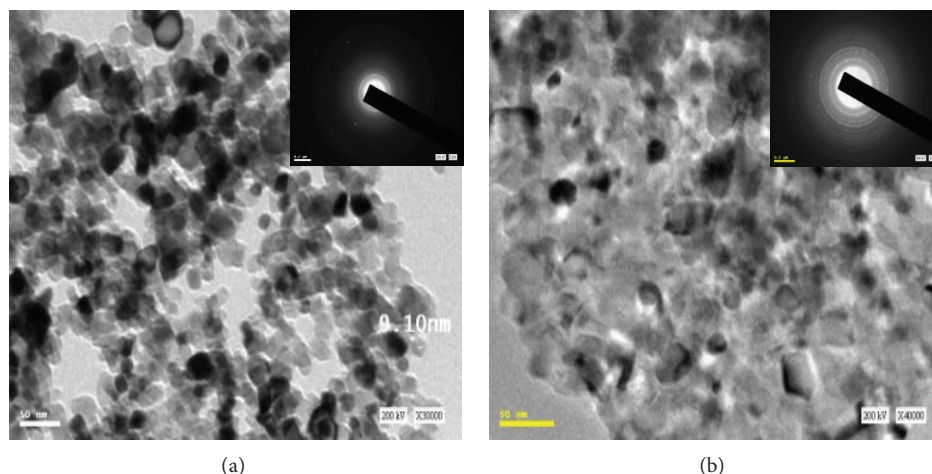
(a)   (b)

FIGURE 3: TEM images of the TiO_2 at different pH.

Pore-size distribution was calculated according to the BJH method applying the desorption branch of the isotherm. Figure 7 shows that the pore-size distribution values occupy a broader pore-size range on using the preparation in basic medium (40–180 Å) relative to that using the acidic medium (40–120 Å). It is observed that the catalyst with the widest pore-size distribution acquires higher surface area and pore volume, as in the case of using CTAB-A catalyst. This agrees with the results of Sasikala et al. [37]. The pore-size range of the synthesized TiO_2 catalysts in acidic medium can be arranged in the surfactant order as follows: CTAB > NPE > DBS, whereas synthesis in the basic medium can be arranged in the surfactant order as follows: NPE > DBS > CTAB.

3.6. UV-Vis Diffuse Reflectance Spectra.

Figure 8 displays the UV-vis reflectance spectra obtained for TiO_2 nanoparticles prepared under different conditions, namely, pH change and absence or presence of surfactants. All samples gave significant red shift towards the visible light region (385–430 nm) which indicates the suitability for applying solar irradiation since the absorbance is related to the sample morphology, surface area, particle size, and crystal phase composition of the particles. The catalysts prepared in absence of surfactants give absorbances at 390 and 385 at pH 3-4 and 8-9, respectively, which is due to the presence of the anatase and rutile of TiO_2 phases [38]. However, the absorption edge is shifted to a longer wavelength with increasing the fraction of rutile phase that acquires a smaller band gap (3.0 eV) than that of the anatase phase (3.2 eV). From Figure 8, the largest red shift is caused by CTAB in acidic medium (400 nm) whereas NPE causes a higher shift in the basic medium (430 nm). This is attributed to high surface area, improved grain size [39], pore volume, and the coexistence of anatase and brookite in the TiO_2 which cause a decrease of the band gap energy [40, 41]. Moreover, a trace residue of organic compounds or remaining surfactant [42] would have contributed to increasing the red shift. The band gap energy, E_g, of the photocatalysts is assigned to the

intrinsic electron transition from the valence band (VB) to the conduction band (CB). E_g values were determined using the absorption UV-vis spectra (Table 1). The optical energy band gap was calculated using the relationship $E_g = h \cdot c / \lambda = 1240/\lambda$ [43], where E_g is the band gap (eV) and λ is the wavelength of the absorption edges in the spectrum (nm).

3.7. Photodegradation of Naphthalene on the Catalysts.

In this work, the decrease of naphthalene in the dark for the initial 30 min is taken as the primary adsorption on the catalyst surface. The adsorption capacity is found to increase as surface area increases (Table 1). Naphthalene removal comprises as high as 35% on CTAB-A, whereas it is only 12% on NPE-A catalyst. It can be suggested that, as the number of Ti^{4+} active sites on the surface increases, the rate of electron transfer and adsorption of the pollutant molecules increases [44]. Hao and Zhang [45] reported that an increase of surface area and porosity of the catalyst can reduce the internal mass transfer limitation of the pollutant to the active sites.

Figure 9 shows that, in absence of any templating agent, the photoactivity of the current catalysts is relatively low (20.0% in basic medium and 37.1% in acidic medium). This can be attributed to acquiring very low surface area (12.0 $m^2 g^{-1}$ and 16.3 $m^2 g^{-1}$, resp.) and very low pore volume (0.0144 $cm^3 g^{-1}$ and 0.0146 $cm^3 g^{-1}$, resp.). Furthermore, the rutile formation is as appreciable being 45.4% in acidic medium and 3.5% in the basic medium. On the other hand, the catalyst prepared using CTAB as a templating agent in acidic medium exhibits the highest activity all over the present study for the photodegradation of naphthalene (97% after 180 min) which may be attributed to acquiring the highest surface area (86.7 $m^2 g^{-1}$) and the highest pore volume (0.0569 $cm^3 g^{-1}$) among all current catalysts. Moreover, this catalyst is composed of 100% anatase phase besides acquiring a particle size as low as 8.0 nm. Furthermore, Figure 8 shows that the largest red shift obtained using this
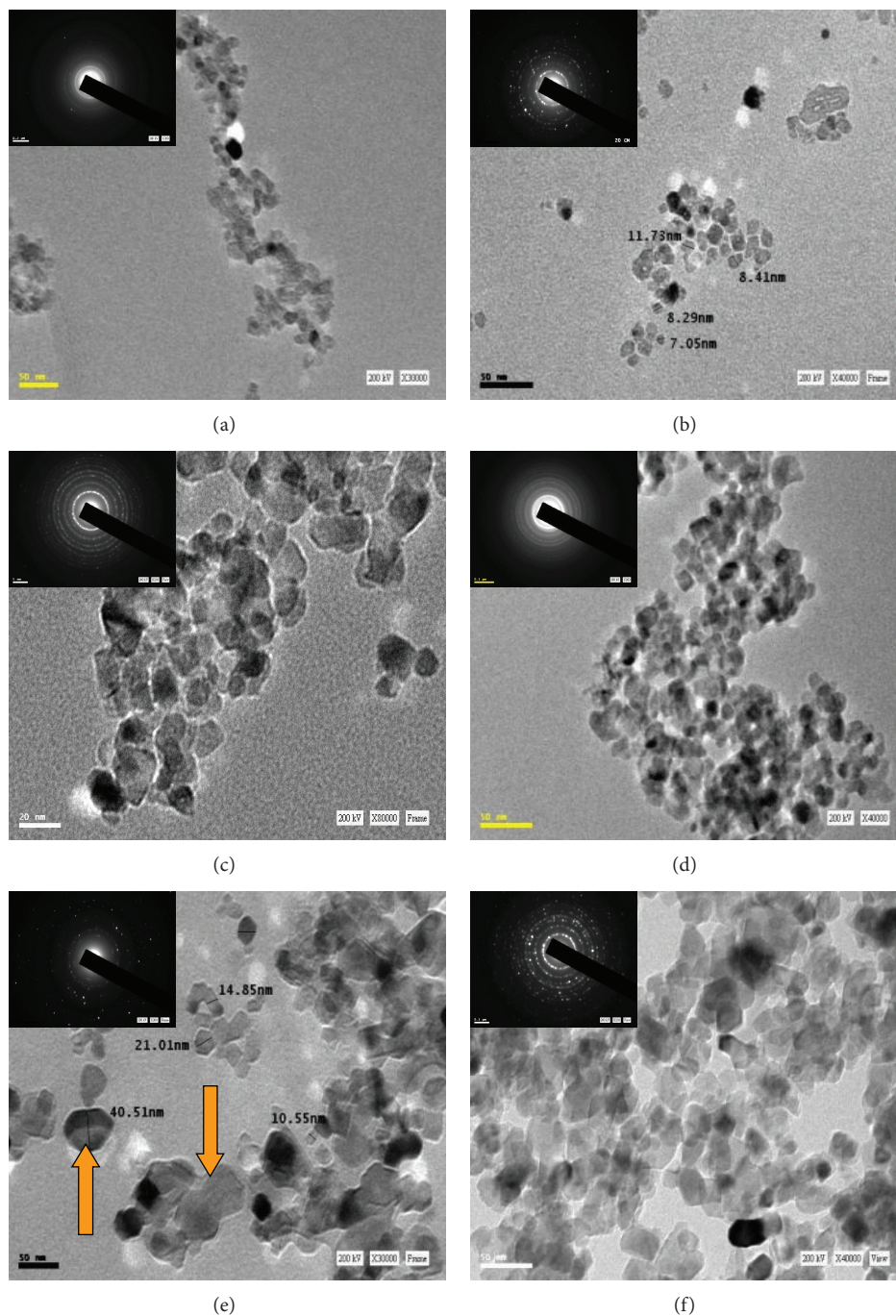
(a)

(b)

(c)

(d)

(e)

(f)

FIGURE 4: TEM images of the TiO_2 at different pH and different surfactants. (a) CTAB-A, (b) DBS-A, (c) NPE-A, (d) CTAB-B, (e) DBS-B, and (f) NPE-B.

catalyst appears at 400 nm indicating a shift towards reducing the band gab from 3.2 to 3.1 ev which is a great privilege for applying visible (solar) irradiation rather than applying UV irradiation. On the other hand, in the basic medium using the same templating agent (CTAB) while keeping the other variables unchanged, a lower photoactivity has been encountered (71.0%), most expectedly due to its lower surface area (60.1 $m^2 g^{-1}$) and lower pore volume (0.0309 $m^2 g^{-1}$) as well as acquiring a significant quantity of brookite.

4. Conclusion

The current TiO_2 photocatalysts have been prepared by sol-gel method using Ti-alkoxide as precursor, in acidic or basic media in absence or presence of different surfactants (templates). XRD analysis showed that addition of surfactants suppressed the transformation of anatase to rutile phase. All catalysts exhibited activities in the visible range at various levels. In both acidic and basic media, *in absence of*

(a)

(b)

(c)

(d)
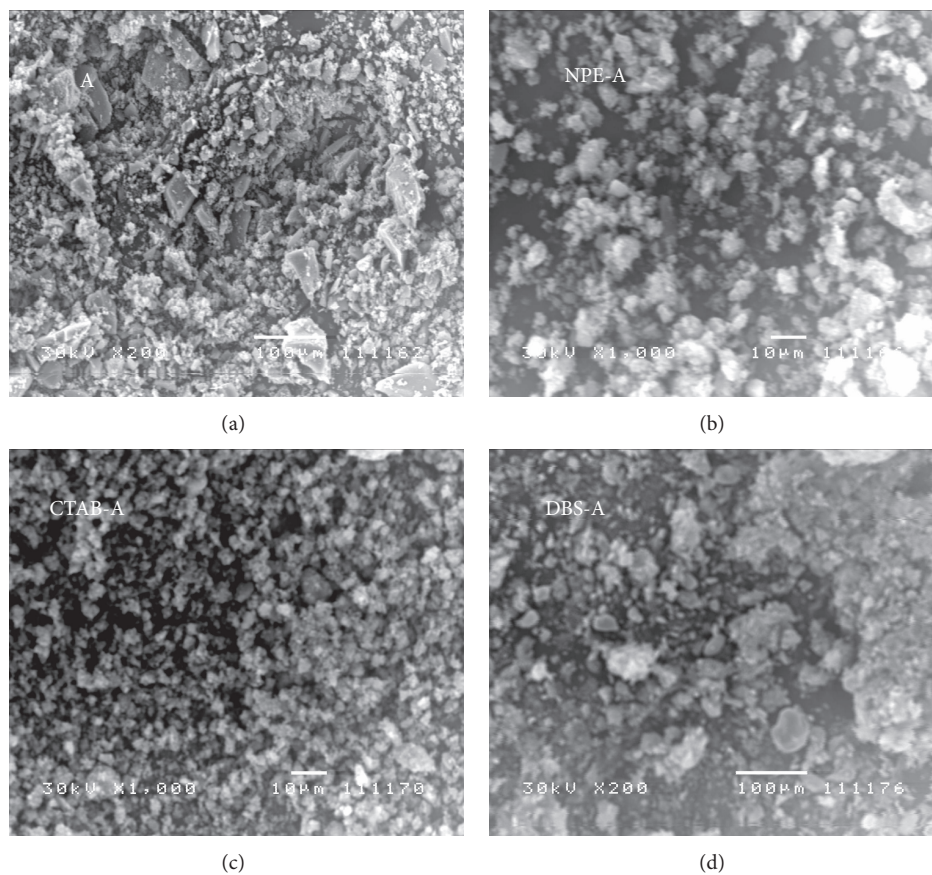
FIGURE 5: SEM images of the TiO$_2$ without and with different surfactants at pH 3-4.

(a)

(b)
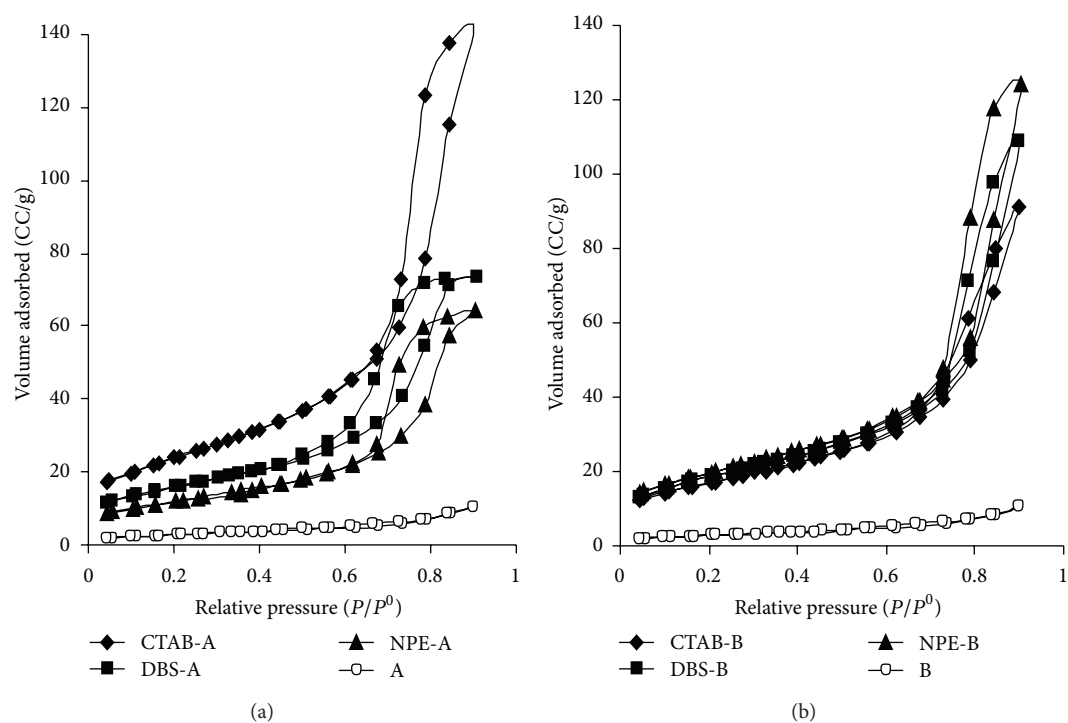
FIGURE 6: N$_2$ adsorption/desorption isotherms for the catalysts.
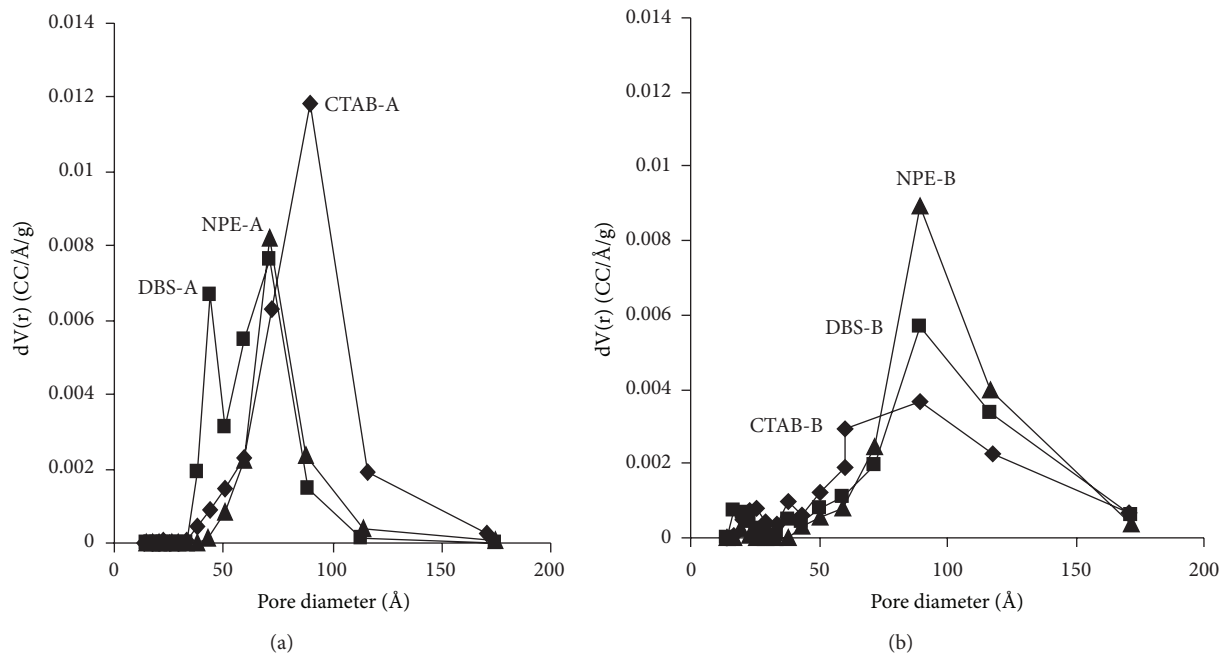
FIGURE 7: Pore-size distribution of TiO$_2$ in acidic and basic media.
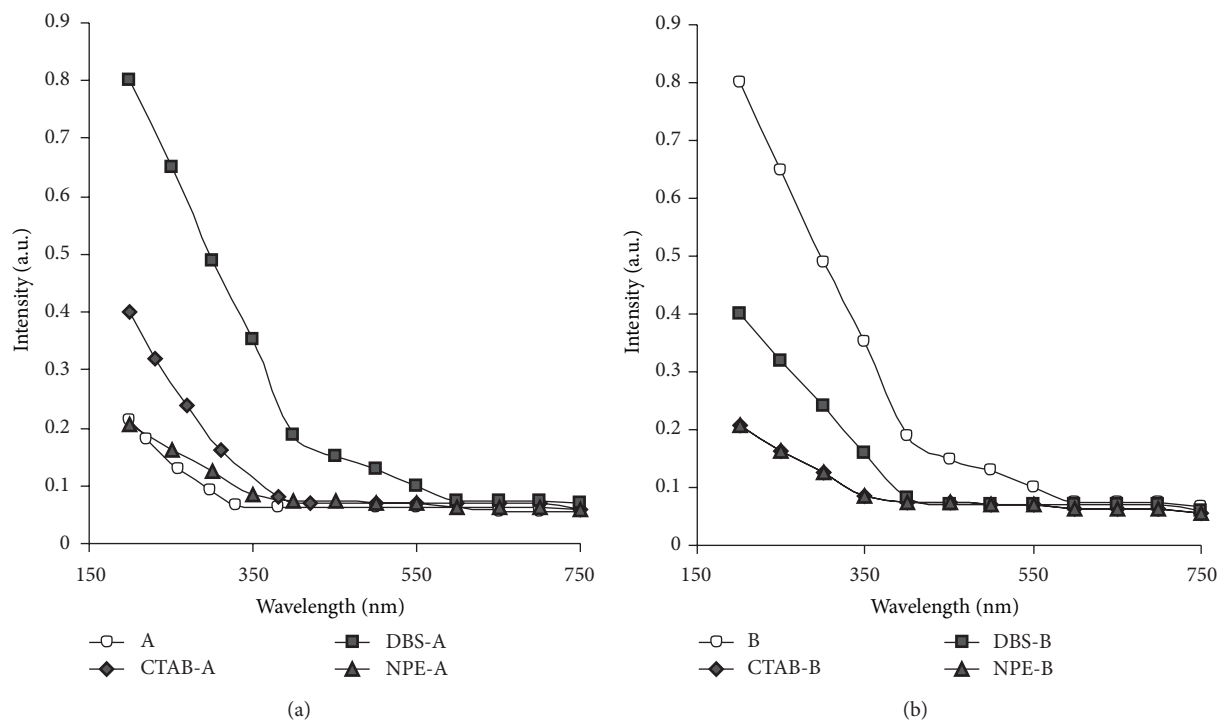
FIGURE 8: UV-vis absorption spectrum of the TiO$_2$ catalysts.

surfactants, the photoactivities for the pollutant degradation were 37% (A: acid medium) and 20% (B: basic medium), respectively, whereas these values jumped by adding the surfactants to ~97% using CTAB-A catalyst and to ~91% using NPE-B sample. The most effective factors for photodegradation improvement were the surface area and total pore volume (mainly described by pore-size distribution).

The pore-size distribution behaviour is found to exhibit the most pronounced relevance to the catalytic activity of the current photocatalytic degradation of naphthalene. The widest mesopores are acquired by the CTAB templated acidic sample but they acquire the narrowest sizes in the pore-size distribution of the basic medium. CTAB-A catalyst gave the highest red shift in the visible range.
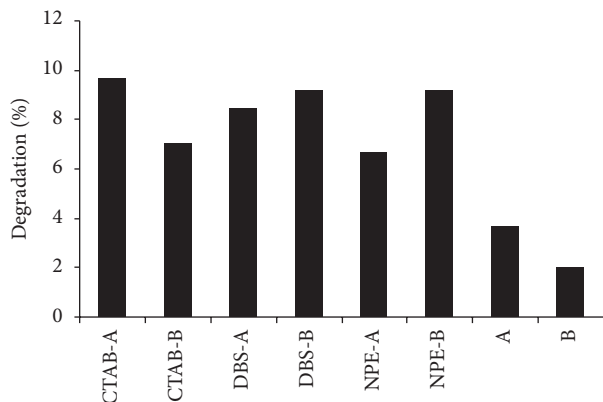
Figure 9: Photocatalytic activity of the current catalysts for naphthalene degradation.

Conflict of Interests

The authors declare that there is no conflict of interests regarding the publication of this paper.

References

[1] G. Tang, S. Liu, H. Tang, D. Zhang, C. Li, and X. Yang, "Template-assisted hydrothermal synthesis and photocatalytic activity of novel TiO_2 hollow nanostructures," *Ceramics International*, vol. 39, pp. 4969–4974, 2013.

[2] T. Suprabha, H. G. Roy, J. Thomas, K. Praveen Kumar, and S. Mathew, "Microwave-assisted synthesis of titania nanocubes, nanospheres and nanorods for photocatalytic dye degradation," *Nanoscale Research Letters*, vol. 4, no. 2, pp. 144–152, 2009.

[3] G. Cappelletti, S. Ardizzone, C. L. Bianchi et al., "Photodegradation of pollutants in air: enhanced properties of nano-TiO_2 prepared by ultrasound," *Nanoscale Research Letters*, vol. 4, no. 2, pp. 97–105, 2009.

[4] J. Yu, M. Jaroniec, and G. Lu, "TiO_2 photocatalytic materials," *International Journal of Photoenergy*, vol. 2013, Article ID 534164, 2 pages, 2013.

[5] A. Mills, N. Elliott, I. P. Parkin, S. A. O'Neill, and R. J. Clark, "Novel TiO_2 CVD films for semiconductor photocatalysis," *Journal of Photochemistry and Photobiology A*, vol. 151, no. 1–3, pp. 171–179, 2002.

[6] D.-S. Lee and T.-K. Liu, "Preparation of TiO_2 sol using $TiCl_4$ as a precursor," *Journal of Sol-Gel Science and Technology*, vol. 25, no. 2, pp. 121–136, 2002.

[7] Y. K. Hwang, K. C. Lee, and Y. U. Kwon, "Nanoparticle routes to mesoporous titania thin films," *Journal of Chemical Communications*, vol. 18, pp. 1738–1739, 2001.

[8] N. Idrissi-Kandri, A. Ayral, M. Klotz et al., "Porous alumina thin layers using mesophase templating," *Materials Letters*, vol. 50, no. 2-3, pp. 57–60, 2001.

[9] J. H. Park, I. Jang, K. Song, and S. G. Oh, "Surfactants-assisted preparation of TiO_2-Mn oxide composites and their catalytic activities for degradation of organic pollutant," *Journal of Physics and Chemistry of Solids*, vol. 74, pp. 1056–1062, 2013.

[10] A. E. Shalan, M. M. Rashad, Y. Yu, M. Lira-Cantú, and M. S. A. Mottaleb, "A facile low temperature synthesis of TiO_2 nanorods for high efficiency dye sensitized solar cells," *Applied Physics A*, vol. 110, pp. 111–122, 2013.

[11] H. Naono, M. Hakuman, T. Tsunehisa, N. Tamura, and K. Nakai, "Formation process of MCM-41 precursor and porous texture of MCM-41," *Journal of Colloid and Interface Science*, vol. 224, no. 2, pp. 358–365, 2000.

[12] J. N. McDougal, D. L. Pollard, W. Weisman, C. M. Garrett, and T. E. Miller, "Assessment of skin absorption and penetration of JP-8 jet fuel and its components," *Toxicological Sciences*, vol. 55, no. 2, pp. 247–255, 2000.

[13] P. J. J. Alvarez and W. A. Illman, *Bioreinediation and Natural Attenuation. Process Ftuiclamentals and Mathematical Models*, John Wiley & Sons, Hoboken, NJ, USA, 2006.

[14] R. N. Landau, S. C. Korré, M. Neurock, and M. T. Kline, in *Catalytic Hydroprocessing of PetroleumDistillates*, M. T. Oballa and S. S. Shih, Eds., pp. 421–432, Marcel Dekker, New York, NY, USA, 1994.

[15] S. J. Masten and S. H. R. Davies, "Efficacy of in-situ ozonation for the remediation of PAH contaminated soils," *Journal of Contaminant Hydrology*, vol. 28, no. 4, pp. 327–335, 1997.

[16] L. Zhang, P. Li, Z. Gong, and X. Li, "Photocatalytic degradation of polycyclic aromatic hydrocarbons on soil surfaces using TiO_2 under UV light," *Journal of Hazardous Materials*, vol. 158, no. 2-3, pp. 478–484, 2008.

[17] X.-W. Zhang, S.-C. Shen, L. E. Yu, S. Kawi, K. Hidajat, and K. Y. Simon Ng, "Oxidative decomposition of naphthalene by supported metal catalysts," *Applied Catalysis A*, vol. 250, no. 2, pp. 341–352, 2003.

[18] P. R. Gogate and A. B. Pandit, "A review of imperative technologies for wastewater treatment I: oxidation technologies at ambient conditions," *Advances in Environmental Research*, vol. 8, no. 3-4, pp. 501–551, 2004.

[19] E. N. Ndifor, T. Garcia, and S. H. Taylor, "Naphthalene oxidation over vanadium-modified Pt catalysts supported on γ-Al_2O_3," *Catalysis Letters*, vol. 110, no. 1-2, pp. 125–128, 2006.

[20] A. Lair, C. Ferronato, J.-M. Chovelon, and J.-M. Herrmann, "Naphthalene degradation in water by heterogeneous photocatalysis: an investigation of the influence of inorganic anions," *Journal of Photochemistry and Photobiology A*, vol. 193, no. 2-3, pp. 193–203, 2008.

[21] T. Ohno, K. Tokieda, S. Higashida, and M. Matsumura, "Synergism between rutile and anatase TiO_2 particles in photocatalytic oxidation of naphthalene," *Applied Catalysis A*, vol. 244, no. 2, pp. 383–391, 2003.

[22] H. Choi, E. Stathatos, and D. D. Dionysiou, "Synthesis of nanocrystalline photocatalytic TiO_2 thin films and particles using sol-gel method modified with nonionic surfactants," *Thin Solid Films*, vol. 510, no. 1-2, pp. 107–114, 2006.

[23] W.-W. Jian, Z.-X. Kang, and Y.-Y. Li, "Effect of hot plastic deformation on microstructure and mechanical property of Mg-Mn-Ce magnesium alloy," *Transactions of Nonferrous Metals Society of China*, vol. 17, no. 6, pp. 1158–1163, 2007.

[24] G. N. Shao, G. Elineema, D. V. Quang et al., "Two step synthesis of a mesoporous titania-silica composite from titanium oxychloride and sodium silicate," *Powder Technology*, vol. 217, pp. 489–496, 2012.

[25] R. Parra, M. S. Góes, M. S. Castro, E. Longos, P. R. Bueno, and J. A. Varela, "Reaction pathway to the synthesis of anatase via the chemical modification of titanium isopropoxide with acetic acid," *Chemistry of Materials*, vol. 20, no. 1, pp. 143–150, 2008.

[26] C. S. Lim, J. H. Ryu, D.-H. Kim, S.-Y. Cho, and W.-C. Oh, "Reaction morphology and the effect of ph on the preparation of TiO_2 nanoparticles by a sol-gel method," *Journal of Ceramic Processing Research*, vol. 11, no. 6, pp. 736–741, 2010.

[27] Y. Hu, H.-L. Tsai, and C.-L. Huang, "Effect of brookite phase on the anatase-rutile transition in titania nanoparticles," *Journal of the European Ceramic Society*, vol. 23, no. 5, pp. 691–696, 2003.

[28] T. Guohui, F. Honggang, J. Liqiang, X. Baifu, and P. Kai, "Preparation and characterization of stable biphase TiO$_2$ photocatalyst with high crystallinity, large surface area, and enhanced photoactivity," *Journal of Physical Chemistry C*, vol. 112, no. 8, pp. 3083–3089, 2008.

[29] B. Guo, H. Shen, K. Shu, Y. Zeng, and W. Ning, "The study of the relationship between pore structure and photocatalysis of mesoporous TiO$_2$," *Journal of Chemical Sciences*, vol. 121, no. 3, pp. 317–321, 2009.

[30] S. Nakade, M. Matsuda, S. Kambe et al., "Dependence of TiO$_2$ nanoparticle preparation methods and annealing temperature on the efficiency of dye-sensitized solar cells," *Journal of Physical Chemistry B*, vol. 106, no. 39, pp. 10004–10010, 2002.

[31] K. Chen, J. Li, W. Wang, Y. Zhang, X. Wang, and H. Su, "Effects of surfactants on microstructure and photocatalytic activity of TiO$_2$ nanoparticles prepared by the hydrothermal method," *Materials Science in Semiconductor Processing*, vol. 15, no. 1, pp. 20–26, 2012.

[32] M. M. Mohamed, W. A. Bayoumy, M. Khairy, and M. A. Mousa, "Synthesis and structural characterization of TiO$_2$ and V$_2$O$_5$/ TiO$_2$ nanoparticles assembled by the anionic surfactant sodium dodecyl sulfate," *Microporous and Mesoporous Materials*, vol. 97, no. 1–3, pp. 66–77, 2006.

[33] V. Štengl, V. Houšková, N. Murafa, and S. Bakardjieva, "Synthesis of mesoporous titania by homogeneous hydrolysis of titania oxo-sulfate in the presence of cationic and anionic surfactants," *Ceramics*, vol. 54, no. 4, pp. 368–378, 2010.

[34] S. Lowell and J. E. Shields, *Powder Surface Area and Porosity*, Chapman & Hall, London, UK, 1992.

[35] S. C. Lee, H. U. Lee, S. M. Lee et al., "Preparation and characterization of bicrystalline TiO$_2$ photocatalysts with high crystallinity and large surface area," *Journal of Materials Letters*, vol. 79, pp. 191–194, 2012.

[36] T.-Z. Ren, Z.-Y. Yuan, and B.-L. Su, "Surfactant-assisted preparation of hollow microspheres of mesoporous TiO$_2$," *Chemical Physics Letters*, vol. 374, no. 1-2, pp. 170–175, 2003.

[37] R. Sasikala, V. Sudarsan, C. Sudakar, R. Naik, L. Panicker, and S. R. Bharadwaj, "Modification of the photocatalytic properties of self doped TiO$_2$ nanoparticles for hydrogen generation using sunlight type radiation," *International Journal of Hydrogen Energy*, vol. 34, no. 15, pp. 6105–6113, 2009.

[38] D. C. Hurum, A. G. Agrios, K. A. Gray, T. Rajh, and M. C. Thurnauer, "Explaining the enhanced photocatalytic activity of Degussa P25 mixed-phase TiO$_2$ using EPR," *Journal of Physical Chemistry B*, vol. 107, no. 19, pp. 4545–4549, 2003.

[39] P. R. Mishra and O. N. Srivastava, "On the synthesis, characterization and photocatalytic applications of nanostructured TiO$_2$," *Bulletin of Materials Science*, vol. 31, no. 3, pp. 545–550, 2008.

[40] D. Morris, Y. Dou, J. Rebane et al., "Photoemission and STM study of the electronic structure of Nb-doped TiO$_2$," *Physical Review B*, vol. 61, no. 20, pp. 13445–13457, 2000.

[41] D. L. Liao, C. A. Badour, and B. Q. Liao, "Preparation of nano-sized TiO$_2$/ZnO composite catalyst and its photocatalytic activity for degradation of methyl orange," *Journal of Photochemistry and Photobiology A*, vol. 194, no. 1, pp. 11–19, 2008.

[42] A. Di Paola, G. Cufalo, M. Addamo et al., "Photocatalytic activity of nanocrystalline TiO$_2$ (brookite, rutile and brookite-based) powders prepared by thermohydrolysis of TiCl$_4$ in aqueous chloride solutions," *Colloids and Surfaces A*, vol. 317, no. 1–3, pp. 366–376, 2008.

[43] B. O'Regan and M. Grätzel, "A low-cost, high-efficiency solar cell based on dye-sensitized colloidal TiO$_2$ films," *Nature*, vol. 353, no. 6346, pp. 737–740, 1991.

[44] Y. Chen, K. Wang, and L. Lou, "Photodegradation of dye pollutants on silica gel supported TiO$_2$ particles under visible light irradiation," *Journal of Photochemistry and Photobiology A*, vol. 163, no. 1-2, pp. 281–287, 2004.

[45] H. Hao and J. Zhang, "Low temperature synthesis of crystalline mesoporous titania with high photocatalytic activity by post-treatment in nitric acid ethanol solution," *Materials Letters*, vol. 63, no. 1, pp. 106–108, 2009.

Research Article

The Influence of Lead Concentration on Photocatalytic Reduction of Pb(II) Ions Assisted by Cu-TiO$_2$ Nanotubes

Srimala Sreekantan,[1] Chin Wei Lai,[2] and Syazwani Mohd Zaki[1]

[1] *School of Materials and Mineral Resources Engineering, Universiti Sains Malaysia, Engineering Campus, Seberang Perai Selatan, 14300 Nibong Tebal, Pulau Pinang, Malaysia*

[2] *Nanotechnology & Catalysis Research Centre (NANOCAT), 3rd Floor, Block A, Institute of Postgraduate Studies (IPS), University of Malaya, 50603 Kuala Lumpur, Malaysia*

Correspondence should be addressed to Srimala Sreekantan; srimala@eng.usm.my

Cu^{2+} ions were successfully loaded into TiO$_2$ nanotubes using wet impregnation technique in 0.6 M Cu(NO$_3$)$_2$·3H$_2$O solution. The effect of reaction temperatures on the nanotube's morphology, crystal structure, and their photocatalytic reduction of Pb(II) ions were investigated. The high reaction temperature could improve the crystallinity of anatase phase. However, irregular and corrugated nanotubular surface covered with Cu precipitates was observed. In the present study, incorporation of an optimum content of Cu element (1.3 at%) into TiO$_2$ nanotubes at room temperature has an important function in enhancing the photocatalytic reduction of Pb(II) ions in alkaline condition (pH 11) due to the higher synergistic effects of photocatalytic reaction under UV illumination. The optimum concentration of Pb(II) ions for effective Pb(II) ions removal performance was found in between 20 and 60 ppm.

1. Introduction

Nowadays, toxic heavy metals are the major contaminants of electronic waste. It is a well-known fact that those heavy metals are elements having high atomic weights between 63.5 and 200.6 and a specific gravity greater than 5.0 [1]. Heavy metal contaminations in the aquatic environment including arsenic (As), cadmium (Cd), lead (Pb), chromium (Cr), copper (Cu), nickel (Ni), zinc (Zn), and mercury (Hg) pose an ecotoxicological effect to living creatures [2–4]. Some of these heavy metal contaminations come from fertilizer and sewage, but the biggest source is the effluent industrial discharged from various industries such as electronic industry, mining, electroplating, and battery manufacturing [5]. Since heavy metal contaminations cause serious health effect, wastewater regulations were established to minimize human and environmental exposure to hazardous chemical. The summary of various heavy metals and their permitted concentration is shown in Table 1.

Among various heavy metal contaminations shown in Table 1, Pb is our special concern due to persistency and recalcitrant of Pb in the environment. According to World Environmental Protection (WEP), Pb accounts for 98% of the total disposal or other releases of persistent, bioaccumulative, and toxic (PBT) chemicals. In addition, US Environmental Protection Agency (EPA) has reported that the disposal or other releases of PBT chemicals increased by 50%, mainly due to increases in Pb and Pb compounds [6]. The total disposal or other releases of Pb and Pb compounds were increased about 51% in 2010. Thus, Pb contaminants need urgent attention in order to save the environment and to overcome the adverse health risk of mankind [7, 8].

In this manner, various remediation methods such as precipitation-filtration, ion-exchange, reverse osmosis, oxidation reduction, electrochemical recovery, and membrane separation are commonly used to treat those heavy metal contaminations [5, 8, 9]. However, among all of the available methods, photocatalytic emerged as a promising advance

TABLE 1: The maximum contaminant level (MCL) standard for the most hazardous heavy metal [4].

Heavy metal	Toxicities	MCL (ppm)
As	Skin manifestations, visceral cancers, vascular disease	0.050
Cd	Kidney damage, renal disorder, human carcinogen	0.01
Cr	Headache, diarrhea, nausea, vomiting, carcinogenic	0.05
Cu	Liver damage, Wilson disease, insomnia	0.25
Ni	Dermatitis nausea, chronic asthma, coughing, human carcinogen	0.20
Zn	Depression, lethargy, neurological signs, and increased thirst	0.80
Pb	Damage the fetal brain, diseases of kidney, circulatory system, and nervous system	0.005
Hg	Rheumatoid arthritis and diseases of kidneys, circulatory and nervous system.	0.00003

technique because it is able to destroy and transform variety of pollutants by oxidative or reductive mechanism and converting them into nontoxic wastes [10–12]. Removal of lead from solutions by photocatalysis using irradiated platinized TiO_2 was carried out by Kabra et al. Lead was found reduced to PbO on the platinum islands and also oxidized to PbO_2 by a valence band process as well as by oxygen radical species. Thus, the advance photocatalytic reduction technique was believed to be capable of removing heavy metal contaminants to low concentration of less than 20 ppm [8]. In this case, titanium dioxide (TiO_2) is regarded as one of the most efficient and environmentally benign photocatalysts for reducing the heavy metal contaminants [13–16]. However, it still exhibit several intrinsic drawbacks, which limit its widespread technological applications [13, 17, 18]. Titanium dioxide photocatalysis has been demonstrated to be a promising method for the pollutant treatment mainly due to its capability of removing metal ions and complete mineralization or at least partly destroying a variety of organic pollutants.

Basically, TiO_2 is widely used in many applications such as water purification, to remove volatile organic compound, water electrolysis, painting, and many more. The major advantages of this TiO_2 photocatalysis are as follows.

(i) Photocatalysis offers a good substitute for the energy-intensive conventional treatment methods with the capacity for using renewable and pollution-free solar energy.

(ii) Unlike conventional treatment measures which transfer pollutants from one medium to another, photocatalysis leads to the formation of innocuous products.

(iii) This process can be used to destroy a variety of hazardous compounds in different wastewater streams.

(iv) It can be applied to aqueous and gaseous-phase treatments, as well as solid-soil phase treatments to some extent.

However, the use of pure TiO_2 has several drawbacks, such as poor visible light absorption and high recombination losses of the photo-induced electron-hole pairs [13, 17–20]. Many studies have highlighted that the coupling mechanism between the Cu^{2+} ions and TiO_2 could facilitate better charge carrier separation in improving the photocatalytic performance [21–23]. However, most of these studies involved incorporation of Cu^{2+} ions into TiO_2 photocatalysts in the form of particles/spheres or thin films, which do not possess high enough surface area for photon absorption [24, 25]. Moreover, most scholars mainly focused on the photo degradation of organic pollutants rather than the inorganic pollutants. The detail studies regarding Pb(II) ions removal at low concentration using photocatalytic activity are still lacking. Thus, a comprehensive study is essential to be explored by optimizing the reaction temperature of wet impregnation to obtain the preferred Cu-TiO_2 nanotubes, resulting in the best performance of Pb(II) removal. Detail studies regarding the synergistic relationship of Cu^{2+} ions incorporated into TiO_2 nanotubes and its application on Pb(II) ions removal have been established in this work.

2. Experimental Procedure

High purity of titanium (Ti) foils (99.6% purity, STREM Chemicals) with thickness of 0.127 mm was used in the present study. The Ti foils (50 mm × 10 mm) were degreased by using sonication in ethanol for 30 min prior to electrochemical anodization process. Then, the Ti foil was placed in 100 mL ethylene glycol electrolyte (99% purity, Merck) composed of 5 wt % ammonium fluoride (NH_4F) (98% purity, Merck) and 1 vol% of hydrogen peroxide (H_2O_2) (30% H_2O_2 and 70% H_2O; J.T. Baker) at 60 V for 1 h. The electrolyte composition was fixed because it favors the formation of highly ordered TiO_2 nanotubes [26, 27]. Two electrodes configuration bath with Ti foil as anode and a platinum rod as cathode was prepared to conduct the electrochemical anodization. The as-anodized Ti foil was washed using distilled water and then dried in a nitrogen stream for 15 min. Next, the as-anodized Ti foil was annealed at 400°C in an argon atmosphere for 4 h. In the present study, the incorporation of copper (Cu^{2+}) ions was conducted by immersing the annealed Ti foil in an optimized 0.6 M copper(II) nitrate trihydrate [$Cu(NO_3)_2 \cdot 3H_2O$] solution (Merck) for 1 h at different reaction temperatures (room temperature, 27°C, 60°C, and 80°C). Subsequently, the resultant sample conducted heat treatment process at 400°C for 4 h under argon gas atmosphere. The main purpose of heat treatment process was obtained high crystalline phases of Cu-TiO_2. The removal rate of Pb(II) ions (Merck at 1000 mg/L of concentration) was determined by using Atomic Absorption Spectrometer (AAS) AAnalyst 700. The measurement of Pb(II) ions absorption was measured after exposing to the UV light (120 W germicidal light) for 5 hours. The changes of the initial and final concentration after photocatalytic
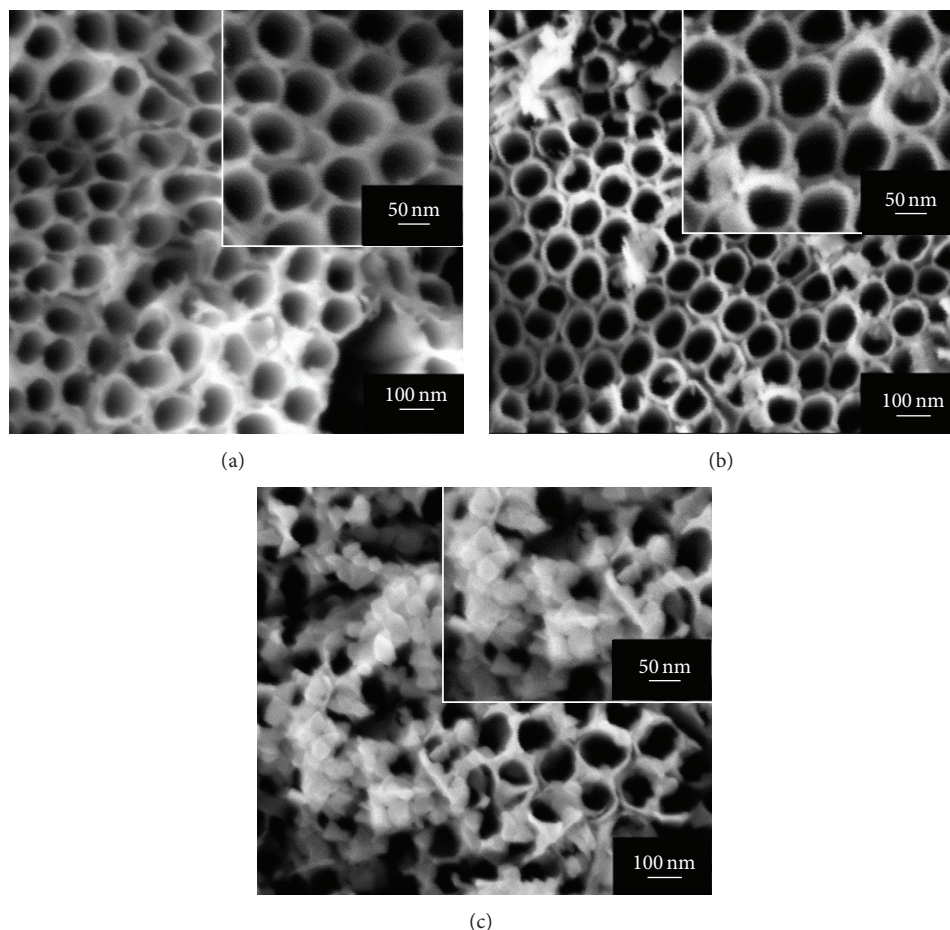
FIGURE 1: FESEM morphology of Cu-TiO$_2$ nanotubes prepared at (a) room temperature, (b) 60°C, and (c) 80°C in an optimize 0.6 M copper(II) nitrate trihydrate [Cu(NO$_3$)$_2$·3H$_2$O] solution for 1 h.

activity were observed and measured. The morphologies of the nanotubes were observed by field emission scanning electron microscopy (FESEM) using a Zeiss SUPRA 35VP at a working distance of 1 mm. The element analysis of Cu^{2+} ions incorporated into TiO$_2$ was determined with Energy Dispersive X-ray (EDX) which is equipped in the FESEM. X-ray diffraction (XRD) was used to attain information about the structure and percentage of crystallinity of the anodized Ti foils and also sample that undergone annealing process. The phase identification of TiO$_2$ was done by using Philip model PW 1729, which was operated at 40 kV and 40 mV.

3. Results and Discussions

In this part of the experimental study, the effect of reaction temperatures on the Cu^{2+} ions loaded on pristine TiO$_2$ nanotubes is discussed. It is a well-known fact that reaction temperatures during the wet impregnation have profound effect on various chemical processes. The reaction temperature affects the adsorption rate by altering the molecular interactions and the solubility of the adsorbate [28]. Figures 1(a) to 1(c) show the morphology of Cu-TiO$_2$ nanotubes prepared at room temperature, 60°C, and 80°C,
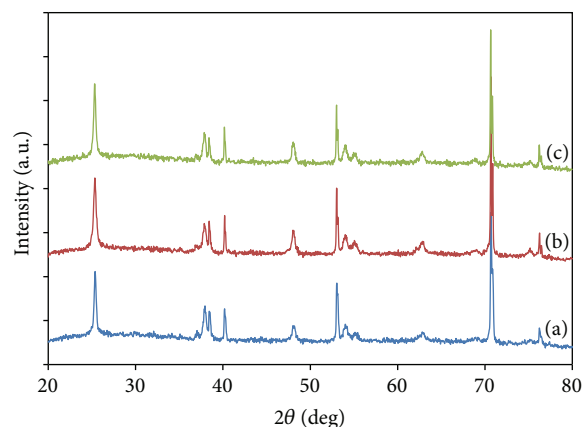

FIGURE 2: XRD patterns for postannealed Cu-TiO$_2$ nanotubes prepared at (a) room temperature, (b) 60°C, and (c) 80°C in an optimize 0.6 M copper(II) nitrate trihydrate [Cu(NO$_3$)$_2$·3H$_2$O] solution for 1 h.

respectively. As shown in the FESEM images, the pore opening of TiO$_2$ nanotubes synthesized at 60°C showed the almost similar appearance to the sample synthesized at
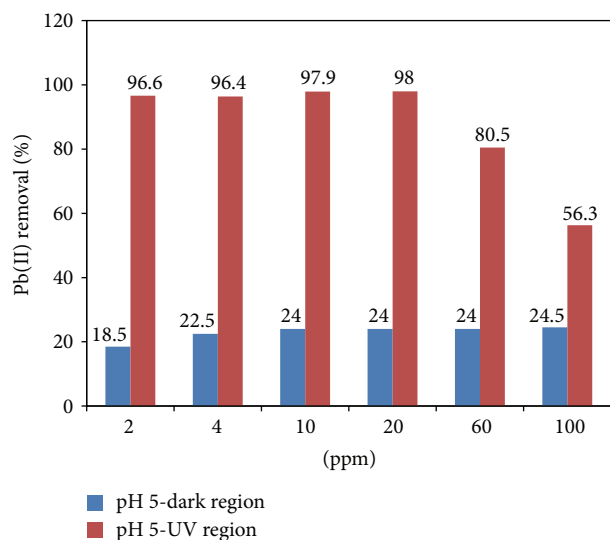
Figure 3: Percentage (%) of Pb(II) removal by Cu-TiO$_2$ nanotubes at pH 5 with different concentration of Pb(II).
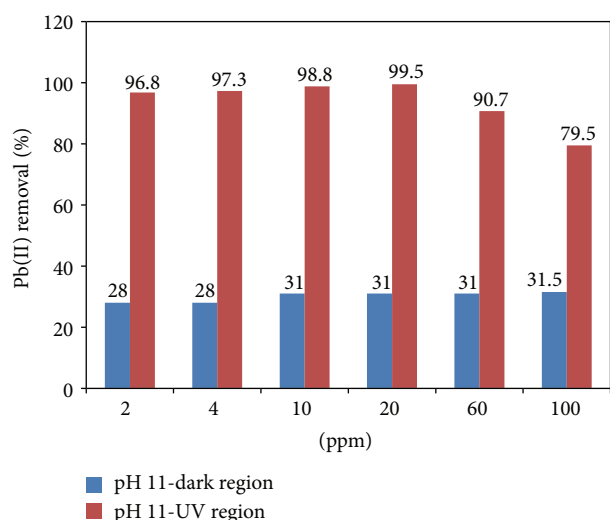

Figure 4: Percentage (%) of Pb(II) removal by Cu-TiO$_2$ nanotubes at pH 11 with different concentration of Pb(II).

sample prepared at 60°C and 80°C was increased to 2.0 at% and 2.9 at%, respectively (not shown). Based on the results obtained, it could be deduced that as the reaction temperature was increased, at% of Cu element loaded in TiO$_2$ nanotubes was increased significantly. By incorporating Cu into titania matrix, new active sites will be introduced and enhance visible light absorption capacity. Both Cu^{2+} and Cu$^+$ can act as effective electron scavenger which resulted in better separation between electron and hole and more free holes are available for oxidation process. Cu^{2+} can act as electron trapper since its reduction potential is more positive than the conduction band of band edge of TiO$_2$. The trapping of electrons by Cu^{2+} and the trapping of holes by its reduced form were proposed to explain the decrease of the electron hole recombination rate and a higher production of HO$^\bullet$ radicals [29]. In the present study, the influence of reaction temperature on the crystal structure of Cu-TiO$_2$ nanotubes was investigated via XRD measurement. The resultant XRD patterns of TiO$_2$ nanotubes prepared at different temperature after photocatalysis are shown in Figure 2. As demonstrated in the XRD patterns, peaks of anatase phase TiO$_2$ were at 2θ of 25.37°, 38.67°, 48.21°, and 54.10°, which corresponded to (101), (112), (200), and (105) crystal planes, respectively [30]. However, no obvious Cu phases could be detected from the XRD patterns although the percentage of Cu has exceeded 2 at%. This result manifested that Cu dopants existed in amorphous form. Besides, it could be noticed that the intensity of the (101) peak at 25.3° was increased by increasing the reaction temperature environment, indicating an increase in crystallinity of anatase phase for Cu-TiO$_2$ nanotubes. The possible improvement in the crystallization anatase structure at 60°C and 80°C could be explained with solid-state mechanism [10, 11]. The adsorption of OH$^-$ ions from water molecule on the surface of nanotubes was accelerated at high temperature. The adsorbed-OH$^-$ ions subsequently reacted with the titanium (Ti^{3+}) ions in amorphous TiO$_2$ nanotubes. Ti^{3+} was obtained during irradiation whereby, the electrons are captured by titanium ions (Ti^{4+} + e$^-$), leading to the formation of paramagnetic Ti^{3+} ions [31]. This forms bridges between surface OH groups of different octahedral of TiO$_6$ within the lattice that shared common vertex. The dehydration consequently occurred and the structure of two octahedral sharing with one edge was formed in order to form anatase phase. Based on the aforementioned results, increasing the reaction temperatures benefits the crystallization of nanotubes but never benefits the incorporation of Cu^{2+} dopants evenly to the nanotubes. Thus, the Cu-TiO$_2$ nanotubes prepared at room temperature were duplicated for the photocatalytic oxidation of Pb(II) ions study [32, 33].

pH at acidic and alkaline condition was selected and evaluated. The performance of Pb(II) ions removal using Cu-TiO$_2$ nanotubes at pH 5 and pH 11 was further investigated. Results also showed that the rates of the photocatalytic reduction of lead increased with pH. This effect was due to both reduction process and hydroxide precipitation. The initial concentration of Pb(II) solution was varied from 2 ppm, 4 ppm, 10 ppm, 20 ppm, 60 ppm, and 100 ppm. It is noteworthy to mention that the removal of Pb(II) ions is

room temperature. The average diameter of the open pores is about 80 nm. Interestingly, it could be observed that an irregular and corrugated nanotubular surface covered with Cu precipitates after synthesizing at reaction temperature at 80°C. Some of the nanotubular pore entrances was completely blocked with Cu precipitates. The reason might be attributed to the capability of Cu^{2+} ions to diffuse into the lattice of TiO$_2$ nanotubes was drastically accelerated and when it exceeds its saturation limits, the Cu^{2+} ions started to precipitate on the nanotubes surface. The incorporation of Cu^{2+} ions on pristine TiO$_2$ nanotubes was further demonstrated by the EDX analysis, which exhibited the presence of Cu element of about 1.30 at % for the sample prepared at room temperature. In addition, other elements such as Ti, C, and O were traced in the EDX spectrum. At% of the Cu element within the

The initial PbO/Pb(OH)$_2$ layer formed further retards the OH$^-$ and O^{2-} penetration and hinders the Pb attachment for further removal

>60 ppm-lack of active site for Pb(II) attachment

Pb^{2+}

OH$^-$

O^{2-}

<20 ppm-more active site available for Pb(II) attachment for PbO formation.
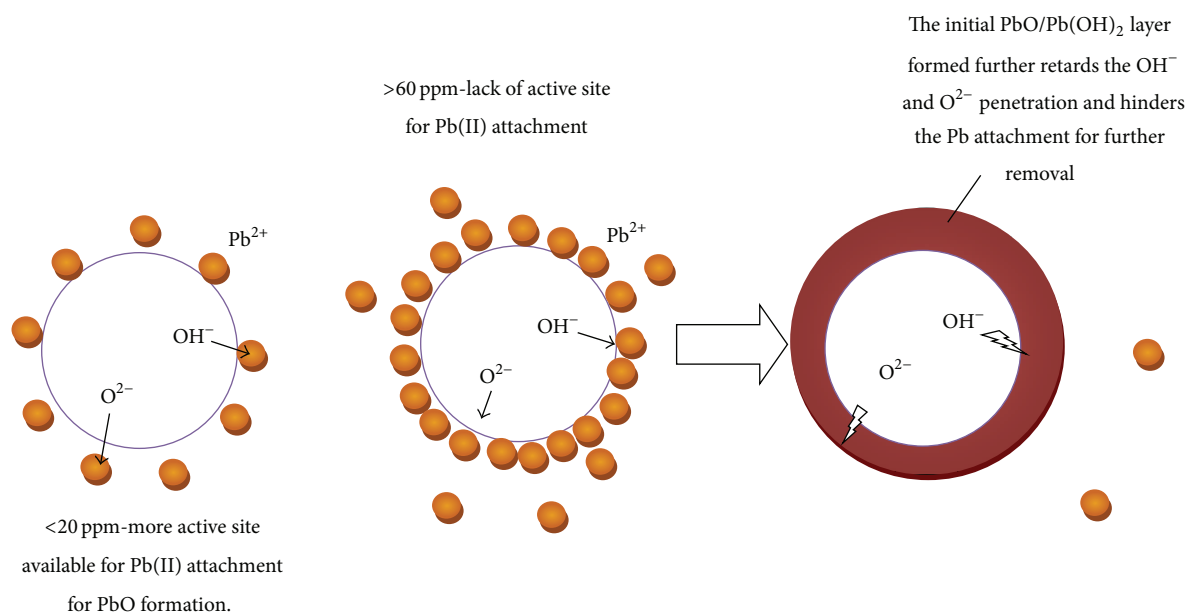
FIGURE 5: Schematic diagram illustrating that the formation of PbO/PbOH layer on TiO$_2$ retards the photocatalytic reaction for more Pb(II) removal.
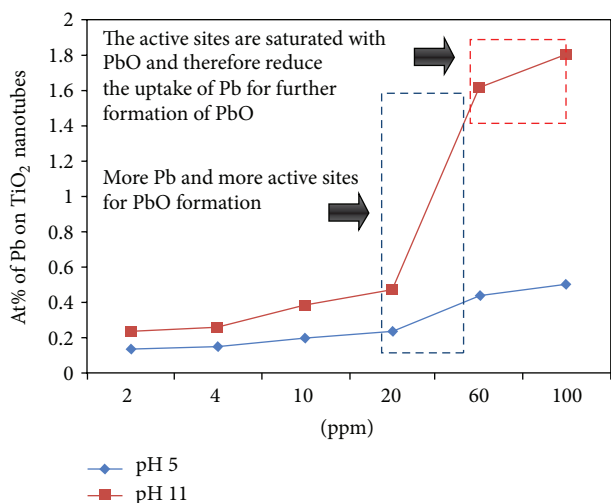

FIGURE 6: Atomic percentage (at%) of Pb on TiO$_2$ nanotubes at different concentration of Pb(II).

high with UV illumination as compared to dark environment regardless to pH 5 (Figure 3) or pH 11 (Figure 4). This clearly indicates that resultant Cu-TiO$_2$ nanotubes as active photocatalyst could be regarded as an applicable process for Pb(II) ions treatment. However, it was found that the Pb(II) ions removal in dark environment was greater at pH 11 as compared to pH 5. It is relevant to note that at pH value above 6, direct reaction within the OH$^-$ in base condition with free Pb(II) ions would be enhanced. As a result, Pb hydroxide complexes such as Pb(OH)$^+$, Pb(OH)$_2$, and Pb(OH)$_3$ could also be formed, which then precipitate from solution. This would reduce the remnant Pb(II) in the solution of pH 11 to greater extent as compared to pH 5. The similar trend could be observed when UV illumination was applied in the

Pb(II) ions treatment. The Pb(II) ions removal was much better for pH 11 as compared to pH 5. So the synergistic effects of photocatalytic reaction under UV illumination with formation of precipitates at pH 11 would reduce the total remnant Pb(II) ions in the solution to greater extent than pH 5 (which only subjected to photocatalytic reaction) [34]. This explains the results obtained at 100 ppm, whereby the percentage of removal of Pb at pH 11 is 79.5%, while at pH 5 was 56.3%. Other than that, the removal of Pb(II) ions under UV illumination was found high up to 20 ppm and slowly reduced after 60 ppm. This could be due to active surface of phorocatalyst available on the surface of the TiO$_2$ nanotubes to attract Pb(II) ions for photocatalytic reaction is sufficient to remove 20 ppm of Pb(II) ions. However, at 60 ppm the removal of Pb(II) ions dropped to 80.5 and at 100 ppm to 56.3%. The reason might be attributed to the lack of active surface for Pb(II) ions attachment for photocatalytic reaction at high concentration and thick initial layer of PbO after photocatalytic reaction that hindered further diffusion of OH$^-$ and O^{2-} ions for reduction of Pb(II). This is schematically illustrated in Figure 5 and was further affirmed with EDX analysis plotted in Figure 6. The results demonstrated that Pb content at the surface of the nanotubes was changing abruptly within 20 ppm to 60 ppm and then slowed down after 60 ppm onwards. This explains the results obtained at 100 ppm, which showed low percentage of Pb(II) ions removal. So the optimum concentration of Pb(II) that is suitable for photocatalytic reaction would be within 20–60 ppm. Additionally, these Cu-TiO$_2$ nanotubes can be reused and need further investigation.

4. Conclusion

In summary, Cu-TiO$_2$ nanotubes were successfully prepared using electrochemical anodization and wet impregnation

techniques. The reaction temperature environment during wet impregnation played an important role in the morphological control and content of Cu^{2+} dopants diffused into the TiO_2 nanotubes. It was found that at% of Cu^{2+} ions loaded into TiO_2 nanotubes was increased significantly with increasing reaction temperatures. An irregular and corrugated nanotubular surface covered with Cu precipitates was observed under high reaction temperature of 80°C. In the present study, Cu-TiO_2 nanotubes were prepared at room temperature for the photocatalytic oxidation of Pb(II) ions removal. It was noticed that the Pb(II) ions removal performance was greater at pH 11 as compared to pH 5 under UV illumination and assisted by Cu-TiO_2 nanotubes due to the more direct reactions within the OH^- in base condition with free Pb(II) ions. In addition, our results show that the Pb content at the surface of the nanotubes was changing abruptly within 20 ppm to 60 ppm and then slowed down after 60 ppm onwards. Thus, the optimum concentration of Pb(II) ions for effective Pb(II) ions removal performance was 20–60 ppm.

Conflict of Interests

The authors declare that there is no conflict of interests regarding the publication of this paper.

Acknowledgments

References

[1] N. K. Srivastava and C. B. Majumder, "Novel biofiltration methods for the treatment of heavy metals from industrial wastewater," *Journal of Hazardous Materials*, vol. 151, no. 1, pp. 1–8, 2008.

[2] A. Ibitz, "Environmental policy coordination in ASEAN: the case of waste from electrical and electronic equipment," *Austrian Journal of South-East Asian Studies*, vol. 5, p. 30, 2012.

[3] S. Sthiannopkao and M. H. Wong, "Handling e-waste in developed and developing countries: initiatives, practices, and consequences," *Science of the Total Environment*, vol. 463, p. 1147, 2013.

[4] S. Babel and T. A. Kurniawan, "Low-cost adsorbents for heavy metals uptake from contaminated water: a review," *Journal of Hazardous Materials*, vol. 97, no. 1–3, pp. 219–243, 2003.

[5] M. A. Barakat, "New trends in removing heavy metals from industrial wastewater," *Arabian Journal of Chemistry*, vol. 4, no. 4, pp. 361–377, 2011.

[6] ICF 2011, *Electronics Waste Management in the United States Through 2009*, U.S. Environmental Protection Agency.

[7] L. Murruni, F. Conde, G. Leyva, and M. I. Litter, "Photocatalytic reduction of Pb(II) over TiO_2: new insights on the effect of different electron donors," *Applied Catalysis B*, vol. 84, no. 3-4, pp. 563–569, 2008.

[8] K. Kabra, R. Chaudhary, and R. L. Sawhney, "Treatment of hazardous organic and inorganic compounds through aqueous-phase photocatalysis: a review," *Industrial and Engineering Chemistry Research*, vol. 43, no. 24, pp. 7683–7696, 2004.

[9] R. O. Abdel Rahman, H. A. Ibrahium, and Y. T. Hung, "Liquid radioactive wastes treatment: a review," *Water*, vol. 3, p. 551, 2011.

[10] M. Kitano, M. Matsuoka, M. Ueshima, and M. Anpo, "Recent developments in titanium oxide-based photocatalysts," *Applied Catalysis A*, vol. 325, no. 1, pp. 1–14, 2007.

[11] A. L. Linsebigler, G. Lu, and J. T. Yates Jr., "Photocatalysis on TiO_2 surfaces: principles, mechanisms, and selected results," *Chemical Reviews*, vol. 95, no. 3, pp. 735–758, 1995.

[12] H. Tong, S. Ouyang, Y. Bi, N. Umezawa, M. Oshikiri, and J. Ye, "Nano-photocatalytic materials: possibilities and challenges," *Advanced Materials*, vol. 24, no. 2, pp. 229–251, 2012.

[13] Y.-C. Nah, I. Paramasivam, and P. Schmuki, "Doped TiO_2 and TiO_2 nanotubes: synthesis and applications," *ChemPhysChem*, vol. 11, no. 13, pp. 2698–2713, 2010.

[14] C. A. Grimes, "Synthesis and application of highly ordered arrays of TiO_2 nanotubes," *Journal of Materials Chemistry*, vol. 17, no. 15, pp. 1451–1457, 2007.

[15] Z. Su and W. Zhou, "Formation, morphology control and applications of anodic TiO_2 nanotube arrays," *Journal of Materials Chemistry*, vol. 21, no. 25, pp. 8955–8970, 2011.

[16] P. Roy, S. Berger, and P. Schmuki, "TiO_2 nanotubes: synthesis and applications," *Angewandte Chemie International Edition*, vol. 50, no. 13, pp. 2904–2939, 2011.

[17] C. W. Lai and S. Sreekantan, "Study of WO_3 incorporated C-TiO_2 nanotubes for efficient visible light driven water splitting performance," *Journal of Alloys and Compounds*, vol. 547, p. 43, 2013.

[18] X. Chen and S. S. Mao, "Titanium dioxide nanomaterials: synthesis, properties, modifications and applications," *Chemical Reviews*, vol. 107, no. 7, pp. 2891–2959, 2007.

[19] C. W. Lai and S. Sreekantan, "Preparation of hybrid WO_3-TiO_2 nanotube photoelectrodes using anodization and wet impregnation: improved water-splitting hydrogen generation performance," *International Journal of Hydrogen Energy*, vol. 38, p. 2156, 2013.

[20] H. Shon, S. Phuntsho, Y. Okour et al., "Visible light responsive titanium dioxide (TiO_2)," *Journal of the Korean Industrial and Engineering Chemistry*, vol. 19, no. 1, pp. 1–16, 2008.

[21] W. Zhang, Y. Li, S. Zhu, and F. Wang, "Copper doping in titanium oxide catalyst film prepared by dc reactive magnetron sputtering," *Catalysis Today*, vol. 93-95, pp. 589–594, 2004.

[22] B. Xin, P. Wang, D. Ding, J. Liu, Z. Ren, and H. Fu, "Effect of surface species on Cu-TiO_2 photocatalytic activity," *Applied Surface Science*, vol. 254, no. 9, pp. 2569–2574, 2008.

[23] S. Xu, A. J. Du, J. Liu, J. Ng, and D. D. Sun, "Highly efficient CuO incorporated TiO_2 nanotube photocatalyst for hydrogen production from water," *International Journal of Hydrogen Energy*, vol. 36, no. 11, pp. 6560–6568, 2011.

[24] J. Yan and F. Zhou, "TiO_2 nanotubes: structure optimization for solar cells," *Journal of Materials Chemistry*, vol. 21, no. 26, pp. 9406–9418, 2011.

[25] A. Kubacka, M. Fernández-García, and G. Colón, "Advanced nanoarchitectures for solar photocatalytic applications," *Chemical Reviews*, vol. 112, no. 3, pp. 1555–1614, 2012.

[26] C. W. Lai and S. Sreekantan, "Dimensional control of TiO_2 nanotube arrays with H_2O_2 content for high photoelectrochemical water splitting performance," *Micro & Nano Letters*, vol. 7, p. 443, 2012.

[27] S. Sreekantan, L. C. Wei, and Z. Lockman, "Extremely fast growth rate of TiO_2 nanotube arrays in electrochemical bath containing H_2O_2," *Journal of the Electrochemical Society*, vol. 158, no. 12, pp. C397–C402, 2011.

[28] M. Ahmaruzzaman and D. K. Sharma, "Adsorption of phenols from wastewater," *Journal of Colloid and Interface Science*, vol. 287, no. 1, pp. 14–24, 2005.

[29] M. I. Litter, "Heterogeneous photocatalysis: transition metal ions in photocatalytic systems," *Applied Catalysis B*, vol. 23, no. 2-3, pp. 89–114, 1999.

[30] C. A. Grimes and G. K. Mor, *Material Properties of TiO_2 Nanotube Arrays: Structural, Elemental, Mechanical, Optical and Electrical. TiO_2 Nanotube Arrays*, Springer, New York, NY, USA, 2009.

[31] L. N. Dias, M. V. B. Pinheiro, and K. Krambrock, "Radiation-induced defects in euclase: formation of O^- hole and Ti^{3+} electron centers," *Physics and Chemistry of Minerals*, vol. 36, no. 9, pp. 519–525, 2009.

[32] P. Yan and H. Bhadeshia, "Mechanism and kinetics of solid-state transformation in high-temperature processed linepipe steel," *Metallurgical and Materials Transactions A*, vol. 44, pp. 5468–5477, 2013.

[33] M. Rotan, E. Rytter, M.-A. Einarsrud, and T. Grande, "Solid state mechanism leading to enhanced attrition resistance of alumina based catalyst supports for Fischer-Tropsch synthesis," *Journal of the European Ceramic Society*, vol. 33, pp. 1–6, 2013.

[34] T. Kanki, H. Yoneda, N. Sano, A. Toyoda, and C. Nagai, "Photocatalytic reduction and deposition of metallic ions in aqueous phase," *Chemical Engineering Journal*, vol. 97, no. 1, pp. 77–81, 2004.